THE UNIVERSITY *of* EDINBURGH

Fibre Reinforced Polymer (FRP) Strengthened Masonry Arch Structures

Thesis submitted in fulfilment of the requirements for the degree of

Doctor of Philosophy

By

YI TAO

The University of Edinburgh

2012

DECLARATION

This thesis entitled “Fibre Reinforced Polymer (FRP) Strengthened Masonry Arch Structures” is submitted to the College of Engineering, The University of Edinburgh, for the degree of Doctor of Philosophy.

The work in this thesis was completed solely by Yi Tao, under the supervision of Dr. Jian-Fei Chen and Dr. Tim Stradford. Where other sources were used, full references are given.

Yi Tao

December 2012

ABSTRACT

Masonry arch bridges have played a significant role in the road and rail transportation network in the world for centuries. They are exposed to damage due to overloading and deterioration caused by environmental actions. In order to re-establish their performance and to prevent their collapse in various hazardous conditions, many of them require strengthening. Fibre reinforced polymer (FRP) systems are increasingly used for repair and strengthening of structures, with particularly widespread application to concrete structures. However, the application of FRP composites to masonry structures is less well established due to the complexity of masonry caused by the material discontinuity. FRP strengthening masonry arch bridges has been even less studied due to the additional complexity arising from the co-existence of the normal interfacial stress and the shear interfacial stress at the curved FRP-to-masonry bondline. This thesis presents an extensive study investigating the behaviour of FRP strengthened masonry bridges.

The study started with a laboratory test of a two span masonry arch bridge with sand backfill. A single ring arch bridge was first tested to near failure, and then repaired by bonding FRP into their intrados and tested to failure. It was found that the FRP strengthening not only improved the loading capacity and stiffness of bridge, but also significantly restrained the opening of cracks in the masonry. Shear and peeling debonding of FRP was observed.

There have been two common strategies in finite element (FE) modelling of FRP

strengthened structures in meso-scale: direct model and interface model. The former is necessary when investigating the detailed bond behaviour but challenges remain due to the difficulties in concrete modelling. A new concrete damage model based on the plastic degradation theory has been developed in this study to study the bond behaviour of FRP strengthened concrete structure. This robust model can successfully capture this bond behaviour and simulate the entire debonding process.

A numerical study of masonry arch bridges including the backfill was conducted to study the behaviour of masonry arch bridge. A total of four modelling strategies were examined and compared. Although they all can successfully predict the behaviour of arch, a detailed solid model newly developed in this study is more suitable for modelling both plain masonry and FRP strengthened structures.

Finally, a numerical study of bond behaviour and structural response of FRP strengthened masonry arch structures with sand backfill was conducted. In addition to the masonry and backfill, the mixed mode interfacial behaviour was modelled by the aforementioned interface model strategy and investigated in detail to achieve a deeper understanding of the behaviour of FRP strengthened masonry arch structures. The results are in close agreement with test results, and highlight the influence of the key parameters in the structural response to failure and revealed the mechanisms on how the load is transmitted through this complex multi-component structural system.

PUBLICATIONS

The following publications are based on the research presented in this thesis:

Tao, Y. and Chen, J.F. (2012). "Finite Element Modelling of FRP-to-Concrete bond behaviour", *Journal of Composites for Construction (ASCE), under review.*

Tao, Y., Chen, J.F. and Stratford, T. (2011). "Behaviour of a masonry arch bridge repaired using fibre-reinforced polymer composites". *Engineering Structures*; 2011, 33(5): 1594-1606.

Tao, Y., Chen, J.F., Stratford, T. and Ooi, J.Y. (2012). "Numerical Modelling Of A Large Scale Model Masonry Arch Bridge", *14th International Conference of Structural Faults and Repair 2012 (SF&R 2012),* Edinburgh, UK, 3rd – 5th July.

Tao, Y., Chen, J.F., Stratford, T. and Ooi, J.Y. (2012). "FE Modelling Techniques for Masonry Arch Bridges with Sand Backfill", *20th UK Conference of the Association for Computational Mechanics in Engineering (ACME 2012), Manchester, UK*, 26th-28th March.

Tao, Y. and Chen, J.F. (2011). "Modelling of FRP-to-Concrete Behaviour", *Proceedings of the 19th UK Conference of the Association for Computational Mechanics in Engineering (ACME 2011)*, Edinburgh, UK, April 5-6, pp125-128.

Chen, J.F. and Tao, Y. (2010). "Finite Element Modelling of FRP-to-Concrete Bond

Behaviour Using the Concrete Damage Plasticity Theory Combined with a Plastic Degradation Model", Keynote paper in *Proceedings of the 5th International Conference on FRP Composites in Civil Engineering (CICE 2010)*, Beijing, China, September 27-29, pp. 45-50.

Tao, Y., Chen, J.F. and Stratford, T. (2009). "Repair of a Model Masonry Arch Bridge using FRP", *Proceedings of 4th International Conference on Advanced Composites in Construction (ACIC 2009)*, Edinburgh, UK, September 1-3, pp. 426-436.

Tao, Y., Stratford, T., Li, X.Q. and Chen, J.F. (2008). "An experimental investigation into the behaviour of a two span masonry arch bridge repaired with FRP", Proceedings of the 9th International Symposium on Fibre Reinforced Polymer for Concrete Structures (FRPRCS-9), Sydney, Australia, July 13-15.

ACKNOWLEDGEMENTS

The undertaking of this thesis project has not only given me a great opportunity to improve my knowledge, but also to meet several intelligent people and therefore to grow and enhance myself both professionally and personally.

Firstly, I would like to express my deepest gratitude and heartfelt thanks to my supervisor: Dr Jian-Fei Chen, for his generous and constant support and guidance through my PhD study over the past five years. The patience, friendship and generosity he donated have enabled me to grow and mature as a researcher. I would also like to thank my second supervisor: Dr Tim Stratford, for lending his unique insight and experience to the experimental work presented herein.

I would like to gratefully acknowledge the finical support provided by EPSRC (the UK Engineering and Physical Research Council) and Shell through a Dorothy Hodgkin Postgraduate Award.

The experimental program would have been much more difficult to be completed without the help and generosity of many people, especially, Dr. Zhijun Zhong, Dr. Xiaoqin Li, Dr. Shiqing Li, Mr. Fengchen An, Dr. Vijayabaskar Narayanamurthy and technicians in the Structural Laboratory, Mr. Jim Hutcheson and Mr. Derek Jardine. To acknowledge all those who have contributed to my works in many different ways is clearly impossible, but a special mention must go to my colleagues in our silos and structures group, Prof. Jin Y. Ooi, Prof. J. Michael Rotter, Dr. Jin Sun, Dr. Jun Ai, Dr.

Yin Wang, and Mr John P. Morrissey. I cannot individually mention all my friends as that would add an extra chapter to this thesis, but my thanks to them all – you all contributed to this work – thank you!

Last but not the least, I wish to express my profound gratitude to my parents, to whom this thesis is dedicated. Without their everlasting love, support and encouragement I would never have embarked on my doctoral study and would not have had the opportunity to write this thesis. Finally my thanks and also apologies are due to my wife Yang Liu and my lovely son Lv-Ning for their measureless love, support and tolerance.

CONTENTS

LIST OF FIGURES

LIST OF TABLES

NOTATION

A	cross sectional area of FRP
b_f	width of FRP plate
b_c	width of substrate strengthened with FRP plate
c	cohesion of the material
D_0	initial elastic matrix
d	damage variable
d_a	maximum aggregate size
e	element length
E_0	Young's modulus of concrete
E_1	Young's modulus of the FRP lamina in longitudinal direction
E_2, E_3	Young's modulus of the FRP lamina in transverse direction
E_b	Young's modulus of bricks
E_f	Young's modulus of fibres
E_m	Young's modulus of masonry assemblage
E_{mx}	Young's modulus of martix of FRP composites
E_{sand}	Young's modulus of sand
E_p	Young's modulus of FRP composites
f_{cb}	compressive strength of concrete brick

f_{tb}	tensile strength of concrete masonry brick
f_{cm}	compressive strength of masonry assemblage
f_{tm}	tensile strength of masonry assemblage
f_{v0}	initial shear strength of masonry assemblage
f_c'	concrete cylinder compressive strength
f_t	tensile strength
f_{ci}	compressive strength of mortar
f_{ti}^0	tensile strength of mortar interface with zero confinement
G_F	fracture energy of concrete
G_{cn}^0	Mode-I fracture energy of mortar interface
G_{ct}^0	Mode-II fracture energy of mortar interface
G_{fb}^I	Mode-I fracture energy of concrete bricks
G_f^I	Mode-I fracture energy of the interface of FRP-to-substrate
G_f^{II}	Mode-II fracture energy of the interface of FRP-to-substrate
G_u	shear modulus of brick
G_m	shear modulus of mortar
h	characteristic length of element
k_n	normal stiffness of mortar interface
k_{nn}	interfacial normal stiffness for the FRP bond interface

k_s	shear tiffness of mortar interface
k_{ss}	interfacial shear stiffness for the FRP bond interface
L_e	effective bond length
L_{frp}	bond length of FRP composite
S_s	length of local slip
S_s^0	local slip at $\tau_{\max}$
S_s^f	local slip when bond stress reduce to 0
t_p	nominal thickness of FRP plate
w_t	crack opening displacement
w_{cr}	crack opening displacement at the complete loss of tensile stress
α	internal angle of friction in Chapter 3
β	shear retention ratio
β_w	width ration factor
ε	strain
$\bar{\varepsilon}$	equivalent strain
ε_{cr}	crack strain
$\varepsilon_{cr,u}$	crack strain at the complete loss of tensile stress
ϕ	angle of friction in the Mohr-Coulomb model
θ	load dispersion angle

σ	stress
σ_c	compressive stress
τ	shear stress
τ^0	initial shear strength of mortar interface
$\tau_{\max}$	maximum interfacial shear strength
v	Poisson's ratio

CHAPTER 1

INTRODUCTION

1. 1 Background

A safe and efficient transportation network is essential to the freedom, civilization and prosperity of modern society. By their nature, bridges are essential elements in the road, railway and waterway transport networks worldwide. For each type of bridges, there exists a relationship between the structural form of a bridge and materials used for its construction. Arches make up the majority of bridge constructions because of their loading bearing and ornamental function.

Masonry is an ancient and still very commonly used construction material. Many historic masonry structures are characterized by the presence of arches and vaults. Masonry has been adopted as bridge materials through historical periods, from the Roman time to the Modern Age. A masonry arch is constructed using a temporary falsework, or centring. This centring is traditionally of timber but steelwork nowadays, and provision must be made, by means of wedge or some similar device, to remove the falsework once the arch has been completed (Heyman, 1982). Modern forms of masonry arch bridge, such as, FlexiArch developed by the Queen's University Belfast (Quinn et al., 2011), do not require centring. Obviously, the arch ring forms the basic structural component of the arch bridge. At least some of the fill must be placed over the extrados of the arch in the region between abutments in

order to stabilize the arch ring. The fill is retained by spandrel walls built on the two sides of the bridge. Figure 1.1 shows the components of a masonry arch. The voussoir, like bricks, is a brittle material with high compressive strength. The mortar between voussoirs and the interfaces between them are usually very weak in tension, so that, there is very weak tensile strength between the bricks. The compressive strength of mortar are generally smaller compared to the voussoirs material (Heyman, 1969). There are commonly three key assumptions when formulating the material properties of masonry: sliding failure cannot occur; masonry has no tensile strength and infinite compressive strength. Therefore, masonry arch bridges must work in compression dominated states.

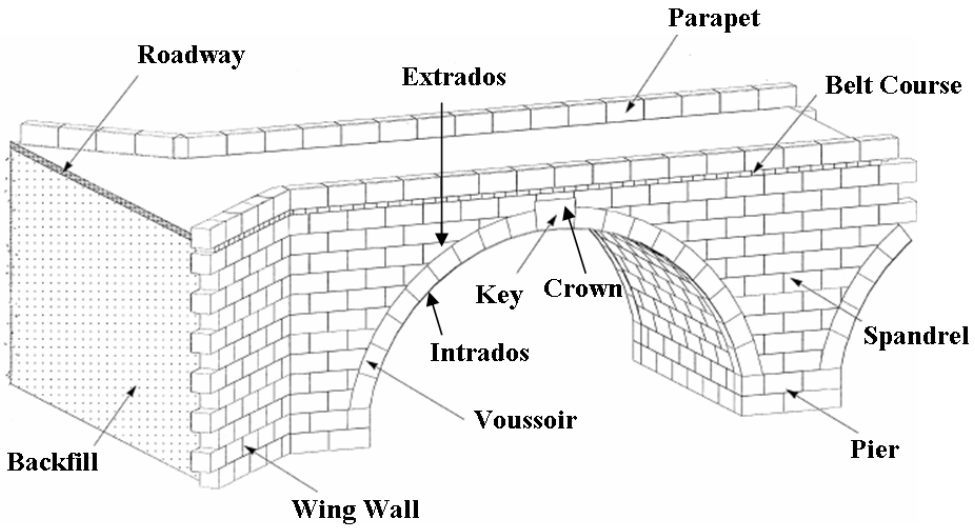

Figure 1.1 Components of a typical masonry arch

The condition that masonry must work in compression means that the internal forces must be transmitted within the masonry itself. It implies that the stress resultant must locate within the profile of the arch. The line formed from every section is named the

line of thrust. A hinge forms once the thrust, the compressive stress resultant, reaches the edge of the arch. These cracks usually alternate between the intrados and extrados of the arch. The entire arch usually fails when sufficient hinges (usually at least four hinges) are formed to turn the arch to a mechanism.

Many masonry arch bridges are hundreds of years old. The amount of traffic on road or railway arch bridges has exploded since they entered service. In addition, the overtime service and extreme loading conditions may cause damage and eventually leads to failure of the structure. Restrictions to the operation of bridges or their closure can have significant effects on transport networks. The contribution of strengthening materials and repair techniques may be required to re-establish their performances and to prevent the collapse of the structures in hazardous conditions. In addition, in order to extend the service life, and/or increase the load carrying capacity of the masonry arch structures, or repair damaged masonry arches, retrofitting techniques are needed to achieve these demands.

Some of the traditional retrofitting techniques for masonry arches, such as, dismantling and remounting with possible improved material substitution (Basilio, 2007), installation of stainless steel reinforcements in the near surface zones of masonry (Sumon, 1997), installation of the iron cramps (Heyman, 1996); widely adopted in the world to ensure an adequate improvement of strength, stiffness and ductility of masonry arches, but they are often short-lived, labour intensive, and unsatisfied to the aesthetic requirements. For example, the results of remounting with improved materials depend on the material properties and the results of dismantling

work. The installation of stainless steel reinforcements in the near surface zones of masonry is a labour consuming technique.

Among the innovation techniques to rehabilitate deteriorated structures, there has been an increasing interest in external bonding of fibre reinforced polymer (FRP) composites. FRP composites are produced by embedding fibres in a resin matrix that binds the fibres together. FRP composites are commonly classified based on the types of fibre: glass fibre reinforced polymer (GFRP); carbon fibre reinforced polymer (CFRP); basalt FRP and aramid fibre reinforced polymer (AFRP). The fibres are oriented in preferred directions, and thus FRP composites are anisotropic materials. Compared with steel, the advantages of FRP bonding system is its excellent corrosion resistance and high strength which is normally at least twice but can be over ten times as high as that of mild steel while the weight is only about 20% of steel. Their high corrosion resistance can ensure durable performance, while the high strength-to-weight ratio leads to easy handling and labour cost reduction (Teng et al., 2002). FRP composites are generally linear-elastic brittle. The modulus of elasticity varies from 30% and 130% (more for CFRP) of that of steel. CFRP composites are usually stiffest and strongest.

FRP bonding system has been widely used as an innovative solution to strengthen and repair existing concrete and steel structures due to the aforementioned benefits. The most common application of FRP bonding system in retrofitting is as an external reinforcement for structural elements by bonding FRP over the surface. Typical applications are as tension reinforcement of beams and slabs; shear reinforcement of

beams, beams-column joints, and walls; and as confinement reinforcement of columns. The small thickness of the FRP bonding system makes it an attractive technique as it would not change the appearance, which is especially important for historical buildings.

Debonding of FRP is a common failure mode and occurs within adherend or adhesive materials or at the interfaces between them, following the weakest path. The bond failure usually initiates at a high stress concentration region, at material or geometrical discontinuities, or at pre-existing cracks. Possible debonding failure paths in an FRP-to-concrete/masonry interface are: 1) in the concrete substrate near the adhesive-concrete interface; 2) at the concrete-adhesive interface; 3) within the adhesive layer; 4) at the adhesive-FRP interface; 5) within the FRP itself. Some times multi debonding mechanisms can take place. Modes 3 and 4 rarely occur because the high strength of the adhesive usually used for bonding FRP. Also mode 5 is not a common failure due to the high strength of FRP. Mode 1 is the one that takes place in most of the strengthened structures, and this is the most likely failure mode.

Compared with FRP strengthened concrete structures, only a small number of studies have been devoted to FRP strengthened masonry structures, especially masonry arch structures. This is largely because of the complexities arising from material discontinuities of the masonry and the mixed mode interface behaviour in curved bond line between FRP and masonry arches. Much of the research into FRP strengthening for masonry to date has been concerned with walls subjected to in-plane loading (Alcaino and Santa-Maria, 2008; ElGawady et al., 2005b; Stratford et

al., 2004; Triantafillou, 1998; Turek et al., 2007) and out-of-plane loading (Albert et al., 2001; Ehsani et al., 1999; Hamoush et al., 2001; Kuzik et al., 2003; Paquette et al., 2001; Triantafillou, 1998). The out-of-plane bending of walls is relevant to the four hinge mechanism failure in arches, as there is a similar interaction between the FRP, the opening of flexural cracks in the walls, and the reliance upon the adhesive joint between the FRP and the masonry. Wall elements, however, do not have the curvature as in arches.

A small number of studies have been conducted on FRP strengthening of masonry arches and vaults. Barrel vaults are similar in appearance to arches. However, the extrados of vaults is often accessible for strengthening. It also might not be acceptable to apply FRP to the intrados of vaults for the consideration of aesthetics. FRP composites restrain the opening of flexural cracks in the arch thus delay on set of cracking, but they do not prevent crack formation (Drosopoulos et al., 2007; Foraboschi, 2004). By restraining the growth of flexural cracks it is possible to prevent the hinge mechanism failure (De Lorenzis, 2008; Foraboschi, 2004), and it has also been demonstrated that the lateral abutment thrust is reduced (Bati et al., 2007; De Lorenzis et al., 2007). Increasing the hinge mechanism failure load, however, means that other failure modes may become more critical. Debonding is one possible failure mode and has been rarely investigated, especially the local debonding mechanics.

1. 2 Objectives and methodologies

The main purpose of this research was to deeply investigate the behaviour of FRP strengthened concrete masonry arch bridges, and the bond behaviour between FRP and concrete masonry structures. It is worth noting that the stone or clay brick are more commonly used in the practical masonry arch structures. The reasons why this study focused on the concrete masonry are the arch bridge in the test was made from the concrete masonry; the constitutive model of concrete developed in this study is expected to be used for the concrete structures as well. A carefully designed experimental study was conducted first. In order to investigate the behaviour of such strengthened structures, several numerical studies were conducted on modelling of FRP strengthened concrete substrates using a concrete damaged plasticity model available in the ABAQUS, eventually on modelling of concrete masonry arch bridges with backfills, and modelling of FRP strengthened concrete masonry arch structures. The following tasks will be addressed in this thesis:

1) Investigating the global responses and local mechanics of FRP strengthened concrete masonry arch structures, especially the bond between FRP and masonry arches. It will be achieved through a well designed experimental study on a larger-scale model.

2) Reviewing the existing numerical studies on the bond behaviour between FRP-to-concrete, and eventually developing a novel concrete damage model to accurately simulate the bond behaviour between FRP and concrete. This numerical model can

be used for the further studying of local bond behaviour. The constitutive model of concrete was used to model concrete masonry in the following tasks.

3) Reviewing the existing numerical studies on masonry arch structures, and applying different methods to model masonry arches. Behaviour of masonry arches and the interaction between the arch and sand backfill will be investigated using the successful models. An advanced FE model was used to simulate FRP strengthened concrete masonry arches.

4) Reviewing the existing numerical studies on FRP strengthened concrete masonry arches, and use the model developed from the unstrengthened arches combined with an interface model for FRP-to-masonry bond joint to simulate the strengthened arches. The behaviour of the strengthened masonry arches will be investigated.

1. 3 Structures of thesis

This thesis is divided into seven chapters including this introductory chapter, a chapter on literature review and four core chapters followed by a conclusion chapter. A brief introduction for each chapter is described following:

Chapter 2 reports a comprehensive literature review about masonry arch structures and FRP strengthened structures. It includes the behaviour of both unstrengthened and strengthened masonry arch structures, and numerical and analytical studies on both types of structures.

Chapter 3 reports a well-designed experimental study on a larger scale (one third) two span masonry arch bridge built in 1996. The bridge was loaded until a four hinge mechanism was formed and then repaired by externally bonding FRP composites into their intrados, and then loaded again to failure. A great amount of data was collected and the behaviour of the structure was investigated. The debonding process was studied, both case sensitive and general conclusions are drawn.

Chapter 4 develops a finite element (FE) model to simulate the bond behaviour of FRP-to-concrete. It is worth nothing that the purpose of this chapter is to develop a constitutive model of concrete for the later chapters. That was the reason why this chapter only focused on the FRP-to-concrete instead of FRP-to-concrete masonry which includes concrete (voussoirs) and mortar. After reviewing existing numerical studies, a new concrete damaged plasticity model was developed which successfully simulates the entire process of debonding failure. The proposed model is validated against a large amount of test data. The bond-slip relationships extracted from the proposed model are compared with test data and existing models to show its accuracy.

Chapter 5 reports a numerical study on concrete masonry arch structures with backfills. Four different models are developed to model the test on the unstrengthened masonry arch bridge reported in chapter 3. The accuracy and suitability of each model are compared. An advanced detailed solid model is finally developed to be used to model the FRP strengthened masonry arch bridges in the next chapter. Apart from the study on the behaviour of masonry arch bridges, the

effects of several key parameters involved in both masonry and backfill are investigated.

Chapter 6 develops a FE model to simulate the FRP strengthened concrete masonry arch bridges. The proposed model included a detailed solid model for masonry arches and an interface model for bond joint of FRP-to-masonry. The behaviour of FRP strengthened masonry arches is investigated and several parameters are analysed to address their effects, especially the interface model of FRP-to-concrete masonry.

Chapter 7 summarises the most significant contributions and findings of this thesis. Future research related to this work will be identified and some recommendations are made to improve the current understanding of the FRP strengthened concrete masonry arch bridges.

CHAPTER 2

LITERATURE REVIEW

2. 1 Introduction

Masonry structures have been used for centuries. They have excellent aesthetic appeal and long-term durability. Many of these historic masonry structures have survived for centuries across the world, and most are historic structures that survive in active service largely due to the inherent stability of the arch form.

Masonry arch bridges are an important part of many countries' rail and road transport infrastructure. The combined effects of modern traffic loads for which they were not designed, and degradation of the masonry mean that some of these bridges suffer from significant damage. It is important to safeguard and extend the life of these structures, especially where arch bridges form critical links in the transport network and where major disruption would result from their closure (Boothby et al., 1998).

Masonry is an assemblage of masonry units (bricks or blocks) that are joined with mortar. Masonry structures are dominated by their composite behaviour (Lourenço, 1996). Masonry usually has a high compressive strength, but a lack of tensile strength. Failure of the masonry is generally governed by a mechanism type failure which is directly related to the arch ring thickness, the type and density of backfill and the height of the backfill at the crown.

For a single ring masonry arch bridge, based on the researches from Boothby (1995) and TRL reports (Crisfield, 1985; Hendry et al., 1985; Hendry et al., 1996), an arch bridge can collapse as a results of five possible collapse modes:

a) shear (sliding) mechanism Figure 2.1a;

b) hinge mechanism Figure 2.1b;

c) combined shear and hinge mechanism Figure 2.1c;

d) ring separation for a multi-ring masonry arch bridge;

e) the crushing mode, which occurs at a few conditions: an extremely flat arch with tie-rods at the springing, made of poor-quality masonry and loaded symmetrically (Foraboschi, 2004). Crushing failure is usually in combination with hinge development (Hughes and Blackler, 1997); and

f) the snap-through failure mode, which was identified in a full-scale experimental studies reported by Page (1993). During a snap-through failure, the hinges start to form but instead of the final gradual formation and rotation of the hinges a rapid change of the local geometry occur with the section of arch under the load snapping through (Harvey, 1988; Hughes and Blackler, 1997). That means the bridge failed by snap-through due to the relatively large deflection before the failure mechanism would occur (Yang, 1991). Snap-through mode is considered more likely to occur in the shallow thin arches (Hughes and Blackler, 1997).

The critical failure mode is the four hinge mechanism (Heyman, 1982), the critical loading position is usually between one third to quarter span depends on the properties of the fill (Hughes, 1995; Quinn et al., 2011). Shear or crushing modes are unlikely to occur because the critical loads are well above that of the hinge mechanism (Audenaert et al., 2007; Foraboschi, 2004; Heyman, 1982). In multi-ring arch bridges, ring separation failure mode may be occurred as well (Gilbert and Melbourne, 1994).

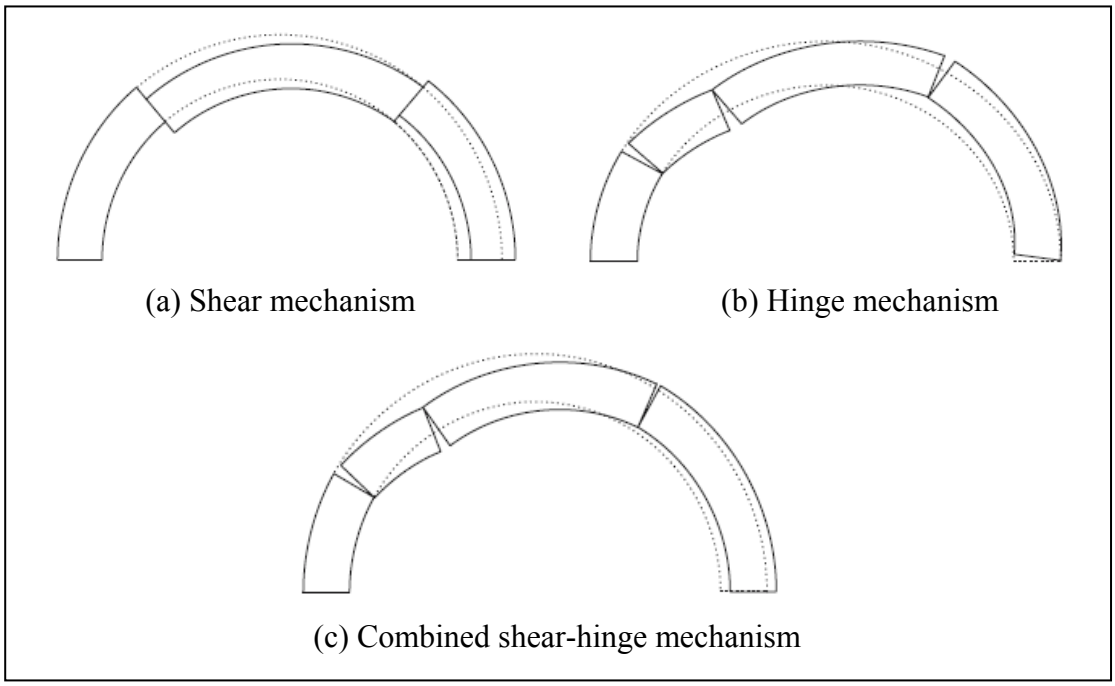

Figure 2.1 Collapse modes of a masonry arch

Fibre-reinforced polymer (FRP) composites are increasingly used for bridge repair and strengthening, with particularly widespread application to concrete structures (ACI, 2008; Concrete Society, 2004). The FRP is adhesively bonded to the surface of the existing structure, where it provides tensile capacity and restrains the opening of cracks. FRP has the advantages of a low weight to strength ratio, short installation

periods and minimal intervention upon the structure (Teng et al., 2002). The small thickness of FRP required for strengthening is especially important for historic bridges, as it minimizes changes to the bridge's appearance. The application of FRP composites to masonry structures is less well established, although it has been the subject of research and development in recent years (De Lorenzis, 2008), demonstrating that FRP can be used to upgrade the structural performance of a variety of masonry elements, and has resulting in design guidance being issued by the National Research Council in Italy (CNR, 2004) and by the American Concrete Institute (ACI, 2007). Further work is required, however, to apply FRP strengthening to increase the load capacity and enhance the performance of masonry arch bridges.

This literature review firstly considers the fundamental behaviour and theories about masonry arch structures and FRP strengthened structures, then focuses on the existing studies on FRP strengthened masonry arch structures, and finally reviews the numerical and analytical studies on the FRP strengthened masonry arch bridges.

2. 2 Masonry structures

Masonry is a construction material where a larger number of small modular units, either natural or artificial, are assembled together, typically with mortar, to form a predominantly compression structure (Drysdale et al., 1994). Masonry had been used as a primary construction material for centuries. Although there have been several studies, such as, Lourenço (1996; 1998); Atkinson, et al. (1989); Heyman (1982; 1996), devoted to the behaviour of the masonry structures, it needs to be emphasized

that the analysis of masonry structures is still a challenge because masonry is a composite material and the movement of thrust line which can be difficult to assess, thus its behaviour is complex. In this section, the material properties of masonry are reviewed first. The masonry arch structures and its behaviour are then discussed.

2.2.1 Materials properties of masonry constituents

The properties of masonry are strongly dependent on the properties of its constituents. Masonry simply refers to brickwork or stonework. There are three components included in masonry: the masonry unit, the mortar, and the interface between the unit and the mortar (Lourenço et al., 1998). The masonry constitutive relationship is complex due to the composite material and the distinguishing material properties. Masonry structures are thus dominated by their composite behaviour, the geometry and the backfill. The assembly of units into masonry structures creates a form which has its own particular property of plastic deformability (Heyman, 1996).

The most common units in masonry constructions are stones (both regularly and irregularly shaped), bricks, concrete blocks, stucco or tiles (Heyman, 1982; Heyman, 1996). A masonry unit (stone or brick) is essentially a brittle material and lacks ductility. The brick's properties are generally related to its types. In general, a brick usually has adequate compressive strength, which makes the compression failure is rarely. It is difficult to relate the tensile strength of the masonry unit to its compressive strength due to the different shapes, materials, manufacture processes and volume of perforations of the units (Lourenço and Rots, 1997; Lourenço et al.,

1998). However, because quasi-brittle materials like masonry units, rock or concrete, fail due to the progress of internal crack growth. Therefore, constitutive models for concrete, such as the Drucker-Prager failure criterion (Domède et al., 2009; Giordano et al., 2002; Thavalingam et al., 2001) and the William and Warnke model (Fanning and Boothby, 2001), could be used to model a masonry unit (Lotfi and Shing, 1994; Lourenço, 1996).

Mortar is composed of cement and/or lime, sand and water. Ancient mortar was made by mixing of sand and lime and sometimes, a mixture of sand, clay and water also known as "adobe" (Vermeltfoort, 2005). Although the lime mortars are still used in the repair of historic structures, lime has been replaced by cement and a mixture of sand and cement in the new constructions. Modern mortar is made of many constituents, inorganic materials, sand and sometimes admixtures mixed together in proper ratios for specific application (Juhásová et al., 2008). The properties of mortar thus depend on the proportions of these constituents (Ricamato, 2007); for instance, mortar with a high water cement ratio has lower compressive strength than one with a low water cement ratio.

This interface is the weakest link in the masonry assemblies, and it is one of the most important features of masonry behaviour. Two different phenomena occur in the unit-mortar interface, one associated with tensile failure (mode-I) and the other associated with shear failure (mode-II). The interface between unit and mortar is usually very weak in tension due to its negligible adhesion (Heyman, 1996), so that, there is nothing to prevent the pulling apart action. There is no widely known

equation to calculate the tensile strength and the mode-I fracture energy of the interface. It is suggested that both parameters are defined from test results (Fanning and Boothby, 2001; Lourenço et al., 1998). Pluijm (1997) introduced a displacement controlled test in small masonry specimens of solid clay and calcium-silicate units. These tests resulted in an exponential tension softening curve with a mode-I fracture energy ranging from 0.005 to 0.02Nmm/mm^2 for a tensile strength of the interface ranging from 0.3 to 0.9MPa. Shear strength at the interface comes from friction due to the asperities between the surface of mortar and the surface of the unit, and the chemical bond between mortar and brick units (Lourenço and Rots, 1997). Confinement perpendicular to the interface further increases its shear strength and the mode-II fracture energy because the asperities cannot easily slide over one another, which is the Mohr-Coulomb behaviour. The arch form is thus maintained due to the friction generated between the masonry units by self-weigh of backfill as well as bricks, and, as the friction coefficient is very high, sliding failure usually does not occur (Heyman, 1982).

2.2.2 Materials properties of masonry composite

The properties of masonry are different to those of each of its components because masonry is a composite material composed of units, mortar and the interface between them.

There are five types of failure modes that characterize masonry (Atkinson et al., 1989; Gilbert and Melbourne, 1994; Heyman, 1982; Lourenço, 1996) as shown in Figure

2.2:

(a) cracking of the joints caused by the tension loading perpendicular to the bed joint;

(b) sliding along the unit-mortar joints;

(c) cracking of the units in direct tension when the tensile loading parallel to the bed joints;

(d) diagonal tension cracking of the units at values of normal stress sufficient to resist the sliding along the joints; and

(e) splitting of the units in tension as a result of mortar dilatancy at high values of normal stress. This can be explained as follows: the masonry prism expands laterally in the plane normal to the direction of loading. However, the stiffer units expand less than the softer mortar, and restrain the expansion of mortar. Consequently, masonry units experience a compression-bilateral tension state of stresses.

It is clear that modes (a) and (b) are joint failure mechanism, (c) is the unit failure mechanism, and (d, e) are combined mechanism in both units and mortar. In mechanism failure, the joint opening failure is caused by the failure mechanism (a) and eventually the hinge forms, which turn the masonry arch to a kinetic state.

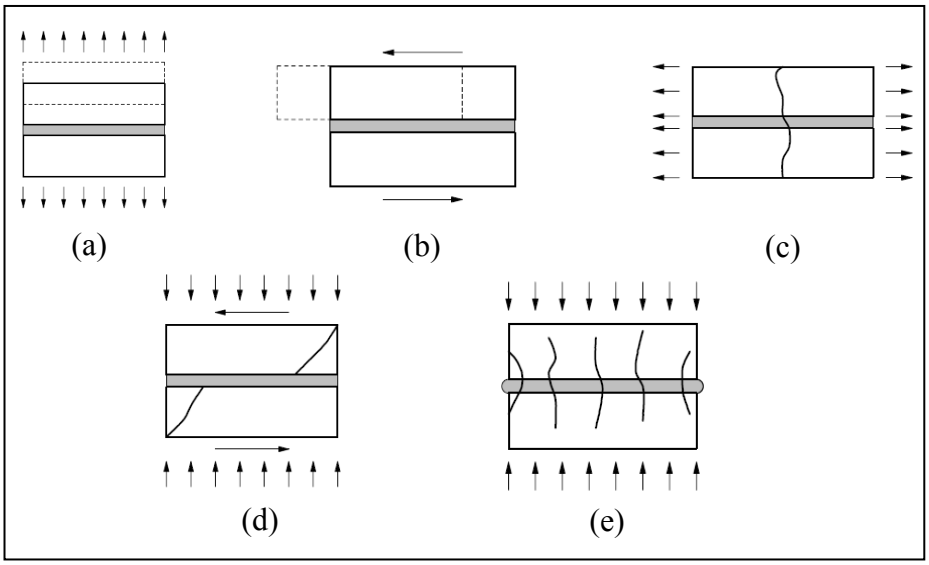

Figure 2.2 Failure modes of masonry: (a) joint tensile failure; (b) joint slipping failure; (c) unit tensile failure; (d) unit diagonal tensile cracking failure; (e) masonry crushing (redrawn after Lourenço et al. (1998))

2.2.3 Masonry arch structures

Masonry arches can be classified into different categories. The common categories are by (a) types of construction materials, (for example, stone masonry arches, brick masonry arches, block masonry arches); (b) by type of structure, (for example, bridge masonry arches, building masonry arches); (c) by type of structural system, (for example, the three-pinned arches, two-pinned arches); (d) and by shape, (for example, round arch or semi-circular arches, elliptical arches, etc).

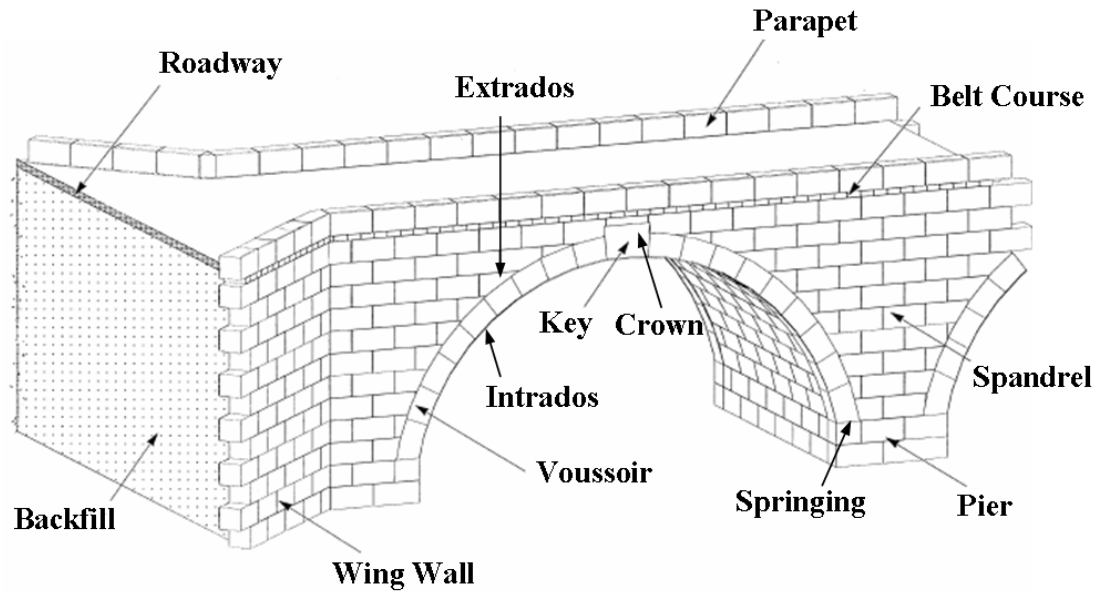

Figure 2.3 Typical parts of masonry arch (redrawn from Fanning et al. (2001) and Heyman (1982))

The details of parts of masonry arch are shown in Figure 2.3. Each structural element of masonry arches has a specific function or plays a general function by interaction with other elements. It is important to understand these functions so as to be able to judge the capacity and performance of an arch. The critical elements of a typical masonry arch bridge as shown in Figure 2.3 are:

a): Arch barrel: The main element of a masonry arch bridge made up of a single or multiple layers of voussoirs. This is the basic load bearing element of an arch bridge.

b): Spandrel and Wing Wall: The spandrel is an area, while spandrel wall is a masonry wall built at this area at the edges of the barrel to limit and retains the backfill materials. Wing wall has the same function as spandrel wall but it located at the bridge abutment, beyond the bridge (Fanning et al., 2001; Heyman, 1982;

Hughes and Blackler, 1997).

c): Extrados and Intrados: They are the outer and inner profiles of an arch barrel, respectively.

d): Backfill: This transfers load from the roadway to the backfill, which is then distributed on to the arch ring. The backfill also resists lateral movement of the arch (Fairfield and Ponniah, 1994; Royles and Hendry, 1991). The vertical dead weight of backfill effectively pre-stress the masonry arch, thereby increasing its load carrying capacity (Gilbert and Melbourne, 1994; Heyman, 1980). The backfill also has two other beneficial effects: it disperses the live load; and it can provide a passive restraint to the movement of the arch. All of above effects can potentially significantly enhance the carrying capacity of a masonry arch bridge (Harvey, 1988; Heyman, 1982; Hughes et al., 2002).

e): Pier and Abutment: A pier is an intermediate support for bridges with more than one span, and the abutment is the end support of the bridge. Both provide resistances to the vertical forces and push forces of the arch (Heyman, 1982; Heyman, 1996).

Most masonry arches are constructed using a temporary falsework, or centreing. The FlexiArch has no centreing which are designed by the Queen's Belfast University (Quinn et al., 2011; Taylor et al., 2007). This centreing is traditionally of timber and steelwork nowadays, and provision must be made, by means of wedge or some similar device, to remove the falsework once the arch has been complete (Heyman,

1982). The arch ring is a critical structural element and comprises wedge-shaped stones or normal building bricks called voussoirs, and a keystone located at the crown. The keystone has the same function as other voussoirs in structural proposes, therefore, it is not compulsory to be used. The keystone is the highest and last placed stone, and there are series of keystones across the width of the bridge. The keystone is used for construction purpose, making striking the falsework easier once the arch is complete (Heyman, 1982). Once the arch barrel is completed, the spandrel walls are constructed to stabilize the arches.

The extrados of the arch is to be filled with loose materials, such as soil, to increase the stability of the arches. The road is then paved and other necessary things like parapets are provided.

2.2.4 Structural behaviour of masonry arch

Masonry must act in compression. It results in a severe geometrical limitation for an arch: the internal forces must be transmitted within the masonry. The point of application of the stress resultant in every section must lie within the profile of arch. The profile of these points forms a curve as shown in Figure 2.4, which is named the line of thrust (Heyman, 1982). Safety is maintained as long as the line of thrust is kept inside the thickness of the arch. The shape of the thrust line depends upon the applied loads to the arch and can be determined mathematically (Heyman, 1982). When the load distribution produces an equilibrium state with a sufficient number of hinges that form a mechanism of collapse, the structure will fail. The collapse does

not involve strength failure, but a stability failure (mechanism failure) (Heyman, 1982). This mechanism failure is caused by the aforementioned failure mode of cracking in the unit-mortar joints.

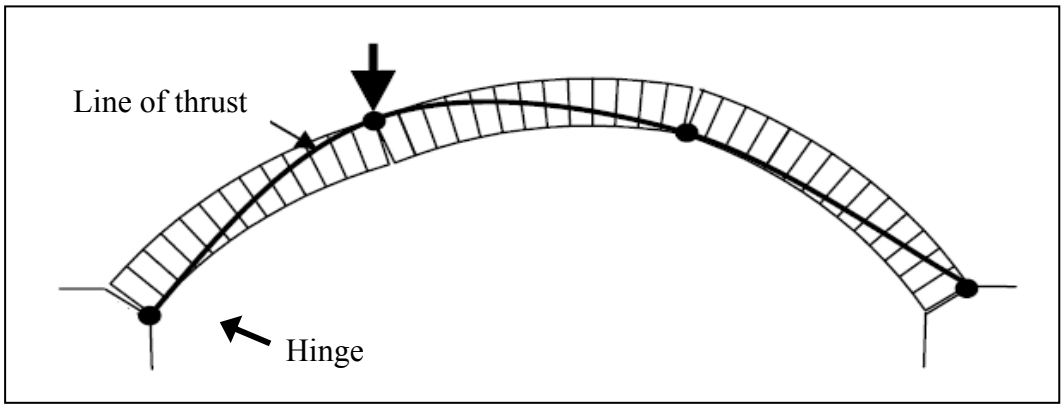

Figure 2.4 Thrust line in a masonry arch

The presence of the backfill significantly affects the arch behaviour. The fill material increases the stability of arch, either directly by inducing additional compression in the arch, or indirectly by allowing a dispersion of the concentrated forces over greater lengths and widths, and provides a passive lateral restraint to the arch by its interaction with the surrounding soil medium (Betti et al., 2008; Fanning and Boothby, 2001). The sufficiently stiff backfill material can carry compressive force as well. These benefits lead to an increase of the load carrying capacity of the arches. (Gilbert and Melbourne, 1994; Heyman, 1980).

The behaviour of the masonry arch bridge is therefore influenced by the interaction of the structural elements of masonry arch itself and the backfill. The properties of the backfill materials and the interaction between the backfill and the arch also play an important role in the loading carry capacity of an arch. Interactions of structural

elements, geometry of the arch bridge and materials properties are important aspects when looking at the behaviour of masonry arch bridges.

2.2.5 Masonry arch analysis methods

Over the years, there have been four common methodologies developed to assess and analyse the behaviour of the masonry arch (Gilbert et al., 2006; Hughes and Blackler, 1997; Ng, 1999).

a) The semi-empirical method, the prime one is MEXE (Military Engineering Experimental Establishment). The MEXE method is based on a classic elastic analysis by Pippard who modelled the arch barrel as linear elastic, segment in shape, pinned at both ends and carrying an axle load. The ultimate load determined by this method is modified by a number of highly subjective parameters. The MEXE method is known to be over-conservative but is quick and easy to use (Hughes and Blackler, 1997).

b) The mechanism method, the classical mechanism method established by Heyman (1982). It considers the actual way in which arches failed by formation of mechanism. The hypotheses on the masonry behaviour are: no tensile strength; infinite compressive strength and absence of sliding failure. Under these hypotheses, the collapse of masonry arch bridges can be approximated by an assemblage of rigid parts, held up by mutual pressure, and the collapse of the structural elements is characterised by the development of non-dissipative hinges transforming the structure into a mechanism (Heyman, 1982). The mechanism method is based on the

estimation of the thrust line, which is related to the hinge positions. The critical loading position is assumed, and it can be determined once the hinge positions are selected. Each hinge position is then relocated until a minimum capacity is determined. The loading position is then moved and the process repeated until a set of hinge position associated with a critical mode is determined (Y. Chen et al., 2007; Hughes and Blackler, 1997; Robinson, 2000). The mechanism method cannot provide the information about the stresses of masonry arches. The assessment results are sensitive to the passive coefficient values adopted for backfill (Hughes and Blackler, 1997; Hughes et al., 2002).

c) The Pinned-elastic analysis method, which was firstly introduced by Castigliano (1897), secondly Pippard (Pippard and Baker, 1968) and then Huges (Bridle and Hughes, 1989; Bridle and Hughes, 1990). The basic assumptions of the analyses are that the arch is pinned, soundly built and fails in compression whilst retaining the full arch section. The elastic method is based on the Castigliano's strain energy analysis and the arch ring is treated as a linear elastic material. A load is applied incrementally and stresses at every section are calculated. Areas subjected to tensile stress are discounted which reduces the effective depth of the ring at those section. The same procedure is repeated until the thrust line is just contained within the reduced cross sectional area (Ng, 1999). The most critical limitations of this method are the following. The masonry material does not show elastic behaviour and opposed to the assumption of this method. The arch tensile strength could significantly influence the collapse load prediction (Hughes and Blackler, 1997; Ng, 1999).

d) The finite element (FE) method, which using FE programs to model the masonry arch bridge and backfills and investigate the behaviour of them, such as, Betti et al. (2008), Cavicchi and Gambarotta (2005; 2006; 2007), Drosopoulos et al. (2006), Ng (1999), etc. Compared with the conventional assessment methods, such as the MEXE, mechanism and elastic methods, the numerical simulation by the FE method permits a more comprehensive analysis for investigating the behaviour of masonry arches.

2. 3 FRP strengthened structures

Structures experience ageing effects or movements in the foundations or other accidental factors causing structural damage during their service life, and eventually affecting the structural global stability. In order to extend the structural life and re-establish the performance of these structures, there has been research and engineering focused on efficient strengthening techniques. Modern retrofitting techniques are based on the concepts that strengthening procedures should be light, removable and should not change the structural scheme and construction. FRP externally bonded to the surface of the structural elements has been used as a retrofitting technique, has several advantages; for example, a low weight-to-strength ratio, short installation period, and very little effects on existing structures (Teng et al., 2002).

2.3.1 FRP materials

FRP materials are composites made of high strength fibres, such as glass, carbon and aramid, usually surrounded by an epoxy resin matrix (Teng et al., 2002). The

stiffness and strength of FRP are provided by the fibre, and the epoxy resin protects the fibre and helps the fibres work as a composites. The epoxy has good mechanical properties, chemical and adhesive strength, long durability, and good bond with steel and concrete structures. FRP is an anisotropic material because the fibres are directional. FRP has a linear-elastic brittle behaviour, with an ultimate strain about ten times the yield strain of steel (Teng et al., 2002). The modulus of elasticity varies from 33% to 125% of that of the steel. Carbon fibres are stiffest and strongest of FRP.

2.3.2 FRP strengthened concrete structures

The most common use of FRP in strengthening concrete structures is externally bonding plates or fabric over the surface of the retrofitted elements. The applications of FRP systems are typically as flexural reinforcement of beams and slabs; shear reinforcement of beams, beam-column joints, and walls; and confinement reinforcement of column (Teng et al., 2002). Failure of the bond between the FRP and concrete often governs strength of these structures, and occurs at a region of high stress concentration, at material discontinuities, or at cracks (ACI, 2008; Chen and Teng, 2001; J. F. Chen et al., 2007; Teng et al., 2002). Debonding failure in the FRP-to-concrete joint can occur within or at the interfaces of materials, following the path of least energy (Buyukozturk et al., 2004; Teng et al., 2002). There are several possible crack propagation paths in an FRP-to-concrete bond joint as shown in Figure 2.5: a) in the concrete substrate, close to the concrete-adhesive interface; b) in the concrete-adhesive interface; c) within the adhesive layer; d) in the adhesive-FRP interface; e) delamination of the FRP. More than one debonding failure mechanisms

can occur in the same time (Buyukozturk et al., 2004; Teng et al., 2002; Teng et al., 2003a; Teng et al., 2003b).

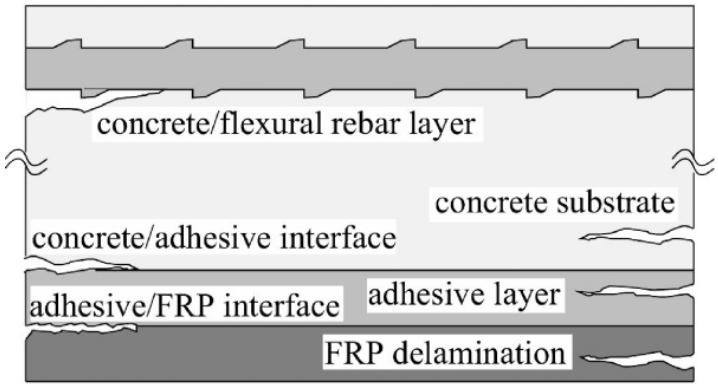

Figure 2.5 Possible debonding mechanisms of FRP-to-concrete joint (Buyukozturk et al., 2004)

Debonding in the adhesive layer and in the adhesive-FRP interface rarely occur due to the high strength of the adhesive usually used to bond the fibres (Chen and Teng, 2001). For the same reason, the delamination of the FRP is not the common failure mode. Concrete substrate failure must have occurred in a large part of the bond length, which controls the failure of the joint, before the fibre delamination occur (Chen and Teng, 2001). Debonding in the concrete-adhesive interface occurs if the surface of the concrete is not properly prepared and cleaned, or if the water content of the concrete is too large and the curing of the adhesive does not occur as expected (Chen and Teng, 2001; Teng et al., 2003a). Debonding in the concrete substrate is the one that takes place in most of the bond test specimens (Chen and Teng, 2001), and in beams with external FRP overlays for bending and shear strengthening.

There are larger quantity of experimental works related to bond failure of FRP-to-

concrete joints, such as, Buyukozturk et al. (2004), Chen and Teng (2001), Coronado and Lopez (2008), Wu et al. (2001) and Yao et al. (2005). Some of the key findings are:

a) the bond strength increases as the FRP thickness increases, which is addressed in design guides (ACI, 2008) when calculating the maximum strain accepted for design;

b) extending the tensile FRP reinforcement of beams as close to the supports as possible decreases the potential for debonding;

c) anchorages can increase the debonding resistance, failure load and ductility of beams, by adding anchorage with several transverse FRP strips bonded over the ends of the longitudinal FRP (ACI, 2008; Teng et al., 2003a); and

d) deterioration of the FRP-to-concrete interface produced by environmental exposure conditions such as freeze-thaw, wet-dry, and temperature cycles can lead to debonding problems (Bisby, 2003; Buchan and Chen, 2007).

In flexural strengthened concrete beams with FRP the debonding may initiate at the flexural or flexural-shear crack at an intermediate section subjected to high moments (J. F. Chen et al., 2007; Teng et al., 2006). The other place where debonding may initiate is the end of the FRP strip due to a diagonal crack, concrete cover separation, or a concrete crack close to the interface with the FRP (Toutanji et al., 2007; Yao and Teng, 2007). Shear strengthened concrete beams can be applied by completely

wrapping the beam with FRP, using U jackets or adding side strips (Chen et al., 2010; Chen and Teng, 2003). Chen and Teng (2003) reviewed a large number of shear test and have shown that the wrapping strengthening scheme fails due to rupture of the fibres, while the other two schemes fail due to debonding of the FRP. The most effective positive of the side strip is where the bond length is largest, crossing at mid-length of a shear crack.

2.3.3 FRP strengthened masonry structures

The use of FRP bonding system in masonry structures has not been widely adopted as with other type of structures. Due to the mentioned positive aspects of application of FRP system, it is an attractive retrofitting technique for buildings that cannot change their appearance, which is more appropriated in the case of historical masonry buildings (De Lorenzis, 2008). The principal role of the FRP system in strengthening masonry is to transfer tensile stresses both within a structural element and between different elements of the structure. Debonding failure of FRP-to-concrete occurs mostly through cracking of the concrete, and the same mode has been observed in masonry walls and panels reinforced with FRP strips (De Lorenzis, 2008), where debonding typically occurs within a layer of the masonry.

Out-of-plane bending of masonry wall may be critical, especially in unreinforced masonry walls. Most of those buildings were originally designed to resist vertical load. On the other hand, reinforced walls can have a ductile out-of-plane behaviour, depending on the amount of vertical steel reinforcement (Abboud et al., 1996). FRP

can be bonded parallel to tensile actions over the wall to increase the strength of walls subjected to out of plane bending action. Several researchers (Albert et al., 2001; Ehsani et al., 1999; Galati et al., 2006; Gilstrap and Dolan, 1998; Hamilton III and Dolan, 2001; Kuzik et al., 2003; Lunn and Rizkalla, 2011; Triantafillou, 1998) have shown that FRP strengthening system can effectively increase the out of plane strength and ductility of walls regardless the type of masonry unit.

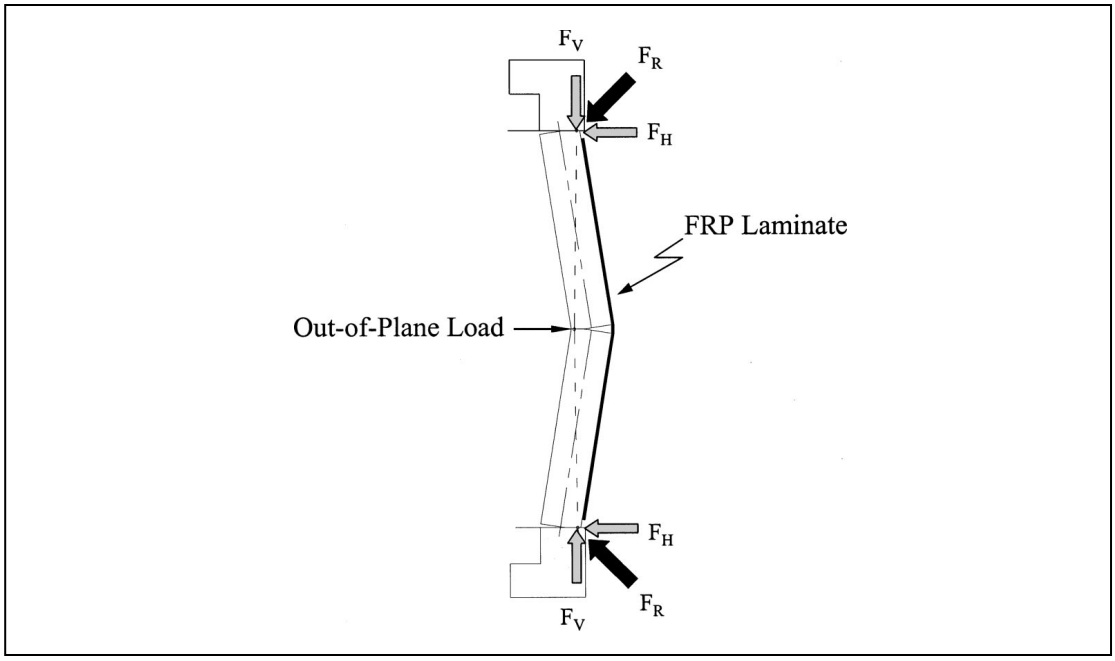

Figure 2.6 Out-of-plane failure mechanism (redrawn after Tumialan et al. (2003))

Figure 2.6 shows the failure mechanism of a masonry wall subjecting the out-of-plane load. The main failure mode observed was shear of the masonry unit as the supports of the walls (Kuzik et al., 2003; Paquette et al., 2001; Tumialan et al., 2003; Tumialan et al., 2002). This was expected because only the bending strength of the specimens was increased by the FRP reinforcement. Other typical failure mode observed was flexural failure due to crushing of the masonry unit (Mosallam, 2007;

Tumialan et al., 2002); flexural-shear cracking of the masonry (Galati et al., 2006; Mosallam, 2007); or rupture of FRP fibres (Albert et al., 2001; Ghobarah and El Mandooh Galal, 2004). And the last important failure mode was debonding of the FRP composites (Ehsani et al., 1999; Kuzik et al., 2003; Tumialan et al., 2002). There have been two debonding failure modes observed from the literature: intermediate crack (IC) debonding (Galati et al., 2006; Ghobarah and El Mandooh Galal, 2004) and plate end debonding (Ghobarah and El Mandooh Galal, 2004).

Masonry walls subjected to in-plane actions have basically three types of failure mechanisms (Tomazevic, 1999): 1) sliding shear failure: sliding of part of the wall over a mortar joint; 2) shear failure: diagonal cracks through the mortar joints or the masonry units caused by the tensile failure of the masonry; and 3) flexural failure: crushing of the compressed units at the end of the blocks due to in-plane bending of the wall.

There are several different FRP strengthening schemes have been tested to address the shear failure mechanism (Alcaino and Santa-Maria, 2008). Tests of masonry walls/panels externally bonded with FRP strips and subjected to diagonal monotonic compression to model shear action also showed large improvement of strength of the masonry walls/panels (Valluzzi et al., 2002).

Monotonic shear load of masonry walls with FRP bonded, parallel to the bed joints, in diagonal directions or in full wall have shown large increase of lateral resistance (Stratford et al., 2004). Cyclic shear tests have also shown dramatic increases of

shear strength, and also effective control the cracking formation and pattern (Alcaino and Santa-Maria, 2008; ElGawady et al., 2007; Haroun et al., 2005). Dynamic testing of masonry walls externally strengthened with FRP subjected to a series of earthquake motions, showed an improvement of the lateral resistance (ElGawady et al., 2005b; Turek et al., 2007). As well as strengthening the wall specimens were strengthened with FRP before testing, in some cases the walls were pre-loaded to simulate the damage and later repaired with FRP strips. These also showed improvement of strength (ElGawady et al., 2005a). In the case of the diagonally compressed panels failure occurred due to debonding of the FRP strips.

The failure mechanism of the walls subjected to in-plane shear depended on the relative flexural, sliding and shear strengths obtained after strengthening (Zhuge, 2010). When the flexural strength was large enough the failure mode was the debonding of the FRP strips (ElGawady et al., 2007; Stratford et al., 2004; Valluzzi et al., 2002; Zhuge, 2010). In masonry panels and walls under in-plane shear loading, debonding initially started at an intermediate location of the FRP strips, where the main diagonal crack developed crossed the FRP reinforcement. Later, the final brittle failure occurred by debonding of the overlays from the end of the strips (Alcaino and Santa-Maria, 2008).

To sum up, externally bonded FRP strips can increase the strength and deformation capacity of masonry walls subjected to both out-of-plane and in-plane loading. And one of the main failure modes is debonding of the FRP composites.

2. 4 FRP strengthened masonry arch structures

There has also been prior research upon FRP strengthened arches and vaults. Barrel vaults are similar in form to arches; however, unlike arches, the extrados is often accessible for strengthening, whereas it might not be acceptable to apply FRP to the visible intrados of the vault. FRP composites restrain the hinging behaviour in an arch, but they do not prevent crack formation (Drosopoulos et al., 2007; Foraboschi, 2004). Depending on the extension and location of the FRP strengthening portions of the arch and the loading scheme, the formation of hinges may be either altered or completely prevented. The location of two consecutive hinges is alternate between extrados and intrados, hence strengthening FRP on the whole extrados or intrados can completely prevents the formation of mechanism (De Lorenzis, 2008). By restraining the growth of flexural cracks it is possible to prevent the hinge mechanism mode of failure (De Lorenzis, 2008; Foraboschi, 2004), and it has also been demonstrated that the lateral abutment thrust is reduced (Bati et al., 2007; De Lorenzis et al., 2007). Increasing the hinge mechanism failure load, however, this means that other failure mechanisms may become more critical. Five characteristic failure modes have been identified for FRP-strengthened arches in previous work (Bati and Rovero, 2008; De Lorenzis, 2008; Foraboschi, 2004; Valluzzi et al., 2001):

a) the hinge mechanism (local rotation about flexural cracks);

b) sliding along the mortar joints (shear cracks);

c) compressive failure of the masonry;

d) tensile rupture of the FRP; and

e) separation of the FRP from the masonry (debonding failure of the adhesive joint).

As well as complete detachment of the FRP strengthening from the masonry (failure mode e), debonding plays an important role in the failure modes (a) and (b). The FRP bonding system strengthens bridges local flexural or shear cracks, but as the cracks grow a portion of the adhesive joint fails adjacent to the crack, the extent of which increases with crack opening. It is the interaction of local debonding, crack opening, and compatibility of the partially debonded FRP with the curved surface of the masonry that determines how well the FRP restrains the hinge rotation at the position. An understanding of the debonding mechanism is therefore an important part of understanding the failure of FRP strengthened masonry arches.

Adding FRP strengthening to a masonry arch thus changes its failure mode. An arch without strengthening forms a kinematic mechanism. The presence of FRP, however, allows tension to be carried across an opening crack, and the strength of the component parts must be examined, in a similar manner to the sectional analysis of a curved reinforced concrete beam. Several researchers have developed analytical predictions of the ultimate strength of FRP strengthened masonry arches. Some can simplistically be described as discrete block models, in which the contact properties between the FRP and masonry and between adjacent masonry blocks are modelled (Caporale et al., 2006; Drosopoulos et al., 2007). Other analyses take a sectional analysis of the strengthened arch (Bati and Rovero, 2008; Chen, 2002; Foraboschi,

2004; Valluzzi et al., 2001). This broad classification is rather crude: all of the previously proposed analysis methods combine aspects of mechanism failure and component failure to different extents, reflecting the possible failure modes in an FRP strengthened arch. Prior research has thus demonstrated that the load carrying capacity of a masonry arch can be increased using externally bonded FRP strengthening. However, a clear understanding of the failure mechanics (and in particular the bond between the FRP and the masonry) has yet to be fully developed.

2. 5 Bond behaviour between FRP and masonry

Comparing the literature about the bond behaviour of FRP to concrete, very little research on the bond of FRP to masonry has been developed (Aiello and Sciolti, 2006; Capozucca, 2010; Fedele and Milani, 2012; Grande et al., 2011a; Kashyap et al., 2011; Oliveira et al., 2011; Seim and Pfeiffer, 2011; Willis et al., 2009), involving the analysis of different key parameters as substrate materials, composite systems, bonded length, and test setup.

The bond behaviour between FRP and masonry is usually experimentally investigated using the same setup for the concrete substrates as shown in Figure 2.7.

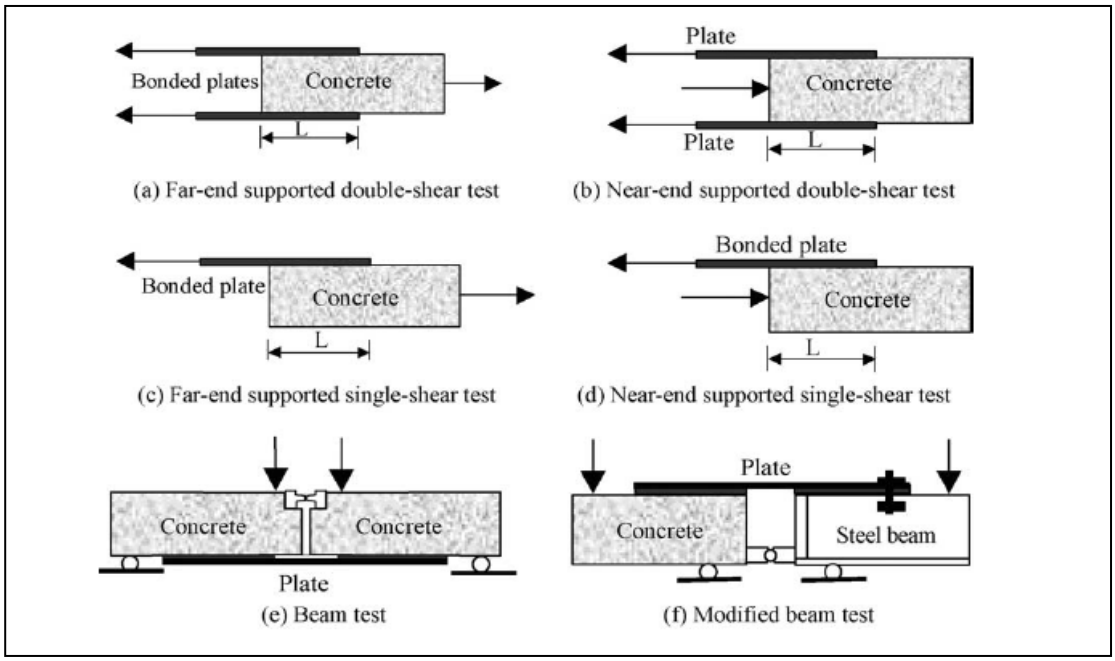

Figure 2.7 Classification of bond tests (redrawn after Yao et al. (2005))

Aiello and Sciolti (2006) adopted double shear test to investigate the bond behaviour between FRP and leccese stone/naples tuff units. It is found that the larger strength of masonry lead to the greater bond strength and longer effective bond length. The debonding failure has been observed in the masonry substrate. They concluded that the bond behaviour and load transfer mechanism of FRP bonded to masonry are similar to FRP bonded to concrete. However, it will be different once there are porous in the clay brick because it leads to weaker bond strength (Willis et al., 2009).

From Camli and Binici (2007)'s tests, double shear tests were carried out on FRP bonded to clay bricks. The results showed that the different failure mechanisms were dependent upon the bond length, the FRP width and the type of test.

An experimental investigation on the bond behaviour of historical clay brick

strengthened with different types of composites materials has been reported in Capozucca (2010). Different debonding mechanisms were observed, although there was not a clear relationship between the debonding mechanism and the reinforcing systems.

Grande et al. (2011a) presented single shear tests carried on FRP bonded clay bricks. There were two important results reported: (1) bond strength increases with bond length until bond length reaches the effective bond length; (2) the effective bond length is affected by the mechanical properties of the masonry and by the type of strengthening system. Similar results on clay bricks, calcium-silicate bricks and sandstone were also observed in Seim and Pfeiffer (2011).

There has been even less concern on the bond behaviour between FRP and masonry assemblies compared with the tests on the masonry units.

Willis et al. (2009) reported an experimental investigation on the bond behaviour of clay brick masonry assemblies strengthened with different types of composites materials. The appearance of the mortar joint does not have a significant impact on the bond behaviour as crack propagation occurred primarily through the brick units. The bond strength increases with bond length until bond length reaches the effective bond length. Similar results on clay masonry assemblies were also identified in Oliveira et al. (2011). The bond strength of the FRP bonded masonry assemblies is controlled by the mechanical properties of masonry assemblies (Oliveira et al., 2011). The concave substrates caused a slight decrease of the bond strength due to the

interfacial normal stresses along the FRP-masonry interface (Oliveira et al., 2011).

In Willis et al. (2009), it is also found that the bond strength and ductility of NSM (near surface mounted) is much higher than that of externally bonded because of greater confinement of the debonding cracks. The orientation of FRP perpendicular to the bed joints leads to an increase of bond strength compared to orientation parallel to the bed joints. That is because there are more brick elements which are activated for bonding (Seim and Pfeiffer, 2011; Willis et al., 2009).

Similar to that of FRP-to-concrete, the local bond stress-slip relationship of FRP-to-masonry can be represented by a three stages law as shown in Figure 2.8: elastic, microcracking (softening) and macrocracking (debonding) (Capozucca, 2010; Grande et al., 2011b; Kashyap et al., 2011; Oliveira et al., 2011; Su et al., 2011; Willis et al., 2009).

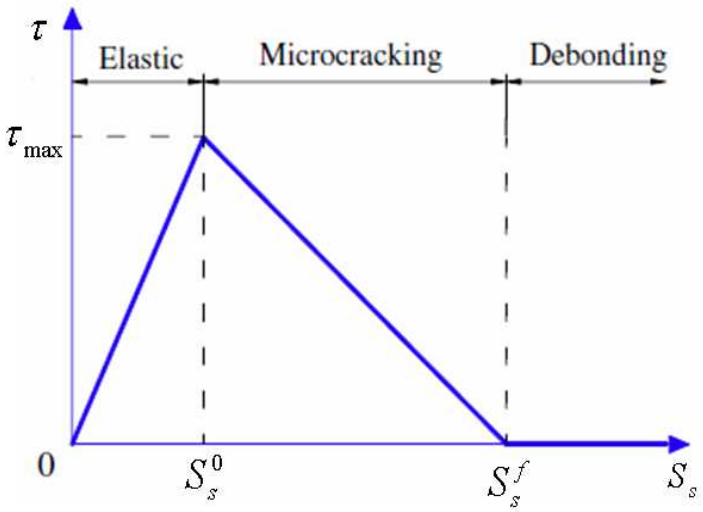

Figure 2.8 Idealised bond-slip model for FRP-to-masonry (redrawn after Su et al. (2011))

To compare with the test results of the maximum bond stresses of FRP-to-masonry units, a bilinear bond-slip curve was used by Grande et al. (2011b) and the parameters are calculated from the Italian document CNR-DT200 (2006). However, the proposed linear bond-slip model cannot be considered satisfactory for any possible masonry construction. The same authors then adopted an exponential bond-slip law, original for FRP-to-concrete (Nakaba et al., 2001), to predict the bond strength of FRP-to-clay bricks in FE modelling (Grande et al., 2011a). This exponential bond-slip law leads to a better prediction.

The bond-slip model used by Willis et al. (2009) was the one for FRP-to-concrete proposed by Seracino et al. (2007) to predict the bond strength of FRP-to-masonry assemblies. The bond-slip parameters obtained from the test delivered a better prediction than that from the original Seracino's model while using the identical equations.

Kashyap et al. (2011) compared predictions on the pull-off test on FRP-to-masonry assemblies using the homogeneous analysis (FRP-to-masonry) and the heterogeneous analysis with disparate material properties for the mortar and bricks. A bilinear bond-slip law was assumed for both homogeneous and heterogeneous analysis as shown in Figure 2.9. The results showed that the homogeneous analysis led to a slight lower prediction on the bond strength of FRP-to-masonry assemblies. For the heterogeneous analysis, only a slight reduction in the bond strength was observed when zero shear stress for the FRP-to-mortar was assumed. This is because the mortar only has small amount of bond length compared to masonry unit.

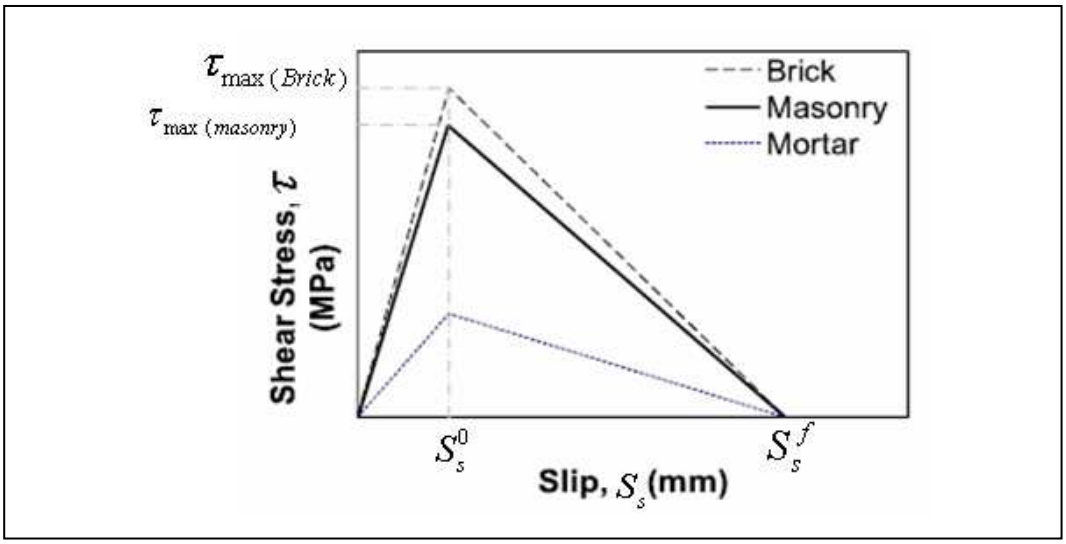

Figure 2.9 Load bond-slip models for homogeneous and heterogeneous analysis (redrawn after Kashyap et al. (2011))

To investigate the effects on the bond strength from the ratio between the FRP width and masonry's, Fedele and Milani (2010; 2011; 2012) developed a series of FE models. It is found that the overall ductility, namely the maximum slip at failure, depend significantly on the ratio between the FRP width and masonry's. The increase of this ratio leads to the decreases on the maximum shear stress and the maximum slip at the failure. Eventually, the width ratio coefficient in the bond-slip law from the Italian document CNR-DT200 (2006) was modified based on the results from FE modelling.

To investigate the tensile behaviour (mode-I failure) of the bond interface of FRP-to-masonry, Oliveira et al. (2011) conducted a pull-off test with action being perpendicular to the bond interface. The results showed that failure was due to the ripping of a thin layer of brick and mortar. Therefore, the tensile strength of the brick and mortar controls the tensile strength of the FRP-to-masonry interface.

To sum up, the key findings from the literature about the bond behaviour between FRP and masonry are:

a) the bond and load transfer mechanism of FRP bonded to masonry are similar to FRP bonded to concrete;

b) for mode-II bond behaviour, the bond strength of FRP-to-masonry is controlled by the mechanical properties of masonry assemblies;

c) the bond-slip law for FRP-to-concrete may need to be modified for the FRP-to-masonry, especially for the lower strength bricks; and

d) for mode-I bond behaviour, the tensile bond stress is dominated by the tensile strength of the masonry assemblies.

2. 6 Numerical modelling of FRP strengthened masonry structures

In order to develop better understanding of the behaviour of masonry arch structures and FRP strengthened such structures, several numerical studies have been produced to analyse them. Different model strategies and constitutive laws for masonry have been proposed corresponding to different accuracy and efficiency demanded (Lourenço, 1996). In terms of the modelling of FRP strengthened structures, modelling the FRP-to-masonry interface is critical to the behaviour of such structures. The modelling of masonry, constitutive model of masonry and modelling of the bond behaviour between FRP and masonry are reviewed in the following section.

2.6.1 Modelling of masonry

The definition and use of suitable material constitutive models dominates the accuracy and effectiveness of simulating masonry structures. Depending on the level of accuracy and the simplicity desired, the modelling strategies of masonry proposed in the literature can be classified into three different types (Lourenço, 1996; Lourenço and Rots, 1997): a) micro model approach; b) micro-macro model approach; and c) macro model approach, as shown in Figure 2.10.

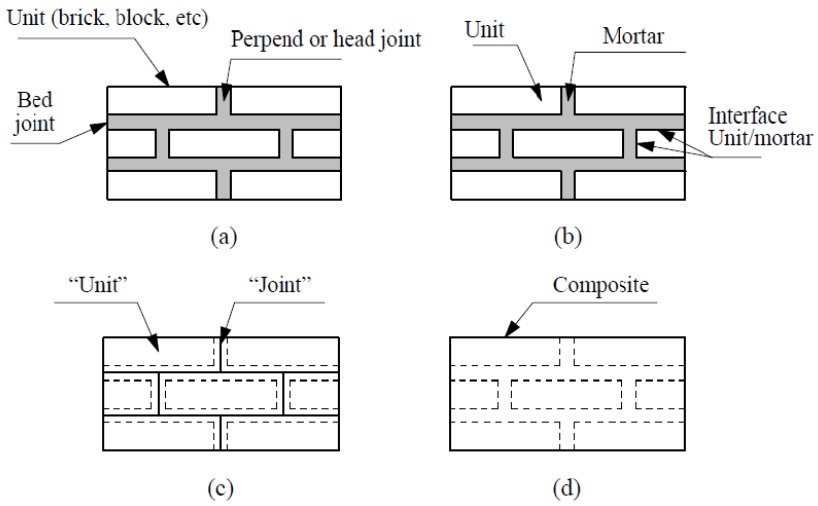

Figure 2.10 Modelling strategies for masonry structures: (a) masonry sample; (b) micro-model; (c) micro-macro model; (d) macro model. (Lourenço (1996))

Micro model (Figure 2.10b): masonry units and mortar both are modelled separately with individual properties which are obtained through experimental tests conducted on the single material components, using continuum elements. The unit-mortar interface is modelled by interface element or discontinuous elements. This approach leads to structural analyses that required great computational effort (Alfano and

Sacco, 2006; Giambanco and Di Gati, 1997; Giambanco et al., 2001; Lotfi and Shing, 1994; Sacco and Toti, 2010).

Micro-macro model (Figure 2.10c): A homogenization procedure is used to obtain the constitutive model for masonry, or homogenised response is obtained from tests. The behaviour of the mortar-masonry unit joint interface is also considered in this approach. This approach can lead to effective models, that require reduced computational effort for a structural analysis (Chaimoon and Attard, 2007; Lourenço and Rots, 1997; Milani et al., 2006a; Milani et al., 2006b; Thavalingam et al., 2001). The mortar thickness and the unit–mortar interfaces are lumped into a zero-thickness interface while the dimensions of the masonry units are expanded to keep the geometry unchanged due to the mortar not being explicitly modelled. Accuracy is decreased because the Poisson's effect of the mortar is not considered.

Macro model (Figure 2.10d): This approach does not distinguish between masonry units and the mortar joint but treats masonry as an isotropic continuum. All of the components, including units, mortar and unit-mortar joint, are smeared out in the continuum (Fanning and Boothby, 2001; Giordano et al., 2002; Lourenço, 1996; Lourenço et al., 1998; Marfia and Sacco, 2005). A weak tensile strength is usually adopted to capture the unit-mortar interface behaviour.

Regarding finite element (FE) model, the micro-model approach adopts discontinuum or continuum model which explicitly models each bricks and joints between bricks and mortar, and the macro-modelling approach uses continua model

(Lourenço and Rots, 1997). Each of the modelling strategies has advantages and disadvantages, and hence apply to different requirements. The micro-model approach is used to obtain the better understanding about the global and local behaviour of masonry structures. Micro-macro model is applicable when the structures are in the medium geometry scale, masonry does not occupy the majority part of structures or the effects of unit-mortar joint cannot be smeared out in the masonry continuum as macro modelling strategy. Macro-model approach is applied to analysis the structures including backfills and walls with greater dimensions so that the stress state in the macro length scale will be almost uniform (Lourenço et al., 1998).

2.6.2 Constitutive model of masonry

Accurate micro and macro models of masonry structures require appropriate material properties and constitutive models. However, the properties of masonry are influenced by a larger number of factors, such as the material properties of the unit, mortar, and unit-mortar joint. There are two material models involved in the aforementioned three modelling strategies: continuum solid materials (units, mortar, or isotropic masonry composites) and the unit-mortar interface.

A feature of quasi-brittle materials like masonry, rock or concrete, is that they fail due to the progress of internal crack growth. Therefore, constitutive models for concrete, such as Drucker-Prager failure criterion (Domède et al., 2009; Giordano et al., 2002; Thavalingam et al., 2001) and the William and Warnke model available in ANSYS (Fanning and Boothby, 2001), can be used to model masonry (Lotfi and

Shing, 1994; Lourenço, 1996). The masonry defined here is referred to composite involved in macro-model and the units involved in micro and micro-macro models. The uniaxial compression strength and the initial elastic modulus of the unit and mortar can be obtained from the test. However, the tensile behaviour, especially the full softening behaviour, and the biaxial behaviour of masonry are difficult to obtain from the test (Lourenço, 1996; Pluijm, 1997).

The unit-mortar joint interface is explicitly modelled in the micro and micro-macro models. The unit-mortar joint is usually modelled as an interface with zero thickness (Lourenço, 1996; Milani et al., 2006a; Milani et al., 2006b; Sacco and Toti, 2010). The interface is a potential crack-opening and traction-slip plane with dummy stiffness to avoid interpenetration of the continuum in the micro model. In the micro-macro model approach the interface elastic stiffness has to be calculated taking into account the properties of the mortar and the unit-mortar joint because the mortar is not explicitly modelled (Lourenço and Rots, 1997; Sacco and Toti, 2010).

The nonlinear response of the unit-mortar joints controls the features of masonry arch behaviour. Two different phenomena occur in the unit-mortar joint interface, one associated with mode-I failure (tensile failure) and the other associated with mode-II (shear failure). In terms of mode-I failure, the tensile bond strength, mode-I fracture energy and the shape of the tension softening curve dominate the behaviour of unit-mortar joint interface under tension action. For mode-II, the shear strength and the mode-II fracture energy of the interface are related to the confinement stress. There are several constitutive laws to describe the behaviour of unit-mortar joint

interface. These constitutive laws can be classified into two types. One is the composite interface model by combining some plastic theories (Chaimoon and Attard, 2007; Drosopoulos et al., 2007; Lourenço, 1996; Lourenço and Rots, 1997; Milani et al., 2006a; Milani et al., 2006b); the other is a cohesive interface model by defining two failure modes (mode-I and mode-II) and their interactions (Brasile et al., 2007; Sacco and Toti, 2010). A composite interface model may include, for example, a tension cut-off criterion for mode-I failure, a coulomb friction criterion for mode-II failure and a compression cap criterion for compression failure mode as shown in Figure 2.11. Each criterion of the composite model corresponds with different failure modes (Chaimoon and Attard, 2007; Drosopoulos et al., 2007; Lourenço, 1996). A cohesive interface model combines damage and friction to capture the behaviour of a cohesive zone through defining the constitutive laws of both mode-I and mode-II and the relationship of mixed mode (Alfano and Sacco, 2006; Sacco and Toti, 2010).

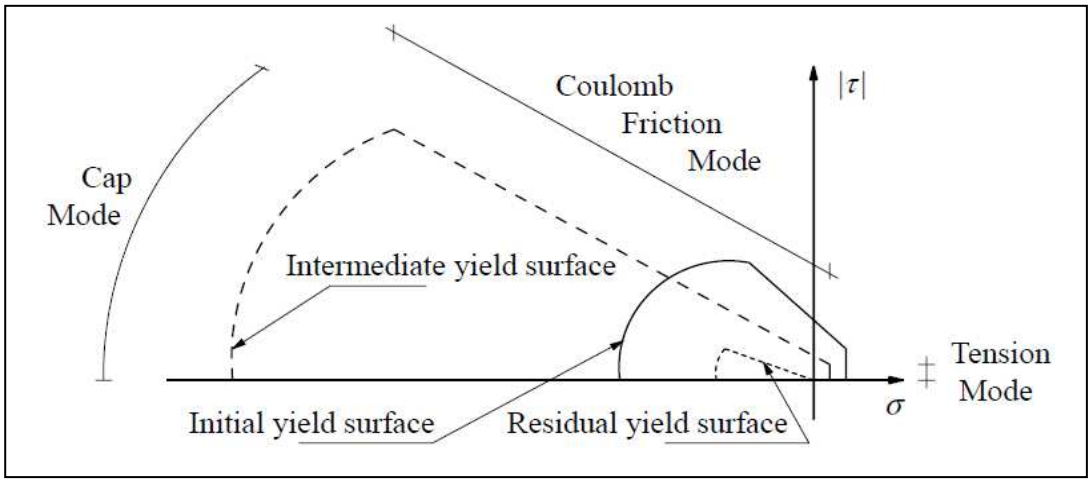

Figure 2.11 A composite interface model (Lourenço (1996))

2.6.3 Modelling of bond behaviour between FRP and masonry

The local bond behaviour between FRP and masonry is quite similar to FRP-to-concrete bond because failure occurs within the brittle masonry and the material properties of masonry are quite similar as concrete (Aiello and Sciolti, 2006; Capozucca, 2010; Oliveira et al., 2011). This bond behaviour is even more critical when FRP strengthening masonry arch structures fail by debonding. To model the bond behaviour between FRP and masonry/concrete, three modelling approaches can be identified from the literature: direct model approach, interface model approach and crack band approach described below:

Direct model approach: the behaviour of the masonry/concrete is accurately modelled in a meso-scale, usually using 0.5-2mm element size, with an appropriate constitutive model. The debonding progress is modelled by the failure of masonry/concrete substrates (Lu et al., 2006; Lu et al., 2005b);

Interface model approach: the bond behaviour is modelled using a layer of interface elements usually with zero thickness. Therefore, debonding is caused by the failure of interface elements (Diab and Wu, 2007; Salomoni et al., 2011);

Crack band approach: the debonding failure is assumed to take place within a band in the masonry/concrete adjacent to the FRP bond interface and a modified constitutive law needs to be provided for this band (Coronado and Lopez, 2007; Coronado and Lopez, 2010).

The direct model approach can be used to predict not only the entire debonding failure process but also the bond-slip relationship for the FRP-to-masonry/concrete interface. The interface model approach relies on the appropriate use of a bond-slip model, as the constitutive law for interface element, which may be developed from either the first approach or from test. This is thus not a predictive approach for the bond behaviour but appropriate for modelling large structures where meso-scale modelling of masonry is unrealistic, like the large-scale of masonry arch bridges (Chen et al., 2012). The crack band model approach requires a different material constitutive model for the crack band which needs to be obtained from experiments. It means this approach is not truly predictive. In addition, the varying epoxy resin may affect the properties of such band. Therefore, for simulating the detailed bond behaviour, the direct model approach is more appropriate. In fact there were very limited numerical researches on bond behaviour using this approach due to the difficulties of modelling masonry. The details of modelling the bond behaviour of the FRP-to-concrete joint are reviewed in Chapter 4. This section focuses on the modelling of FRP strengthened masonry arch structures.

Nonlinear spring elements with a contact-friction model were used to model the bond behaviour of FRP-to-masonry arch by Drosopoulos et al. (2007). The bond-slip relationship was modelled using the contact-friction model and the spring element was used to model the mode-I bond behaviour. However, no details of bond models, such as the values, were described in the paper.

A prefect bond joint was assumed and no interface model was involved to capture a

shear failure mode of a smaller scalar masonry arch test (Cancelliere et al., 2010; Sacco and Toti, 2010). No bond-slip model is involved in this study because the failure was dominated by the shear failure in the unit-mortar joint.

Homogenization procedure was introduced to model FRP strengthened masonry substrates through considering a modified constitutive model for masonry without considering bond-slip model (Cecchi et al., 2005; Milani et al., 2006c). Grande et al. (2008) used a macro-modelling procedure to simulate masonry and the constitutive laws of masonry were modified when the FRP strengthening system used. There was no bond-slip model involved in this study.

Milani assigned the bond-slip model proposed by CNR (2004) to interface elements in order to capture the bond behaviour between FRP-to-masonry (Milani, 2010; Milani et al., 2009a; Milani et al., 2009b). However, only shear stress-slip (Mode-II) model was considered for masonry structures in this study, which is not appropriated for a FRP strengthened structures failed by mixed mode, such as FRP strengthened masonry arch bridges.

Basilio (2007) used a six-node interface element to model the bond joint of FRP-to-masonry, and a composite interface model as shown in Figure 2.11 to describe the constitutive law of bond interface. The softening behaviour of bond interface, such as fracture energies of both modes, was assumed and opened to further research.

To summarise, the key findings from the existing studies on the numerical modelling

of FRP strengthened masonry structures are:

a) in order to properly model the FRP strengthened masonry structures, especially for those failed by debonding, the interface model is required to capture the bond behaviour between FRP and masonry;

b) the mode-II bond behaviour of FRP-to-masonry can be modelled using the existing bond-slip relationship, for example, bond-slip model proposed by Lu et al. (2005a) or CNR (2004);

c) the mode-I bond behaviour still needs to be investigated for the FE modelling; and

d) the interaction between two modes (mode-I and mode-II) has less concerned in the literature although only one mode is dominant and occurs firstly.

2. 7 Conclusion remarks

This chapter is a review of existing knowledge relevant to masonry arch structures and FRP strengthened arch structures.

The knowledge of masonry and arch structures has been reviewed to create a solid background about the material properties of masonry and the behaviour of masonry arch structures, which is needed to be used in Chapter 3 to conduct a well-designed experimental study. The critical failure mode of masonry arch bridges is hinge mechanism. The mechanism method and FE modelling are two popular methods to

access and analyse masonry arch bridges. After reviewing the existing numerical studies on the masonry structures, it is clearly that the model of the mortar interface dominates the performance of FE models. A numerical study onto the unstrengthened masonry arches is thus presented in the Chapter 5.

The knowledge of FRP strengthened masonry and concrete structures are reviewed. The debonding failure is one critical mode in the FRP strengthened structures. It usually occurs at a region of high stress concentration, at material discontinuities, or at cracks in a strengthened system. Externally bonding FRP to the masonry structures can improve their loading capacity and deformation capacity. In terms of FRP strengthened masonry arch bridges, the mechanism failure is to prevent other failure modes of failure will occur, such as debonding. In particular, the bond behaviour between FRP and masonry arches needs to be further studied due to the lack of contributions, which highlights the demands for the work presented through this dissertation.

In terms of the numerical modelling of FRP strengthened concrete structures, it is clear that the existing FE studies suffer the various deficiencies. More specially, the existing studies failed to capture the entire debonding failure due to the lack of accurate modelling of concrete material. This leads to the necessary basis for the advanced FE model and constitutive law introduced in the Chapter 4.

The bond behaviour between FRP and masonry is similar as that for the FRP to concrete. The bond strength of FRP-to-masonry is dominated by the mechanical

properties of masonry assemblies. The bond-slip law for FRP-to-concrete may need to be modified for FRP-to-concrete masonry. The tensile strength of masonry controls the mode-I bond behaviour of FRP-to-concrete masonry.

FE modelling of FRP strengthened masonry arch structures has been very less concerned in the existing literature. The application and effects of the bond-slip law for FRP-to-concrete masonry and the mixed mode model need to be addressed in this study. An advanced model of masonry arch bridge developed in the Chapter 5 is used in the Chapter 6 to model the FRP strengthened masonry arch bridges. An interface model considering the mixed mode behaviour of FRP-to-concrete masonry arches is developed as well because the lack of knowledge existed.

CHAPTER 3

EXPERIMENTAL STUDY ONTO A CONCRETE MASONRY ARCH BRIDGE REPAIRED USING FIBRE REINFORCED POLYMER COMPOSITES

3. 1 Introduction

Masonry arch bridges are an important part of many countries' rail and road transport infrastructure. Most are historic structures that survive in active service largely due to the inherent stability of the arch form. The combined effects of modern traffic loads (for which they were not designed) and degradation of the masonry mean that some of these bridges suffer from significant damage. It is important to safeguard and extend the life of these structures, especially where arch bridges form critical links in the transport network and where major disruption would result from their closure.

Fibre-reinforced polymer (FRP) systems are increasingly used for bridge repair and strengthening, with particularly widespread application to concrete bridges (ACI, 2008; Concrete Society, 2004). The FRP is adhesively bonded to the surface of the existing structure, where it provides tensile capacity and restrains the opening of cracks. FRP has the advantages of a low weight to strength ratio, short installation periods and minimal intervention upon the structure (Teng et al., 2002). The small thickness of FRP required for strengthening is especially important for historic bridges, as it minimises changes to the bridge's appearance. The application of FRP

composites to masonry structures is less well established, although it has been the subject of research and development in recent years (De Lorenzis, 2008), demonstrating that FRP can be used to upgrade the structural performance of a variety of masonry elements, and has resulting in design guidance being issued by the National Research Council in Italy (CNR, 2004) and by the American Concrete Institute (ACI, 2007). Further work is required, however, to apply FRP strengthening to increase the load capacity of masonry arch bridges.

3.1.1 Masonry arch mechanics

Masonry is an assemblage of bricks or blocks that are generally joined with mortar. Failure of the masonry is usually governed by the low interfacial strength between the brick and mortar in tension and shear. In a single ring masonry arch bridge, the critical failure mechanism is a four-hinge mechanism (Figure 3.1), when the arch is loaded at its quarter span (Heyman, 1966; Heyman, 1982). Sliding or crushing mechanisms (discussed further below) are also possible in a masonry arch, but these are unlikely to occur because the critical loads are well above that of the hinge mechanism (Foraboschi, 2004; Heyman, 1982). In multi-ring arch bridges, ring separation may become critical.

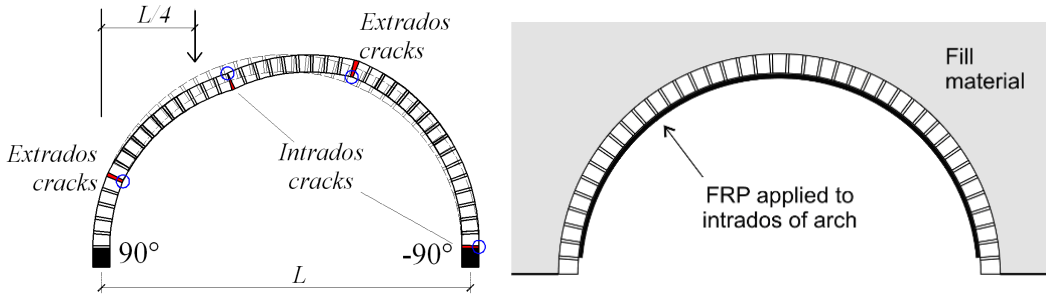

Figure 3.1 The use of FRP strengthening to resist the formation of the four-hinge mechanism in a masonry arch

Figure 3.1 shows only the arch, as this is the principal load-carrying member of the bridge. However, the arch does not act in isolation: fill is placed above the arch to provide the required top profile, and this is retained by spandrel walls on either side of the bridge, which extend upwards to act as parapets. The bridge abutments both retain the fill material and prevent springing of the arch.

The critical hinge mechanism involves flexural cracks that open along the mortar joints at the hinge locations. These cracks alternate between the intrados and extrados of the arch as shown in Figure 3.1 (Heyman, 1982). Externally bonded FRP can be used to provide tensile capacity and restrain the opening of the cracks, just as for concrete strengthening. Ideally, the FRP would be bonded to both the intrados and extrados of the arch so that both types of crack can be effectively restrained; however, the extrados is usually not accessible without removing the fill material. As a consequence, only intrados FRP strengthening can usually be applied to a masonry arch bridge.

3.1.2 FRP strengthening for masonry structures

Much of the research into FRP strengthening for masonry has so far studied walls subjected to in-plane (Alcaino and Santa-Maria, 2008; ElGawady et al., 2005a; Stratford et al., 2004; Triantafillou, 1998; Turek et al., 2007) and out-of-plane (Albert et al., 2001; Ehsani et al., 1999; Hamoush et al., 2001; Kuzik et al., 2003; Paquette et al., 2001; Triantafillou, 1998) loading. The out-of-plane bending of walls is relevant to the four-hinge mechanism failure in arches, as there is a similar interaction between the FRP, the opening of flexural cracks in the walls, and the reliance upon the adhesive joint between the FRP and the masonry. Wall elements, however, do not include the curvature present in arches.

There has also been prior research upon FRP applied to arches and vaults. Barrel vaults are similar in form to arches. However, unlike arches, the extrados is often accessible for strengthening, whereas it might not be acceptable to apply FRP to the visible intrados of the vault. FRP composites restrain the opening of flexural cracks in an arch, but they do not prevent crack formation (Drosopoulos et al., 2007; Foraboschi, 2004). By restraining the growth of flexural cracks it is possible to prevent the hinge mechanism mode of failure (De Lorenzis, 2008; Foraboschi, 2004), and it has also been demonstrated that the lateral abutment thrust is reduced (Bati et al., 2007; De Lorenzis et al., 2007). Increasing the hinge mechanism failure load, means that other failure mechanisms may become more critical. Five characteristic failure modes have been identified for FRP-strengthened arches in previous work (Bati and Rovero, 2008; Chen, 2002; De Lorenzis, 2008; Foraboschi, 2004; Valluzzi

et al., 2001):

- the hinge mechanism (local rotation about flexural cracks);
- sliding along the mortar joints (shear cracks);
- compressive failure of the masonry;
- tensile rupture of the FRP; and
- separation of the FRP from the masonry (debonding failure of the adhesive joint).

Debonding of the strengthening occurs in the weakest link between the FRP, adhesive, and masonry; this is often slightly below the surface of the masonry (Foraboschi, 2004; Stratford et al., 2004). As well as complete detachment of the strengthening from the masonry (the last failure mode), debonding plays an important role in the first two failure modes. The FRP strengthening bridges local flexural or shear cracks, but as the cracks grow a portion of the adhesive joint fails adjacent to the crack, the extent of which increases with crack opening. It is the interaction of local debonding, crack opening, and compatibility of the partially debonded FRP with the curved surface of the masonry that determines how well the FRP restrains the hinge rotation at the position. An understanding of the debonding mechanism is therefore an important part of understanding the failure of FRP strengthened masonry arches.

Adding FRP strengthening to a masonry arch thus changes its failure mode. An arch without strengthening forms a kinematic mechanism. The addition of FRP, however, allows tension to be carried across an opening crack, and the strength of the

component parts must be examined, in a similar manner to the sectional analysis of a curved reinforced concrete beam. Several researchers have developed analytical predictions of the ultimate strength of FRP strengthened masonry arches. Some can simplistically be described as discrete block models, in which the contact properties between the FRP and masonry and between adjacent masonry blocks are modelled (Caporale et al. 2006; Drosopoulos et al. 2007). Other analyses take a sectional analysis of the strengthened arch as their starting point (Bati and Rovero, 2008; Chen, 2002; Foraboschi, 2004; Valluzzi et al., 2001). This broad classification, however, is rather crude: all of the previously proposed analysis methods combine aspects of mechanism failure and component failure to different extents, reflecting the possible failure modes in an FRP strengthened arch.

Prior research has thus demonstrated that the load carrying capacity of a masonry arch can be increased using externally bonded FRP strengthening; however, a clear understanding of the failure mechanics (and in particular the bond between the FRP and the masonry) has yet to be fully developed. The tests described in this chapter examine both the global response of a FRP strengthened masonry arch bridge and the local mechanics of failure.

3. 2 Experimental methodology

Tests were conducted upon a model two-span concrete masonry arch bridge. In outline, the tests involved:

- Loading each of the masonry arches in turn (north first) at quarter-span until a four-hinge mechanism formed so as to simulate damage to the arch prior to strengthening.
- Application of the FRP strengthening.
- Testing each of the arches in turn until failure of the strengthening system occurred, but without complete collapse of the structure.
- A final destructive test upon the south arch, resulting in complete collapse.

The methodology is described in more detail in the following sections.

3.2.1 General arrangement

A 1/3 scale single ring two-span concrete masonry arch bridge model was built in the Structures Laboratory of the University of Edinburgh in 1996. The two semi-circular single ring arches (2080mm span, 1040mm rise, 100mm ring thickness and 1680mm width) were constructed from concrete bricks (100mm×65mm×215mm) and cement mortar (nominally 15mm thick), as shown in Figure 3.3 in the original shape. There were 41 brick units in the arch ring and 1 brick unit in the ring thickness. The bricks were laid in a stretcher bond with the bed joints across the arch width. After the arches were built, they were covered by sand fill to a height of 240mm above their crowns as shown in Figure 3.4. The fill was contained by plastic sheeting and timber spandrel walls and abutments; the timber walls were not in contact with the arches so did not directly affect their structural performance. The abutments were supported using laboratory steelwork attached to the laboratory strong floor, and were effectively rigid.

The arches were originally tested to investigate their behaviour under various positions of load and cracks had already initiated in the arch (Robinson, 2000), at the same position as the four-hinge mechanism investigated in the current tests. This existing damage was simply quantified by measuring the shape of the arches and the joint opening width before the current test. Figure 3.2 shows the shape of the arches before the current test. It can be found that the maximum deflecion located at the crown of the arches, 11mm at north arch and 13mm at south arch, which can be contributed to the weight of the backfill and the residual deformation from the past tests. There was no significant opening on the mortar joints at both arches (i.e. smaler than 1mm), indicating that the existing damage was significantly smaller than that from the current test as shown in Figure 3.20.

The current tests were conducted on the arches in 2008. It should be noted that no previous tests have been carried out on FRP strengthened arches that included fill material.

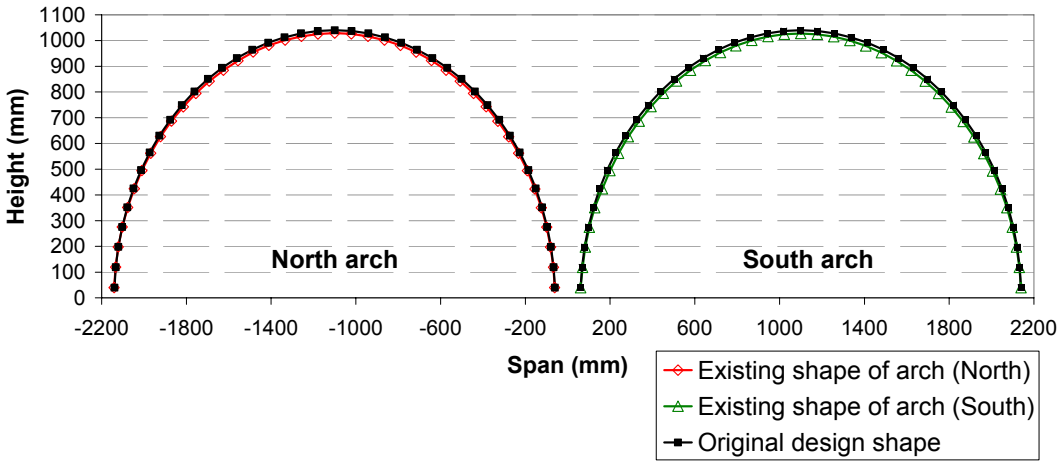

Figure 3.2 The shape of the arches before the current test

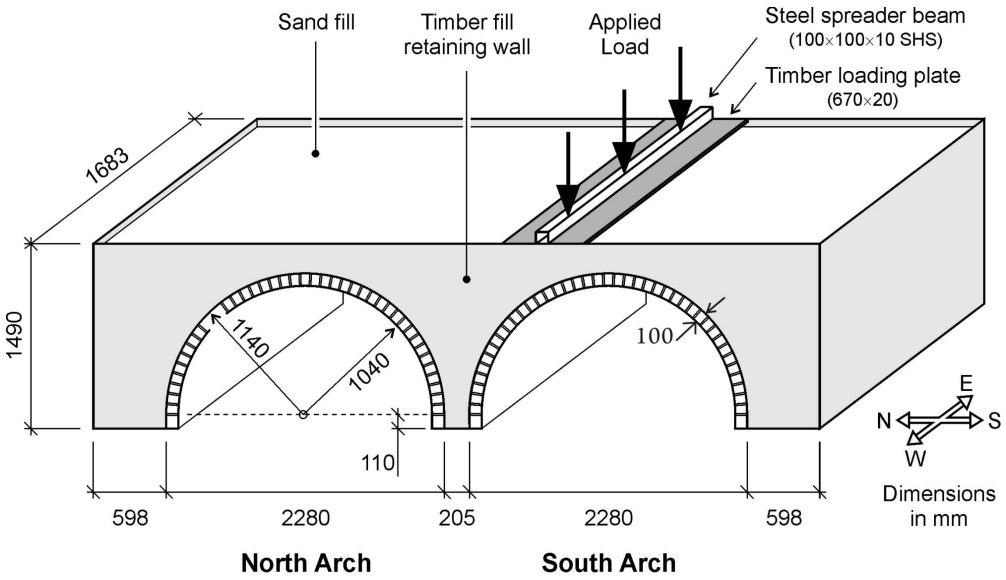

(a) Schematic Arrangement

(b) Photograph, taken from the west

Figure 3.3 General arrangement of the two-span arch bridge

3.2.2 Arrangement and application of the FRP strengthening

A commercial FRP system intended for structural strengthening was used that comprises 100mm wide unidirectional pultruded carbon fibre-reinforced polymer (CFRP) plates and a two-part ambient-cure epoxy adhesive. An initial assessment of the quantity of strengthening to apply to the arches was made using the method described by Chen (2002). Three FRP plates were distributed across the intrados of the north arch, and six plates were similarly applied to the south arch. The FRP plates were labelled P_{N1} to P_{N3} and P_{S1} to P_{S6}, from east to west, and were positioned as shown in Figure 3.4 and Figure 3.5.

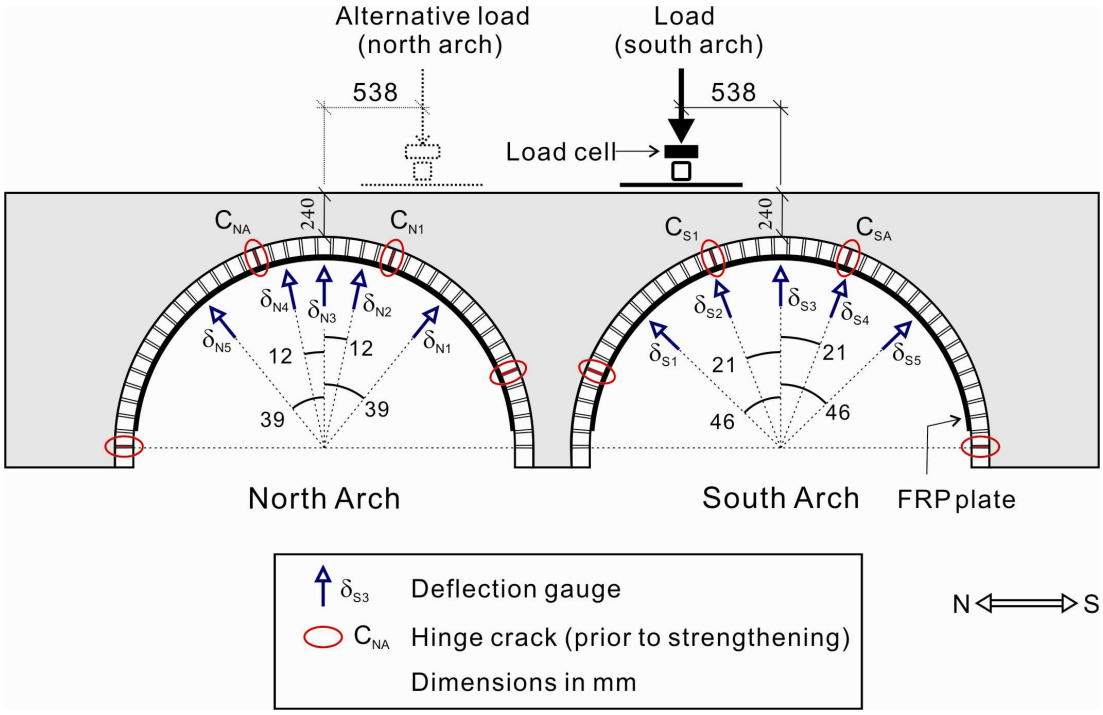

Figure 3.4 The western elevation of the arches, showing the strengthening plates, instrumentation, and crack locations prior to strengthening

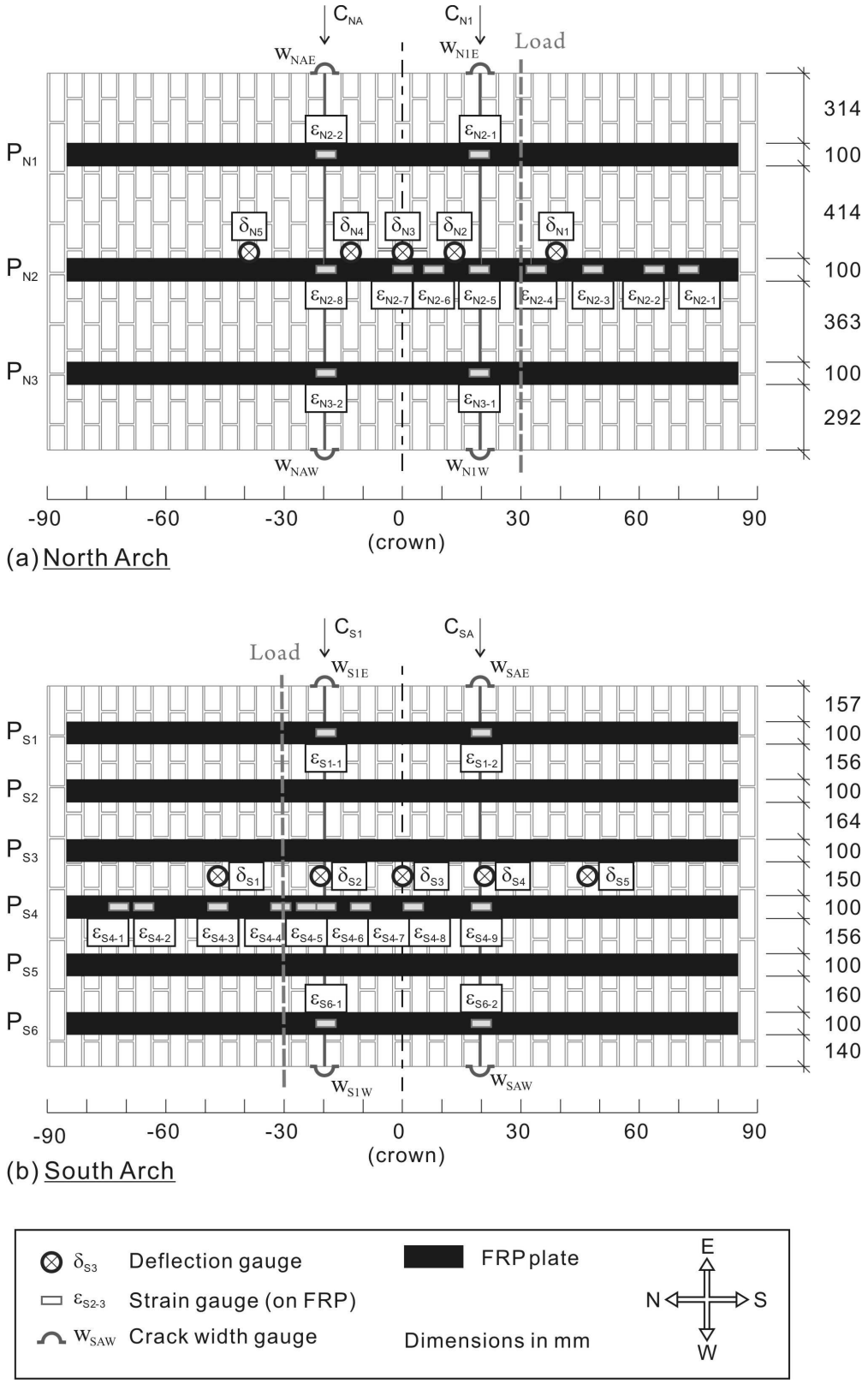

Figure 3.5 Developed plan view of the two arches' intrados, showing the strengthening plates, instrumentation crack locations prior to strengthening

Prior to strengthening, sharp irregularities in the surface profile of the arch were removed by grinding, and the bonding surface was cleaned through a combination of grinding, wire brush, dry vacuum and solvent cleaning. An epoxy primer was applied to seal the porous masonry, and the plates were then bonded to the arch according to the manufacturer's instructions. The adhesive was nominally 2mm thick, but this thickness varied considerably due to the profile of the arch. Temporary support was provided to the plates for 24 hours during the initial cure of the adhesive.

3.2.3 Material properties

The properties of the masonry materials were determined from specimens cut from the arches after the final test. Tests were conducted to determine:

- the compressive strength (f_{cb}), elastic modulus (E_b) and flexural tensile strength (f_{tb}) of the concrete bricks;
- the compressive strength (f_{cm}), elastic modulus (E_m) and flexural tensile strength (f_{tm}) of masonry assemblages; and
- the initial shear strength (f_{v0}) and the internal angle of friction (α) of a bed joint, derived from 'triplet' tests.

Table 3-1 lists the masonry material properties obtained from these tests. This table also lists the direction of the property being tested relative to the direction of the bed joints. 'Parallel to the bed joints' is across the width of the arch, and 'perpendicular to the bed joints' is in the circumferential direction. The test methods were based upon the British Standards listed in Table 3-1 in so far as was possible given the

specimens that could be cut from the arches after the current tests. The test details are described in the following sections.

Table 3-1 Properties of the masonry materials

	Material property (number of samples)		Value	Direction relative to bed joints	Test standard
Brick properties	Compressive strength (7)	f_{cb} (MPa)	58.2	Perpendicular	BS EN 772-1 (2000)
	Modulus of elasticity (7)	E_b (MPa)	16600	Parallel	Based on BS ISO 1920-10 (2009)
	Flexural tensile strength (6)	f_{tb} (MPa)	8.84	Parallel	BS 772-6 (2001) in 3 point bending
Masonry properties	Compressive strength (3)	f_{cm} (MPa)	25.0	Parallel	BS 1052-1 (1999)
	Modulus of elasticity (3)	E_m (MPa)	11800	Parallel	Based on BS ISO 1920-10 (2009)
	Flexural tensile strength (3)	f_{tm} (MPa)	0.1	Perpendicular	BS 1052-2 (1999), in 4 point bending
Mortar joint in shear	Initial shear strength (17)	f_{v0} (MPa)	0.39	Across bed joint	BS 1052-3 (2002) Type 1
	Internal angle of friction (17)	α (°)	43.0		

The sand fill had a density of 1520kg/m^3 and an internal friction angle of 33° obtained from the shear test using the Jenike Shear Cell. The test result was shown in

Figure 3.6.

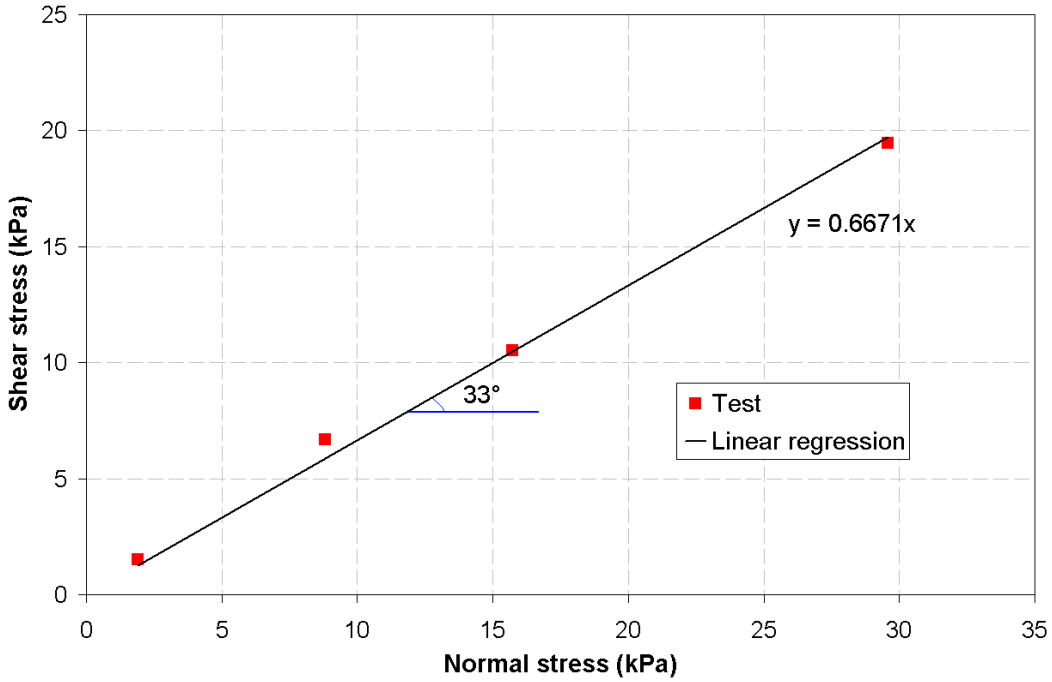

Figure 3.6 The internal friction angle of sand from the shear test

Based upon the manufacturer's datasheet values, the FRP plates had a nominal cross-section of 100mm×1.4mm, Young's modulus of 170GPa and tensile strength of 3100MPa. The epoxy adhesive had a Young's modulus of 10GPa and minimum shear strength of 17MPa.

3.2.4 Loading and instrumentation

A load-control method was adopted in the current test. A line load was applied across the width of the arches. The load was applied to the backfill, at the quarter-span position above each arch in turn (Figure 3.3 and Figure 3.4) because the most critical loading position is between the third and middle span. The load was applied by

means of three calibrated 10-tonne hydraulic jacks, attached to a portal reaction frame that was bolted to the laboratory strong floor. A steel beam beneath the three jacks spread the applied load into a line, and a timber plate distributed this load over a wider area. A 570mm wide timber plate was used prior to strengthening the arches; after strengthening the width of the timber was increased to 670mm (as indicated in Figure 3.3) to prevent the load punching into the fill material.

The load was applied using a hand pump and was controlled manually by observing the output from three load cells positioned beneath the hydraulic jacks. The loading rate was about 0.63kN/min per jack. Displacement transducers were used to measure radial displacements (δ) of the arch along a line halfway across their width (Figure 3.4 and Figure 3.5). A sequence of digital photographs was taken on either side of the arch to allow crack formation to be monitored.

When the strengthening was applied, the load cells and displacement gauges were augmented by electrical resistance strain gauges and crack width gauges. 25 strain gauges were bonded to the FRP at the locations shown in Figure 3.5 (12 under the north arch and 13 under the south arch) to measure the longitudinal strain (ε) on the centreline of the plates. The majority were installed on the central FRP plate, so as to record the variation in axial strain along the plate, with four gauges on the outer plates at the position of the hinge cracks created during the initial stage of loading. Five crack width gauges were used to measure crack openings (w); four were positioned over the hinge cracks on the arch being tested, and the fifth gauge was placed over a hinge crack in the adjacent arch (Figure 3.5). The gauges were placed

25mm from the open end of the crack.

Not all of the instrumentation was used in every test. Tests on the north arch used:

- five displacement transducers (δ_{N1} to δ_{N5}) under the north arch and 2 under the south arch (δ_{S1} and δ_{S2});
- all of the strain gauges (ε) under the north arch, but none of those under the south arch; and
- four crack width gauges (w_{N1} to w_{N4}) on the north arch, with 1 (w_{S1}) on the south arch.

The instrumentation was reversed for the tests on the south arch.

3. 3 Material properties test

This section describes the procedures and results of each test used to determine the material properties which summarized in Table 3-1. It is also worth nothing that all samples were cut from the arches after the current strengthening test.

3.3.1 Compressive strength test of masonry units and composite

3.3.1.1 Test setup and loading procedure

The aim of these testes is to obtain the compressive strength and Young's modulus of masonry unit, which is concrete brick at this study, and masonry itself (brick and mortar). All the specimens were picked from the masonry arch test and were per-

loaded. It is believed that the compressive behaviour of specimens will not be affected significantly because the masonry arch was not failed due to compression. Total of 13 concrete brick were test based on the specifications in British Standard 772-1 (2000). 7 specimens (BC-1 to BC-7) were loaded at the direction of the line of thrust of arch as shown in Figure 3.7a. 6 specimens (BC-8 to BC-13) were loaded at the direction perpendicular to the line of thrust of arch as shown in Figure 3.7b. Total of 3 masonry blocks (Figure 3.7c) were tested following the specifications in British Standard 1052-1. It maybe noticed that it is difficult to set the loading direction as the line of thrust of real arch due to geometry. Moreover, the loading eccentricity will also occur if the loading direction is set in vertical direction. Therefore, the direction of loading was set perpendicular to the line of thrust of real arch as shown in Figure 3.7c. It needs to be noticed that the behaviour of masonry under this condition will be different as the real arch because there are no continuous horizontal bed joints in specimens.

Based on the specifications in BS 772-1 (2000), a thin layer cement capping mortar was applied to both top and bottom surfaces for all specimens to obtain smooth and flat contact surface. It took one day to allow the capping to be hardening. Single brick under load perpendicular to bed joint were tested using the 2000kN AVERY-DENSION test machine and under load parallel to bed joint were tested using the 1000kN AVERY universal machine in the Structural laboratory. The loading rate was chosen as about $0.6(N/mm^2)/s$ as guide given in BS 772-1. Each specimen was loaded until it was crushed. The deformation of specimens with loading area about $215 \times 65 mm^2$ was recorded using two LVDTs.

Masonry block were tested using the AVERY universal machine based on the specifications in BS 1052-1 (1998). A same cement capping mortar was applied at both top and bottom of each specimen. Two LVDTs were used to record the deformation of each specimen. A steadily loading rate about 0.5(N/mm^2)/min was chosen based on the BS 1052-1 recommendation. All specimens were load until crushed.

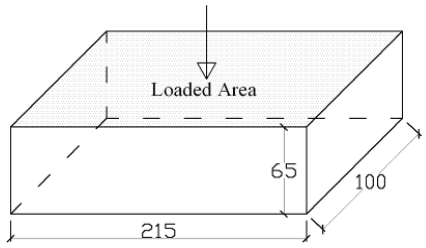

(a) Perpendicular direction

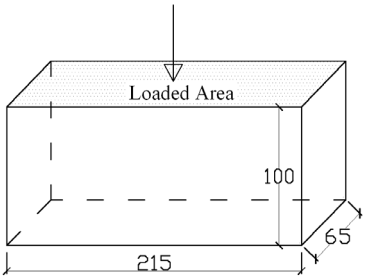

(b) Parallel direction

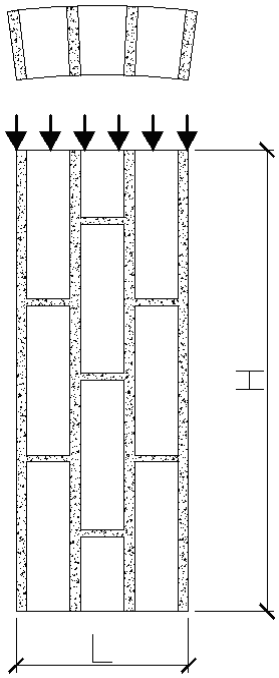

(c) Compression test on masonry block (parallel)

Figure 3.7 Compression loading tests on masonry units and itself

3.3.1.2 Test results of concrete brick

For the concrete brick under load perpendicular to bed joint, the ultimate load of specimens was recorded. Test results were summarized in Table 3-2. This loading direction is perpendicular to the bed joint.

Table 3-2 Results of compressive strength of concrete brick under load perpendicular to bed joint

Specimens	Ultimate load (kN)	Dimensions of loading area (mm)	Strength (MPa)	Average value (MPa)	Standard deviation
BC-1	1141	215 × 100	53.1	58.2	6.1
BC-2	1218	215 × 103	55.0		
BC-3	1241	216 × 103	55.8		
BC-4	1417	216 × 103	63.7		
BC-5	1368	215 × 102	62.4		
BC-6	1132	217 × 103	50.6		
BC-7	1484	215 × 103	67.0		

The typical failure mode is shown in Figure 3.8.

(a) (b)

Figure 3.8 Typical failure mode of compressive test on unit (a): BC-1, (b): BC-7

For the concrete brick under load parallel to bed joint, the test results are summarized in Table 3-3. A typical stress-strain curve is shown in Figure 3.9.

Table 3-3 Results of compressive strength of concrete brick under load parallel to bed joint

Specimens	Ultimate Load (kN)	Dimensions of loading area (mm^2)	Compressive strength (MPa)	Average value (MPa)	Standard deviation
BC-08	487.6	217 × 68	33.0	40.0	7.6
BC-09	512.6	216 × 69	34.4		
BC-10	629.4	216 × 66	44.1		
BC-11	682.7	216×65	48.6		

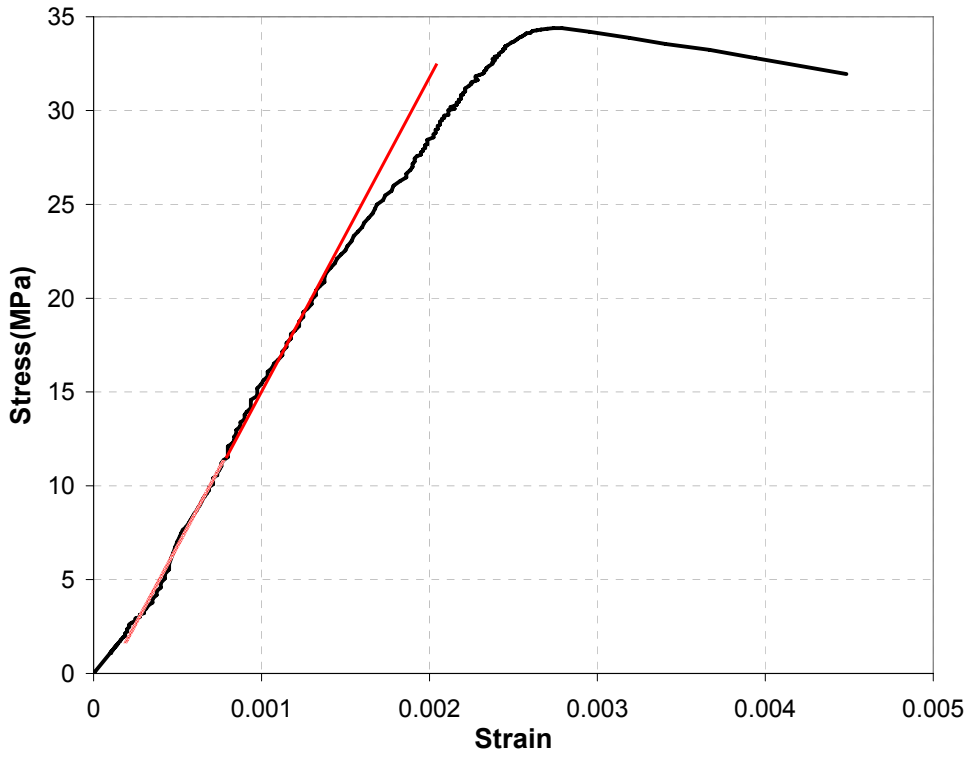

Figure 3.9 Stress-strain curve of specimen BC-09

The typical failure mode is shown in Figure 3.10. Brick is failed and formed incline

failure surface. This shear band failure mode is due to the friction between bricks and loading plate, as shown in Figure 3.11. The mean value is 40.0MPa from the bricks under load parallel to bed joint, which is smaller than the mean value (58.2MPa) obtained from the bricks under load perpendicular to bed joint. That is because the friction between specimens and loading plate has more effect on the middle part of specimens when the height of specimen decreasing, such as height of specimens decreasing from about 100mm (parallel to bed joint) to about 65mm (perpendicular to bed joint).

Figure 3.10 Failure of brick (BC-10) under load parallel to bed joint

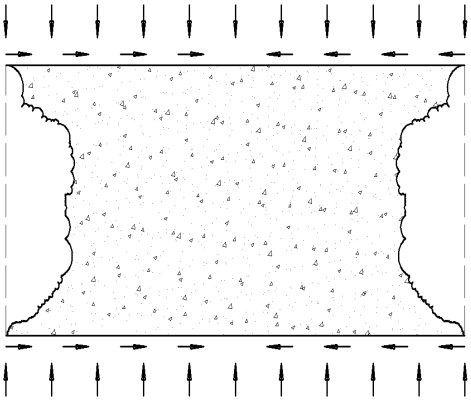

Figure 3.11 Sketch of failure pattern of compression test on brick

Based on the specifications in BS ISO 1920-10 (2009), the Young's modulus of

concrete brick E_c from compression test under load parallel to bed joint can be calculated using $E_c = \frac{\Delta_\sigma}{\Delta_\varepsilon} = \frac{\sigma_a - \sigma_b}{\varepsilon_a - \varepsilon_b}$, where σ_a is the upper loading stress ($\sigma_a = f_c/3$); σ_b is the basic stress (i.e. 2MPa in this study); ε_a and ε_b are the strain corresponding to the two limit stresses. Results are summarized in Table 3-4. The average test results (16569MPa) are close to the test done by Fairfield (1994a) on same material (15000MPa).

Table 3-4 Results of Young's modulus of concrete bricks

Specimens	Upper loading stress (MPa) $\sigma_a = f_c/3$	Range of stress to calculate E_c (MPa)	E_c Young's modulus (MPa)	Average value (MPa)	Standard deviation
BC-08	11.0	2~11	17266	16569	1279
BC-09	11.4	2~11	15482		
BC-10	14.7	4~14	18023		
BC-11	16.2	2~16	15506		

3.3.1.3 Test results of masonry blocks

All three specimens were tested on the 1000kN AVERY universal machine. The test setup is shown in Figure 3.12. Load and deflection were recorded to obtain the compressive strength and Young's modulus of masonry. Results are summarized in Table 3-5. LVDTs were removed away when stress over about 10MPa to avoid potential damage for specimens.

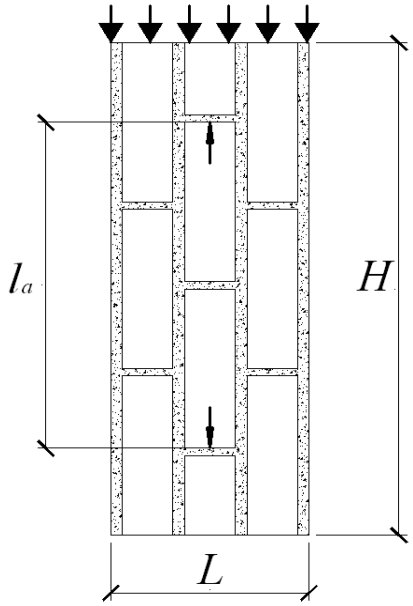

Figure 3.12 Sketch of compression test on masonry block (l_a =distance between two LVDTs)

Table 3-5 Results of compressive strength of masonry

Specimens	Peak load (kN)	Loading area (mm^2)	H (mm)	Strength (MPa)	Average strength (MPa)	Standard deviation
MB-1	574.5	23192	675	24.8	25.0	0.25
MB-2	588.7	23424	673	25.1		

The test result of the specimen MB-2 is shown in Figure 3.13.

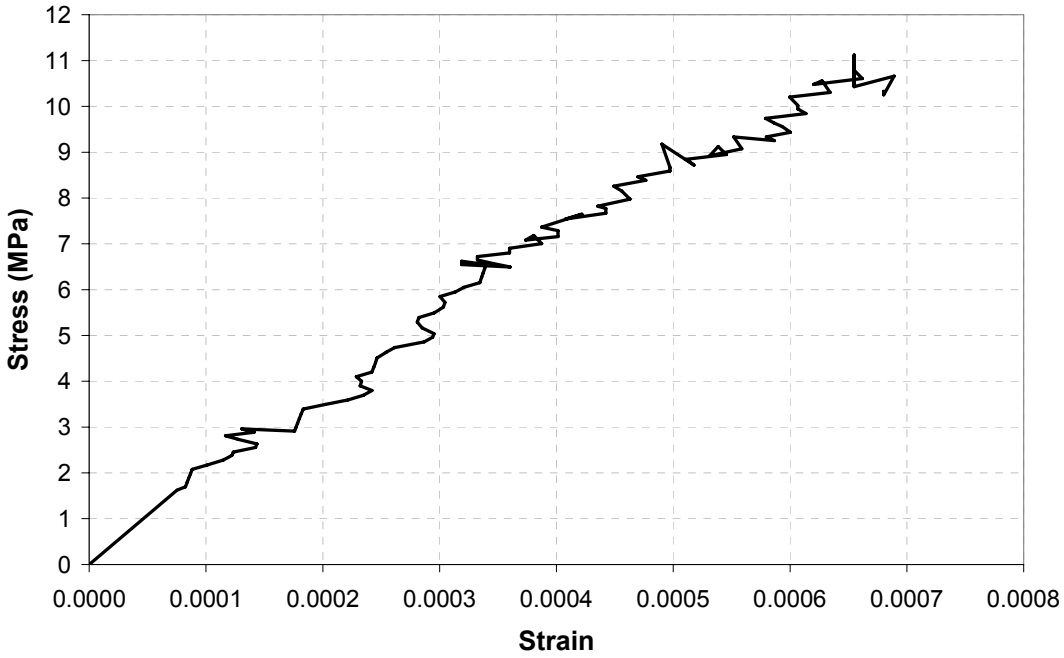

Figure 3.13 Stress-strain curve for specimen MB-2 from LVDT

The failure of this specimen was dominated by the cracks at the interface of mortar joints which are parallel to the loading direction. This is cause by the different dilation behaviour of mortar and concrete brick. After the applied load passing the peak load, the cracks at the interface continuously grew and led to the bricks on sides tend to fall down. Eventually, the collapse of the bricks on side and the crush failure on the middle bricks will lead to final failure of masonry blocks.

The Young's modulus of masonry block E_m can be calculated as the same as that for concrete brick (BS ISO 1920-10). The results are summarized in Table 3-6.

Table 3-6 Results of the Young's modulus of masonry

Specimens	Upper loading stress (MPa) $\sigma_a = f_c/3$	Range of stress to calculate E_m (MPa)	E_m Young's modulus (MPa)	Comments
MB-1	8.2			The stress-strain curve is missing in this range.
MB-2	8.4	3.0~8.3	11815	

3.3.1.4 Compressive strength and Young's modulus of concrete brick and masonry composite

This section described a series laboratory test on masonry units and itself to obtain the compressive strength of each material. The compressive strength of concrete brick is 58.2MPa in the direction of line of thrust. The average compressive strength of masonry samples was 25.0MPa which is substantially lower than the compressive strength of brick because of the contributions from the weaker mortar filling the bed joints. This reason also results in that the Young's modulus of masonry 11815MPa being lower than that from concrete brick. The failure of masonry is due to the development of crack at the interface parallel to the direction of loading, which is caused by the different dilation behaviour of mortar and units.

3.3.2 Bending tensile strength test of masonry units

3.3.2.1 Test setup and loading procedure

The aim of this test was to obtain the bending tensile strength of the masonry unit of

the arch bridge. Total of eleven (CBF-1 to CBF-11) specimens picked after the arches test were based on the specifications in British Standard 772-6 (2001). It is believed that the behaviour of concrete brick has insignificant effects from the arch bridge test as the failure mode of arch was mechanism failure with debonding rather than crushed. Three point bending test was set as the specifications in BS 772-6 (2001). Three steel bars were used to provide two bottom supports and one upper loading roller. 7 specimens with greater bending stiffness *EI* (CBF-1 to CBF-7) were tested as shown in Figure 3.14 and 4 specimens with smaller bending stiffness *EI* (CBF-8 to CBF-11) were tested as shown in Figure 3.15.

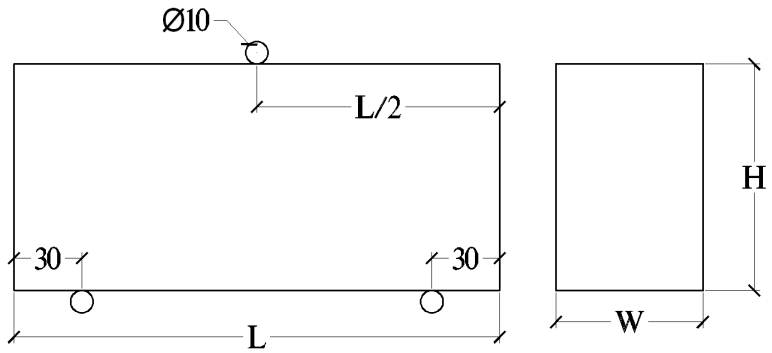

Figure 3.14 Bending tensile test of concrete brick with greater bending stiffness (mm)

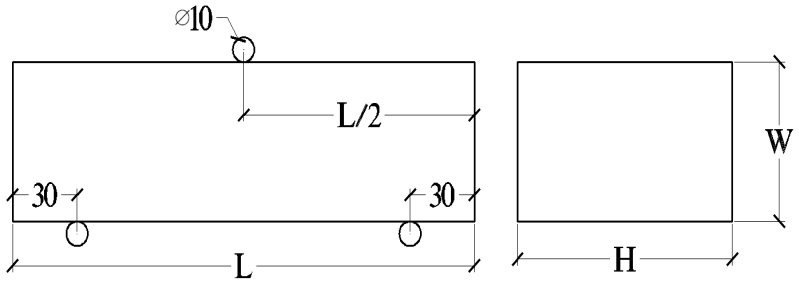

Figure 3.15 Bending tensile test of concrete brick with smaller bending stiffness (mm)

All testes were done in the Structural laboratory using the AVERY universal test machine and loading was applied until specimens failed. The loading rate was chosen as 40 N/s based on the recommendation of BS 772-6 (2001).

3.3.2.2 Test results of bending tensile strength

The ultimate load was recorded to calculate the bending tensile strength of each brick. The test results are summarized in Table 3-7.

Table 3-7 Results of bending tensile test on concrete brick

Specimens	Dimensions ($L \times W \times H$) mm	Ultimate load (kN)	Bending tensile strength (MPa)	Failure pattern
CBF-1	$217 \times 65 \times 103$	31.6	10.79	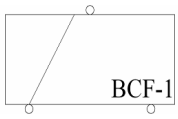
CBF-2	$230 \times 65 \times 100$	26.2	10.28	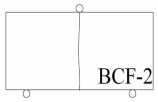
CBF-3	$217 \times 65 \times 104$	32.6	10.92	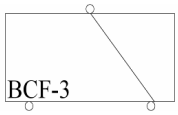
CBF-4	$218 \times 67 \times 103$	25.1	8.37	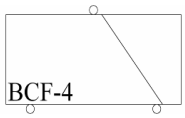
CBF-5	$216 \times 67 \times 103$	25.8	8.49	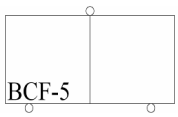
CBF-6	$220 \times 66 \times 103$	25.0	8.57	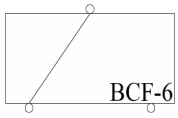
CBF-7	$216 \times 66 \times 102$	26.1	8.89	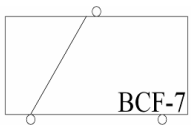
CBF-8	$216 \times 64 \times 106$	21.5	11.59	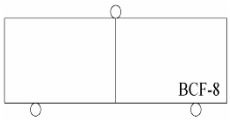
CBF-9	$215 \times 66 \times 105$	12.9	6.56	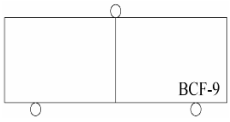
CBF-10	$217 \times 66 \times 104$	15.2	7.90	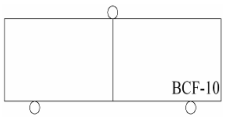
CBF-11	$216 \times 67 \times 101$	15.9	8.21	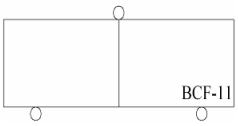

It can be seen from the Table 3-7 there are only 2 (CBF-2 and CBF-5) out of 7 bricks with greater bending stiffness were failed due to flexural crack. The rest of bricks in this group were failed due to shear crack. The more possible failure mode for these testes (CBF-1 to CBF-7) is shear failure, which can be contributed to the deep beam effect and greater bending stiffness. The failure of deep beam is dominated by shear failure.

In order to decrease the deep beam effect and bending stiffness, 4 bricks (CBF-8 to CBF-11) were loaded as shown in Figure 3.15. All four bricks were failed due to the flexural crack at the middle of brick. The bending tensile strength of concrete brick will be obtained from the specimens failed due to the flexural crack.

3.3.2.3 Bending tensile strength of concrete brick

There were total of 6 specimens failed due to flexural crack as shown in Table 3-8. The bending tensile strength of concrete brick is 8.84MPa.

Table 3-8 Bending tensile strength of concrete bricks

Specimens	Bending tensile strength (MPa)	Average value (MPa)	Standard deviation
CBF-2	10.28	8.84	1.8
CBF-5	8.49		
CBF-8	11.59		
CBF-9	6.56		
CBF-10	7.90		
CBF-11	8.21		

3.3.3 Masonry mortar joint bending test

3.3.3.1 Test setup and loading procedure

The purpose of this experiment is to obtain the bending tensile strength of masonry. Total of 2 (MF-1 and MF-2) specimens from the arch test were tested based on the BS 1052-2 (1999), as shown in Figure 3.16. The geometry of each specimen presented in the following section. The width of specimens was assembled by two bricks and one mortar. Four point bending test was set as specified in BS 1052-2 (1999). All testes were done in the Structural laboratory using the AVERY universal test machine and loading was applied until specimens failed. The loading rate was chosen as 50 N/s based on the recommendation of BS 1052-2 (1999).

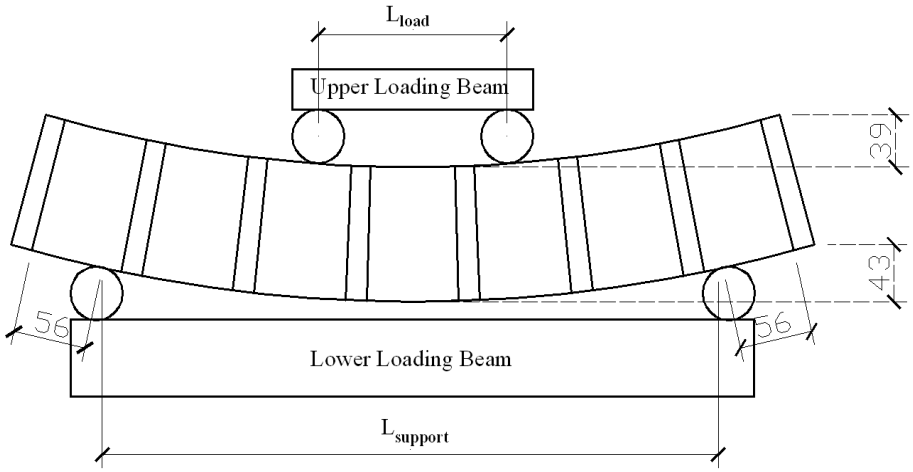

Figure 3.16 Bending tensile test of masonry (mm)

3.3.3.2 Test results of bending tensile strength of masonry

The ultimate load was recorded to calculate the bending tensile strength of each

specimen. The test results are summarized in Table 3-9.

Table 3-9 Results of bending tensile test on masonry

Specimens	Geometry (mm)		Ultimate load (kN)	Failure pattern
	$L_{support}$	L_{load}		
MF-1	455	182	4.8	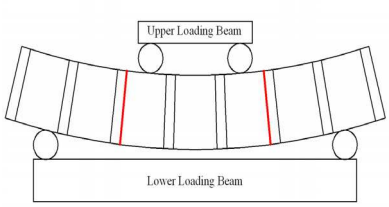
MF-2	285	143	2.3	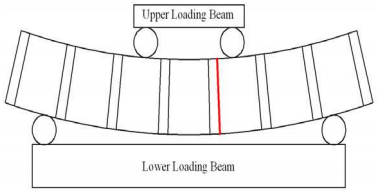

It can be seen from the Table 3-9 there are only one (MF-2) specimen was failed due to flexural because the crack located at the pure flexural zone. The other specimen (MF-1) was failed due to shear-flexural action. Only specimen (MF-2) can be used to calculate the tensile strength of masonry. It should be noticed that the failure occurred at the unit-mortar interface at both specimens.

3.3.3.3 Bending tensile strength of masonry

The bending tensile strength of masonry is obtained from the specimen MF-2. The tensile strength of masonry is 0.1MPa, which is as expected to be a significant small value. This value dominates the behaviour of masonry arch due to the mechanism

failure is caused by the formation of hinge at the unit-mortar interface. This failure mode verifies the characters of masonry, usually a negligible tensile strength.

3.3.4 Shear strength test of masonry

3.3.4.1 Test setup and loading procedure

A total of 17 specimens (shear-1 to shear-17) were taken from the bridge to test the shear strength of the masonry (Figure 3.17). It may be noted that BS 1052-3 (2002) specifies that the shear strength should be tested from the horizontal bed joints as the failure planes in common structures such as masonry walls pass through them. For practicality, the shear force was applied in the arch plan (Figure 3.17) which is perpendicular to the main shear force developed in the arch bridge. Whilst the behaviour of the joints can be slightly different in the two directions, the difference is believed to be small and insignificant. Furthermore, the masonry specimens had been pre-loaded as they were taken out from the tested arch. Whilst their behaviour may be different from unloaded specimens, they should more closely represent the actual behaviour in the bridge.

Specimens shear-1, shear-3 to shear-9 were bare masonry specimens without any CFRP attached. Specimen shear-2 was tested with some fibres and epoxy attached. Specimens shear-10 to shear-17 had some CFRP attached when cut out from the tested arch bridge. The attached CFRP and adhesive were removed using machine grinding.

Based on the specifications in BS 1052-3 (2002) for masonry units with a compressive strength greater than 10MPa, the specimens were tested under pre-compression stresses of approximately 0.2, 0.6 and 1.0MPa, equivalent to confining loads of 4.3, 12.9 and 21.5kN as the specimens had a cross-section of about $215 \times 100 mm^2$. The confining loads were applied through a compressive jack connected to the LOS hydraulic loading machine. The shear load was applied using the AVERY test machine in the Structures Laboratory. The specimens were supported using two pieces of steel with 12mm thick and two steel rollers with diameter of 12mm. The shear load was applied through a same steel plate placed at the top of specimen. Confining load was applied initially and was kept constant during the test. The shear load was applied until the failure occurred. A 0.2MPa/min loading rate was chosen based on the recommendation of BS 1052-3.

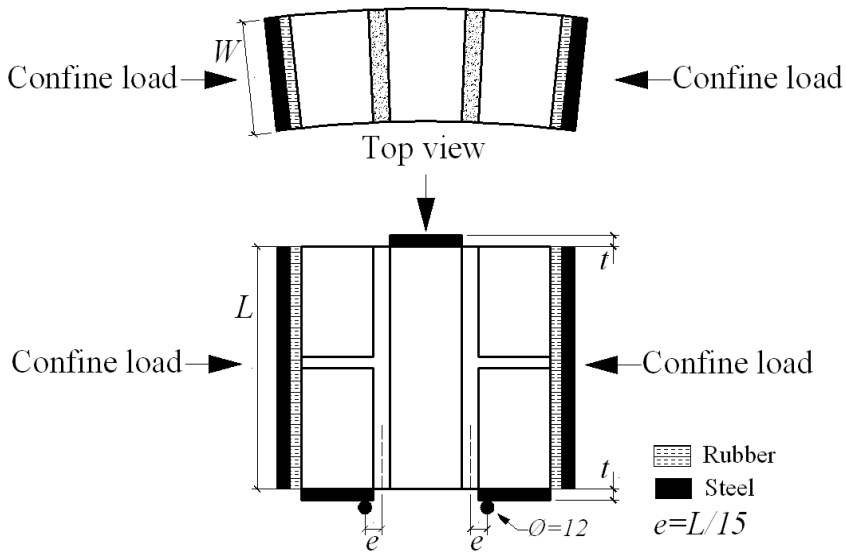

Figure 3.17 Shear strength test of masonry unit (mm)

3.3.4.2 Failure modes

Table 3-10 summarized the failure modes of each specimen.

Table 3-10 Failure modes of shear strength test

Specimen	Failure pattern	Specimen	Failure pattern	Specimen	Failure pattern
Shear-1	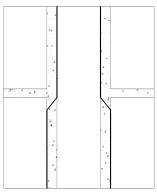	Shear-2	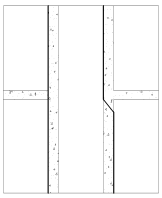	Shear-3	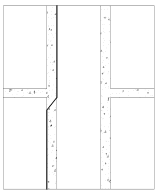
Shear-10	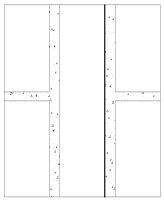	Shear-11	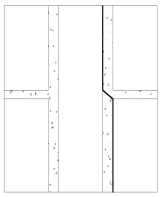	Shear-12	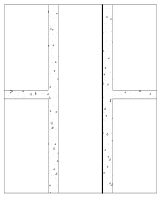
Shear-4	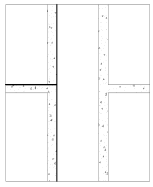	Shear-5	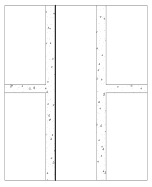	Shear-6	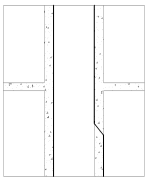
Shear-13	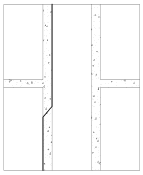	Shear-14	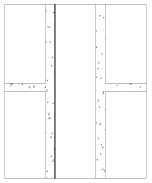	Shear-7	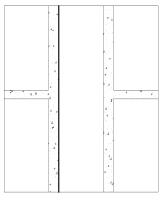
Shear-8	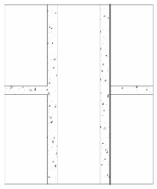	Shear-9	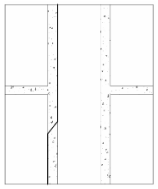	Shear-15	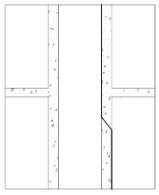
Shear-16	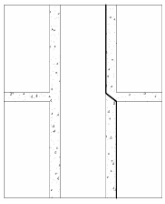	Shear-17	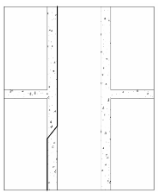		

All 17 specimens were failed due to the sliding along the interface between concrete brick and mortar with the direction of movement being parallel to the shear plane. That is because the interface is the weakest part of the specimens.

3.3.4.3 Test results of shear strength of masonry

It can be seen from the Table 3-11, the shear strength generally became greater once the larger confining load was applied. The value from the specimen Shear-2 was much greater than the other specimens under the same confining load even the failure still located at the interface between brick and mortar, which was due to some FRP and epoxy still attached on the surface. It can be seen from Table 3-11, the results obtained from two specimens (Shear-7 and shear 9) showed greater value. The data from this confining load (21.5kN) will be analysed with both including these two values and excluding them in the following part.

Table 3-11 Test results of shear strength of each specimen

Specimen	Cross-sectional area A (mm^2)	Confining load F_p (kN)	Confining stress F_p / A (MPa)	Failure shear force F_s (kN)	Shear strength $F_s / 2A$ (MPa)
Shear-1	235 × 103	4.3	0.178	27.4	0.566
Shear-2	216 × 103	4.3	0.193	37.6	0.845
Shear-3	221 × 102	4.3	0.191	29.3	0.650
Shear-10	215 × 105	4.3	0.190	16.3	0.361
Shear-11	225 × 105	4.3	0.182	23.0	0.487
Shear-12	225 × 104	4.3	0.184	24.0	0.513
Shear-4	215 × 103	12.9	0.583	44.0	0.993
Shear-5	217 × 105	12.9	0.566	32.0	0.702
Shear-6	210 × 103	12.9	0.596	44.2	1.022
Shear-13	217 × 105	12.9	0.566	42.4	0.930
Shear-14	220 × 103	12.9	0.569	35.5	0.783
Shear-7	236 × 105	21.5	0.868	83.4	1.683
Shear-8	223 × 105	21.5	0.918	47.0	1.004
Shear-9	211 × 105	21.5	0.970	79.2	1.787
Shear-15	208 × 103	21.5	1.004	49.0	1.144
Shear-16	234 × 102	21.5	0.901	41.1	0.861
Shear-17	219 × 103	21.5	1.130	51.0	0.953

3.3.4.4 Initial shear strength and angle of internal friction of masonry

Figure 3.18 shows the all individual shear strength against the normal precompressive stress and the linear determined from a linear regression of the

individual points. The initial shear strength f_{vo} at zero normal precompressive stress is 0.39MPa, which was obtained from the intercept of the line with the vertical axis (shear strength). The angle of internal friction is 42.9°, which is from the slop of the line.

The characteristic value of the initial shear strength is $f_{vok} = 0.8 f_{vo} = 0.31 MPa$ and the characteristic angle of internal friction from $\tan \alpha_k = 0.8 \tan \alpha$, which is 36.6°.

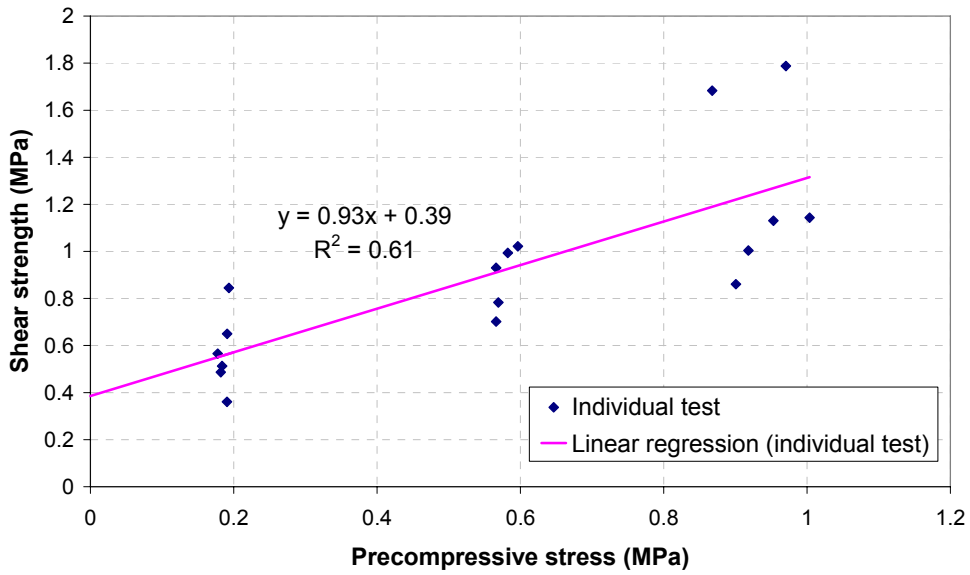

Figure 3.18 Shear strength and angle of internal friction (All specimens included)

There are two tests (shear-7 and shear-9) with 21.5kN precompressive load showed greater value than the other specimens under same precompressive load. To eliminate the effects from dispersed values, these two samples are discharged from the data. The modified results were shown in Figure 3.19.

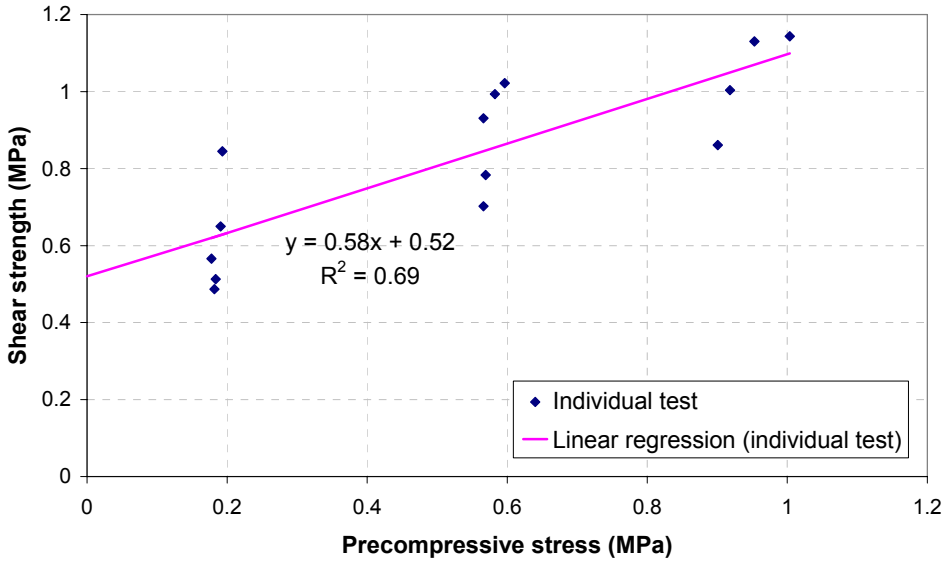

Figure 3.19 Shear strength and angle of internal friction (Exclusive shear-7 and 9)

The average initial shear strength f_{vo} at zero normal precompressive stress was 0.52 MPa. The angle of internal friction is 30.1°, which is from the slope of the line. The characteristic value of the initial shear strength is $f_{vok} = 0.8 f_{vo} = 0.42 MPa$ and the characteristic angle of internal friction from $\tan \alpha_k = 0.8 \tan \alpha$, which is 24.9°. All the data are summarized in Table 3-12.

Table 3-12 Initial shear strength and angle of internal friction

	Initial shear strength (MPa)	Angle of internal friction (Degree)
All 17 specimens	0.39	42.9°
Exclusive shear-7 and 9	0.52	30.1°

To sum up, this section described a series laboratory test on masonry to obtain the initial shear strength of the masonry. Total of 17 specimens were test under three different levels of confining load and all specimens were failed due to the cracks at

the interface between masonry unit (concrete brick) and mortar. The initial shear strength of masonry and the angle of internal friction were 0.39MPa and 43°, respectively.

3. 4 Test Results

This section presents the results for the tests carried out prior to strengthening, the tests carried out after strengthening, and the final collapse test on the south arch.

3.4.1 Tests prior to strengthening

Prior to strengthening, the north arch and south arch were individually loaded until a four-hinge mechanism had been established. Figure 3.4 shows the locations of the hinge cracks. The cracks are labelled in the form C_{NA}, where the first subscript identifies the arch (North or South). The second subscript identifies the crack, using numbers for intrados cracks (e.g: C_{N1}) and letters for extrados cracks (e.g: C_{NA}). Typical intrados and extrados cracks after the final unloading are shown in Figure 3.20.

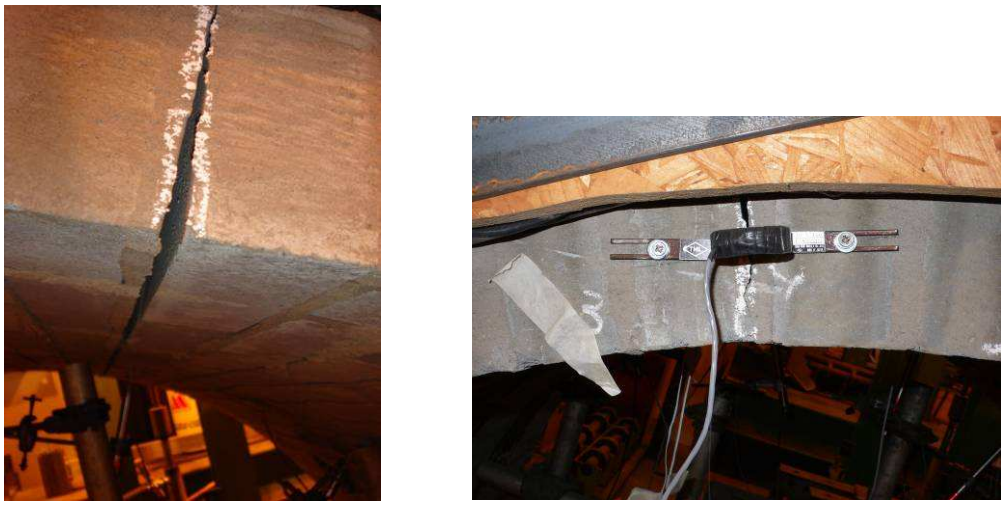

(a) Intrados Crack C_{N1} (b) Extrados Crack C_{NA}

Figure 3.20 Typical hinge cracks after the final unloading, viewed from the west

Figure 3.21 plots the load-deflection responses of the north and south arches. The response of the arches prior to strengthening is shown in the lower part of the responses. The load-deflection response is approximately bi-linear, with a change in stiffness when the hinge mechanism was established. This occurred at similar loads in the two arches: 35kN for the north arch, and 39kN for the south arch. Upon further loading, the arch behaved as an anti-symmetric four-hinge mechanism. The displacements were consistent with hinge mechanism.: the radial displacement was close to zero at the crown of the arch (δ_{N3} & δ_{S3}), outwards (positive) in the region of the extrados cracks (δ_{N4}, δ_{S4}, δ_{N5} & δ_{S5}), and inwards (negative) in the region of the intrados cracks (δ_{N1}, δ_{S1}, δ_{N2} & δ_{S2}). Minimal deflections were recorded in the adjacent unloaded arch, indicating little interaction between the two arches.

A number of unload-reload cycles were conducted, only the last of these is shown in

Figure 3.21. The north arch was loaded to 46.2kN and the south arch to 49.7kN, when it was deemed that the arches were approaching their unstrengthened load capacities. Irrecoverable damage occurred as the hinge cracks opened, resulting in residual deformations once the load had been removed. The cracks were allowed to open wider on the north arch, resulting in greater residual displacements than for the south arch. Figure 3.22 plots the load-radial displacement at the crown of each unstrengthened arch. It is clear that the displacement at the crown was smaller than those from the others closed to hinge positions. Moreover, the deflection reversing due to rotation at the crown of both arches at about 40kN indicated that it was close to the load carrying capacity of the arches.

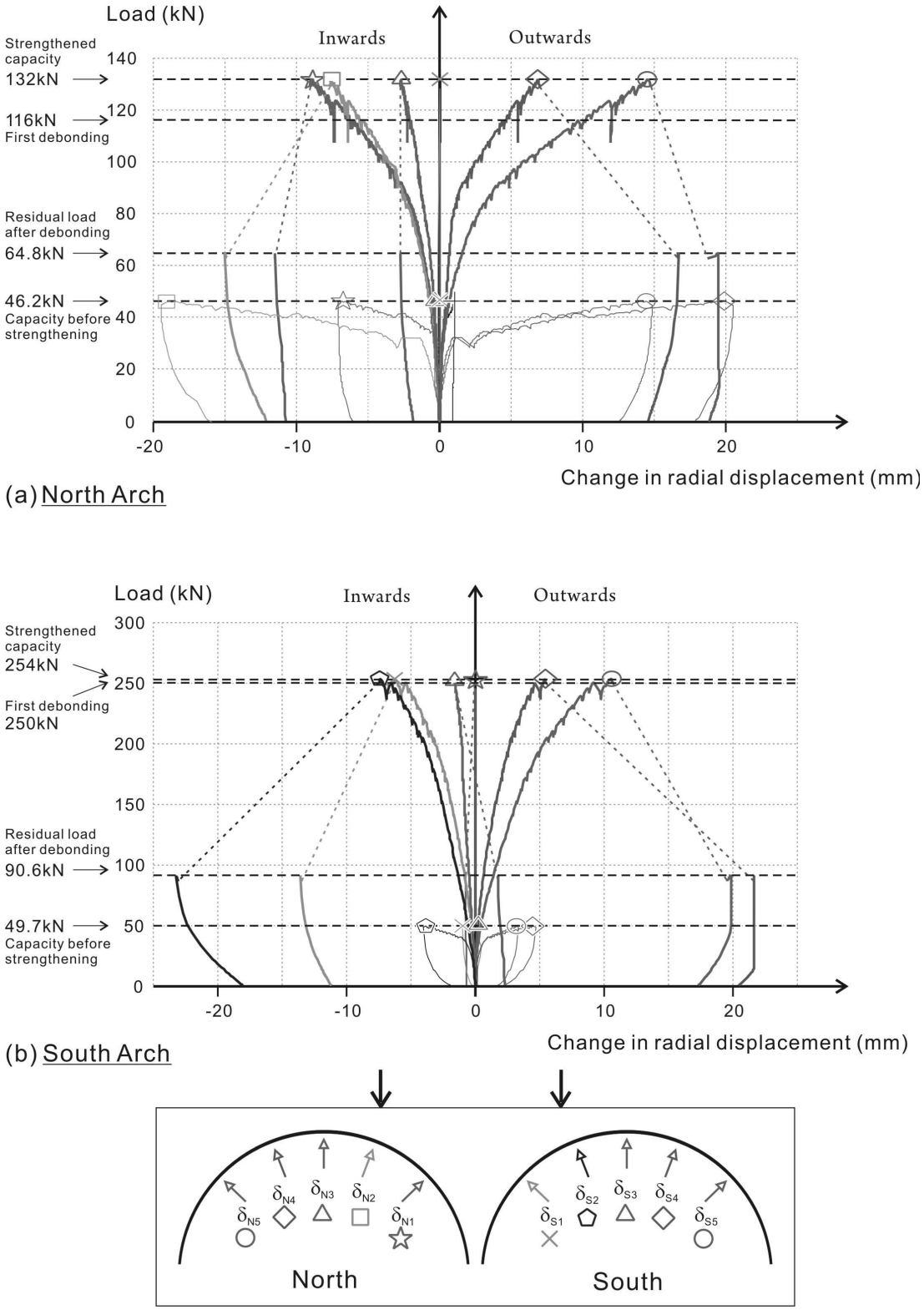

Figure 3.21 Load vs. radial displacement curves for both strengthened and unstrengthened arches

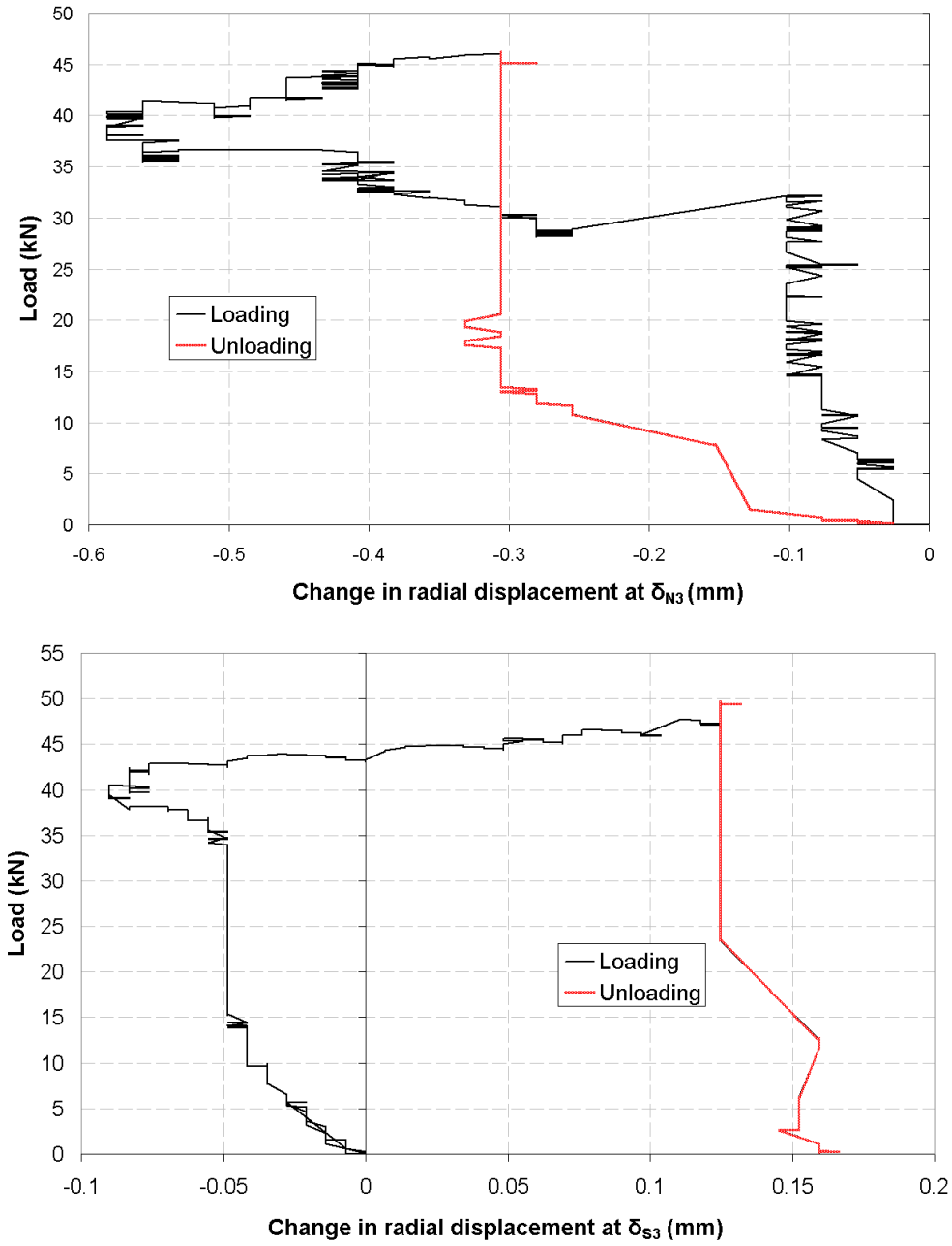

Figure 3.22 Load vs. radial displacement curves for both unstrengthened arches at the crown (δ_{N3} and δ_{s3})

3.4.2 Tests after strengthening

3.4.2.1 Overview of the test results

After strengthening, each of the arches was loaded in turn until the ultimate limit state was reached due to debonding failure of the strengthening system. In the previous section, five failure mechanisms were identified for an FRP-strengthened masonry arch. A combination of three of those failure mechanisms occurred during the current tests: the hinge mechanism (involving rotation about flexural cracks), the sliding mechanism (involving shear along mortar joints), and debonding of FRP. In both arches, the tests were terminated after sudden debonding of the FRP from the masonry in the vicinity of the local masonry cracks. This debonding resulted in a sudden drop in the load-carrying contribution of the strengthening, and determined the maximum load capacity of the strengthened arches; however, the FRP did not completely separate from the masonry, and retrained some post-peak load capacity.

In the following sections (3.4.3 and 3.4.4), the performance of the arches is reported and discussed in terms of its load-deflection behaviour, failure mechanism, crack width evolution, and FRP strain response. Each of the tests on the arches is discussed in turn.

3.4.3 North arch test after strengthening

The north arch was strengthened using 3 FRP plates (Figure 3.5a). The following data were recorded during the test on the north arch:

- Load vs. radial deflection response (Figure 3.21a). Note that the displacement transducers were reset at the start of this test, so the figure plots additional displacement and does not include the residual displacements from the end of the test prior to strengthening.
- Crack width development (Figure 3.23a). The figure plots the crack displacement at the mouth of the crack, calculated from the displacement at the gauge position by assuming that the crack rotates about the opposite fibre of the arch.
- The development of strain in the FRP plates, presented as a load-strain response for the gauges coincident with cracks C_{N1} and C_{NA} in Figure 3.24a, and as profiles of strain in the central FRP plate (P_{N2}) for different applied loads in Figure 3.25a.
- The failure mode of the arch, showing the location of cracks in the masonry and the extent of debonding of the FRP strengthening form the masonry. This is presented as a plan view along the developed length of the arch in Figure 3.26a, and as sections taken along the strengthening plates in Figure 3.27.

3.4.3.1 Initial loading (0 to 50kN)

The load-displacement response of the strengthened arch was stiffer than for the arch prior to strengthening. The FRP bridged the cracks, and resisted their opening.

As discussed in section 3.1, a four-hinge mechanism (with an extrados crack at C_{NA} and an intrados crack at C_{N1}) was established in the arch prior to strengthening (Figure 3.4). After strengthening, the same four-hinge mechanism opened up during

the initial stages of loading, as shown by the positive crack widths in Figure 3.23. The strains in the FRP plate at the crack positions are also consistent with the hinge mechanism, giving tension at the intrados crack and compression at the extrados crack (Figure 3.24) during the early stages of loading.

The north arch test had negligible affect upon the unloaded south arch at any point during the test: no deflection was recorded by gauges δ_{S1} or δ_{S2} in the south arch, and crack w_{S1W} did not widen.

The four-hinge mechanism can also be seen in the strain profile along FRP plate P_{N2} (Figure 3.25a). For loads less than 110kN, the peak strain is recorded in gauge $\varepsilon_{N2\text{-}5}$, coincident with the intrados crack C_{N1}. The strain decreases to either side of this crack, with a compressive strain at $\varepsilon_{N2\text{-}8}$, coincident with the extrados crack C_{NA}. The load-strain response shows that there was little variation in the load carried by each of the plates, with only a small difference in the plate strains up to 110kN.

3.4.3.2 Increased loading (50 to 110kN)

A true four-hinge mechanism only acted up to a load of around 50kN (approximately the capacity of the original arch without strengthening). Above this load, intrados crack C_{N1} continued to open as the load was increased (Figure 3.23a), as did the strain in the FRP at this location (Figure 3.24a). The extrados cracking, however, became more distributed. Extrados crack C_{NA} started to close up (the crack widths in Figure 3.23a and FRP plate strains in Figure 3.24a returned to zero), at the same time

as extrados cracks C_{NB} and C_{NC} (Figure 3.26a & Figure 3.27) formed and opened up. A consequence of the more distributed cracking was that the arch no longer deflected in an anti-symmetric mode (Figure 3.21a): the crown (δ_{N3}) displaced inwards, and the outwards deflections of the arch were greater than the inwards deflections.

At loads above 80kN, there are frequent fluctuations in the load-deflection, load-strain and load-crack width graphs (Figure 3.21a, Figure 3.23a and Figure 3.24a). These fluctuations were accompanied by audible damage events. The exact nature of the damage could not be observed. This might have been caused by a combination of micro-cracking and softening of the FRP to masonry interface (either within the adhesive, the masonry surface, or (unlikely) within the FRP plate), and damage elsewhere in the masonry, such as cracking in the mortar joints and local crushing of the masonry in compression in the hinge region. The progressive build up of damage within the arch led to softening of the load-deformation response. Other possible causes may include the slip-stick behaviour between the sand fill and the arch, or localised intermitted local failure planes formed in the sand fill, both leading to redistribution of pressures on the arch and thus fluctuations on the response curves.

All of the crack width gauges except w_{N1W} were removed at a load of 100kN to avoid damage to the gauges.

3.4.3.3 Debonding of the FRP from the masonry (above 110kN)

Additional damage continued to occur within the arch as the applied load was

increased beyond 110kN. The micro-cracks that had formed up to this point coalesced to form macro-cracks, particularly along the masonry to FRP interface, which resulted in sudden debonding of portions of the FRP from the masonry.

A number of significant debonding events can be picked up from the plots of strain and deflection:

- At 116kN, the central FRP plate (P_{N2}) partially debonded along a short distance either side of intrados crack C_{N1}. This can be seen in the load-strain response (Figure 3.24a), in which there is a small sudden drop in strain at the central plate ($\varepsilon_{N3\text{-}1}$), and in the strain profile (at 119kN in Figure 3.25a), in which there is a sudden increase in strain at the gauges adjacent to the crack ($\varepsilon_{N2\text{-}4}$ and $\varepsilon_{N2\text{-}6}$), indicating debonding along this length.
- At 123kN, a second debonding event resulted in a dip in the load-deflection curves (Figure 3.21a). This was due to further debonding of the central plate, as shown by the second sudden but far bigger drop in strain in plate P_{N2} (Figure 3.24a).
- The partial debonding of the central plate from the masonry required the outer plates to pick up additional load and undergo higher strains (Figure 3.24a). Consequently, the third significant debonding event occurred in the plate that carried the highest strain (P_{N3}) at a load of 129kN, as can be seen on the load-strain plot for plate P_{N3} (Figure 3.24a).
- At 132kN, all three plates debonded simultaneously along a substantial length. This resulted in a sudden increase in deflection and crack widening, a

drop in the FRP strain and consequently a drop in the load carried by the arch (Figure 3.21a, Figure 3.23a and Figure 3.24a).

At plates P_{N2} and P_{N3}, debonding occurred on both sides of the flexural intrados crack C_{N1} (Figure 3.26a and Figure 3.27). On the east side of the arch (plate P_{N1}), however, a shear crack formed through the masonry at the crown of the arch, which joined the intrados crack C_{N1} between plates P_{N1} and P_{N2} (Figure 3.26a and Figure 3.27). This shear crack caused plate P_{N1} to debond from the masonry on only one side of the crack, in a peeling mode that was compatible with the shear deformation across the crack (Figure 3.28a).

3.4.3.4 Residual load and deformation

Failure of the FRP strengthening was caused by simultaneous debonding of the three FRP plates described above. However, it should be noted that the FRP had not completely separated from the masonry and still bridged across the cracks and helped prevent collapse of the arch. The residual load carried by the north arch after debonding was 64.8kN, a value that was dependent upon the stiffness of the hydraulic loading system. Figure 3.21a also shows that there were substantial residual radial deformations after unloading.

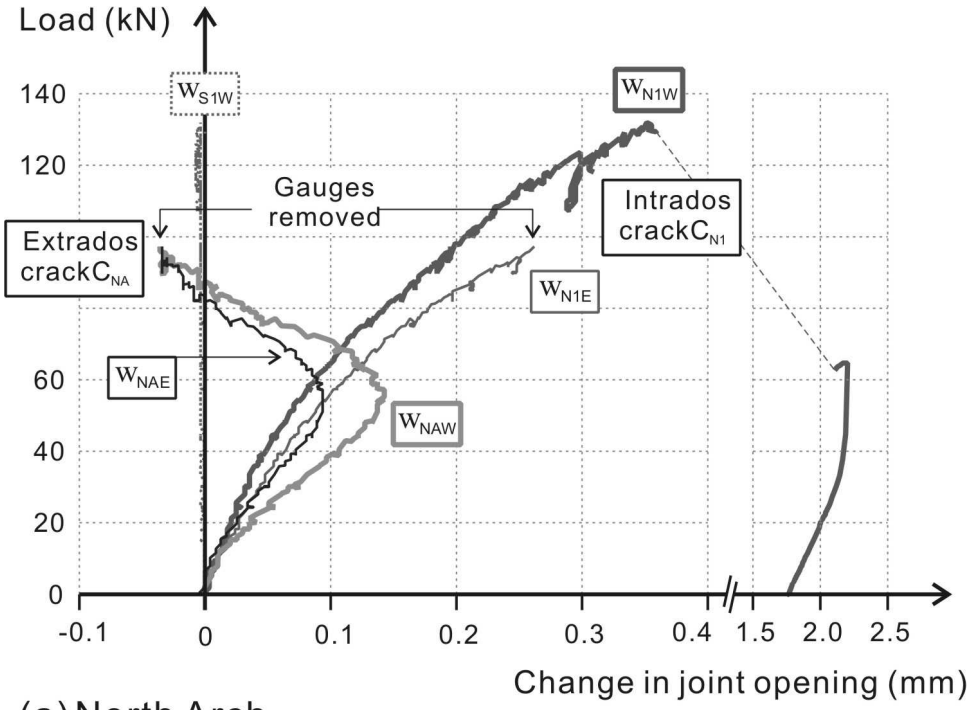

(a) North Arch

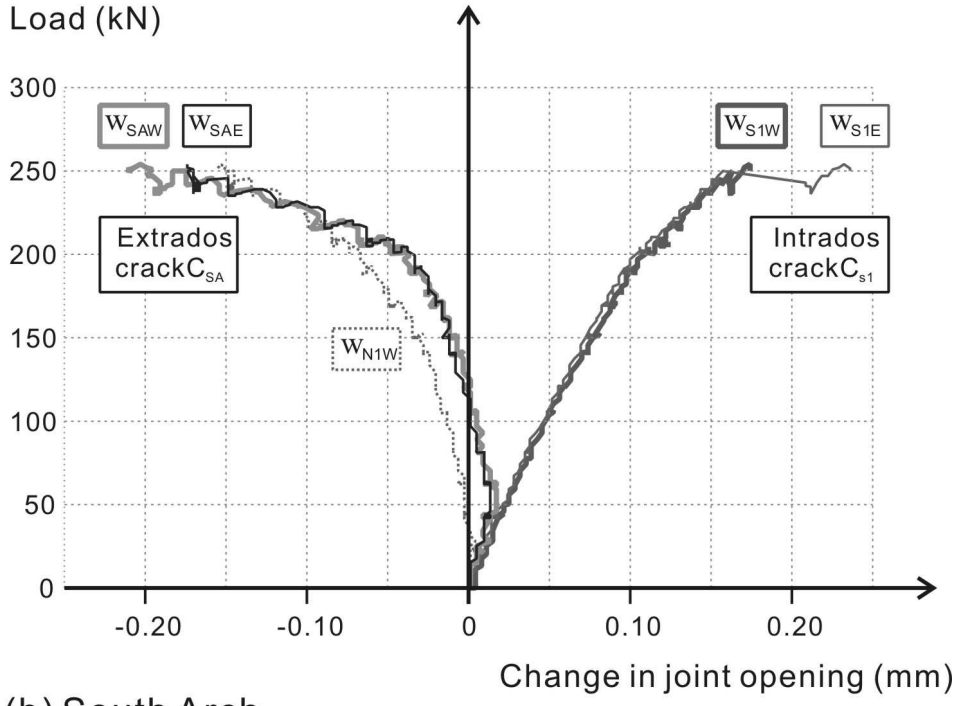

(b) South Arch

Figure 3.23 Load vs. change in joint opening response of the arches after strengthening

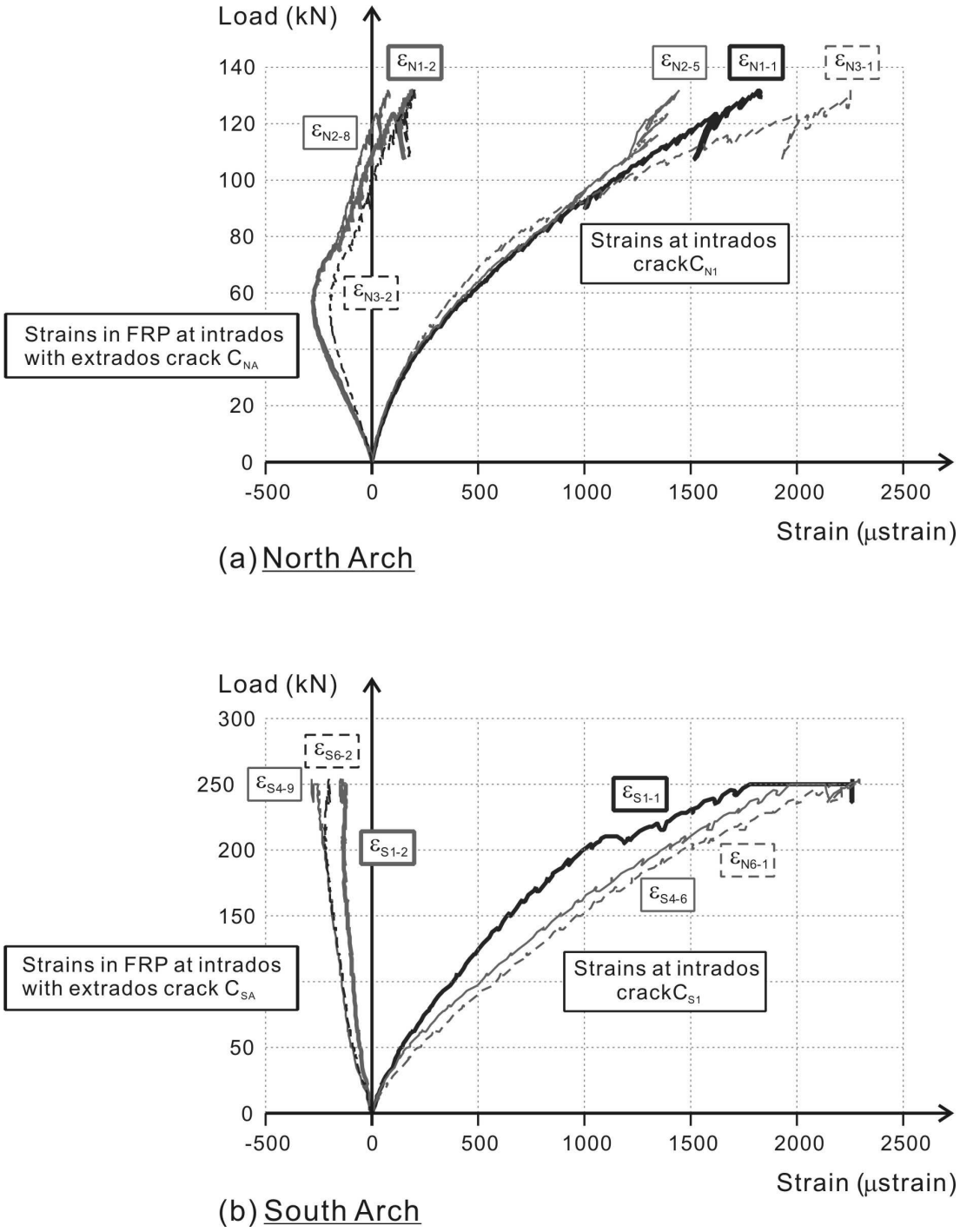

Figure 3.24 Development of FRP longitudinal strain at the cracks

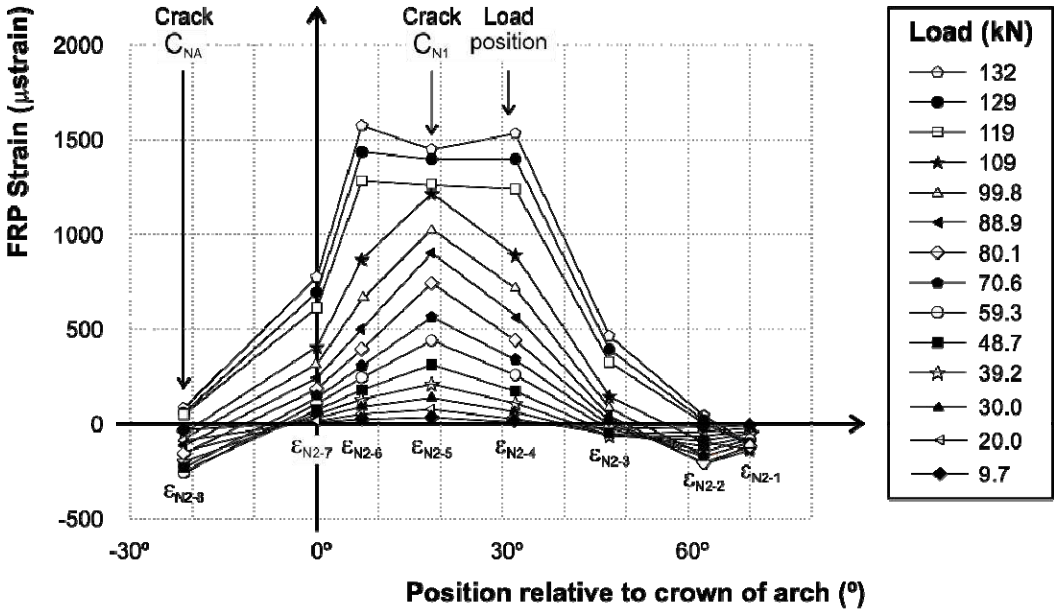

(a) North Arch: Plate P_{N2}

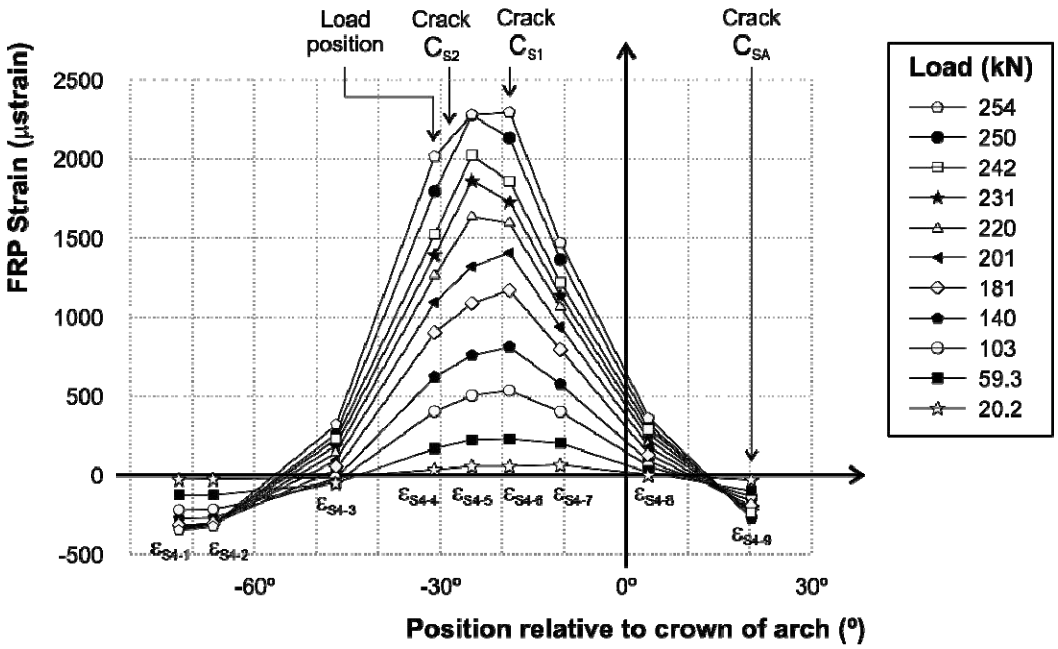

(b) South Arch: Plate P_{S4}

Figure 3.25 Distributions of longitudinal FRP strain along the central plates at different applied loads

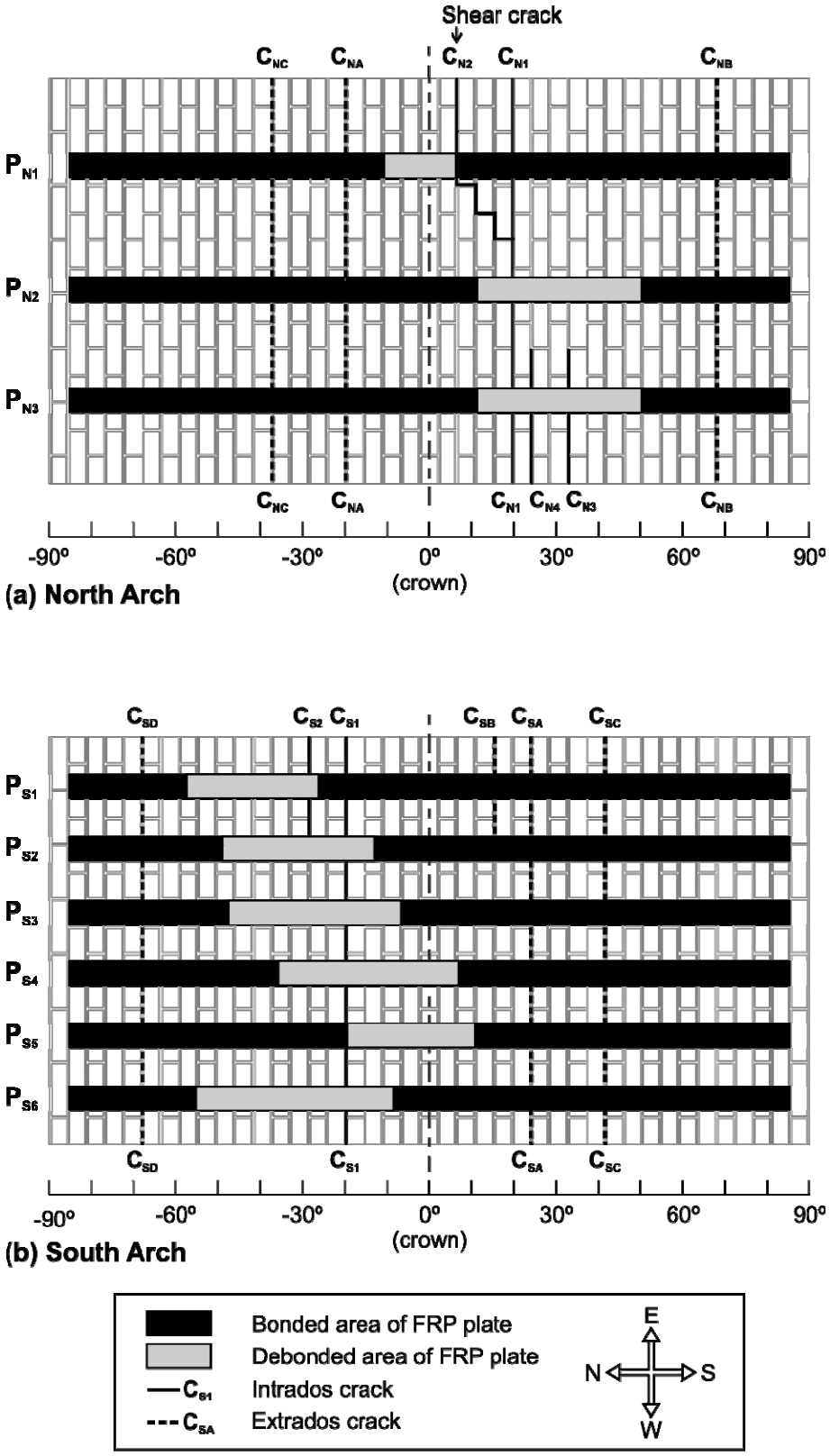

Figure 3.26 Developed plan view of the arches showing crack locations in the masonry and the extent of debonding after failure of the strengthening system

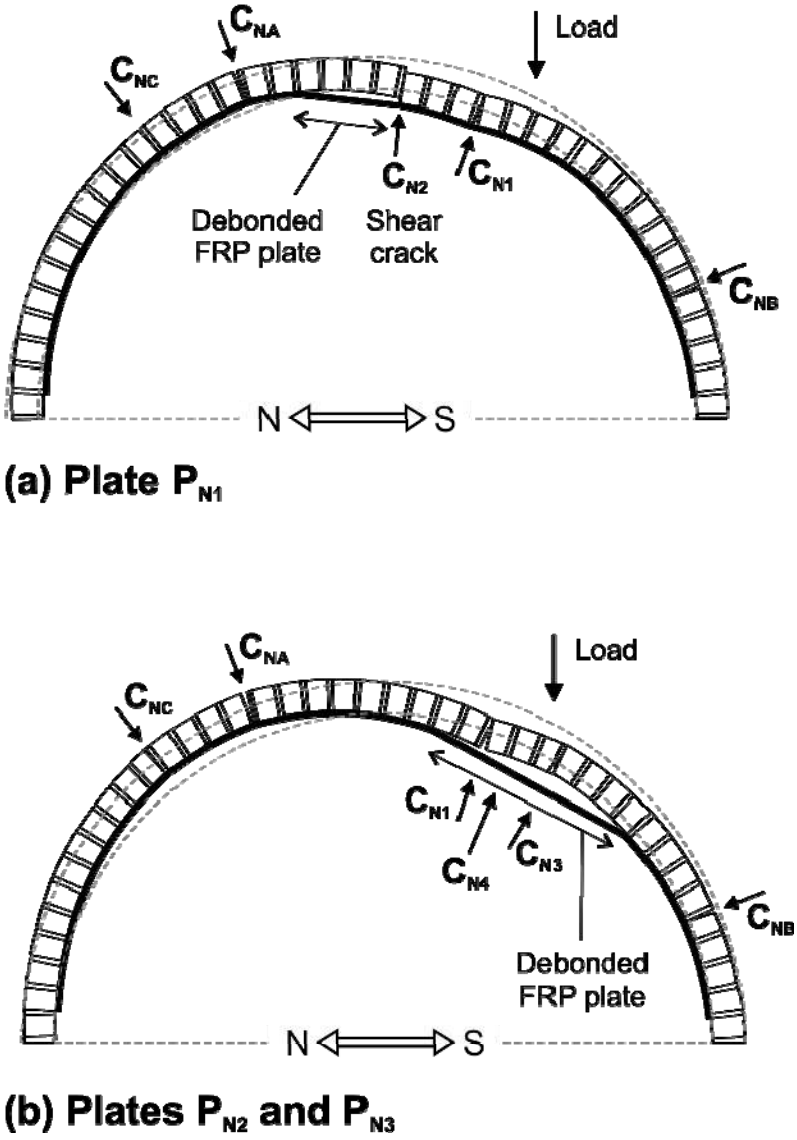

Figure 3.27 Sections along the FRP plates in the north arch, showing the failure mechanism post peak load

(a) Shear crack and debonding at Plate P_{N1}

(b) Flexural crack and debonding at Plate P_{S4}

Figure 3.28 Detailed view of debonding of the FRP from the masonry post peak load

3.4.4 South arch test after strengthening

The strengthened south arch behaved in a broadly similar manner to the north arch;

however, more FRP was applied to the south arch (6 FRP plates, Figure 3.5b). Similar data were recorded as for the north arch:

- Load vs. deflection response (Figure 3.21b).
- Crack width development (Figure 3.23b).
- FRP plate strains, in terms of load-strain at gauges coincident with cracks (Figure 3.25b) and strain profiles along the central plate (Figure 3.25b).
- The failure mode of the arch, in plan view along the arch developed length (Figure 3.26b), and sections along the plates showing the initial debonding event (Figure 3.29) and the final failure (Figure 3.30).

3.4.4.1 Initial loading (0 to 50kN)

During the early stages of loading, the arch behaved as a true four-hinge mechanism, with crack opening at both the intrados (C_{S1}) and extrados (C_{SA}) cracks that were established prior to strengthening (Figure 3.23b). As for the north arch, the FRP plate strains were tensile adjacent to intrados crack and compressive adjacent to the extrados crack (Figure 3.24b and Figure 3.25b), and the load-deflection response was stiffer than the unstrengthened arch (Figure 3.21b).

3.4.4.2 Increased loading (50 to 250kN)

As the load was increased above 50kN (the approximate unstrengthened arch capacity), extrados crack C_{SA} started to close up (Figure 3.23b), and the formation of a second extrados crack C_{SC} was observed (Figure 3.26b). This modified four-hinge mechanism is consistent with the distributed extrados cracking seen in the north arch.

The FRP remained in compression at extrados crack C_{SA} throughout the test (Figure 3.24b).

The equal crack widths to either side of the arch (Figure 3.23b) and similar FRP strains at similar locations in the different plates (Figure 3.24b) indicate uniform load carrying across the width of the arch. Figure 3.23b also shows that the width of the intrados crack C_{N1} on the north arch reduced as the south arch was loaded, indicating some interaction between the two arches. The north arch was severely damaged after FRP debonding failure and contained wide cracks during the south arch test, so it is not surprising that it was much more sensitive to load than the south arch.

The strain profile along the central plate P_{S4} had its peak at the intrados crack C_{S1} (gauge $S_{S4\text{-}6}$) for loads up to 200kN. As expected, the strain drops away to either side, with compressive strains at the extrados crack locations.

At 210kN, a new intrados crack C_{S2} formed in the arch two bricks away from the original crack C_{S1} on the east side of the arch (Figure 3.26b and Figure 3.31). The crack could be seen to cross the first two strengthening plates (P_{S1} & P_{S2}), and was not present under the two western-most plates (P_{S5} & P_{S6}), but it was not clear whether the crack extended across the two central plates (P_{S3} & P_{S4}) because it was not safe to inspect the underneath of the arch at these high load levels. The formation of this intrados crack increased the rate of strain increase in plate P_{S1} (which bridged the new crack) with loading ($\varepsilon_{s1\text{-}1}$ in Figure 3.24b) and increased the rate of crack closure (Figure 3.23b). The former phenomenon is consistent with the findings of

recent research that shows that the bond resistance is increased when an FRP plate bridges multiple cracks in a concrete beam (J. F. Chen et al., 2007; Teng et al., 2006). The location of the peak strain in plate P_{S4} shifted towards the new crack at the same time, suggesting that the new crack may have extended under this plate.

There are frequent fluctuations in the load-deflection and load-strain graphs (Figure 3.21b and Figure 3.24b) above 200kN. Just as for the north arch, these indicate progressive damage to the masonry and masonry-FRP interface, initially as micro cracks that cause material softening.

3.4.4.3 Debonding of the FRP from the masonry (above 250kN)

Damage accumulation along the masonry-FRP interface resulted in sudden debonding of the FRP from the masonry:

- The first significant debonding event occurred at a load of 250kN, when plate P_{S2} debonded over a short length to either side of the two intrados cracks (C_{S1} and C_{S2}). The extent of debonding at this stage is shown in Figure 3.29; the other five FRP plates remained bonded to the masonry. Debonding was accompanied by a drop in the load-displacement response (Figure 3.21b), an increase in crack opening on the east side of the arch (Figure 3.23b), and an increase in the strain in plate P_{S1} (Figure 3.24b), which picked up some of the load shed by plate P_{S2}.
- The capacity of the strengthened arch was reached at 254kN, when debonding occurred along a substantial length of all of the FRP plates. It was not

possibly to determine whether failure initiated in one plate in particular; all six plates appeared to debond simultaneously. However, the strain profile (Figure 3.25b) shows that the peak FRP strain at the intrados crack did not increase as the load was increased from 250 to 254kN, and that the debonded region expanded to either side. Failure of the FRP strengthening caused a sudden increase in deflection and a drop in the load carried by the arch (Figure 3.21b).

The details of the masonry cracking and FRP debonding varied across the width of the arch, as shown in Figure 3.26b and Figure 3.30. (It was not possible to determine the full extent of the extrados cracks C_{SC} and C_{SD} as they were beneath the sand fill). Flexural cracking of the masonry led to failure at plates P_{S1}, P_{S2}, P_{S3} & P_{S4} (the east and centre of the arch), where the FRP debonded on both sides of the critical crack. The debonded length was approximately the same at all of these positions. Plate P_{S4} (typical of debonding across a flexural crack) is shown in Figure 3.28b.

On the west side of the arch, failure was due to a combined flexure-shear failure deformation along crack C_{S1}, as shown in Figure 3.32. Consequently, P_{S5} debonded from the masonry on one side of the crack by peeling; P_{S6}, however, debonded to either side of this mixed-mode crack.

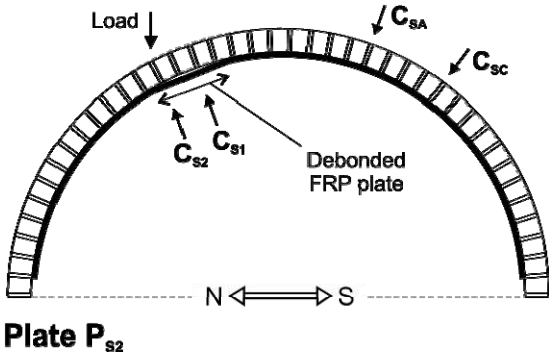

Figure 3.29 Plate P_{S2} on the south arch after initial debonding (250kN)

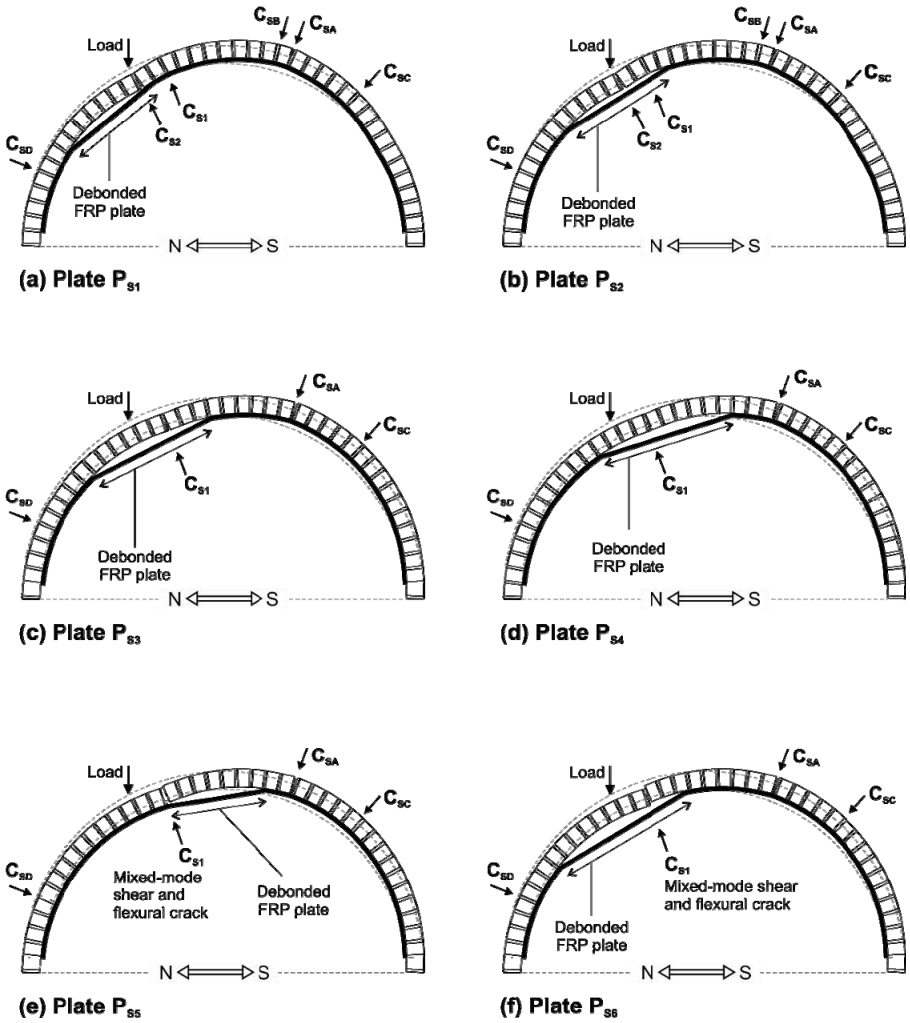

Figure 3.30 The deformed shape of the south arch and position of FRP post peal load

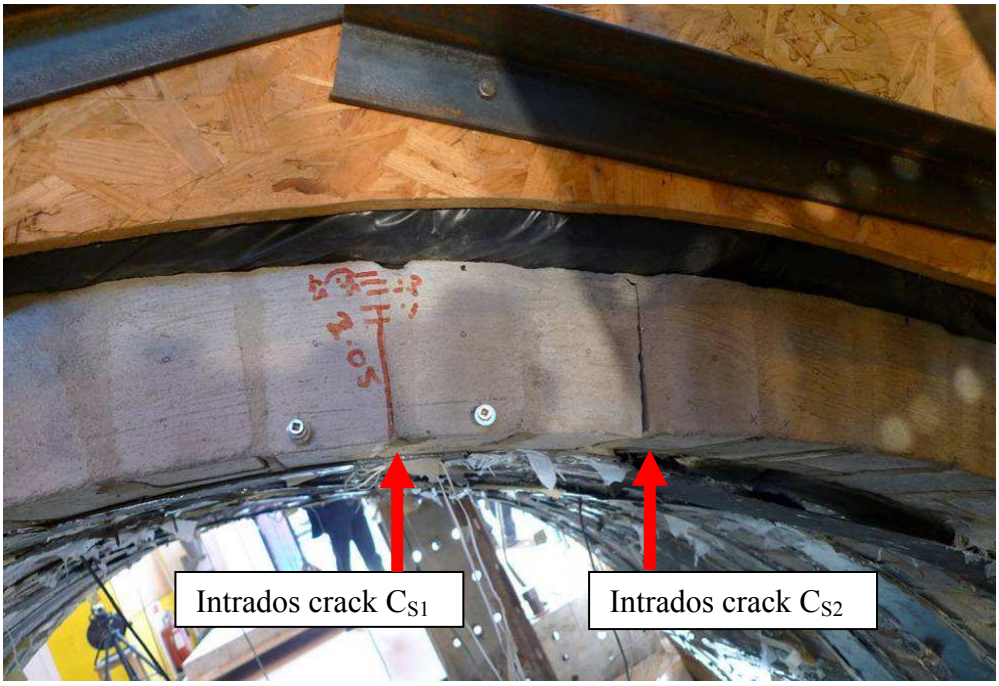

Figure 3.31 The second intrados crack (C_{S2}) on the east side of the south arch, which formed adjacent to the first intrados crack (C_{S1})

Figure 3.32 Mixed-mode flexural and shear failure at intrados crack (C_{S1}), on the west side of the bridge

3.4.4.4 Residual load and deformation

The residual load on the south arch after the FRP strengthening had failed was 91kN, and residual radial displacements of up to 18mm remained after unloading (Figure 3.21b).

3.4.5 Collapse test on the south arch

The arches were completely unloaded after the debonding failure of the FRP strengthening so that the instrumentation could be removed. The south arch was reloaded to determine its collapse mode and strength. Digital image correlation (using geoPIV software (White et al., 2003)) was used to determine the radial deflections at the same positions as the displacement gauges (except for δ_{S1}, which was not visible behind the loading frame), allowing the load-deflection response of the arch to be plotted in Figure 3.33.

The FRP plates debonded from the arch over a considerable length when the strengthening failed (Figure 3.26), but they still remained attached. During the collapse test they acted as ties that bridged the cracks in the masonry and contributed to the load carrying capacity of the arch. The debonded length of the FRP ties increased as the arch was re-loaded, accompanied by the opening of hinge cracks with the masonry. The FRP tie action allowed the arch to carry 113kN, substantially higher than the strength of the arch prior to strengthening (49.7kN). Large deformations were observed at this load (Figure 3.33), during which the FRP ties gradually debonded from the masonry arch.

Final collapse occurred when the FRP strengthening completely separated from the masonry portion beneath the loading area and the arch collapsed in a hinge mechanism.

There was no deflection reversing at the crown (δ_{S3}) in this test. However, it was observed in the unstrengthened arches as shown in Figure 3.22. This was because the FRP gradually debonded only from the masonry portion beneath the loading area and still remained attached to the symmetric portion. This tie-action led to the crown continuously deform outward. This consistent outward deflection implied the debonding mostly occurred at the masonry beneath the loading area as observed from the test.

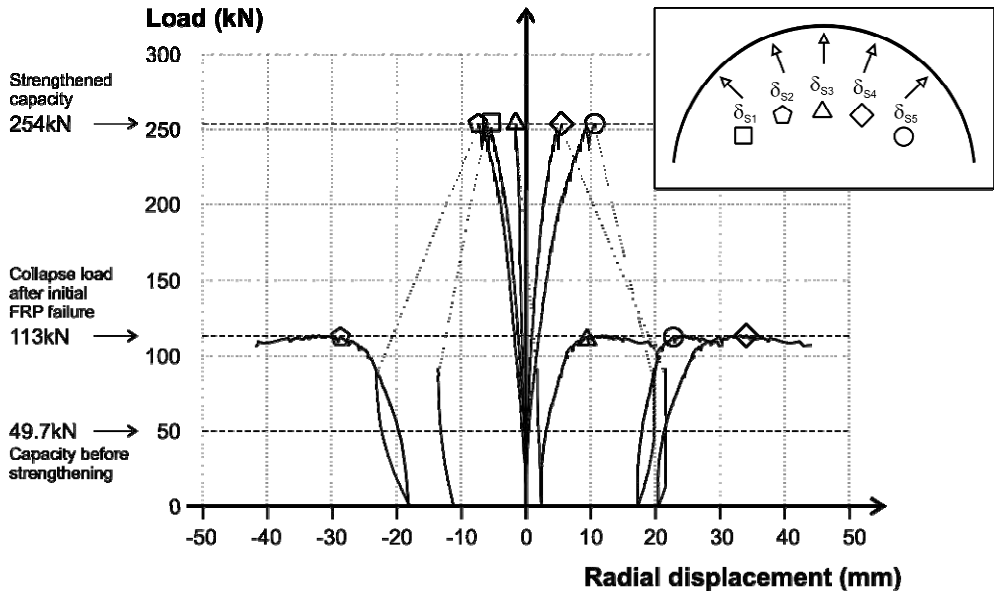

Figure 3.33 Load vs. equivalent radial displacement curves for the south arch, including the collapse test after debonding failure of the FRP strengthening

3. 5 Discussion

3.5.1 The effectiveness of the FRP strengthening system

3.5.1.1 Load capacity

The FRP strengthening plates significantly increased the load carrying capacities of the north and south arches. The capacity of the north arch (strengthened with 3 plates) was increased by 285%, from 46.2kN to 132kN. The capacity of the south arch (strengthened with 6 plates) was increased by 510%, from 49.7kN to 254kN. The four-hinge collapse mechanism can therefore be prevented and the load capacity of the arch increased substantially using externally-bonded FRP strengthening.

It needs to be stressed that the length of loading plate changed before (570mm) and after (670mm) strengthening. The longer loading plate implies a greater confinement for the backfill, and thus leads to a greater load carrying capacity of the masonry arch. This effect was analysed by using the classical mechanism method for masonry arch bridge. The details of the mechanism analysis was presented in the Chapter 5 (section 5.6.4) and the spreadsheet calculations was reported in Appendix 2. The results were summarized in Table 3-13. It is clear that the wider plate gives a greater load carrying capacity, increasing by 108% obtained from mechanism analysis, for the original masonry arch. After eliminating the effects on the load carrying capacity from the increase of the loading plate width, the improvements of the load carrying capacity by FRP strengthening should be reduced to 263% for the northern arch and 470% for the southern arch.

Table 3-13 Comparison of the results from test and mechanism analysis

	Original arches			Strengthened arches
Width of plate	570mm		670mm	670mm
	Test (kN)	Mechanism analysis (kN)		Test (kN)
North arch	46.2	41.9	45.5	132
South arch	49.7			254

It should be noted, however, that such a large increase in capacity is unlikely to be allowed in design; the Concrete Society (2004), for example, require the structure to carry the unfactored loads without strengthening, to avoid catastrophic collapse due to unforeseen damage to the strengthening. Furthermore, the current work was carried out upon a single-ring arch, and not a multi-ring arch as found in many real structures. Ring separation failures may occur in strengthened multi-ring arches, especially as the FRP can only be applied to the intrados ring of the arch. Other appropriate strengthening would be necessary if ring separation becomes critical.

3.5.1.2 Strengthening mechanisms and modes of failure

The strengthening acted in the same manner in both arches: the FRP bridged the hinge cracks and resisted flexural opening. By resisting the four-hinge mechanism, the FRP allowed additional cracks to form within the arch because it allowed the line of thrust to move outside of the arch ring; in both arches, an additional extrados crack (C_{NC}, C_{SC}) and additional intrados crack (C_{N2}, C_{S2}) formed adjacent to the original cracks (Figure 3.27 & Figure 3.30). It is worth noting that additional extrados cracks formed despite the fact that the FRP was applied only to the intrados

of the arch. However, it remains unclear whether (and if any, how much) the FRP strengthening contributes to the shear capacity of the arch ring. In both arches shear deformation occurred across masonry cracks at failure (Figure 3.27 & Figure 3.30).

The two arches differed only in the number of strengthening plates applied to them, and the fact that the north arch was tested prior to the south arch. Using twice as many FRP plates on the south arch resulted in smaller crack widths compared to the north arch (Figure 3.23).

Failure of the FRP strengthening system occurred when the FRP plate debonded from the masonry at an intrados plate beneath the loading position. For both arches, this occurred when the strain in one of the FRP plates reached about 2250μstrain (Figure 3.24). This is in good agreement with the debonding strain predicted by Chen and Teng's (2001) anchorage model, using the material properties of the masonry assemblage in place of concrete. This predicts that debonding occurs at a strain of 2430μstrain for the north arch (with 3 strengthening plates), or 2164μstrain for the south arch (with 6 strengthening plates). The calculation was shown in Appendix 1. This anchorage model is essentially designed for the flat surface (Mode II). However, this closed prediction indicates that there is no significant influence of curvature on the debonding load, which confirmed the studies conducted by De Lorenzis (De Lorenzis and Zavarise, 2009; De Lorenzis and Zavarise, 2010).

There was considerably less warning of failure of the strengthening system for the south than the north arch, with far less separation between first debonding of the FRP

and the capacity of the strengthened arch (Figure 3.21). As previously noted, there was a series of debonding events in the north arch above 116kN, in plate P_{N2} and P_{N3}, allowing the load to be re-distributed between the strengthening plates before failure of all three plates simultaneously at 132kN (Figure 3.24a & Figure 3.25a). In the south arch, however, there was only one debonding event prior to failure and very little re-distribution of load (Figure 3.24b & Figure 3.25b), a consequence of the higher reinforcement ratio using a brittle material.

There were also differences in the crack opening behaviour in each arch. In both arches, the original extrados crack (C_{NA}, C_{SA}) initially opened (Figure 3.23) and the FRP at this location was consequently in compression (Figure 3.24). As the load increased, however, the width of this crack gradually reduced (Figure 3.23), partly due to the formation of neighbouring extrados cracks (e.g.: C_{NC}, C_{SC}). (Note that negative crack widths in Figure 3.23 indicate a reduction of the crack width relative to its original width; the crack surfaces were not in contact; i.e. the crack was not fully closed). In the south arch, the FRP at the extrados crack remained under compression, but in the north arch it changed to tension (Figure 3.24). It is difficult, however, to attribute this difference in behaviour to the different number of strengthening plates applied to the arches; it is possible that some of the sand fill material had entered the crack in the north arch, and that this acted as a pivot that put the FRP into tension as the crack tried to close.

Following the initial failure of the strengthening system, the FRP did not completely separate from the arch, but acted as ties that continued to contribute to the load

carrying capacity of the arch. The ties gradually debonded from the masonry as the hinge cracks grew, giving a degree of ductility albeit at a load lower than the peak capacity of the strengthened arch.

3.5.2 Debonding along the FRP to masonry interface

Brittle debonding of the FRP from the masonry is critical in the failure of FRP strengthened masonry arches. Debonding occurs in the weakest link of the FRP to masonry interface. Close to the hinge crack, failure occurred within the masonry, leaving a layer of brick (approximately 2mm thick) and mortar (approximately 10mm thick) attached to the plates. Further away from the hinge, failure occurred within the surface of the FRP plate, leaving some of the plate fibres attached to the arch (Figure 3.28b). In neither case did failure occur within the bonding adhesive, demonstrating that the surface preparation and FRP installation work were correctly carried out.

The two different locations of debonding are indicative of two different modes of debonding. Debonding occurred within the surface of the FRP in regions where peel debonding was significant, due to the low transverse strength of the FRP plate. Where shear debonding dominated, however, failure occurred within the surface of the masonry.

- Shear debonding dominates close to a flexural hinge crack (such as C_{S2} crossing plate P_{S2}, Figure 3.30b). Load is transferred between the FRP and the masonry predominantly by shear stress across the adhesive interface.

- Peel debonding dominates to one side of a shear or mixed mode flexure-shear crack (such as C_{N2} crossing plate P_{N1}, Figure 3.27b). Shear across the crack requires normal (peel) stresses to be carried across the adhesive.
- Peel also plays an important part once the FRP has debonded over a substantial length and the FRP forms a tie, due to the angle at which the plate joins the intrados of the arch.

This chapter has focused upon the experimental results from the arch tests, but additional work is being carried out to interpret and model the debonding failure in detail.

3.5.3 Alternative strengthening materials

Whilst the arch bridges were strengthened with externally bonded FRP plates on their intrados, they may be strengthened in a similar manner using other suitable materials, such as near surface mounted (NSM) bars made of FRP or stainless steel bars. The behaviour of these systems is likely to be similar to externally bonded FRP, although the bond characteristics will differ. It must also be noted that, whilst the FRP strengthening is very effective for enhancing the loading capacity due to the four hinge mechanism failure, other failure modes such as shear and ring separation may become critical in a strengthened bridge they must also be carefully considered in design.

3. 6 Conclusions

The load capacity of a masonry arch bridge can be significantly increased by bonding FRP plates to its intrados. This chapter has presented tests conducted upon a large model two-span single-ring masonry arch bridge, topped by a sand fill. Each of the arches was initially loaded to determine their capacity prior to strengthening. Carbon FRP plates were then bonded to the intrados of the arches, and the arches were again tested to determine their strengthened response. Measurements were taken of both the global arch response (load and displacement) and of local behaviour (FRP strains and masonry crack widths) to achieve a detailed understanding of the FRP strengthened arch.

The FRP strengthening restrained the opening of the hinge cracks that form in a masonry arch and consequently reduce their deformation. By restraining the flexural crack opening required for a four-hinge mechanism, additional cracks are able to form within the masonry. The load capacity of the arch is increased because the FRP strengthening allows the line of thrust to move out of the extrados. Furthermore, masonry shear cracks (or mixed-mode flexure-shear cracks) are more likely to form when the four hinge-mechanism failure load is significantly increased by the FRP strengthening.

The capacity of the strengthened arches was governed by the behaviour of the bond between the masonry and the FRP plate. Debonding occurred at an intrados crack, and two debonding modes were observed. Flexural opening of the masonry crack

resulted in shear debonding of the FRP on both sides of the crack, whereas shear deformation in the masonry results in peel debonding of the FRP to one side of the crack. Some load redistribution occurred between initial debonding and collapse for the arch strengthened using 3 FRP plates, but collapse occurred with little warning in the arch with 6 plates.

The FRP did not completely separate from the masonry arch at the ultimate load, but remained attached at either end. Thus, post-debonding tie action prevented catastrophic collapse and maintained the integrity of the arch despite it being greatly deformed. It should be noted, however, that whilst the capacity of the tie mechanism was above that of the unstrengthened arch, it was substantially below the strengthened capacity and hence collapse would have occurred immediately in a load-controlled situation.

CHAPTER 4

MODELLING OF FRP TO CONCRETE BOND BEHAVIOUR USING A CONCRETE DAMAGED PLASTICITY MODEL

4. 1 Introduction

Externally bonding fibre reinforced polymer (FRP) has been widely used to upgrade and retrofit concrete structures (Teng et al., 2002). One of the critical failure modes of flexurally and shear strengthened structures is the debonding failure of the externally bonded FRP (Chen and Teng, 2001). This has led to extensive research on the bond behaviour between FRP and concrete in the last two decades. This bond behaviour is typically investigated experimentally using the 'shear' test of FRP-to-concrete bonded joints where a plate is bonded to a concrete substrate and subjected to a tension force (e.g., Ali-Ahmad et al. (2006); Täljsten (1996); Wu et al. (2001) and Yao et al. (2005)) as shown in Figure 4.1.

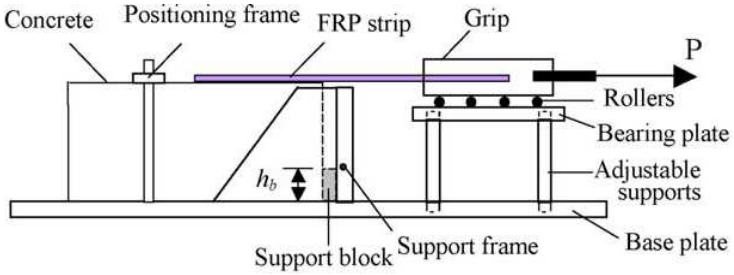

Figure 4.1 Typical setup for shear test of FRP-to-concrete bond joint (Yao et al. (2005))

Typical failure in the shear test occurs in the concrete a short distance away from the adhesive-concrete interface. The bond behaviour is thus usually controlled by the behaviour of the concrete. In addition to the experimental studies, the bond characteristics of the FRP-to-concrete interface have also been investigated in a number of analytical (e.g., Chen et al. (2007); Yuan et al. (2004)); and numerical (e.g., Chen and Pan (2005); Coronado and Lopez (2007); Diab and Wu (2007); Lu et al. (2006; 2005b) and Pham and Al-Mahaidi (2007)) studies.

Existing finite element (FE) studies on the FRP-to-concrete bond joint may be classified into three approaches: a) direct model approach where the behaviour of concrete is accurately modelled in meso-scale with an appropriate constitutive model (e.g., Lu et al. (2006; 2005b)); b) interface model approach where the bond behaviour is modelled using a layer of interface elements (e. g., Diab and Wu (2007)); and c) crack band approach where the debonding failure is assumed to take place within a band in the concrete adjacent to the FRP-concrete interface and a modified constitutive law is required for this band (Coronado and Lopez, 2007; Coronado and Lopez, 2010). The first approach can be used to predict not only the entire debonding failure process but also the bond-slip relationship for the FRP-to-concrete interface. The second approach relies on the appropriate use of a bond-slip model as the constitutive law for interface element, which may be developed from either the first approach or from test. This is thus not really a predictive approach for the bond behaviour but appropriate for modelling large structures where meso-scale modelling of concrete is unrealistic (Chen et al. 2012; Chen et al. 2011). The third approach requires different material constitutive model for the crack band which needs to be

obtained from experiments and could be sensitive to the adhesive used. It means that this approach is also not truly predictive. Therefore, for simulating the detailed bond behaviour, the first approach is more appropriate. However, numerical studies on the bond behaviour using this approach have been very limited due to the difficulties of modelling concrete.

The purposes of this study are to develop an accurate predictive FE model, eliminating the above-mentioned deficiencies, and mainly to develop a constitutive model of concrete for the following chapters. To this end, existing numerical studies on FRP-concrete bond behaviour are reviewed first to analyses the advantages and disadvantages of each approach. A new FE model is then proposed to overcome the shortcomings. In the proposed model, the concrete is accurately simulated using a concrete damage plasticity model, incorporating a new damage model based on the plastic degradation theory. The proposed model is then validated by comparing its predictions with test results for the bond behaviour of single shear test of the FRP-to-concrete bonded joint. Predictions using existing concrete damage models are also compared with those of the new damage model. It needs to be noticed that this work mainly focused on the FRP-to-concrete instead of FRP-to-concrete masonry which includes both concrete (units) and mortar.

4. 2 Existing numerical modelling on FRP-to-concrete bond behaviour

4.2.1 (a) Direct model approach

Previous studies on numerical simulation of the FRP-to-concrete bond behaviour

may be summarised in Table 4-1 according to the aforementioned three modelling approaches. In terms of the direct model approach, a meso-scale FE mesh (it has been commonly in the range of 0.5~2mm for the smallest element size) has to be adopted to model the detailed behaviour near the FRP-to-concrete bond so that the bond-slip behave can be obtained. Lu et al. (2005b) adopted fixed angle crack model together with a shear retention model for concrete. The bond-slip model (Lu et al., 2005a) developed based on Lu et al. (2005b) has been very widely accepted by the research community. The same author (Lu et al., 2006) adopted rotation angle crack model in conjunction with a user-defined constitutive model for concrete. However, these two FE models were implemented through a user-subroutine in MARC (2003) which very few researchers in structural engineering have the skills to execute nowadays. The predictions are also sensitive to the choice of the shear retention model. Pham and Al-Mahaidi (2007) directly adopted the concrete model in DIANA (2003). There were transition layer of elements (2mm-10mm for the element size) and coarse layer of elements (10mm for the element size) involved in the FE model. However, the effects of the range of the fine layer elements have not been investigated even the results showed the concrete cracks propagated into the transition layer and coarse layer. Apart from the smeared crack model of concrete, in some studies (e.g., Camata et al. (2004); Pham et al. (2006)), combined models involving both the smeared and discrete crack model to simulate the concrete have been developed. However, this approach usually requires an additional interface crack model to define the discrete crack behaviour, making it even more complex. Moreover, it is difficult to locate the pre-embedded cracks in the model.

4.2.2 (b) Interface model approach

The interface model approach used to simulate the single shear bond test is less concerned because the constitutive law (e.g., bond-slip law) for the interface elements is needed to obtain from the direct model approach or pull-off test. Therefore, this approach is usually adopted to simulate the problems when the meso-scale model is not appropriate, especially in three-dimensional model (Salomoni et al., 2011). The concrete-to-FRP interface layer is usually represented by interface elements (Diab and Wu, 2007) or a contact interfaces model (Salomoni et al., 2011).

4.2.3 (c) Crack band model approach

The crack band approach assumes that debonding occurs within a thin band in the concrete adjacent to the adhesive-to-concrete interface, and the properties of the concrete within this band are different from the nearby plain concrete because of the presence of adhesive (Coronado and Lopez, 2007; Coronado and Lopez, 2008). Consequently, a modified concrete constitutive law is required for this band (Coronado and Lopez, 2007; Coronado and Lopez, 2010). Test is required to obtain the constitutive law, especially the tension softening behaviour, of the band. This means that it is debatable whether the approach is predictive. Furthermore, debonding occur within this band or in the concrete outside of this thin band. If it is within the band, the properties can be significantly affected by the adopted adhesive, rendering the approach more complex for practical applications.

Based on the above discussion, it may be concluded that the direct model approach is

the most appropriate for modelling the FRP-to-concrete bond behaviour as a truly predictable model. It is thus adopted in this study.

Table 4-1 Summary of FE studies on FRP-to-concrete bond behaviour

Numerical approach	Reference	Modelling of concrete		Remarks (Software)
		In compression	In tension	
Direct model approach				
FEM, Smeared crack model, Fixed angle crack model	Lu et al. (2005b)	Hognestad's model (1951)	Linear softening	User defined shear retention model (MARC)
FEM, smeared crack model, Rotating angle crack model	Lu et al. (2006)	User defined constitutive model through subroutine		User defined constitutive model, 2-D plane stress assumption, (MARC)
		Saenz's model (1964), isotropic	exponential strain-softening path, orthotropic	
FEM, Smeared crack model, Rotating angle crack model	Pham and Al-Mahaidi (2007)	Total strain crack model		(DIANA)
		Thorenfeldt et al. model (1987)	Hordijk model (1991)	
FEM, Smeared & discrete crack model	Camata et al. (2004); Pham et al. (2006)	Nonlinear fracture mechanics-based model		Pre-defined cracking in concrete, Re-meshing technique (MERLIN)
		Three-invariant plasticity model proposed by Menétrey & Willam (1995)	Rankine (1857) smeared crack model	

Interface model approach				
FEM, Smeared crack model	Diab and Wu (2007)	CEB-FIP model		Interface modelled (DIANA)
FEM Smeared crack model	Salomoni et al. (2011)	Drucker-Prager constitutive law		Interface modelled according to Mazars' model (ABAQUS)
Crack band approach				
FEM, Smeared crack model,	Coronado and Lopez (2007; 2010)	Todeschini's model (1964) for both plain concrete and crack band	Parameters of tension softening obtained from test for both plain concrete and crack band	A damage model is applied. (ABAQUS)

4. 3 Modelling of concrete

4.3.1 Crack band theory of concrete fracture

There are two common methods which can be used to describe the computational mechanics of concrete cracking: discrete crack model and smeared crack model (Rots, 1991). In the former, a crack is treated as a geometrical identity so it is either pre-embedded in the FE mesh or through continuous re-meshing (Yang and Chen, 2005; Yang et al., 2003). The latter keeps the geometry constant and the cracking is modelled through the concrete constitutive law (Rots, 1991). The smeared crack approach is adopted in this study as it is impossible to track multiple cracks, especially the numerous micro-cracks in the single shear test where failure occurs within a few millimetres in the concrete adjacent to the bond line.

One of the drawbacks in the smeared concrete model is that it involves the strain localisation phenomenon due to strain-softening, where the energy consumption approaches to zero during crack propagation when the element size approaches to zero (Bažant and Jaime, 1998). This can be overcome by adopting the crack band theory (Bažant and Oh, 1983):

$$w = h\int \varepsilon_{ct} \tag{4-1}$$

where w is the crack opening width, h is the width of the crack band and ε_{ct} is the crack strain caused by the opening of a crack. The crack band width h represents the effective width of the fracture process zone over which micro-cracks are assumed to be uniformly distributed. In FE analysis, the cracking strain is assumed to be uniformly distributed over h which is referred as the characteristic length of an element and it is related to the element size, type and integration scheme. Results of numerical simulations should not depend on subjective aspects such as the choice of mesh or element size. Therefore, the crack band theory is used in the present FE model to minimise the mesh sensitivity.

4.3.2 Compressive and tensile behaviour of concrete

The concrete is modelled using the concrete damage plasticity model available in ABAQUS (2007). The plasticity model adopts the yield function proposed by Lubliner et al. (1989) and modified by Lee and Fenves (1998), and follows a non-associated flow rule. The concrete under uniaxial compression is described by the

following stress strain relationship proposed by Saenz (1964):

$$\sigma_c = \frac{E_0 \varepsilon_c}{1 + \left(\frac{E_0 \varepsilon_p}{\sigma_p} - 2 \right) \left(\frac{\varepsilon_c}{\varepsilon_p} \right) + \left(\frac{\varepsilon_c}{\varepsilon_p} \right)^2} \tag{4-2}$$

where σ_c and ε_c are respectively the compressive stress and strain, σ_p and ε_p are the experimentally determined maximum stress and its corresponding strain which are taken to be the cylinder strength f_c' (MPa) and 0.002 respectively in this study. The elastic modulus of the concrete E_0 is estimated from $E_0 = 4730\sqrt{f_c'}$ (MPa) following ACI318 (2002).

Under uni-axial tension, the problem involves tensile cracking. The fracture energy G_F, the energy required to create a unit area of stress free crack surface, instead of the descending branch of the stress-strain curve, is treated as a material property of the concrete. The stress-crack opening displacement relationship proposed by Hordijk (1991) is adopted:

$$\frac{\sigma_t}{f_t} = \left[1 + \left(c_1 \frac{w_t}{w_{cr}} \right)^3 \right] e^{\left(-c_2 \frac{w_t}{w_{cr}} \right)} - \frac{w_t}{w_{cr}} \left(1 + c_1^{\,3} \right) e^{(-c_2)} \tag{4-3}$$

$$w_{cr} = 5.14 \frac{G_F}{f_t} \tag{4-4}$$

where w_t is the crack opening displacement, w_{cr} is the crack opening displacement at the complete loss of tensile stress, σ_t is the tensile stress normal to the crack direction, f_t is the concrete uniaxial tensile strength, and c_1=3.0 and c_2 =6.93 are constants determined from tensile tests of concrete. f_t and G_F may be estimated from the CEB-FIB (1991) and Bazant and Becq-Giraudon (2002) models:

$$f_t = 1.4\left(\frac{f_c'-8}{10}\right)^{\frac{2}{3}}, \text{MPa} \tag{4-5}$$

$$G_F = \left(0.0469 d_a^2 - 0.5 d_a + 26\right)\left(\frac{f_c'}{10}\right)^{0.7}, \text{N/mm} \tag{4-6}$$

where d_a is the maximum aggregate size. In the present study, d_a is assumed to be *20mm* if no test data is available. Once the stress-crack opening displacement relationship is known, the stress-strain relationship can be determined for each element based on its size through Eq. 4-1.

4.3.3 Damage model of concrete

Both the strength and stiffness of concrete reduces with the development of micro-cracks. This can be characterised by several phenomena of concrete such as strain softening, progressive deterioration, volumetric expansion etc. Apart from the plasticity model, the nonlinear behaviour of concrete can also be attributed to process of damage in concrete, such as, micro-cracking, coalescence, decohesion, etc. (Cicekli et al., 2007; Grassl and Jirásek, 2006; Lubliner et al., 1989). Damage

associated with the failure mechanism of the concrete (cracking and crushing) therefore results in a reduction in the elastic stiffness. An isotropic scaled damage model from the continuum damage mechanics is introduced in ABAQUS (2007) to describe the stiffness degradation, which can be represented by the Eq. 4-7:

$$\sigma = (1-d)D_0(\varepsilon - \varepsilon_p) \tag{4-7}$$

where σ , ε and ε_p represent the stress tensor, total strain tensor and the plastic strain tensor respectively; D_0 is the initial (undamaged) elasticity matrix and d is the damage variable, which characterizes the degradation of the elastic stiffness, and can take values in the range from zero (undamaged material) to one (fully damaged material).

When concrete is subjected to uniaxial loading and assumed there is no damage included (d=0), the Eq. 4-7 can be simplified to Eq. 4-8 as shown in Figure 4.2b.

$$\sigma = E_0(\varepsilon - \varepsilon^P) \tag{4-8}$$

where ε^p is the plastic strain without stiffness degradation.

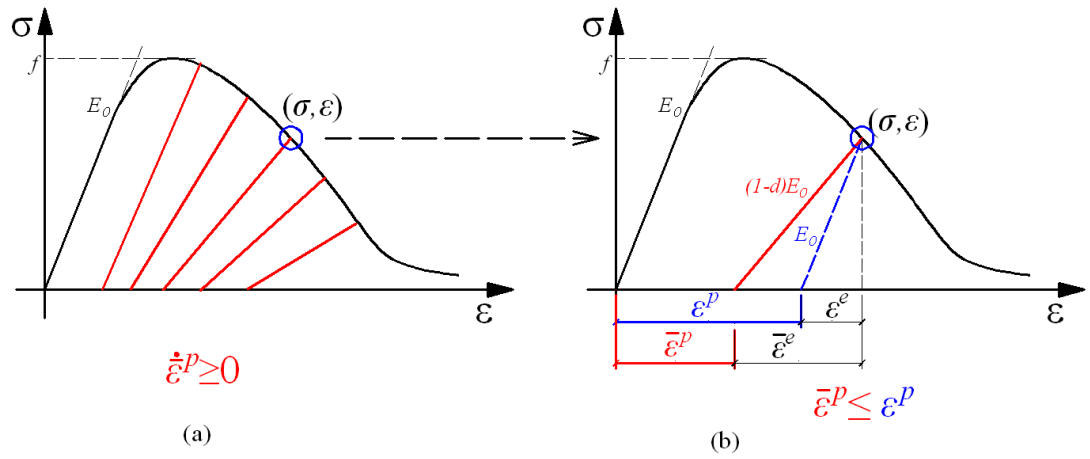

Figure 4.2 Concrete damaged plasticity model (a) and plastic strain degradation (b) in uniaxial load

When damage effects are included in the model of concrete ($d \neq 0$), the model of stiffness degradation can be classified into two types according to the presence of irreversible deformation/plastic strain: elastic degradation model and plastic degradation model (Lubliner et al., 1989). The elastic degradation model is associated with total deformation/strain, implying that no irreversible deformation/plastic strain exists ($\bar{\varepsilon}^p = 0$), which means that the unloading path of the stress-strain curve always passes through the origin of the coordinate system in Figure 4.2. Eq. 4-7 in this case can be rewritten as:

$$\sigma = (1-d)E_0\varepsilon \tag{4-9}$$

where ε is the total strain. Lubiner et al. (1989) stressed that the concept of elastic degradation is associated with the total deformation but without the necessity of a damage criterion. A plastic degradation, in which the stiffness degradation is

associated with the plastic deformation instead of the total deformation, was introduced to overcome the weaknesses of elastic degradation model (Lubliner et al., 1989). It means that irreversible deformation/plastic strain exists after damage occurred ($\bar{\varepsilon}^{p} \neq 0$). Eq. 4-7 in this case can be rewritten as:

$$\sigma = (1-d)E_0\left(\varepsilon - \bar{\varepsilon}^{p}\right) \tag{4-10}$$

in which $\bar{\varepsilon}^{p}$ is the equivalent plastic strain (plastic strain with stiffness degradation) in the loading direction.

4.3.3.1 Lubliner's damage model

Lubliner et al. (1989) proposed a simple damage model that plastic degradation occurs only in the softening range and the stiffness is proportional to the cohesion of the materials:

$$\frac{D}{D_0} = \frac{c}{c_{\max}} = 1 - d \tag{4-11}$$

$$d = 1 - \frac{c}{c_{\max}} \tag{4-12}$$

where d varies from 0 (no stiffness degradation) to 1 (total stiffness degradation); c is the cohesion in the yield criteria which is proportional to stress and c_{max} is proportional to the strength of the concrete (Lubliner et al., 1989). Under uniaxial

tension or compression, Eq. 4-12 converts to:

$$d = 1 - \frac{E_d}{E_0} = 1 - \frac{\sigma}{f} \tag{4-13}$$

in which f is either the tensile or compressive strength of concrete as appropriate, E_d is the elastic modulus with stiffness degradation. Lubliner et al. (1989) damage model was implemented to model the bond behaviour in the shear bond test but it did not lead to reasonable predictions in comparison with test data.

4.3.3.2 New damage model

A new model is thus introduced in this study as follows. Once concrete enters into the softening range, the stiffness is degraded resulting in a plastic strain degradation (so $\bar{\varepsilon}^p \le \varepsilon^p$) as shown in Figure 4.2. It needs to be stressed that within the entire range, the plastic strain still increases or at least remains constant ($\dot{\bar{\varepsilon}}^p \ge 0$) under an increased deformation despite $\bar{\varepsilon}^p \le \varepsilon^p$. Instead of assuming that the stiffness is proportional to the cohesion of the material, it is assumed here that the ratio of the plastic strain with stiffness degradation ($\bar{\varepsilon}^p$) to that without stiffness degradation (ε^p), k, is proportional to the cohesion of the material. In case of uniaxial loading, this ration can be expressed as:

$$k = \frac{\bar{\varepsilon}^p}{\varepsilon^p} = \frac{\sigma}{f} \tag{4-14}$$

4.3.4 Implementation of the new damage model into ABAQUS

In ABAQUS (2007), the relationship between the plastic strain without stiffness degradation ε^p and damage factor d needs to be defined as a constitutive law of concrete. Therefore, the relationship between the ratio of the plastic strain with stiffness degradation to that without stiffness degradation, k, and the damage variable d needs to be established in order to implement the new damage model. Based on the geometry in Figure 4.2b, the equivalent plastic strain $\bar{\varepsilon}^p$ can be related to the damage variable d as:

$$\bar{\varepsilon}^p = \varepsilon^p - \frac{d}{(1-d)}\frac{\sigma}{E_0} \tag{4-15}.$$

Substituting Eq. 4-14 into Eq. 4-15 yields

$$d = \frac{(1-k)\varepsilon^p}{(1-k)\varepsilon^p + \sigma/E_0} \tag{4-16}.$$

Figure 4.3 shows a typical stress-strain curve for concrete under uniaxial tension, where the subscript t represents tension. In such a case, the stress-crack strain curve for a given element can be obtained from the stress-crack opening displacement curve (Eq. 4-3) depending on the element type and size through Eq. 4-1. The relationship between the crack strain and tension damage factor d_t can then be calculated from Eqs. 4-15 and 4-16.

The compression damage factor d_c versus compressive plastic strain can be calculated from Eqs. 4-2, 4-15 and 4-16. Note that the compressive plastic strain is calculated from $\varepsilon_c^P = \varepsilon_c - \sigma_c / E_0$. Damage is assumed to occur only after the concrete enters softening in both tension and compression. The two damage factors (d_t and d_c) versus plastic strain curves (tension and compression) are used as user input data in ABAQUS. All the modelling parameters were summarized in the Appendix 3.

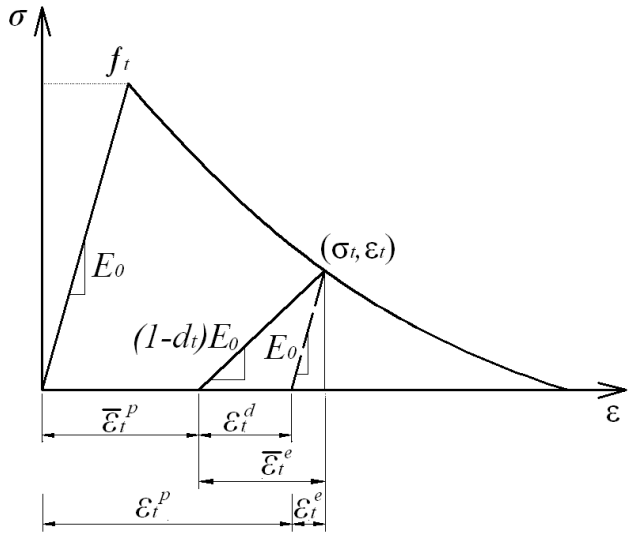

Figure 4.3 Stress-strain relationship of concrete under uniaxial tension

4. 4 FE modelling of pull-off test

4.4.1 Geometry of the model

A 45 mm thick concrete prism as shown in Figure 4.4 has been modelled as a plane stress problem in the FE analysis. This thickness is smaller than most specimens in experiments but the rest of the concrete should have little effect on FE results as the

test commonly fails by debonding in concrete a few millimeters away from the FRP-to-concrete interface and only this failure mode is concerned in this study. The specimen is restrained vertically along the base and horizontally along part of the right edge h_s (Figure 4.4). For specimens with a free height h_c smaller than 30mm, the actual h_c value is used. For specimens with h_c greater than 30mm, h_c is set to 30mm. The thickness of the FRP plate t_p is set equal to 1mm but the modulus of elasticity of the plate E_p is modified so that the FRP plate has the actual axial stiffness $E_p t_p$. The implicit steady-state dynamic analysis method available in ABAQUS was adopted.

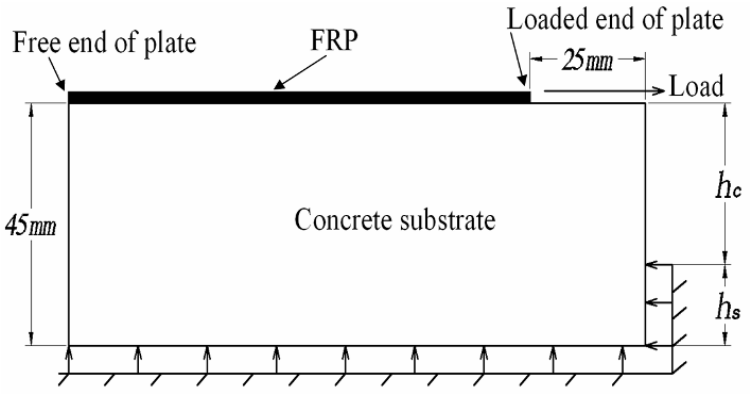

Figure 4.4 FE model of pull-off test

4.4.2 Constitutive model of materials

As aforementioned, the concrete damaged plasticity model is used to describe the concrete behaviour. The plastic behaviour of concrete is modelled following the compressive and tensile behaviour described in Section 4.3.2. The damage is modelled using the proposed damage model in Section 4.3.3. The FRP is modelled as a linear elastic material.

The concrete is modelled using square plain stress elements with four integration points (CPS4). Rots' (1988) recommendation is adopted that the characteristic length for a square element with 4 integration points is $\sqrt{2}e$ where e is the element length. The FRP is modelled using the same element with matching mesh.

4.4.3 Interpretation of numerical results

Because the test is modelled as a plane stress problem while the actual behaviour is three dimensional (Chen and Pan, 2005), the predicted load, displacement, stress and strain in the FRP plate are all adjusted following the width ratio factor β_w proposed by Chen and Teng (2001):

$$\beta_w = \sqrt{\frac{2 - b_f / b_c}{1 + b_f / b_c}} \tag{4-17}$$

where b_f and b_c are the widths of the FRP plate and the concrete prism respectively.

4.4.4 Mesh convergence analysis

Specimen II-5 reported in Yao et al. (2005) was used as a reference case for conducting the mesh convergence study. Figure 4.5 shows the effect of element size on the predicted loading capacity. The difference in the loading capacity between the 0.5mm mesh and the 1mm mesh is 2.8%. On the balance of accuracy and computational economy, the 1mm mesh was used for all the modelling reported in the rest of the study.

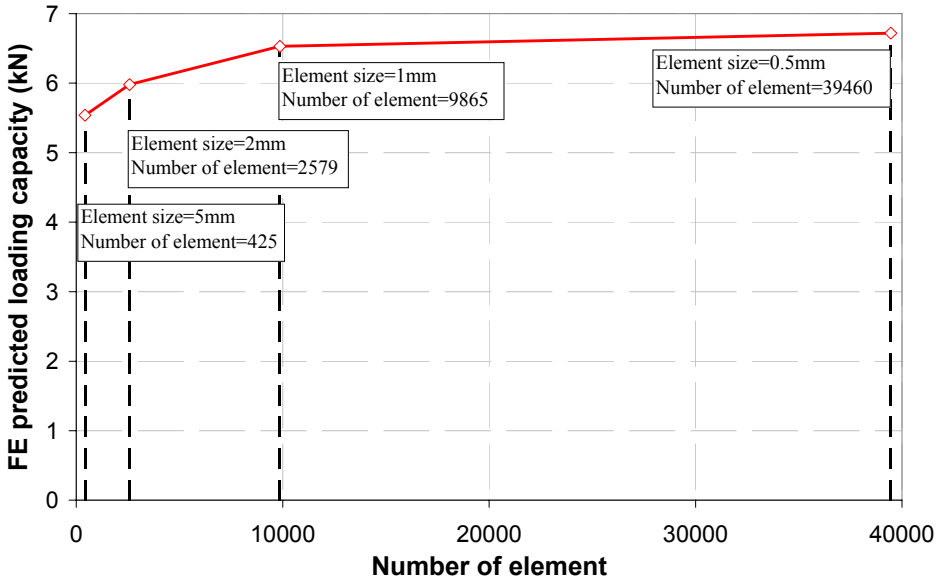

Figure 4.5 Predicted loading capacity for specimen II-5 in Yao et al. (2005)

4. 5 Influence of different concrete damage models

Several concrete damage models have been used for the concrete damaged plasticity model in previous numerical studies, such as Chen et al. (2011); Coronado and Lopez (2007); Grassl and Jirásek (2006) and Yu et al. (2010). The effects of these damage models on the predictions are investigated in this section.

Chen et al. (2011) adopted the classical elastic damage model, assuming that the equivalent plastic strain $\bar{\varepsilon}^{p} = 0$ for throughout the post-cracking, which means that the unloading path of the stress-strain curve always passes through the origin of the coordinate system in Figures 4.2 and 4.3. Yu et al. (2010) assumed that the elastic strain is constant after the peak stress, which is also used by Grassl and Jirásek (2006). A model considering the shear retention is implemented as Chen et al. (2012) used for FRP strengthened concrete beams and the shear retention model developed

by Rots (1988) is adopted:

$$\beta = \left(1 - \frac{\varepsilon_{cr}}{\varepsilon_{cr,\mu}}\right)^n \tag{4-18}$$

where ε_{cr} is the concrete crack strain corresponding to w_t in Eq. 4-3, $\varepsilon_{cr,u}$ is the concrete cracking strain at the complete loss of stress corresponding to w_{cr}, and n is a coefficient controlling the rate of shear degradation and value of 5 was chosen in the this study.

In addition, a model without considering damage, i.e. both $d_t=d_c=0$, is adopted as a reference case. Figure 4.6 and 4.7 show how the damage factor varies with the crack strain (in tension) or inelastic strain (in compression) for these models.

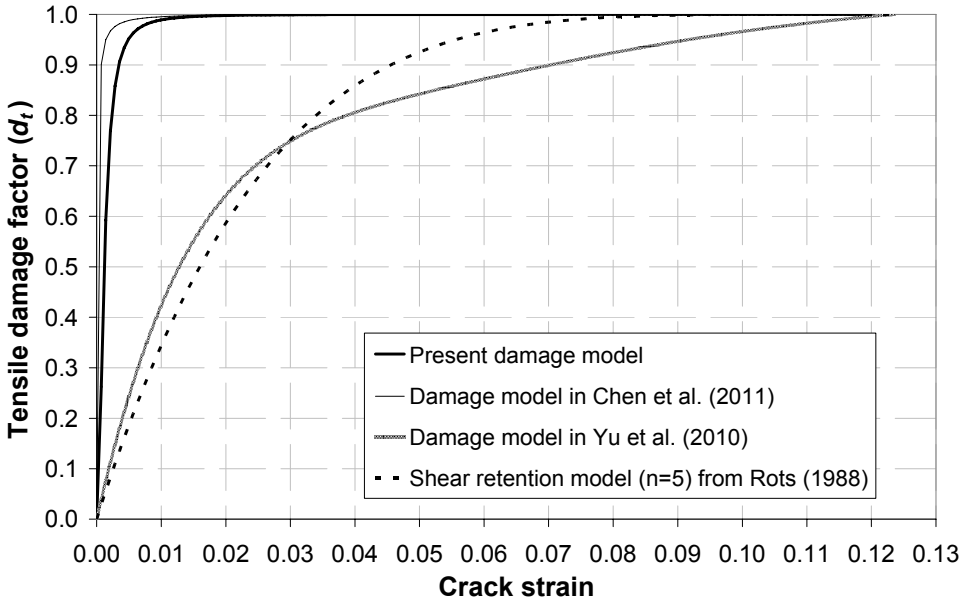

Figure 4.6 Different damage models in tension for specimen II-5 in Yao et al. (2005)

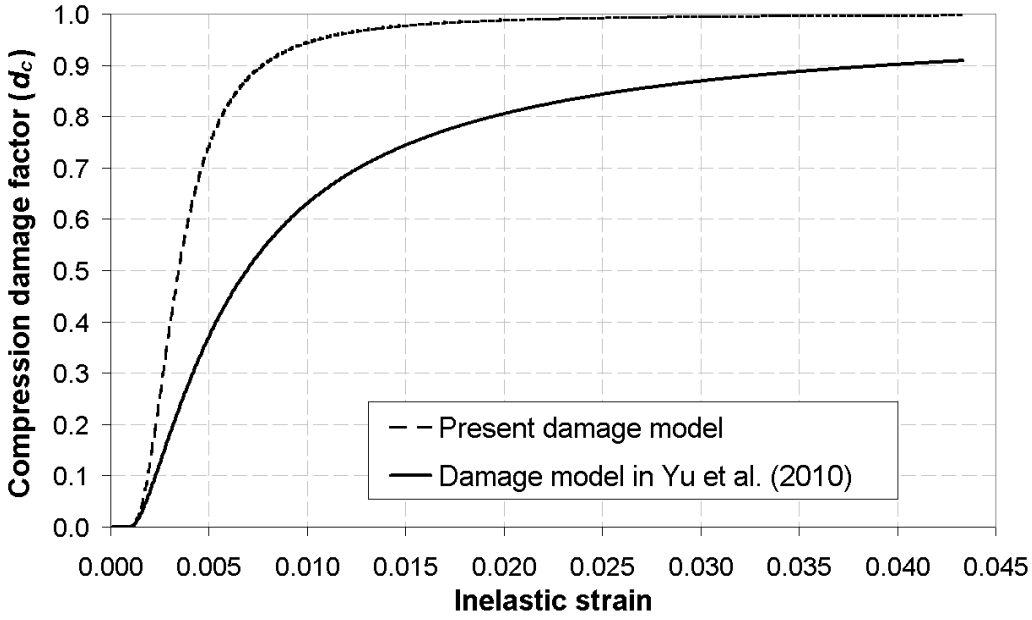

Figure 4.7 Different damage models in compression for specimen II-5 in Yao et al. (2005)

The FE results from the different damage models are shown in Figure 4.8. It is clear that the prediction from the present model is in most close agreement with the test results compared with the other models. It may be noted that the early stage (<2kN) of the curve can be modelled well regardless of the damage model. This is because this is an almost all elastic stage so little damage occurs anyway. The simulation using Chen et al.'s (2011) model was terminated at an early stage due to convergence difficulties. The damage model proposed by Yu et al. (2010) over-estimates the bond strength if only the tensile damage is considered, but under-estimates if the damage model is used to describe both the compressive and tensile behaviour. The shear retention model based on Rots (1988) over-estimates the loading capacity as well. The model without considering any damage in both tension and compression behaviour is also under-estimates the loading capacity.

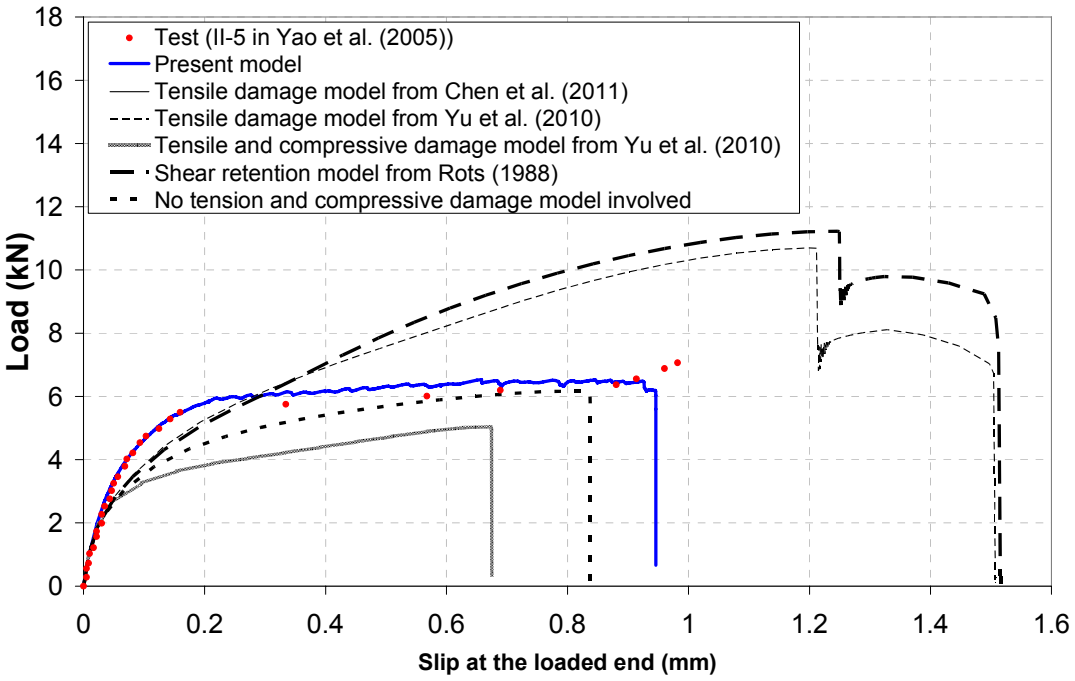

Figure 4.8 FE predictions from the different damage models

4. 6 Comparison of FE predictions with test results

The proposed FE model has been used to simulate all the 56 single shear tests reported in Yao et al. (2005) in which all the geometrical and material properties necessary for the FE modelling are available. It may be noted that Yao et al. (2005) reported a total of 72 tests but 16 of them failed in other modes rather than debonding in concrete so they were excluded in this study. The concrete cylinder strength for the specimens in Yao et al. (2005) varied from 19 to 27MPa. To increase the range of concrete strength, specimen No. 1 from Ali-Ahmad et al. (2006) and three specimens (S-CFS-400-25) from Wu et al. (2001) were further simulated. The concrete cylinder strength was respectively 38MPa for the former and 57.6MPa for the latter. Figure 4.9 shows that the FE predictions are overall in very close agreement with the 60 test data.

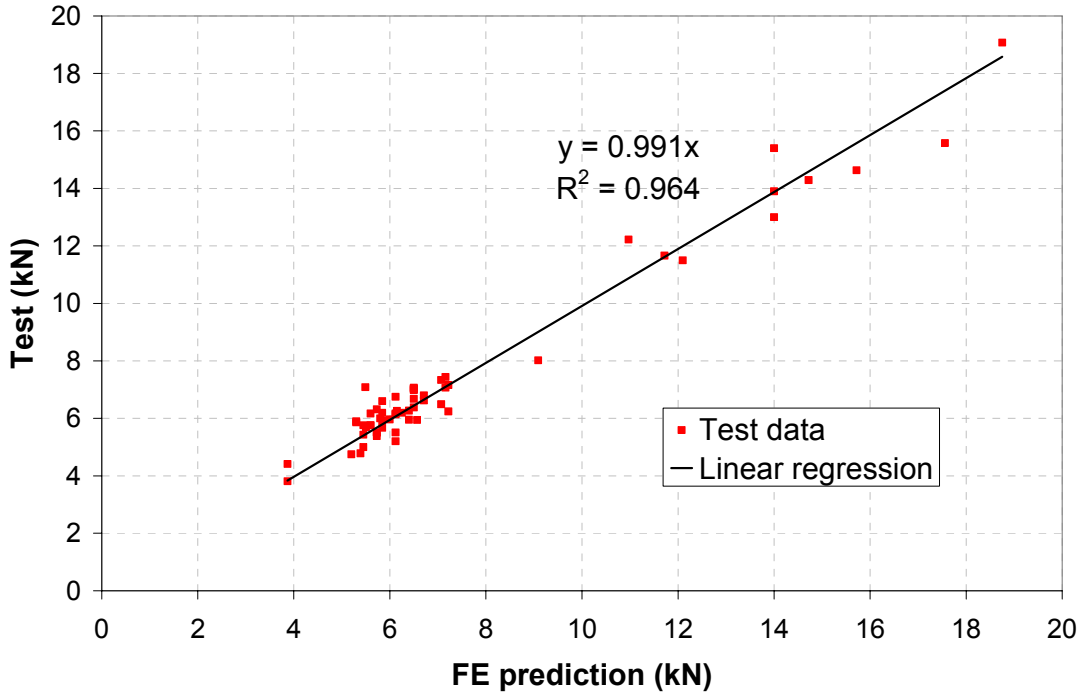

Figure 4.9 Comparison of FE predictions with test results

Figure 4.10 and 4.11 show the predicted and measured load-slip curve at the loaded end for two specimens: specimen II-5 in Yao et al. (2005) which had a concrete strength of 23MPa and specimen No. 1 in Ali-Ahmad et al. (2006) which had a concrete strength of 38MPa. Clearly the predictions are in close agreement with the test data for both specimens in the whole loading range. The loading capacities from both the FE prediction and test are also in close agreement with those predicted from Chen and Teng's (2001) bond strength model which are 6.02kN for specimen II-5 in Yao et al. (2005) and 10.44kN for specimen No. 1 in Ali-Ahmad et al. (2006).

For the reference specimen II-5 in Yao et al. (2005), a number of points on the FE predicted load-slip curve (marked Point A-I in Figure 4.10) are chosen to investigate the debonding process. Figure 4.12 shows the damage contours in the concrete. It

may be noted that the damage is directly related to the cracking strain so the damage contour represent closely the cracking pattern in the concrete.

Concrete at the loaded end exhibits softening in a small zone directly under the FRP when the load is 30% of the ultimate load (Figure 4.12b). The length of this small softening zone has been about doubled and its depth significantly increased when the load increases to about 60% (Figure 4.12d). Micro-cracks start to form with an angel of about 45° to the horizontal. A macro crack only appears when the load is about 90% of the ultimate load (Figure 4.12f) and debonding starts to propagate rapidly thereafter towards the free end of the FRP (Figure 4.12g – 4.12i) leading to the total separation of the FRP plate from the concrete (Figure 4.12j).

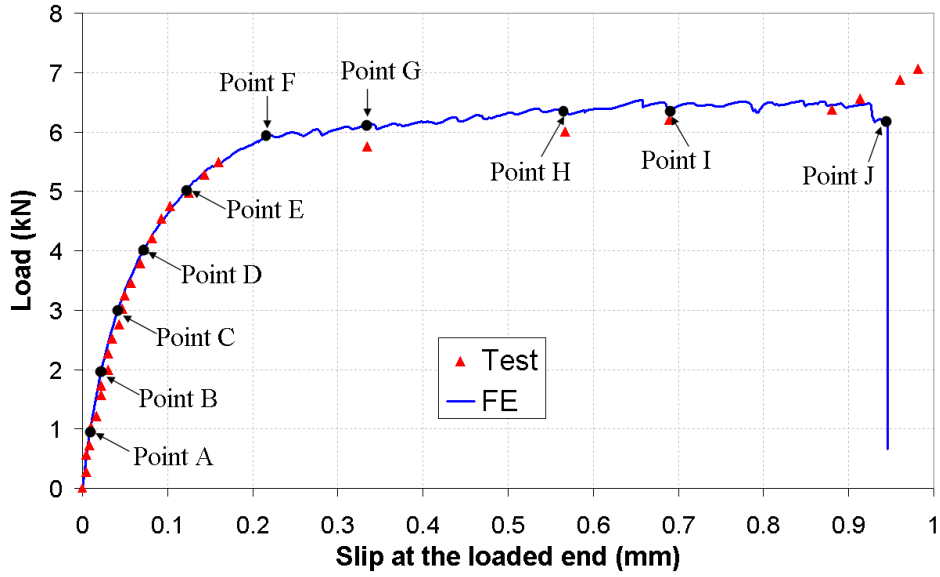

Figure 4.10 Comparison of FE prediction with test for specimen II-5 in Yao et al. (2005)

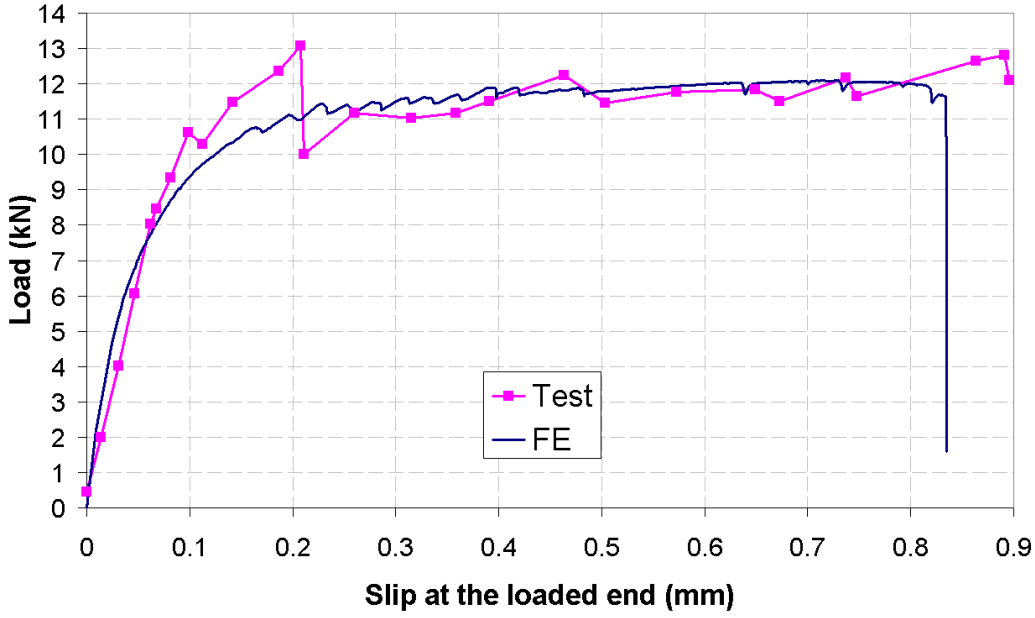

Figure 4.11 Comparison of FE prediction with test for specimen No. 1 in Ali-Ahmad et al. (2006)

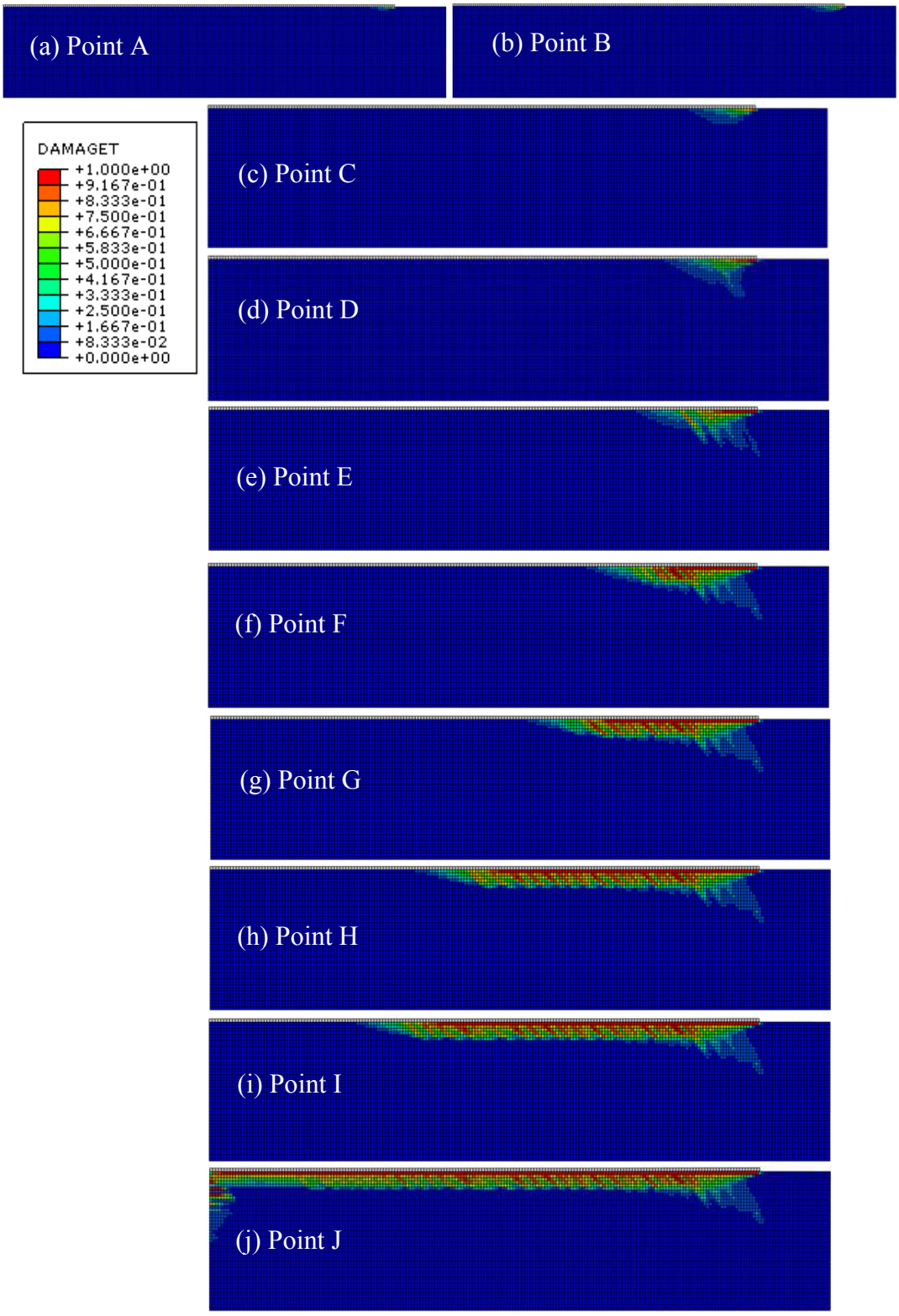

Figure 4.12 Predicted crack pattern at different stages: specimen II-5 in Yao et al. (2005)

It is of interest to note that although the slope (stiffness) reduces rapidly when the load exceeds about 90% of the ultimate load, the load does still increase slowly, that is, there is a lack of the horizontal plateau in contrast with the analytical predictions such as Yuan et al. (2004). This implies that a longer bond length does increase the loading capacity even if it is longer than the effective bond length. This phenomenon may be explained by the different material constitutive models employed in the different analyses. Typically a bi-linear bond-slip model was assumed in analytical analyses such as Yuan et al. (2004). The model assumes that the interface does not resist any stress once the slip exceeds the critical value, leading to a horizontal plateau when the bond length is large. In the present FE analysis, although the tensile stress also reduces to zero when the strain reaches a critical value (Figure 4.3), ABAQUS (and many other FE packages) does not allow the tensile stress do fall below 1% of f_t for numerical stability. Therefore, the difference between the analytical solution and the FE prediction is due to the difference in the assumptions adopted. It is thus difficult to say which one is more close to reality but from test data for both specimens in Figure 4.10 and Figure 4.11 show that the load increase slowly when deformation even at large slip.

4. 7 Bond stress distribution and local bond slip relationship

The local interfacial bond stress can be calculated based on the axial stress in the FRP plate from Eq. 4-19:

$$\tau = \frac{d\sigma_f}{dx} t_f \tag{4-19}$$

where σ_f is the axial stress in the FRP plate and t_f is the thickness of the FRP plate. The local bond stress distribution obtained using Eq. 4-19 for specimen II-5 in Yao et al. (2005) corresponding to different points on the load-slip curve (Figure 4.10) is shown in Figure 4.13. Large fluctuations in those curves can be contributed to the effects of the interfacial cracks in concrete.

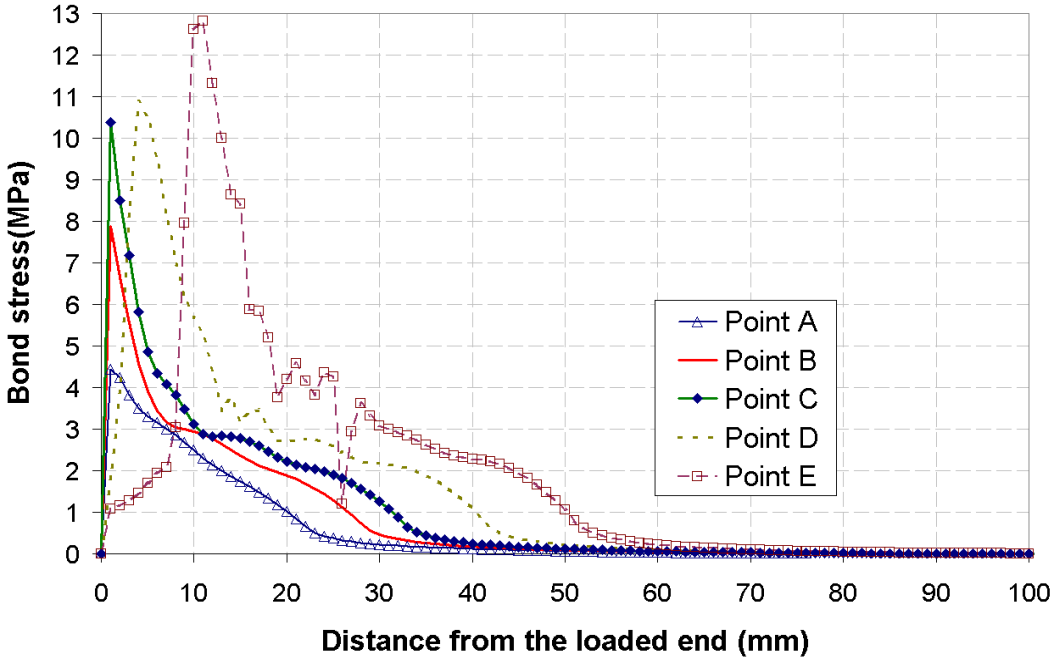

(a) Point A-E

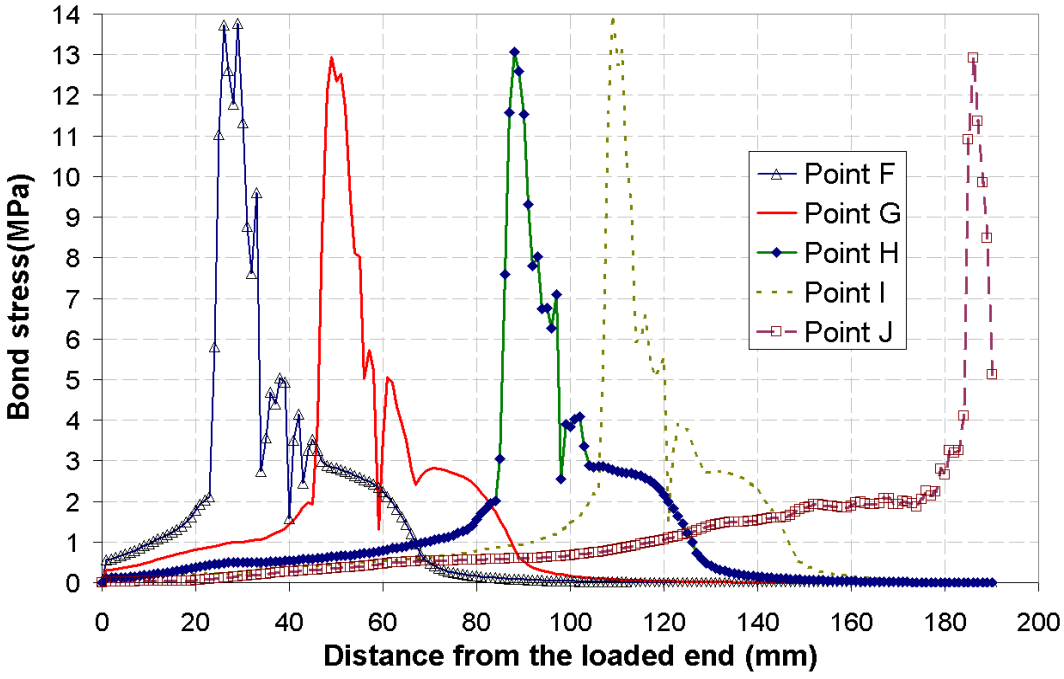

(b) Point F-G

Figure 4.13 FE Bond stress distribution at different points for specimen II-5 in Yao et al. (2005): (a) Points A-E on load-slip curve; (b) Points F-J on load-slip curve

Figure 4.13a shows the bond stress distribution at the early stage of loading (Point A – Point E). A range named as effective bond zone is defined as the interface with significant bond stress. As load increasing, the bond stress increases and the effective bond zone expands. It is noticed that the bond stress at the loaded end decrease when the local bond stress approaching the bond strength (point D and E on Figure 4.13a), indicating that macro cracks had formed. The effective bond zone continuously expands towards the free end because of the propagation of the macro cracks and the bond stress at the loaded end is negligible (Figure 4.13b). The effective bond length, which is defined as the bond length beyond which the ultimate load does not increase, calculated by the model proposed by Chen and Teng (2001) is 94mm for this specimen. The length of the effective bond zone at points G, H, I and J from the bond stress distribution approximately match with it.

The local bond-slip curve at a specified position along the bond interface can be extracted by plotting the smoothed bond stress at the position conjunction with the slip of that point. In order to obtain the reliable bond-slip curve, the smooth processing is needed to filter out the unstable local bond stress caused by the aforementioned interfacial cracks in the concrete, without eliminating the characteristic of the bond stress distribution. Two example of smoothed bond stress distribution curves (Point C and Point G) are shown in Figure 4.14. As the same processing, bond stress distribution curve at each loading stage was smoothed, and eventually the local bond-slip curve for a given position can be extracted as shown in Figure 4.15 and Figure 4.16.

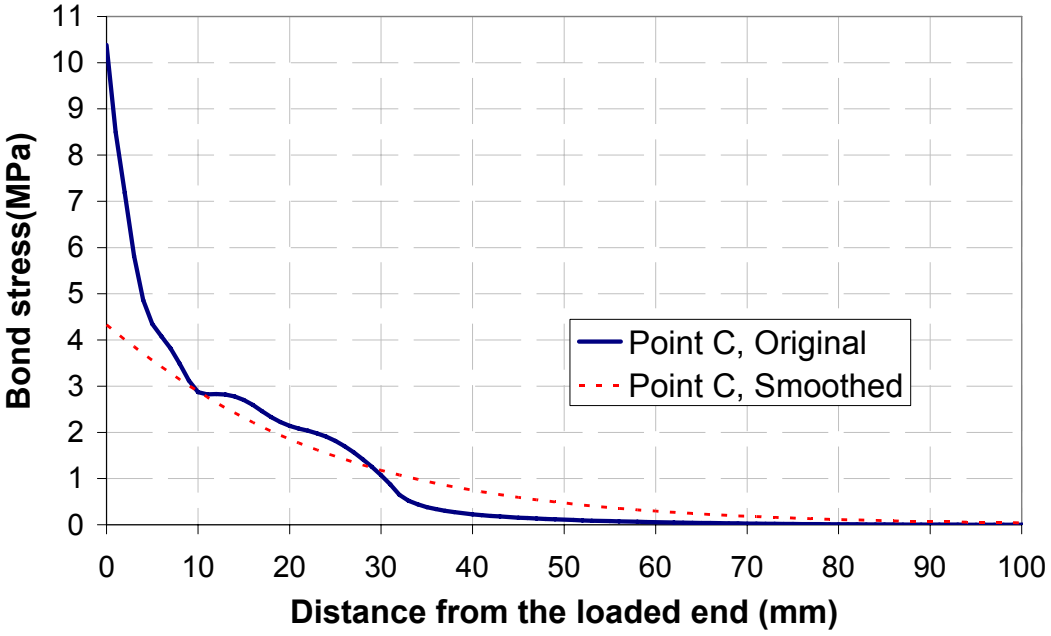

(a)

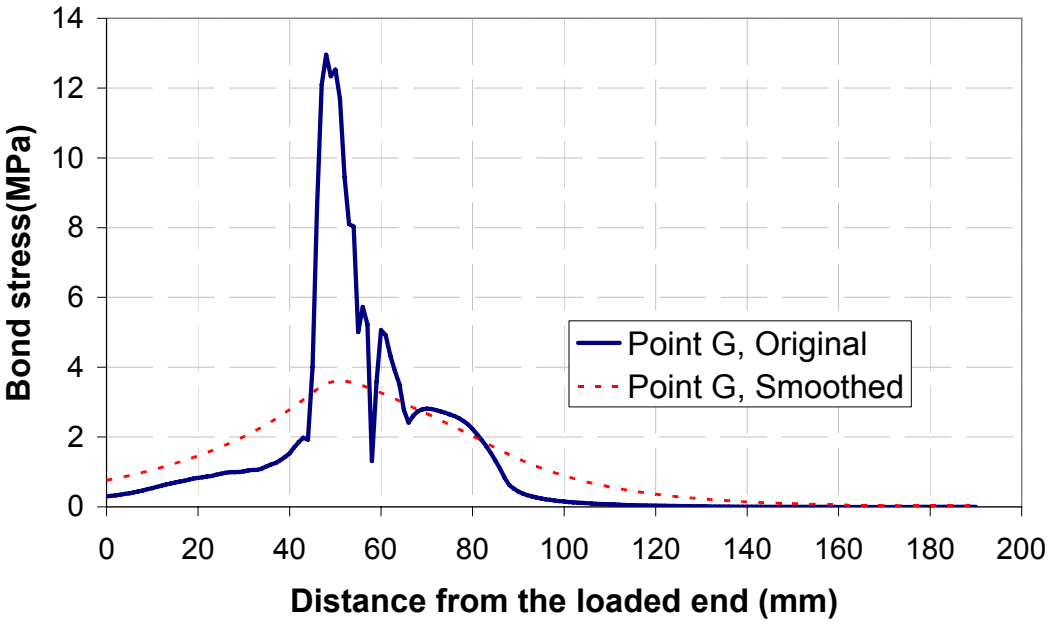

(b)

Figure 4.14 FE bond stress distribution at different point including smoothed bond stress: (a) Point C; (b) Point G

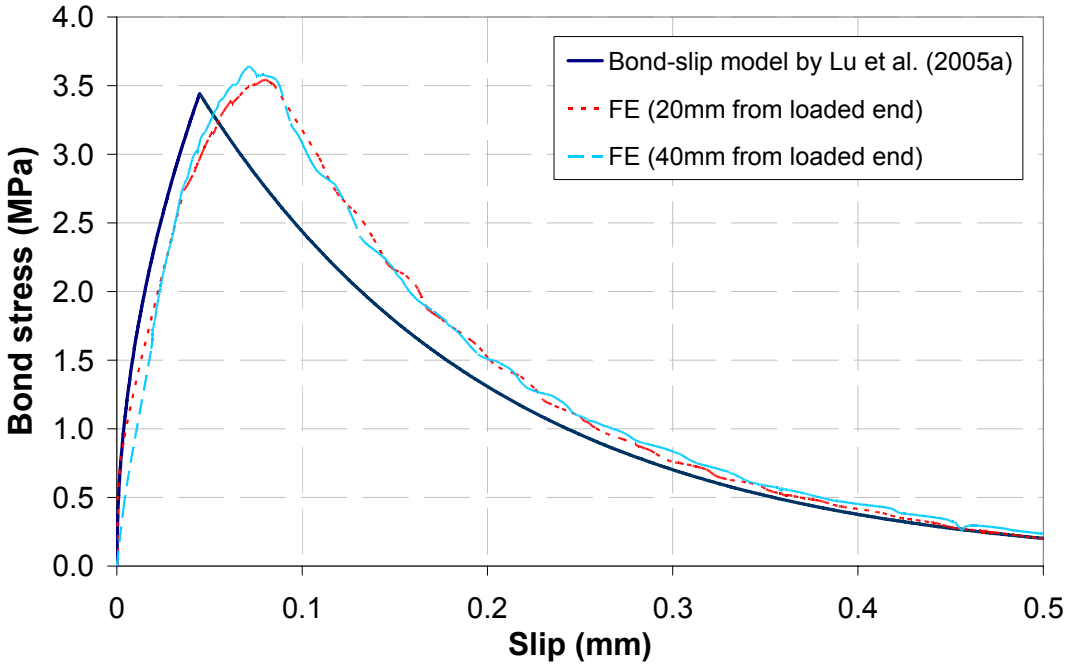

Figure 4.15 Local bond-slip curves for specimen II-5 in Yao et al. (2005)

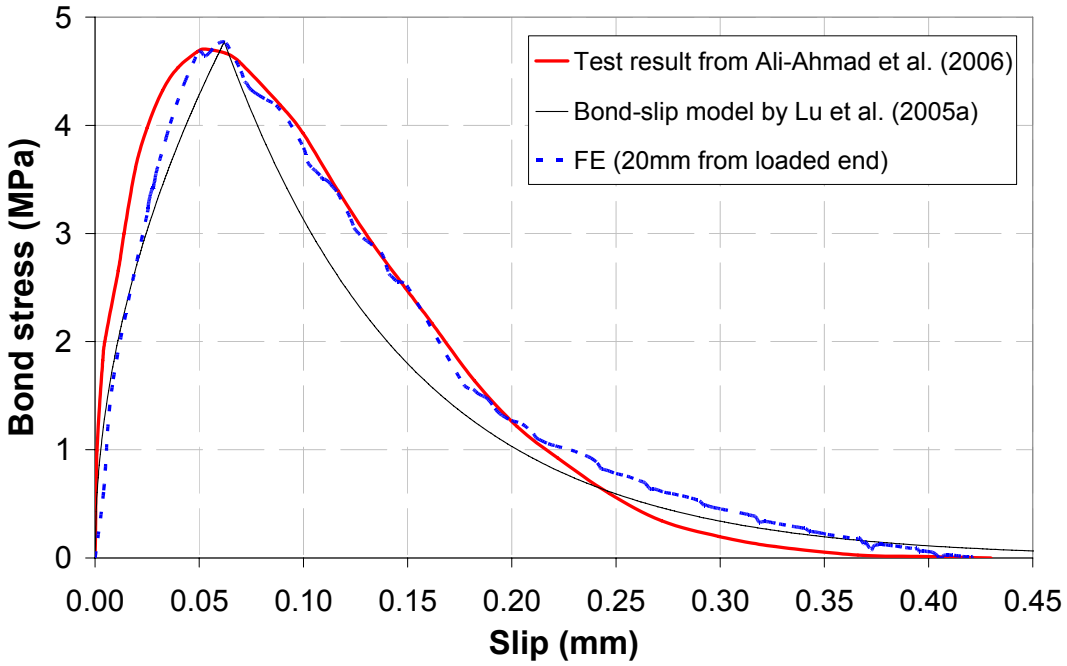

Figure 4.16 Local bond-slip curves for specimen No. 1 in Ali-Ahmad et al. (2006)

It is clearly that the local bond-slip curves extracted from proposed FE model are

close agreement with the test for specimen No. 1 in Ali-Ahmad et al. (2006) (Figure 4.16), close agreement for both specimens II-5 in Yao et al. (2005) and No. 1 in Ali-Ahmad et al. (2006) compared with the bond-slip model proposed by Lu et al. (2005a) (Figure 4.15 and Figure 4.16). The local bond slip curves from different positions, 20 mm and 40 mm from the loaded end for specimen II-5 in Yao et al. (2005), are identical which implies the proposed model can successfully capture the local bond behaviour as shown in Figure 4.15. The fracture energy of the interface, extracting from the area under local bond-slip curve, from the proposed FE model is larger than that from Lu et al. (2005a) model for both specimens because the predicted failure load from FE is larger than that from the bond strength which Lu et al. (2005a) used, such as Chen and Teng (2001).

4. 8 Parametric study

There are several parameters in terms of geometry variations in the pull-off test have influences on the results, such as the bond length L_{frp}, height of free concrete edge h_c and width of FRP. The former two variables will be studied in the following section except the FRP width effects because of the plane stress assumption used in the present model.

4.8.1 Influence of the FRP bond length

As aforementioned, the effective bond length is defined as the bond length beyond which the ultimate load does not increase (Chen and Teng, 2001). The specimens group VII in Yao et al. (2005) were modelled to verify this concept and exam the

proposed FE model. The effective bond length for this group of test was 92mm based on Chen and Teng (2001). The bond length of specimens varied from 95mm to 240mm. Figure 4.17 shows the FE predictions for each specimen and Table 4-2 summarized the ultimate load from test, FE and Chen and Teng's (2001) prediction. It is clear that the ultimate load almost similar from the FE (Figure 4.17), indicating that the proposed model can successfully support the effective bond length theory. It is noticed that the ultimate load increase slightly as bond length increasing (Table 4-2).

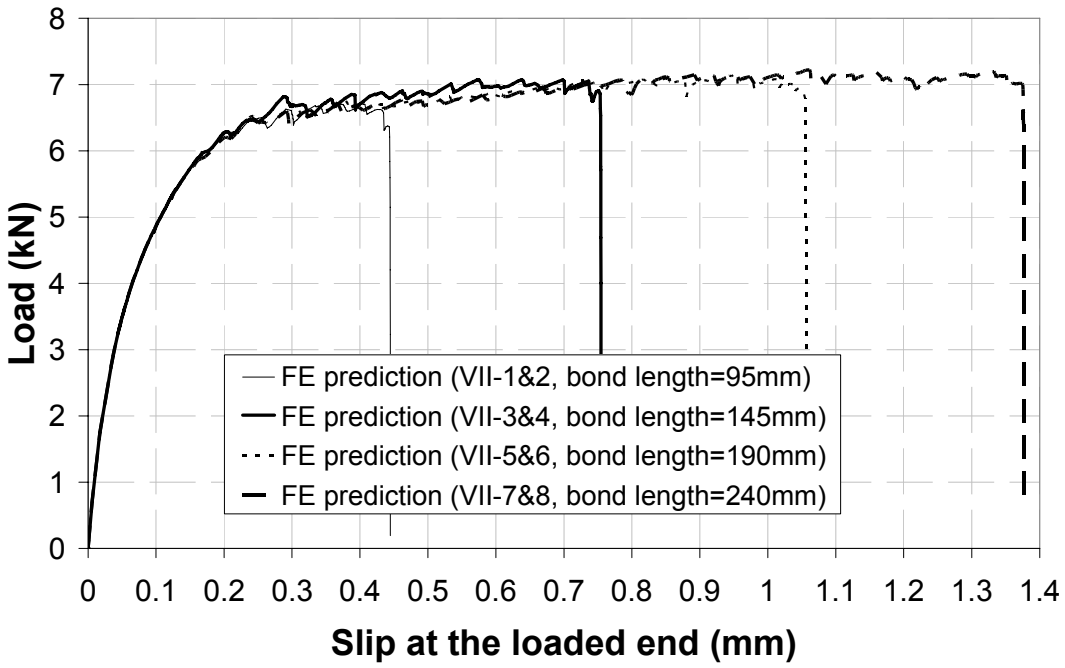

Figure 4.17 FE prediction for specimens group VII in Yao et al. (2005)

Table 4-2 Comparison of FE prediction with test and Chen and Teng's (2001) strength model for specimens group VII in Yao et al. (2005)

Specimens	L_{frp} (*mm*)	Test	[Average]	FE (*kN*)	Chen and Teng's (*kN*)
		(*kN*)			
VII-1	95	6.80	[6.71]	6.71	6.14
VII-2	95	6.62			
VII-3	145	7.33	[6.91]	7.07	
VII-4	145	6.49			
VII-5	190	7.07	[7.26]	7.16	
VII-6	190	7.44			
VII-7	240	7.16	[6.70]	7.20	
VII-8	240	6.24			

The incremental area under the load-slip curves corresponding to each bond length is almost constant when FRP bond length increases with same amount as shown in Figure 4.17, which may imply that the fracture energy to conduct debonding at the portion of FRP plate exceed the effective bond length is proportional to its length. It may be contributed to the constant local bond-slip relationship, and the fracture energy required is only related to the length of FRP plate.

4.8.2 Influence of the boundary conditions

The effects from different height of free concrete edge h_c on the bond strength were also investigated. The shorter height of the free concrete edge leads to local stiffness increasing at the loaded end, which will consequently result in an increased local stress transfer from FRP to the concrete, leading to early debonding and hence a reduced bond strength (Yao et al., 2005). The specimens IV-1, IV-5 and IV-7 with h_c

varying from 5mm to 30mm in Yao et al. (2005) were modelled to verify those findings. Figure 4.18 shows the load slip curves from the loaded end corresponding to each specimen. Table 4-3 summarized the results from test, FE prediction and Chen and Teng's (2001) model. It can be found that the ultimate load increases with the greater h_c values and the initial global stiffness decreases with greater h_c values. Both effects confirm the previous numerical (Chen et al., 2001) and experimental observations (Yao et al., 2005).

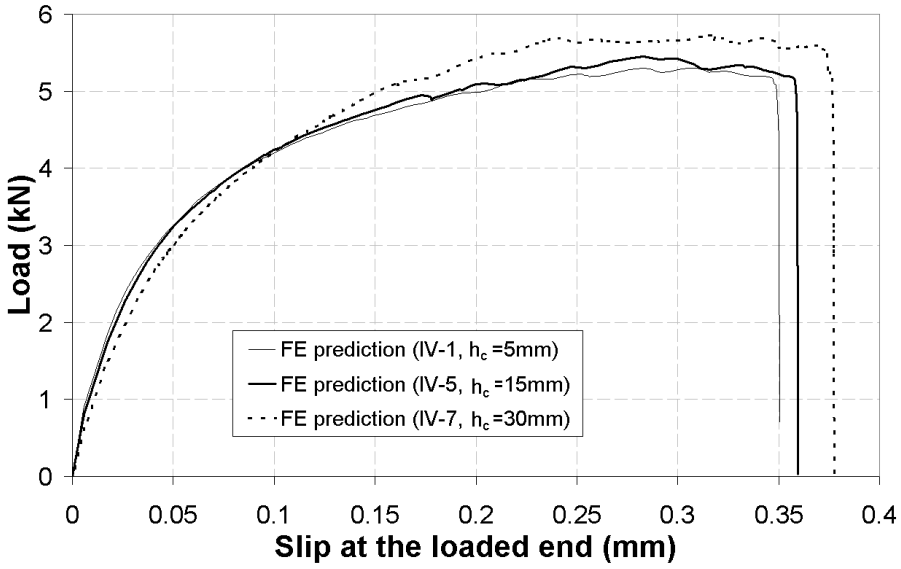

Figure 4.18 FE predictions for specimens IV-1, 5 and 7 in Yao et al. (2005)

Table 4-3 Comparison of FE prediction with test and Chen and Teng's (2001) model for specimens group IV in Yao et al. (2005)

Specimens	h_c (mm)	Test (kN)	FE (kN)	Chen and Teng's (kN)
IV-1	5	5.86	5.30	5.72
IV-5	15	5.00	5.45	
IV-7	30	5.50	5.70	

4. 9 Conclusions

A concrete damage model based on the plastic degradation theory has been proposed and implemented into the concrete damaged plasticity model to simulate the FRP-to-concrete bond behaviour in this chapter. The plastic degradation is used to describe the damage of the concrete after it enters softening in both tension and compression. The damage effects are modelled in terms of plastic strain rather than the stiffness degradation. The proposed model has been implemented in ABAQUS to model the FRP-to-concrete bond behaviour in the pull-off test. It has shown that the model can accurately predict the bond behaviour in the entire loading process and the numerical results are in very close agreement with test data from the literature. In addition, the geometrical parameters were studied and the findings are in good agreement with conclusions drawn in previous studies. The existing damage models were investigated their predictions compared with results from the proposed damage model, indicating that the proposed model delivers predictions in most close agreement with test data.

CHAPTER 5

FINITE ELEMENT MODELLING OF CONCRETE MASONRY ARCH BRIDGES WITH SAND BACKFILL

5. 1 Introduction

Masonry arch bridges have been a significant part of the transport networks in every historical age until nowadays. Understanding the behaviour of masonry arches is important for maintaining the transport networks. A comprehensive review on the masonry arch structures repaired by bonding FRP has been presented in Chapter 2. In the experimental study presented in Chapter 3, a 1/3 scale single-ring two span masonry arch bridge was tested in both original state and then strengthened with fibre reinforced polymer (FRP) to investigate the structural performance, as described in Chapter 3. The failure mode of the masonry arches is a hinge-mechanism, and the failure of the strengthened masonry arches was caused by debonding in the bond-joint between masonry and FRP followed by hinge mechanism.

Finite element method is a powerful tool to analyse structures and understand the local behaviour of structures. In order to compare the results from the test, and hence to analyse and understand the unstrengthened masonry structures in details. A numerical study on the original masonry arch bridge is presented in this chapter. An advanced model will be developed and used for the FRP strengthened masonry

arches in the next Chapter.

As mentioned in Chapter 2, there are three different modelling strategies for masonry structures: micro, micro-macro and macro models (Lourenço, 1996; Zucchini and Lourenço, 2004). The micro-model approach distinguishes the units and mortar, and also assigns a proper constitutive law to the interface between those two materials. The micro-macro model does not explicitly model the mortar, but simulates the unit-mortar interface and expanded unit dimensions. The macro-model approach models masonry as a homogeneous material with artificially low tensile strength. Both the micro model and micro-macro model can deliver a better understanding about the local behaviour of masonry structures, especially when the failure occurs at the unit (block or voussior)-mortar interface rather than in the unit itself. On the contrary, the macro model approach is applicable for the masonry structures with sufficiently large dimensions that the stresses across or along a macro length adopted in numerical model are essentially uniform. The details of each modelling approach were described in Chapter 2.

As mentioned in Chapter 2, the presence of the back-fill affects significantly the arch behaviour. The fill material increases the stability of arch, either directly by inducing additional compression in the arch, or indirectly by allowing a distribution of the concentrated forces over greater lengths and widths, and provides longitudinal restraint to the arch by its interaction with the surrounding soil medium (Betti et al., 2008; Fanning and Boothby, 2001). Because most fill materials are geo-materials, such as sand, clay, gravels, stones or mixture of them, different cohesive–frictional

plastic models have been adopted to model the constitutive behaviour of backfill in the previous research. For example, Mohr–Coulomb failure criterion with tension-cut-off (Cavicchi and Gambarotta, 2005; Cavicchi and Gambarotta, 2006; Cavicchi and Gambarotta, 2007), Mohr–Coulomb failure criterion (Drosopoulos et al., 2006), or Drucker-Prager failure criterion (Boothby and Roberts, 2001; Fanning and Boothby, 2001; Pelà et al., 2009). In 2-D models, the backfill was usually considered as a continuum under plane strain conditions (Cavicchi and Gambarotta, 2006; Drosopoulos et al., 2006).

Several constitutive models have been applied to describe the contact behaviour of the interface between backfill and masonry, such as, interface element with no-tension Coulomb yield criterion (Cavicchi and Gambarotta, 2007), interface element with traction-friction constitutive model in both normal and tangential directions (Cavicchi and Gambarotta, 2005; Cavicchi and Gambarotta, 2006), or unilateral contact-friction interface model (Drosopoulos et al., 2006). To summarise, the interface between extrados and backfill can be modelled by using an interface element with a traction-friction constitutive model or directly defining the contact properties.

This chapter presents a numerical study on the masonry arch bridge in order to achieve a deeper understanding of this type of structure and to develop an advanced model which can be used for modelling of FRP strengthened masonry arch bridges as described in the next chapter. A total of four FE models for masonry arches are developed by adopting different modelling strategies. The behaviour of masonry arch,

including the load capacity, mechanisms, and the contact behaviour between backfill and arches are investigated. The effects of several key parameters involved in the models are analysed as well.

5. 2 FE model

The two-span masonry arch bridge test as described in Chapter 3 is modelled as a 2-D plane strain problem (Figure 5.1) using the commercial FE software package ABAQUS (2007). The whole two-span bridge was modelled because the external load was only applied to a single span in each test so the problem was unsymmetric. Because the loading conditions were the same on each span, modelling one loading case was sufficient.

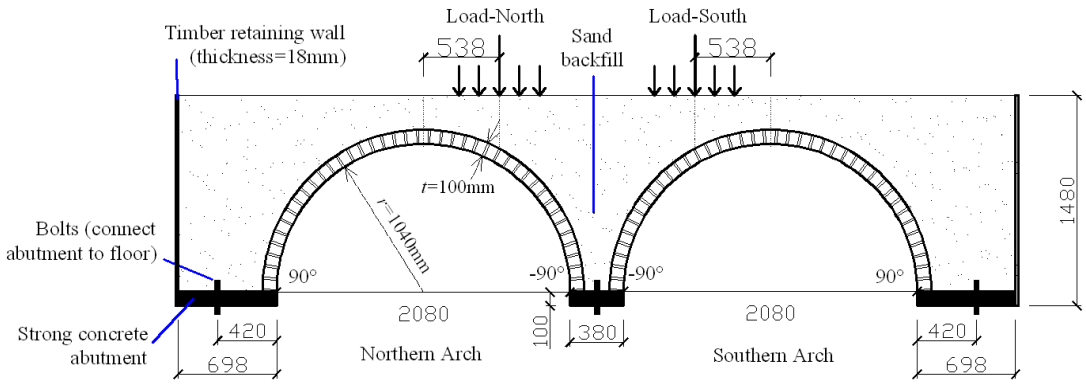

Figure 5.1 Schematic arch model (mm)

The loading on the masonry arches was a combination of its self-weight and the applied load. The load was directly applied to the backfill in the width of 570mm as the width of loading plate. The displacement control method and implicit steady-state dynamic analysis method were adopted to avoid the numerical convergence problem.

5.2.1 FE model description

In the FE model, the timber spandral walls and concrete abutments were modelled as well as arches and sand backfill. The interaction between the sand and the arches, and between the sand and the timber retaining walls, were all included in the models. A model included the loading plate was also conducted to investigate if its presence has any significant effect. The interaction between the sand and the loading plate was also included in the model with loading plate.

In terms of the boundary conditions, the abutments were assumed to be restrained in all directions because they were connected to the strong floor using six steel bolts (Φ=38mm), as shown in Figure 5.1. The timber spandral walls at both ends of the bridge were securely connected to the side walls. Substantial supports of the end walls were provided by an arrangement of steel beams which were bolted to the floor (Prentice, 1996). These steel beams were placed at the top and the bottom of the walls. Despite of this, the boundary at the both ends was not a fully restrained, and might deform laterally. This deformation of end walls was observed during the test and led to a gap between the abutment and the timber walls, consequently some sand leaked out from this gap. The timber end walls were thus considered to be partially restrained laterally using springs, modelled using the spring element (SPRING 1) in ABAQUS (2007). A 330 mm height from the bottom (as the width of steel beam) and the top node were restrained. The timber wall was treated as an elastic plate with three simple support edges and one edge free. A unit load (F) was applied onto the centre line of the elastic plate and the deflections (δ) can be calculated using the

theory of elastic plate. The stiffness of the springs thus can be predicted by $k=F/\delta$.

5. 3 Modelling of masonry arches

A total of four models were used to simulate the masonry arches. The model using the macro modelling strategy is referred as the homogeneous model in this chapter because this approach treats masonry as a homogeneous isotropic continuum without distinguishing the masonry units and mortar. A traction-opening and a damaged plasticity constitutive model were used to simulate the mortar interface and referred as the meso-interface model in this chapter because they use zero thickness interface elements. A detailed solid model, which models the actual units and mortar with smeared interfaces using solid elements, was finally developed to overcome the drawbacks of both homogeneous and meso-interface models. The details of each model are summarized in Table 5-1 and shown in Figure 5.2. The main difference between these models is how to actually capture the behaviour of the unit-mortar interface which dominates the failure mechanism of masonry arches. This section describes the details of each masonry model, including the modelling strategy and the constitutive laws.

Table 5-1 Models developed in the present study

<table>
<tr><td colspan="2" rowspan="2">Model</td><td colspan="2">Brick units</td><td colspan="2">Mortar and interface</td></tr>
<tr><td>Unit size</td><td>Constitutive model</td><td>Representation</td><td>Constitutive model</td></tr>
<tr><td colspan="2">Homogeneous model</td><td>NA</td><td rowspan="4">Concrete damaged plasticity model</td><td colspan="2">Not modelled explicitly</td></tr>
<tr><td rowspan="2">Meso-interface model</td><td>Traction-opening interface model</td><td rowspan="2">Actual size + mortar thickness</td><td rowspan="2">Zero thickness interface element</td><td>Traction-opening model</td></tr>
<tr><td>Damaged plasticity interface model</td><td>Damaged plasticity model</td></tr>
<tr><td colspan="2">Detailed solid model</td><td>Actual unit dimensions</td><td>Solid element with actual mortar thickness</td><td>Concrete damaged plasticity model</td></tr>
</table>

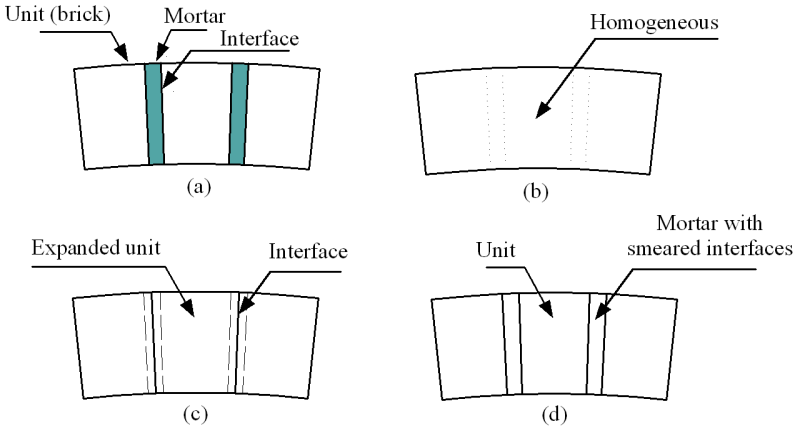

Figure 5.2 Modelling strategies for masonry: (a) local details of masonry work; (b) homogeneous model; (c) meso-interface model; (d) detailed solid model

5.3.1 Homogeneous model

This section describes the FE model of masonry arches using the homogeneous model. The key characteristics of homogeneous model are that no unit-mortar

interface is modelled and a weaker tensile strength is assumed to be smeared into the whole masonry arch. It means that the masonry is treated as a homogeneous material.

5.3.1.1 FE model description

Apart from the contact interactions and boundary conditions introduced in the previous section, the arches were modelled under a plane strain condition using ABAQUS (2007). All components including the arches, timber walls, sand and abutments, were modelled using the four node plane strain element with four integration points (CPE4). The average element size of masonry is 20×20mm^2. The other components of the structure (sand, abutments and timber walls) have matched mesh with the arch. The FE mesh is shown in Figure 5.3.

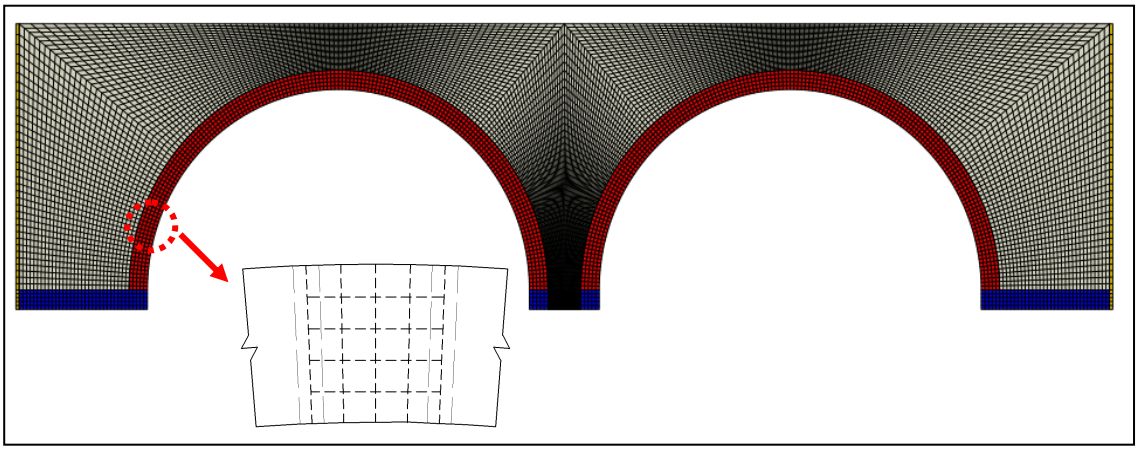

Figure 5.3 FE model of the homogenous model

5.3.1.2 Constitutive models

In the homogeneous model, the tensile strength of the masonry is very small because

it represents the tensile strength of the unit-mortar interface, which is quite weak due to the negligible adhesion between the masonry unit and mortar. The masonry was modelled using a concrete damaged plasticity model available in ABAQUS (2007). It is because the behaviour of the mortar-joints under tension showed a similarly behaviour to that of concrete (Lourenço et al., 1995; Pluijm, 1997). Parameters obtained from the test or determined according to previous studies are shown in Table 5-2.

Table 5-2 Material properties for the homogeneous model

Materials	Parameters	values	References
Masonry	f_{cm} (Compressive strength)	25 MPa	Test; Robinson (2000) tested on the same arches
	f_{tm} (Tensile strength)	0.1 MPa	
	E_m (Elasticity modulus)	16000 MPa	

The uniaxial compressive behaviour of masonry was modelled using the relationship proposed by Saenz (1964) for plain concrete:

$$\sigma_c = \frac{E_0 \varepsilon_c}{1 + \left(\frac{E_0 \varepsilon_p}{\sigma_p} - 2 \right) \left(\frac{\varepsilon_c}{\varepsilon_p} \right) + \left(\frac{\varepsilon_c}{\varepsilon_p} \right)^2} \tag{5-1}$$

where σ_c and ε_c are respectively the compressive stress and strain, σ_p and ε_p are the

experimentally determined maximum stress and its corresponding strain which are taken to be the compressive strength of masonry f_{cm} (MPa) and 0.002 respectively.

Tensile failure at the mortar-interface is brittle in nature. Therefore, it is difficult to conduct the full nonlinear behaviour of masonry under tension (Pluijm, 1997). In Pluijm (1997) it was shown that the descending branch of masonry under tension (for both units and mortar-interface) can be described with a formula developed by Hordijk (1991) for plain concrete:

$$\frac{\sigma_t}{f_t} = \left[1 + \left(c_1 \frac{w_t}{w_{cr}}\right)^3\right] e^{\left(-c_2 \frac{w_t}{w_{cr}}\right)} - \frac{w_t}{w_{cr}}\left(1 + c_1^3\right) e^{(-c_2)} \tag{5-2}$$

$$w_{cr} = 5.14 \frac{G_F}{f_t} \tag{5-3}$$

where w_t is the crack opening displacement, w_{cr} is the crack opening displacement at the complete loss of tensile stress, σ_t is the tensile stress normal to the crack direction, f_t is the uniaxial tensile strength, and c_1 =3.0 and c_2 =6.93 are constants determined from tensile tests.

There is still no widely accepted method for calculating the mode-I fracture energy of the mortar interface. In this study, mode-I fracture energy (G_F) was assumed to be estimated from the CEB-FIB (1991) model related to the compressive strength and maximum aggregate size d_a (assuming 20mm in this study):

$$G_F = (0.0469 d_a^2 - 0.5 d_a + 26)\left(\frac{f_c}{10}\right)^{0.7} \quad (5\text{-}4)$$

Based on the crack band theory introduced by Bažant and Oh (1983) as the Eq. 5-5, the stress-strain curve can be converted from the stress-crack opening displacement relationship and characteristic length of element.

$$w_t = h \int \varepsilon_{cr} \quad (5\text{-}5)$$

where h is the characteristic length of element and and ε_{cr} is the crack strain caused by the opening of cracks. The characteristic length of the chosen element (CPE4) is $\sqrt{2}e$ as Rots (1988) suggested, where e is the element length.

A damage model based on the plastic degradation theory was developed in Chapter 4 is applied here to describe the damage effects of masonry. The details about this damage model can be found in Chapter 4. A brief statement is introduced as follows.

The damage effects are generally characterized by the degradation of stiffness. ABAQUS (2007) uses an isotropic scaled damage model to describe the stiffness degradation, which can be represented by the under uniaxial loading:

$$\sigma = (1 - d) D_0 \bar{\varepsilon}^e \quad (5\text{-}6)$$

where σ and $\bar{\varepsilon}^e$ represent the stress and equivalent elastic strain in the loading

direction respectively; D_0 is the initial (undamaged) elasticity matrix and d is the damage variable. The current degraded stiffness D is defined as:

$$D = (1-d)D_0 \tag{5-7}$$

The damage model assumed that the ratio of the plastic strain with stiffness degradation to that without stiffness degradation, k, is proportional to the cohesion of the material. In case of uniaxial loading, this ration can be expressed as::

$$k = \frac{\bar{\varepsilon}^p}{\varepsilon^p} = \frac{\sigma}{f} \tag{5-8}$$

where $\bar{\varepsilon}^p$ and ε^p are the equivalent plastic strain (plastic strain with stiffness degradation) and total plastic strain (plastic stain without stiffness degradation) in the loading direction, respectively. The relationship between damage variable d and k may be defined as follows:

$$k = 1 - \frac{c}{c_{\max}} = 1 - \frac{\sigma}{f} \tag{5-9}$$

$$\bar{\varepsilon}^p = \varepsilon^p - \frac{d}{(1-d)}\frac{\sigma}{E_0} \tag{5-10}$$

$$d = \frac{(1-k)\varepsilon^p}{(1-k)\varepsilon^p + \sigma/E_0} \tag{5-11}$$

where c is the cohesion in the yield criteria which is proportional to stress σ, and c_{max} is proportional to the strength f (Lubliner et al., 1989). From, the Eq. 5-11, the damage variable d can be calculated. Both tensile and compressive states were considered including damage effects.

5.3.2 Traction opening interface model

The critical feature of the meso-interface models is that zero thickness interface elements used to simulate the mortar interface as shown in Figure 5.2. The size of the bricks needs to be expanded to include the mortar because the mortar is not explicitly modelled. Due to the mechanism failure caused by the tensile failure at mortar interface, the constitutive model of the mortar interface dominates the performance of the models. Two types of constitutive models may be classified from the literature as reviewed in Chapter 2. One is the traction-opening interface model by defining two failure modes together (Mode-I and Mode-II). The other is the composite interface model by combining plastic theories, usually including a tension cut-off criterion, a contact-fraction criterion and a compression cap criterion corresponding to different failure modes. Both types of interface model are developed and compared. Firstly, a traction-opening interface model is developed.

5.3.2.1 FE model description

The masonry arch was modelled by a combination of continuum elements (CPE4) for bricks and zero-thickness cohesive elements (COH2D4) for unit-mortar interfaces. The element size of the bricks was taken as that used in the isotropic model

($20\times20mm^2$) because the thickness of interface element is zero. The FE model and the mesh strategy are shown in Figure 5.4. The behaviour of unit-mortar interface controls the mechanism failure mode, thus the tensile behaviour (Mode-I) of interface is critical. The material properties of units were expected to have no effects on the performance of masonry arch model because failure occurs at the interfaces.

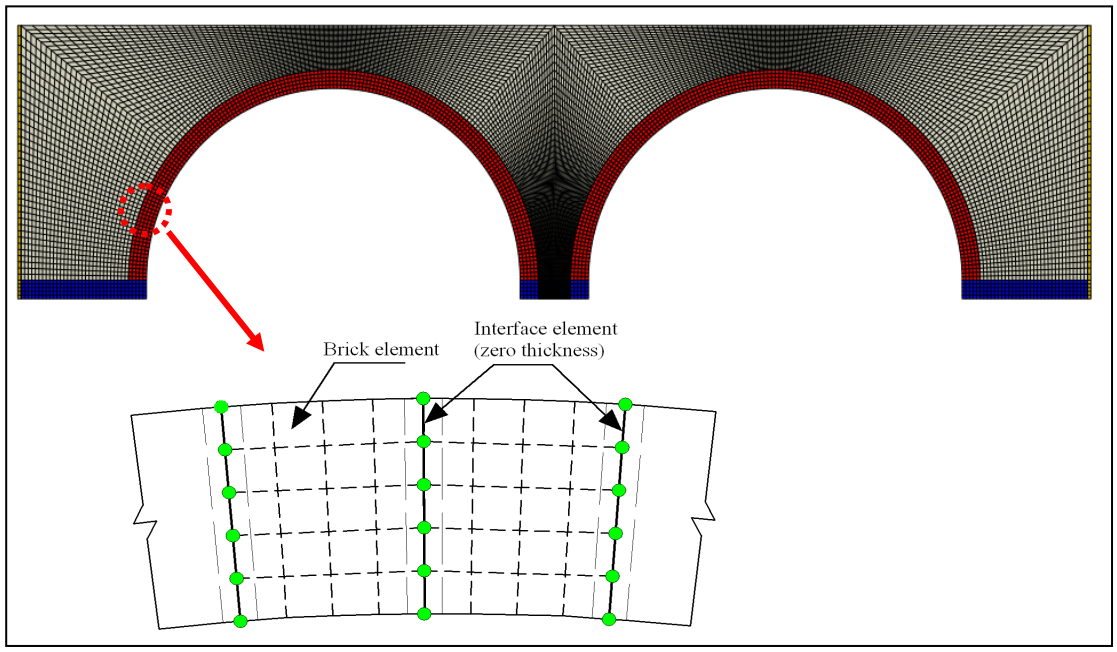

Figure 5.4 FE model of the meso-interface model

5.3.2.2 Constitutive models

The constitutive model of the brick is the same as that used in the homogeneous model, the concrete damaged plasticity model. The compressive behaviour of bricks is modelled using Eq. 5-1. The compressive strength of brick (58.2MPa) obtained from the test was adopted. The tensile behaviour of bricks was modelled using Eqs 5-2 to 5-5. The tensile strength of brick could be estimated based on the CEB-FIB

(1991) model:

$$f_t = 1.4\left(\frac{f_c - 8}{10}\right)^{\frac{2}{3}} \tag{5-12}$$

The constitutive model of the mortar interface is based on a mixed traction-opening law. The normal (Mode-I) and shear (Mode-II) behaviours, and the interaction between two modes are modelled using a damage law. The normal and shear stiffnesses of the interface are determined by homogenizing the composite material obtained considering an expanded unit and interface joint (Lourenço, 1996):

$$k_n = \frac{E_u E_m}{h_m\left(E_u - E_m\right)} \tag{5-13}$$

$$k_s = \frac{G_u G_m}{h_m\left(G_u - G_m\right)} \tag{5-14}$$

where E_u and E_m are the Young's modulus, G_u and G_m are the shear modulus, respectively, for unit and mortar and h_m is the actual thickness of the mortar. The average thickness of mortar was 18 mm measured from the test. The Young's modulus can be calculated from $E = 4730\sqrt{f_c}$ (MPa) following ACI (2002), where f_c is the compressive strength of concrete, if there is no test data available. The compressive strength of mortar was 12MPa which is obtained from BS 998-2 (2010) according to the mixture ratio of components used in the test.

The softening behaviour of each mode was described by the strength, the fracture energy and the evolution law for softening behaviour as shown in Figure 5.5. For mode I, the tension strength of the interface σ^0 was 0.1MPa, which was obtained from the test. The critical fracture energy G_{cn}^0 in mode I was predicted as the method proposed for the homogeneous model. A linear softening behaviour was adopted for simplicity.

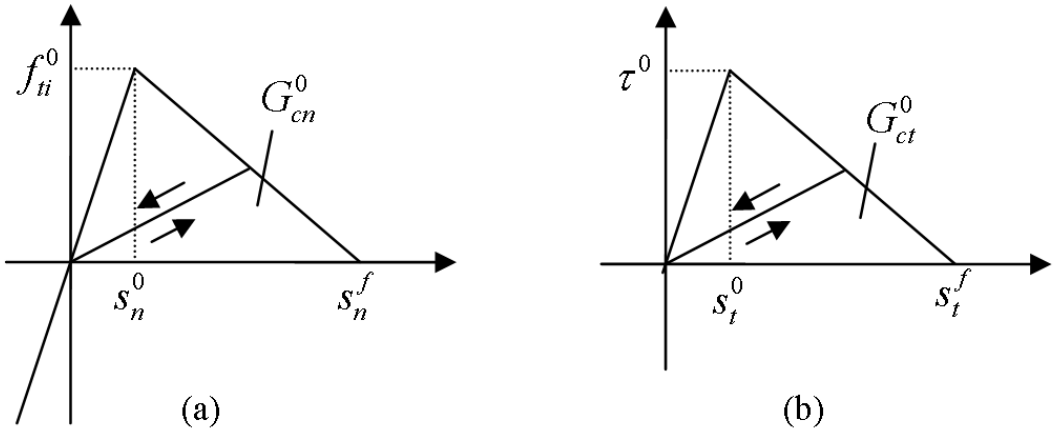

Figure 5.5 Normal (a) and shear (b) traction-opening displacement relationships for the traction-opening interface model

In terms of the shear (mode-II) behaviour, the initial shear strength τ^0 with non-confinement needs to be defined. In this masonry arch model, the shear strength with zero-confinement was 0.39MPa which was obtained from the mortar joint shear test described as in Chapter 3. The critical fracture energy of the mode II G_{ct}^0 was taken as 0.3Nmm/mm^2 as Sacco and Toti (2010) suggested if there is no test data. A linear law was adopted to describe the softening behaviour. The parameters used to define the material properties are summarized in Table 5-3.

Table 5-3 Material properties for the traction-opening interface model

Materials	Parameters	Values
Bricks	f_{cb} (Compressive strength)	58.2 MPa
	f_{tb} (Tensile strength)	4.1 MPa
	G_{fb}^{I} (Fracture energy)	0.12 Nmm/mm^2
Mortar-interface	f_{ti}^{0} (Tensile strength)	0.1 MPa
	G_{cn}^{0} (Mode-I fracture energy)	0.066 Nmm/mm^2
	τ^{0} (Initial shear strength)	0.39 MPa
	G_{ct}^{0} (Mode-II fracture energy)	0.3 Nmm/mm^2

The interaction between the two failure modes is modelled based on an initiation law and an evolution law available in ABAQUS (2007). A criterion based on the maximum nominal stress ratio is chosen to describe the initiation law as Eq. 5-15,

$$\max\left\{\frac{\langle\sigma\rangle}{f_{ti}^{0}},\frac{\tau}{\tau^{0}}\right\}=1 \tag{5-15}$$

where σ and τ are the normal and shear stress, respectively. The Macaulay brackets are used to signify that a pure compressive deformation or stress state does not initiate damage. This implies that the shear failure occurs once the shear stress

reaches the initial shear strength even if the interface is under compression.

A criterion based on the quadratic law of nominal fracture energy is chosen to model the evolution law of mixed-mode state as Eq. 5-16:

$$\left\{\frac{G_n}{G_{cn}^0}\right\}^2 + \left\{\frac{G_t}{G_{ct}^0}\right\}^2 = 1 \tag{5-16}$$

where G_n and G_t are the work done by the traction and its conjugate relative displacement in the normal and shear directions, respectively.

5.3.3 Damaged plasticity interface model

In term of the constitutive law of the mortar interface, except the traction-opening interface model, there is another modelling approach developed from plastic theories. The disadvantage of the traction-opening interface model proposed in Section 5.3.2 is that there is no increase in the shear stress if the interface is under compression, which is usually against the behaviour of the mortar interface. A concrete damaged plasticity model available in ABAQUS (2007) thus was used to model the mortar interface to overcome this weakness. Although this model is originally developed to model concrete, it is also appropriate for modelling the mortar interface because it is developed from the original Drucker-Prager model by considering the damage effects on the yield conditions and the flow rule.

5.3.3.1 FE model description

The same FE model as that for the traction-opening interface model (Figure 5.4) is adopted because only the constitutive law of interface is different between two models. The same interface element (COH2D4) is used.

5.3.3.2 Constitutive models

The brick was modelled in the same way as the traction-opening interface model. The constitutive law of the mortar interface is modelled by defining the compressive and tensile behaviour and a damage law. The compressive behaviour was modelled using Eq. 5-1. The compressive strength of the interface is chosen as the compressive strength of the mortar, 12MPa. A linear softening behaviour was applied to model the tensile behaviour of the interface as shown in Figure 5.6. The tensile strength of the interface f_{ti}^{0} and the mode-I fracture energy G_{cn}^{0} are the same as those used for the traction-opening interface model. The parameters used to define the material properties are summarized in Table 5-4.

Table 5-4 Material properties for the damaged plasticity interface model

Materials	Parameters	Values
Bricks	f_{cb} (Compressive strength)	58.2 MPa
	f_{tb} (Tensile strength)	4.1 MPa
	G_{fb}^{I} (Fracture energy)	0.12 Nmm/mm^2
Mortar interface	f_{ci} (Compressive strength)	12 MPa
	f_{ti}^{0} (Tensile strength)	0.1 MPa
	G_{cn}^{0} (Mode-I fracture energy)	0.066 Nmm/mm^2

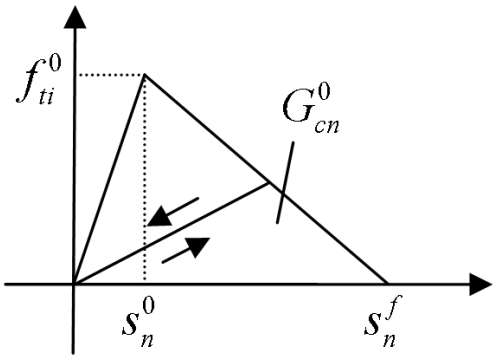

Figure 5.6 Tensile stress-opening displacement relationship for the damaged plasticity interface model

A damage model, as shown in Figure 5.6, was used to describe the tensile damage behaviour of the interface, indicating that the stiffness of the interface is back to the origin once the damage occurs.

5.3.4 Detailed solid model

It usually leads to numerical difficulties when the meso-interface model is used to simulate more complex structures, for example, when the zero thickness interface between FRP and masonry in the FRP strengthened masonry arch bridges meets the brick-unit mortar interface. The coordinates of four nodes of the element are same when two zero thickness interfaces intersect. This is not permitted in the numerical models. Therefore, a detailed solid model was developed to overcome this shortage. In the detailed solid model, the geometries of brick and mortar are actually modelled as shown in Figure 5.1. The behaviour of mortar interface is smeared into the mortar in order to accurately capture the feature of masonry arches, such as, negligible tensile strength at the mortar interface. The advantages of the detailed solid model are, firstly, keeping the accurate geometry of masonry components without smearing the weaker tensile strength into the entire arch; secondly, solid elements can be used to model both bricks and mortar interface instead of zero thickness interface elements.

5.3.4.1 FE model description

The bricks and mortar were modelled using plane strain element (CPE4) connecting with common nodes. The average element size for mortar was about 18mm×20mm. The average element size for brick was about 21mm×20mm. The FE model and the mesh strategy are shown in Figure 5.7.

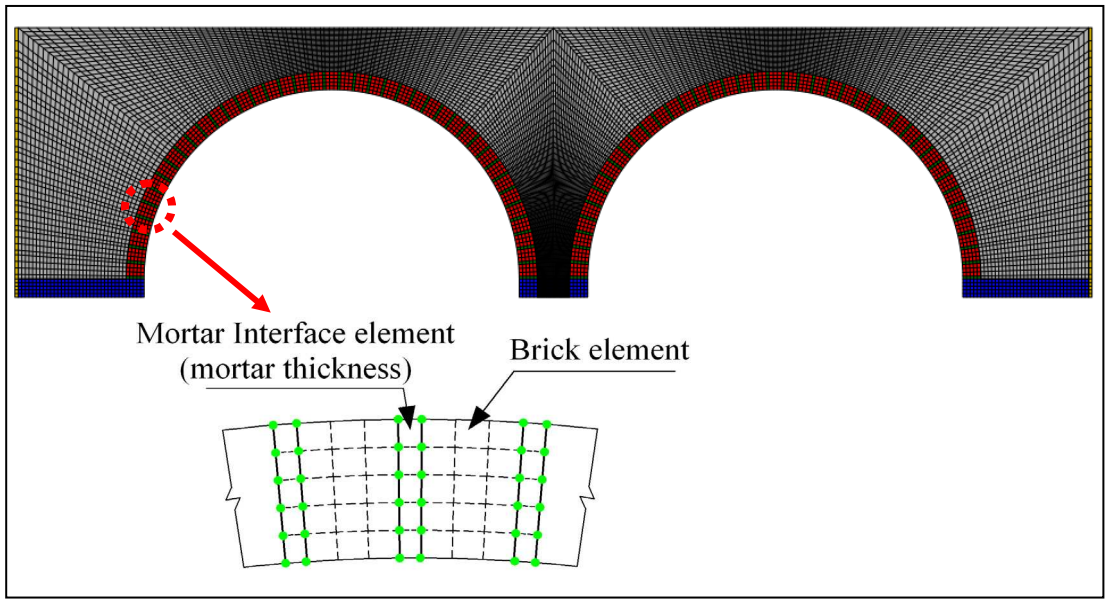

Figure 5.7 FE model of the detailed solid model

5.3.4.2 Constitutive models

The brick was modelled in the same way as the meso-interface model. The constitutive law used to model mortar-interface was the concrete damaged plasticity model available in ABAQUS (2007). The constitutive law of the mortar interface is modelled by defining the compressive and tensile behaviour and the damage laws. The compressive behaviour is modelled using Eq. 5-1. The compressive strength of the mortar interface was chosen as the compressive strength of the mortar: 12MPa. The tensile behaviour of mortar interface was modelled using Eqs 5-2 to 5-5. The damage model mentioned in Section 5.3.1.2 (Eqs 5-6 to 5-11) is used to describe the tensile damage effects. The parameters used to model the bricks and mortar interface are summarized in Table 5-5.

Table 5-5 Material properties for the detailed model

Materials	Parameters	Values
Bricks	f_{cb} (Compressive strength)	58.2 MPa
	f_{tb} (Tensile strength)	4.1 MPa
	G_{fb}^{I} (Fracture energy)	0.12 Nmm/mm^2
Mortar interface	f_{ci} (Compressive strength)	12 MPa
	f_{ti}^{0} (Tensile strength)	0.1 MPa
	G_{cn}^{0} (Mode-I fracture energy)	0.066 Nmm/mm^2

5. 4 Modelling of sand backfill and the contact interfaces

The sand backfill was modelled using the same plane strain element (CPE4). The behaviour of the sand backfill was modelled as an ideal Mohr-Coulomb material. The Mohr-Coulomb plasticity model was used to model sand backfill. The parameters requiring definition are the cohesion stress *c* and the friction angle *Φ* of the sand. Although sand is a cohesion-less material, a small cohesion stress is usually applied to avoid the numerical problem in the numerical modelling (Ai, 2010). In the present study, a cohesion stress of 100Pa was chosen because it is the smallest value which can successfully avoid numerical difficulties and achieve a converged solution. The friction angle of sand was obtained as 33º from the direct shear test. The

Young's modulus of sand was 10MPa as suggested by Fairfield (1994b), Prentice (1996) and Thavalingam et al. (2001) for the same sand. The density is 1520kg/m^3 as obtained from the test.

There are also two sets of contact pairs in all models, that is, contact between the sand and the masonry arches and contact between the sand and the timber retaining walls. All of these contact behaviours were modelled using a contact-friction model introduced in ABAQUS (2007) which uses a Coulomb friction model to simulate the contact shear behaviour. The frictional angle of all contact interfaces was assumed as the internal frictional angle of the sand backfill. The maximum elastic slip was assumed as 0.005mm. The parameters of the contact interfaces are summarized in Table 5-6.

Table 5-6 Parameters for contact interfaces

Contact pairs	Friction coefficient (tan(Φ))	Maximum elastic Slip mm
Arch-Sand	0.67	0.005
Sand-Timber wall	0.67	0.005

5. 5 Modelling of abutments and timber retaining walls

To simplify the model, the timber retaining walls and concrete abutments were modelled as linear elastic materials. The abutments were supported using strong floor and are effectively rigid. The parameters for timer walls and abutments are summarized in Table 5-7.

Table 5-7 Parameters for timber walls and concrete abutments

Materials	Parameters	values	References
Timber	E_{timber}	13 GPa	Yamasaki and Sasaki (2010)
Abutment	$E_{abutment}$	80 GPa	Effectively rigid

All the modelling parameters were summarized in Appendix 3.

5. 6 Results and Discussions

The results from different FE models are analyzed in this section. A mesh convergence analysis and a model simplification are firstly produced in order to finalize the models. The behaviour of masonry arches is then studied about their mechanism, loading capacity, and validation with classical mechanism analysis. The contact behaviour between backfill and arches is investigated as well.

As described in Chapter 3, the symmetric loading cases (Load-North & Load-South) were applied individually and the radial deflections at several locations (N1-N5 in the northern arch) recorded using LVDTs Figure 5.8. Each arch was loaded until a four hinge was mechanism established, and unloaded when it was deemed that the arches were approaching their loading capacities. The results from FE models are compared with that from the test on the northern arch because two arches showed the quite similar behaviour from the test.

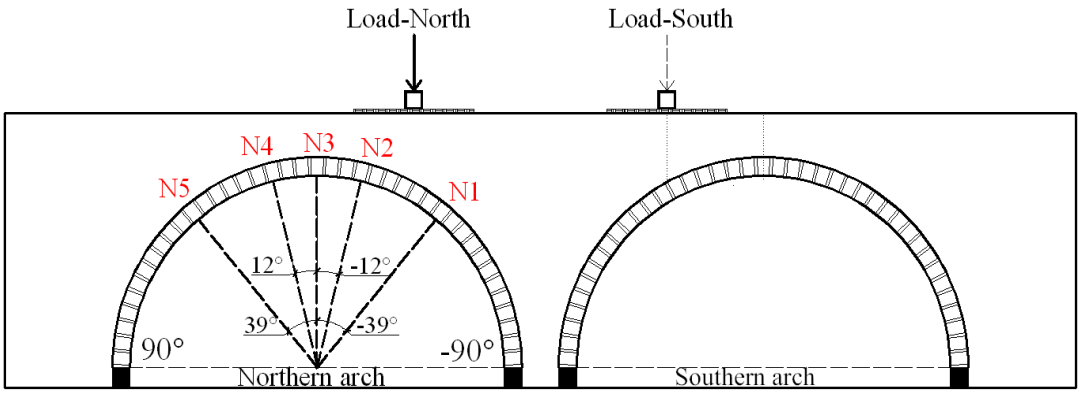

Figure 5.8 Schematic arch including load and instrumentation in the test

5.6.1 Mesh convergence and model simplification

The initial element size used for each model is summarized in Table 5-8. It indicates that all four models have almost same element size. The mesh convergence analysis is conducted based on the homogeneous model.

Table 5-8 Summary of the element size for FE models

Model		Average element size of masonry (mm×mm)	
		Bricks	Mortar interface
Isotropic model		20×20	
Interface model	Traction-opening interface model	20×20 with expanded brick dimensions	Zero thickness interface element
	Damaged plasticity interface model		
Detailed model		21×20 with actual brick dimensions	18×20 with actual mortar dimensions

Three different meshes were used to conduct the mesh convergence analysis. The results (Figure 5.9) indicates that the initial mesh (element size of masonry about

20mm×20mm) and fine mesh strategy (element size of masonry about 10mm×10mm) deliver almost identical results. Therefore, the initial mesh was chosen for further analysis based on consideration of accuracy and computational effectiveness.

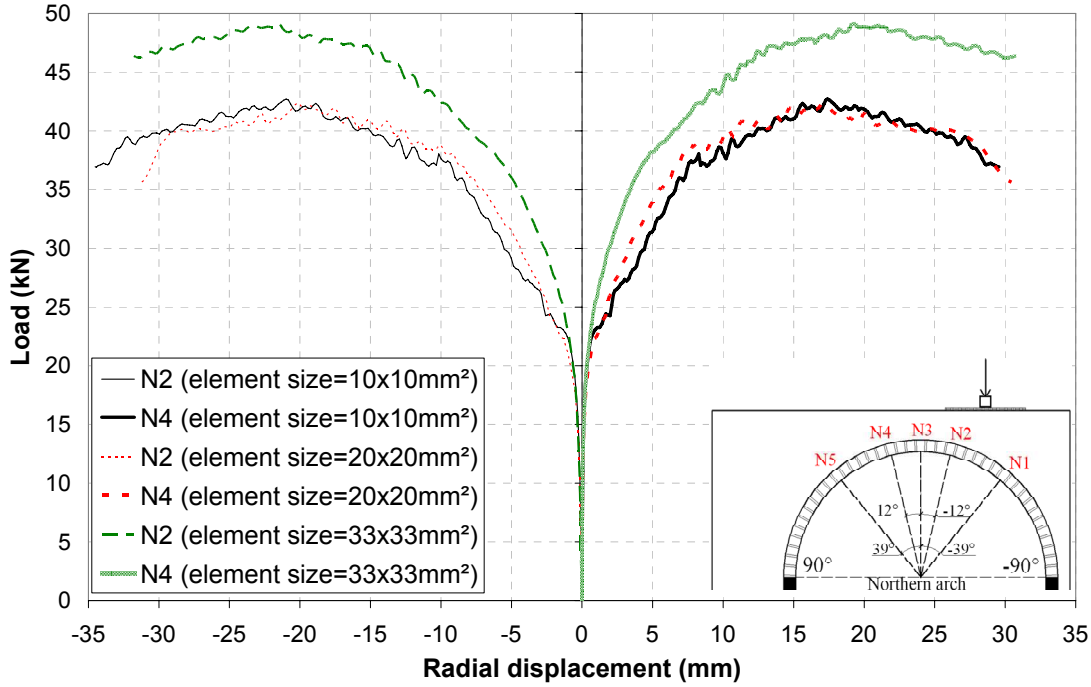

Figure 5.9 Results of the mesh convergence analysis

The results from the model with and without loading plate are compared in Figure 5.10. In the model without loading plate, the load was directly applied to the top of the sand backfill in the range of 570mm as the width of loading plate. The load was applied to the width of the steel loading beam (100mm) in the FE model including the loading plate. It can be found that both models lead to almost identical results, thus the presence of the loading plate has no significant effect. It is because that the loading range was same in both models. Meanwhile, the model including the loading plate requires more computational time. Therefore, the model without the loading

plate is used for the further analysis.

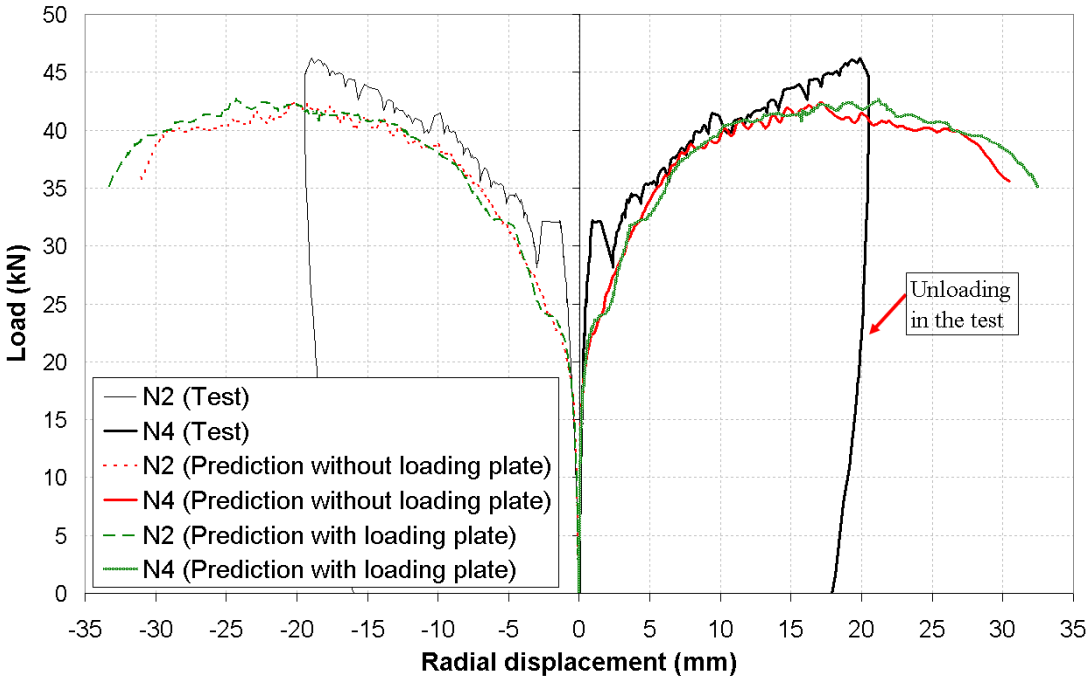

Figure 5.10 FE predictions from the model with and without loading plate

5.6.2 Loading capacity of arch

The formation of the hinge mechanism leads to the failure of arches. The loading capacity of the arch is thus dominated by the formation of the hinge mechanism. The loading capacity predicted from all of FE models are analysed in this section. The load-deflection responses obtained from the homogeneous model is shown in Figure 5.11, from the traction-opening interface model is shown in Figure 5.12, from the damaged plasticity interface model is shown in Figure 5.13, and from the detailed solid model is shown in Figure 5.14. The comparison of load deflection response at location N2 from all the FE models is shown in Figure 5.15. It is clear that all models can successfully capture the loading-deflection responses of the arch compared with

the test results.

The loading-capacity from the test was 46.2kN for the northern arch and 49.7kN for the southern arch. All models predict an ultimate loading-capacity close to that: about 43kN from the homogeneous model, about 50kN from the traction-opening interface model, 47kN from the damaged plasticity interface model and 48kN from the detailed solid model. The loading-capacity obtained from the homogeneous model is the lowest, which can be attributed to the weaker tension behaviour smeared into the whole arch. The traction-opening interface model delivered an unsafe prediction.

The initial stiffness of the arch, below 20kN, is similar for all models. The stiffness reduces once the cracks formed. Further loading increase leads to the development of cracks, and eventually reaches the ultimate load. After reaching the ultimate load, the deflections increases fast while the loading drops.

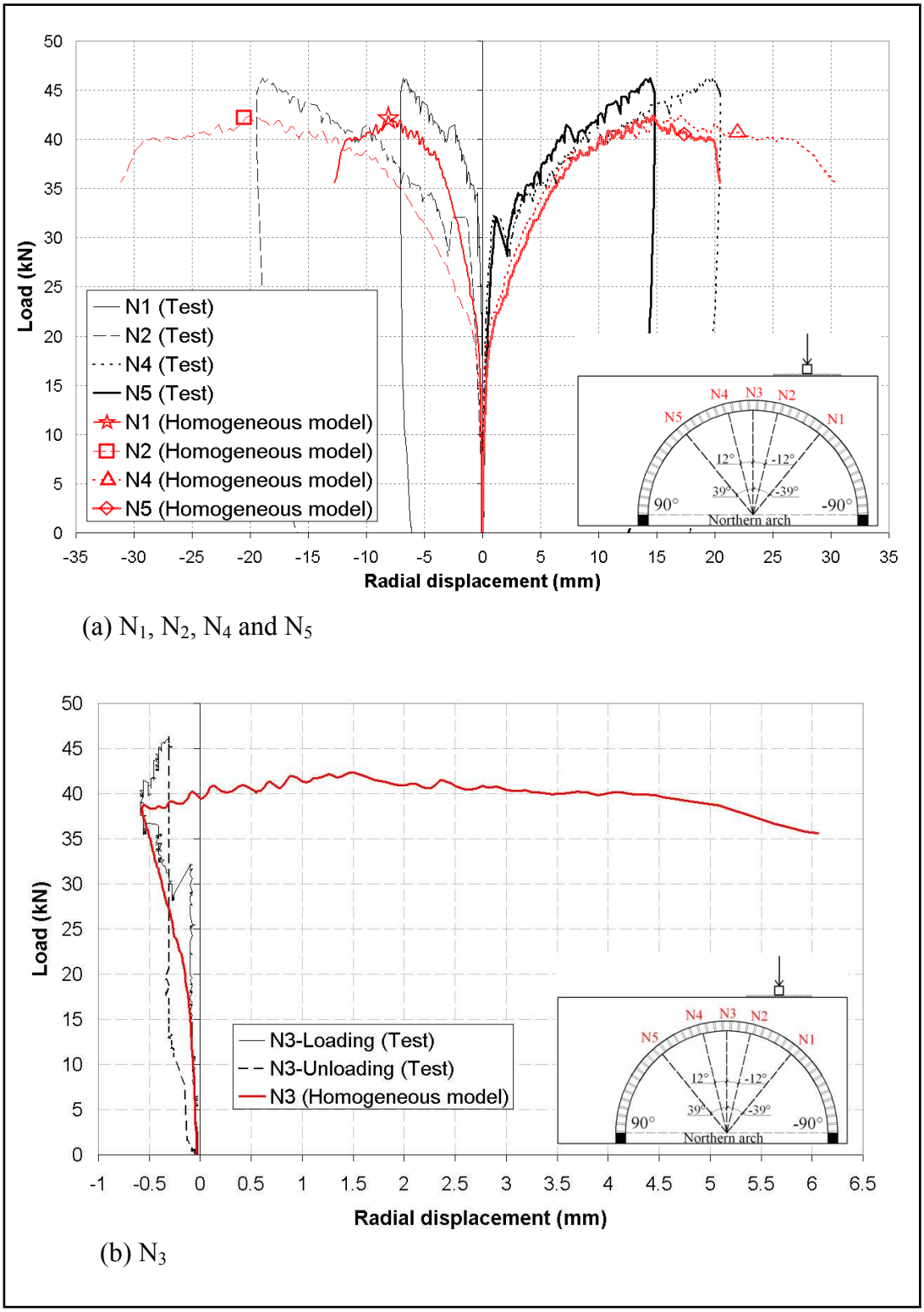

(a) N_1, N_2, N_4 and N_5

(b) N_3

Figure 5.11 Arch load-deflection curves: test vs homogeneous model prediction

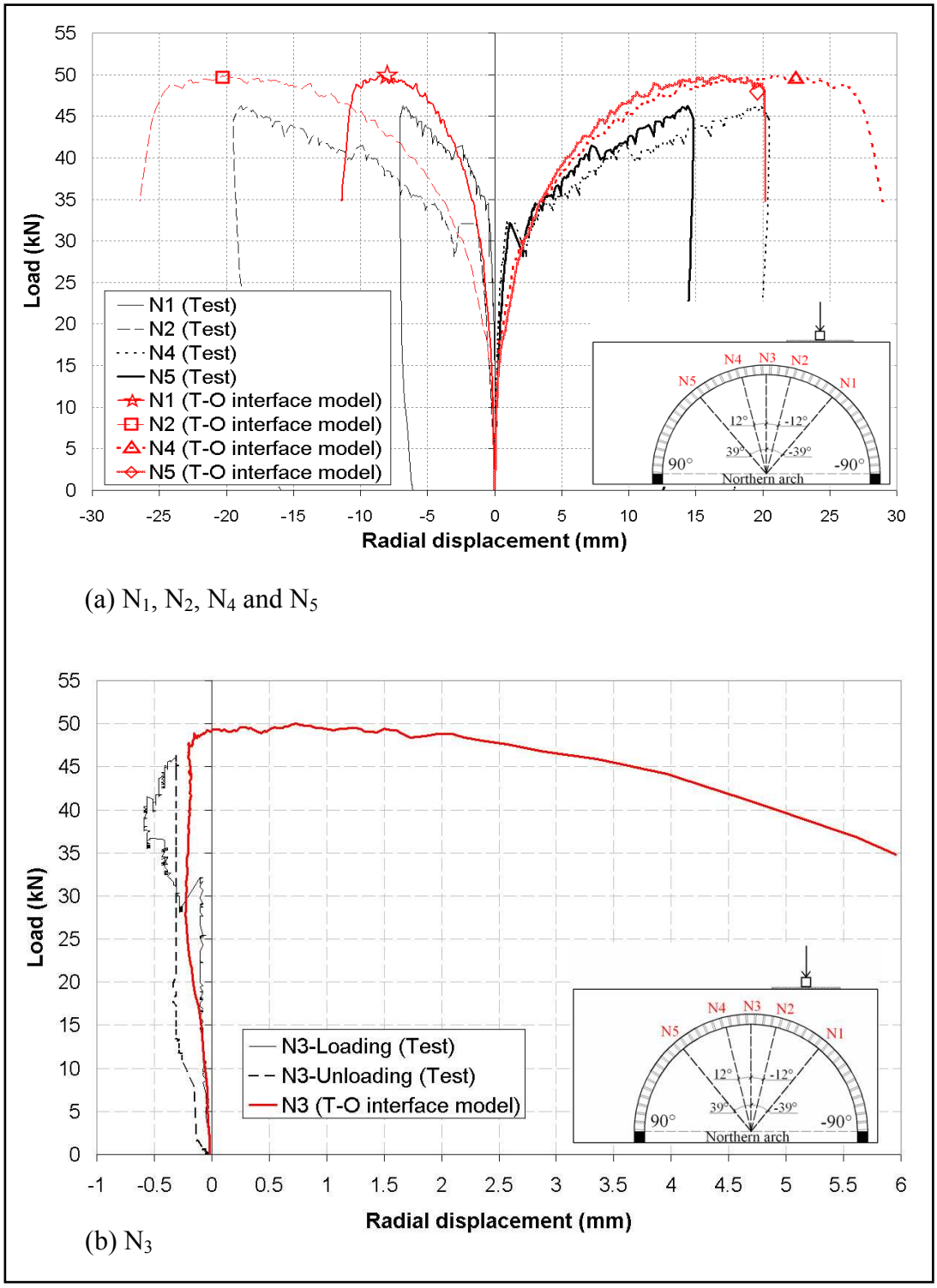

Figure 5.12 Arch load-deflection curves: test vs traction opening interface model (T-O interface model) prediction

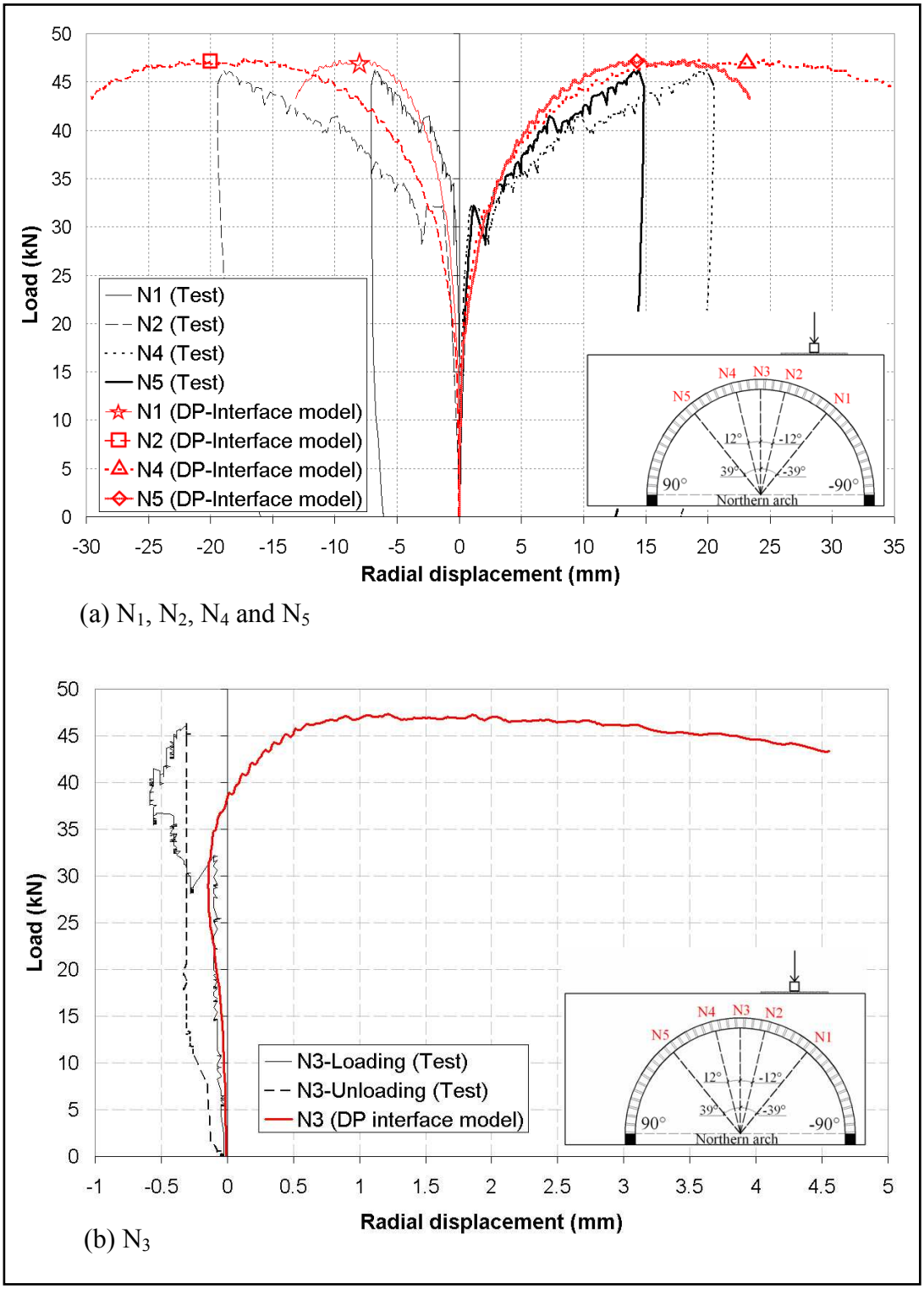

Figure 5.13 Arch load-deflection curves: test vs damaged plasticity interface model (DP-interface model) prediction

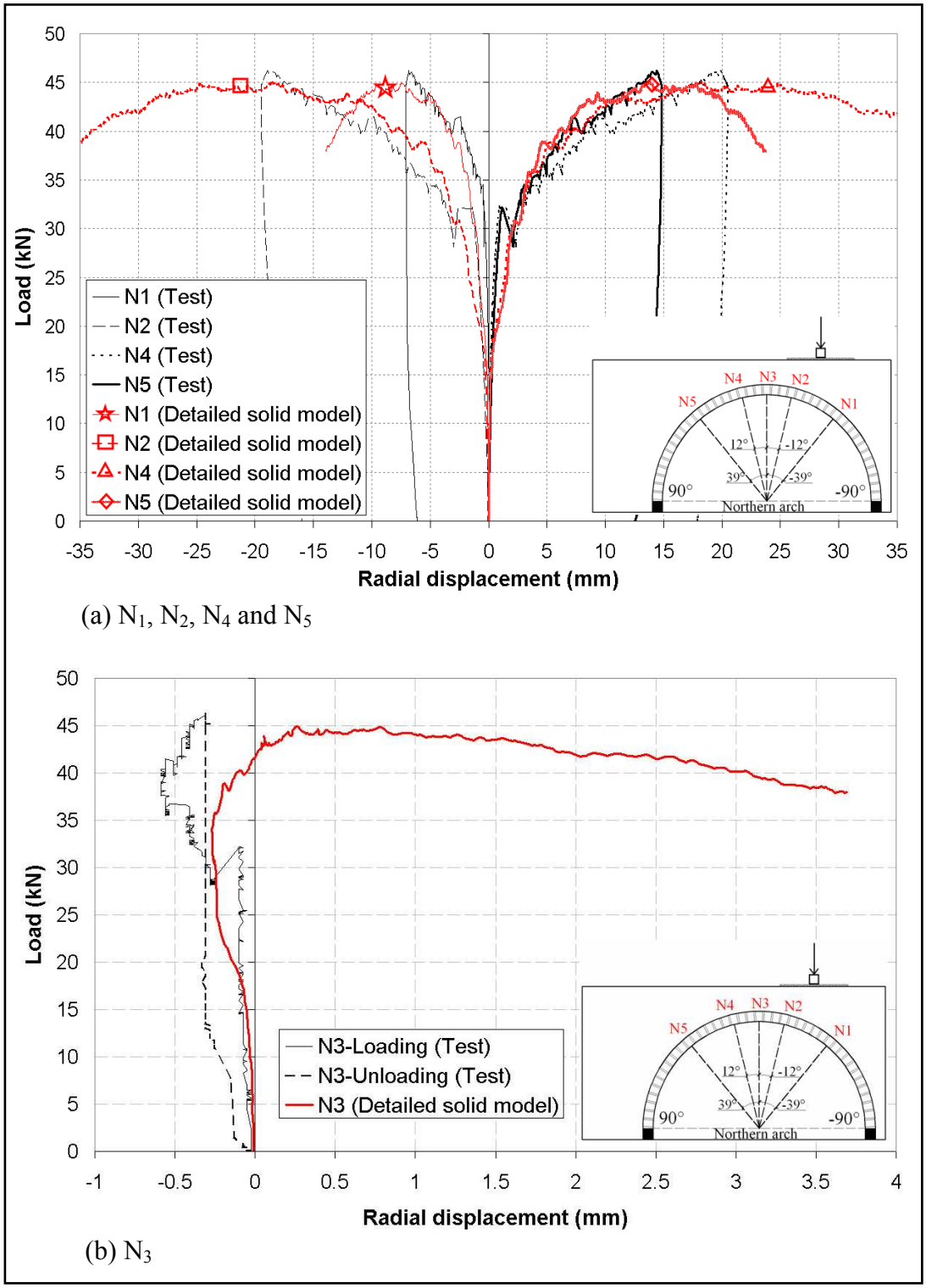

Figure 5.14 Arch load-deflection curves: test vs detailed solid model prediction

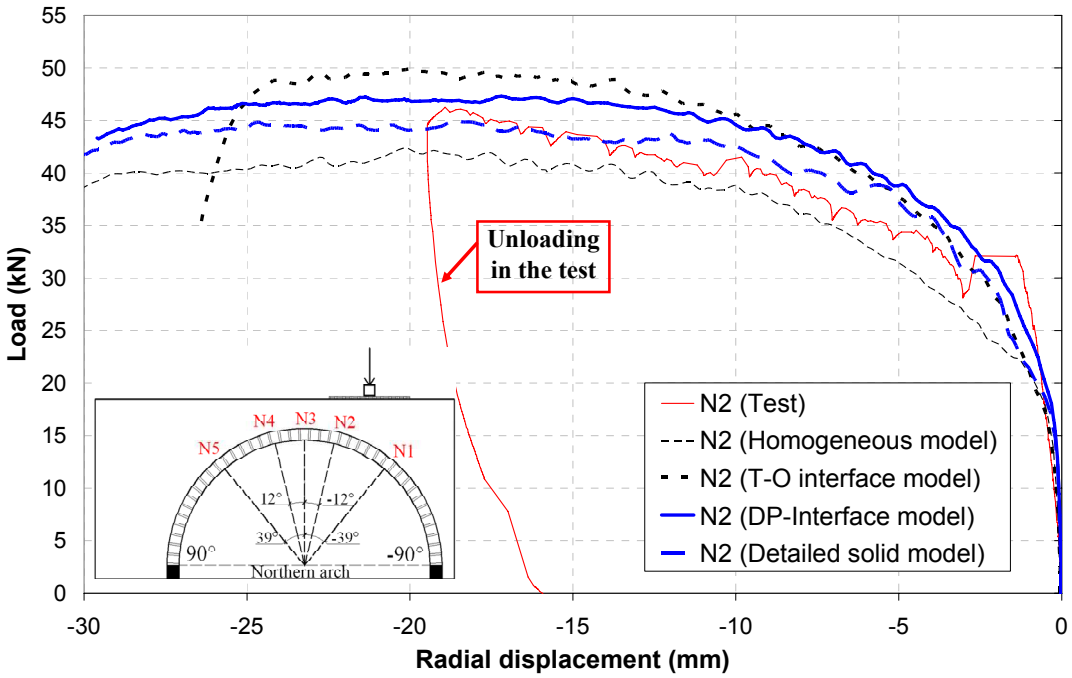

Figure 5.15 Arch load-deflection curves: test vs different model predictions

5.6.3 Hinge mechanism of arch

The hinge mechanism is a critical failure mode for masonry arches. Hinges are usually formed at the mortar-brick interfaces. The four hinge mechanism obtained from the test is shown in Figure 5.16. The hinge mechanism obtained from each model is compared and analyzed in this section.

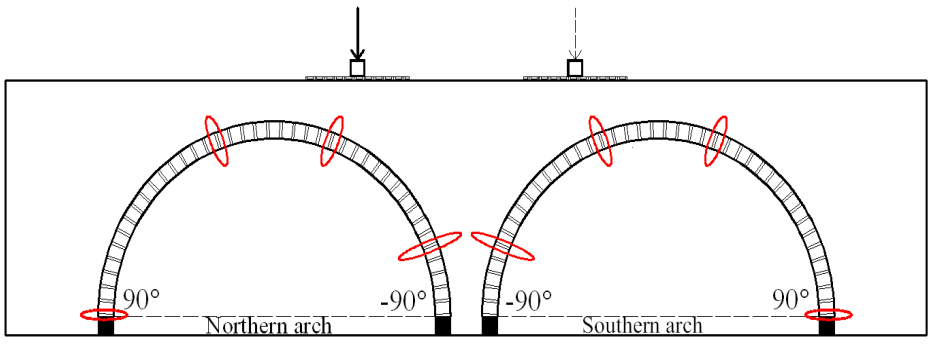

Figure 5.16 The four hinge mechanism obtained from test

In terms of the homogeneous model, the hinge positions can be determined from the radial deflection of the arch (Figure 5.18) and the concrete damage contours (Figure 5.19). Five characteristic points in the load-deflection responses in Figure 5.17 are specified, 0.0kN is the stage just after the self-weight is applied; load level 20kN is at the stage before all cracks opened; load level 33kN is at the stage when the four cracks formed; load level 39kN is during the development of cracks; and load level 42.5kN is at the ultimate state when the four hinge mechanism formed. The arch deflections corresponding to each stage are shown in Figure 5.18. It is clear that four hinges are formed at -65°, -20°, 29° and 90°. The two largest deflection positions (-20° and 29°) correspond to the two major cracks. The alternation of the outwards deflection (positive value) and the inwards deflection (negative value) indicate the alternation of four hinges, which eventually form the mechanism. There is negligible deflection at the crown. The four hinge mechanism at the ultimate load from the homogeneous model is shown in Figure 5.19.

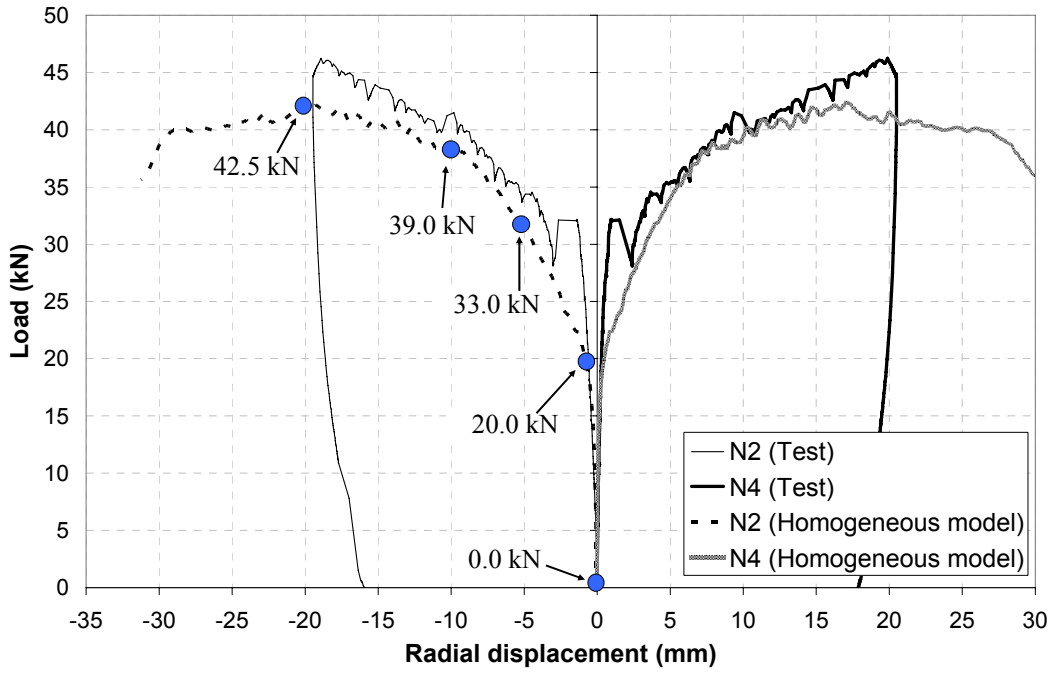

Figure 5.17 Arch deflections from the homogeneous model with specified points

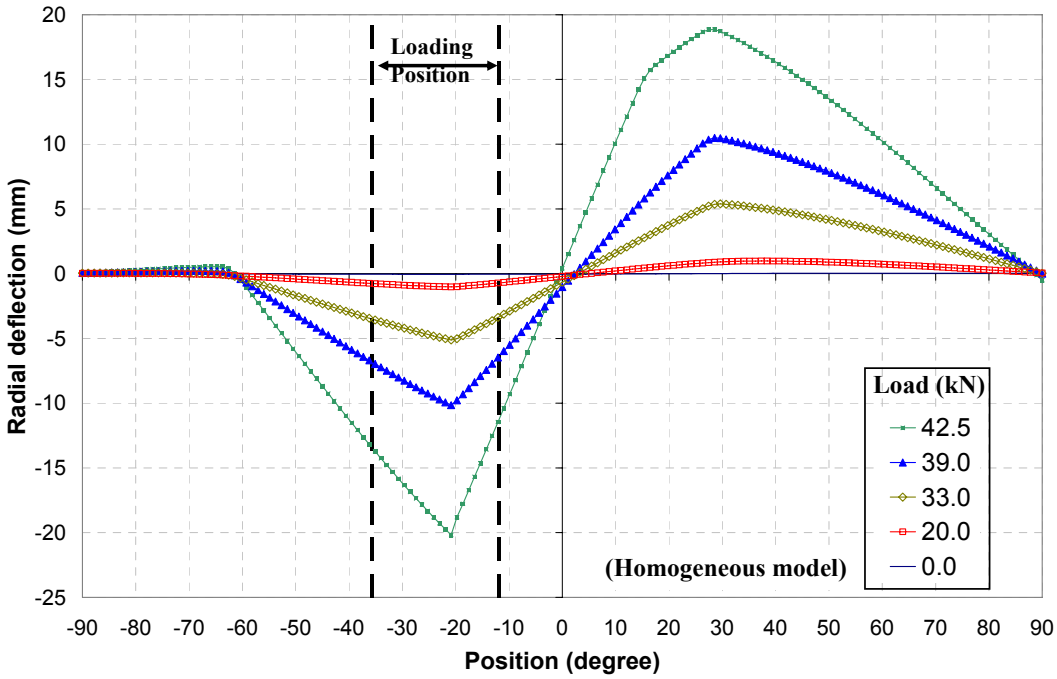

Figure 5.18 Arch deflections obtained from the homogeneous model

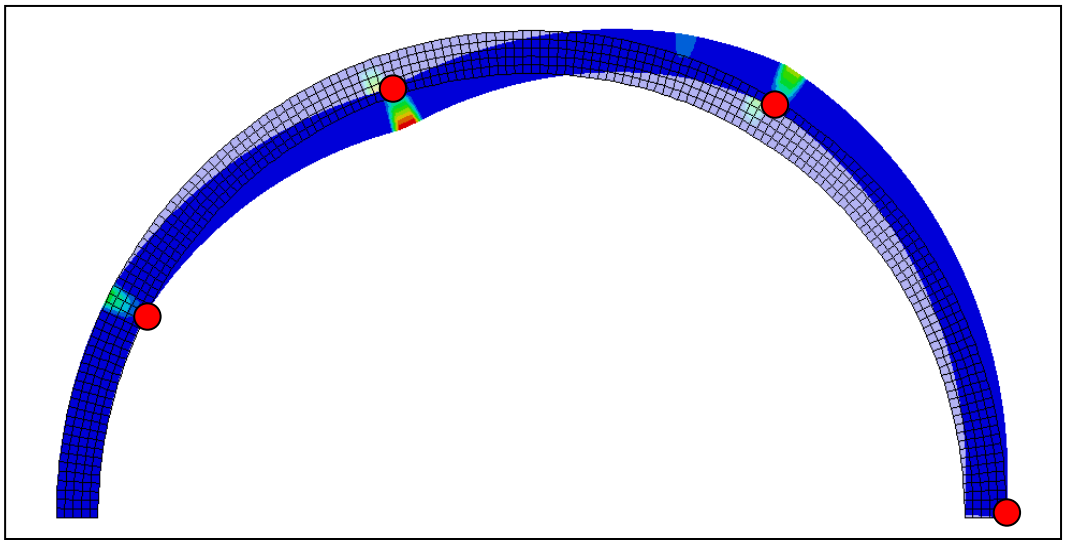

Figure 5.19 Four hinge mechanism obtained from the homogeneous model (scale factor=4)

For both the traction-opening interface model and the damaged plasticity interface model, the crack opening can be directly extracted from the interface elements.

The crack opening width at both intrados and extrados are shown in Figure 5.21 and 5.22 at the five load levels as specified in Figure 5.20 for the traction-opening interface model. It is clear that four cracks are formed at -65°, -20°, 25° and 90°, which are quite similar to that obtained from the test. The four major cracks formed when the load reaches 30kN, which is quite close to that from the test. Due to compatibility of the deformation, the total crack opening width at the intrados was the same as that at the extrados. Two additional cracks are developed at 15° and 85° when the load is increased from 45kN to 50kN. The four hinge mechanism at the ultimate load obtained from the traction-opening interface model is shown in Figure 5.23.

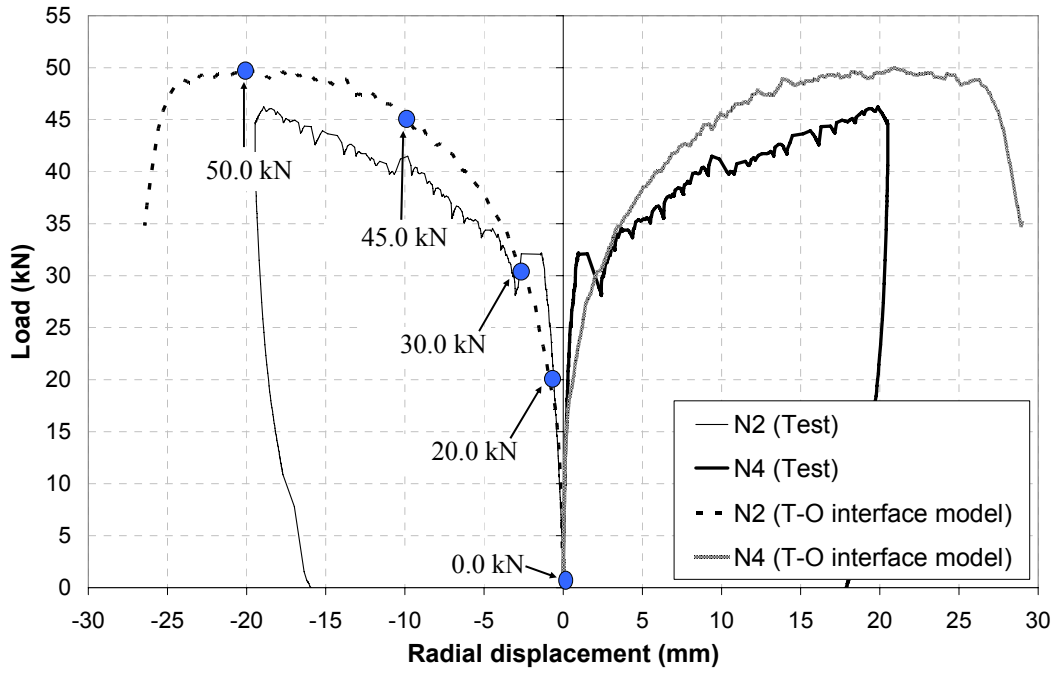

Figure 5.20 Arch deflection from the traction-opening interface model with specified points

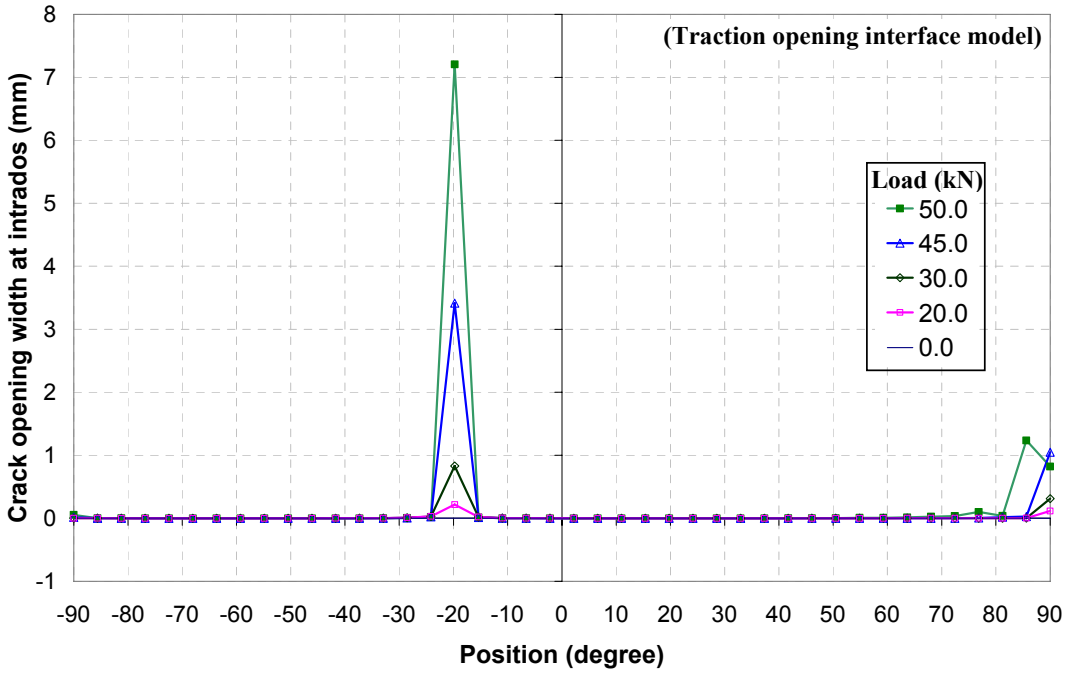

Figure 5.21 Crack opening width at intrados from the traction-opening interface model

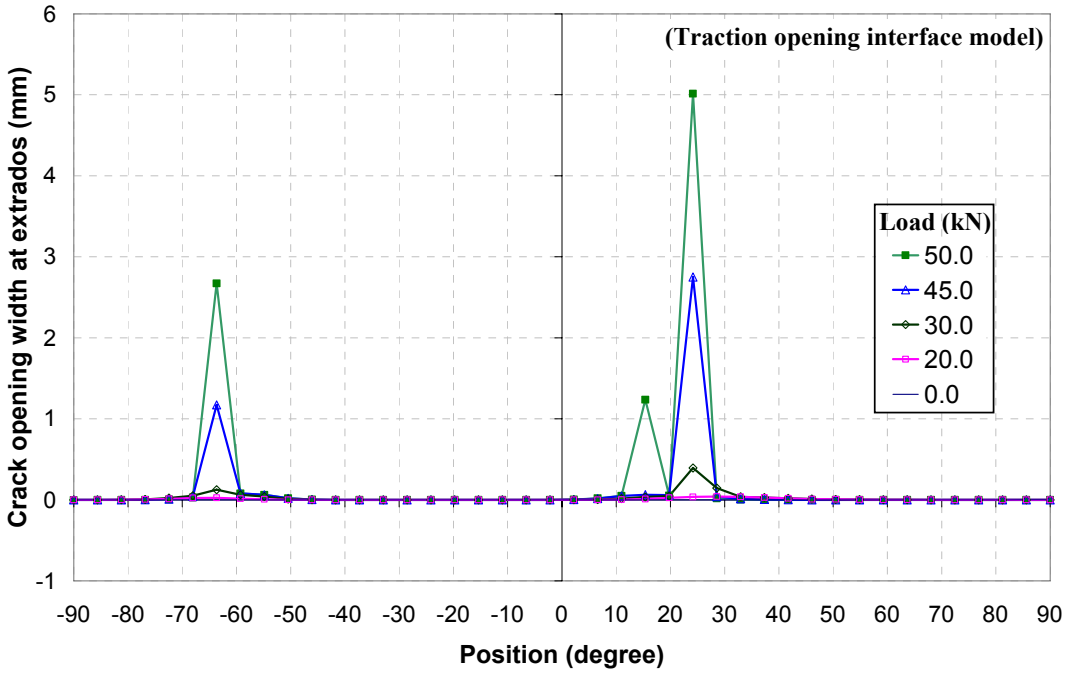

Figure 5.22 Crack opening width at extrados from the traction-opening interface model

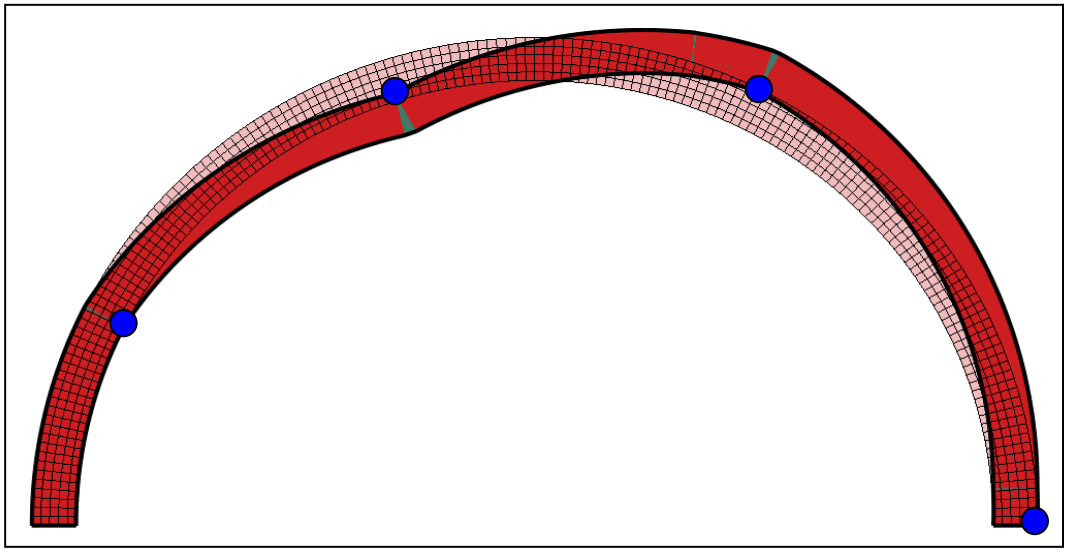

Figure 5.23 Four hinge mechanism obtained from the traction-opening interface model (scale factor=4)

The crack opening width at both the intrados and extrados obtained from the

damaged plasticity interface model are shown in Figure 5.25 and 5.26 corresponding to the five load levels specified in Figure 5.24. It is shown that a four hinge (-65°, -20°, 20° and 90°) mechanism is formed, which is quite similar to that obtained from the test. The four major cracks opened when load was increased to about 33kN. As the load further increased, the cracks continuously opened and eventually lead to the formation of the four hinge failure mechanism. The total crack opening width at the intrados was the same as that at the extrados due to the compatibility of deformations. The four hinge mechanism at the ultimate load obtained from the damaged plasticity interface model is shown in Figure 5.27.

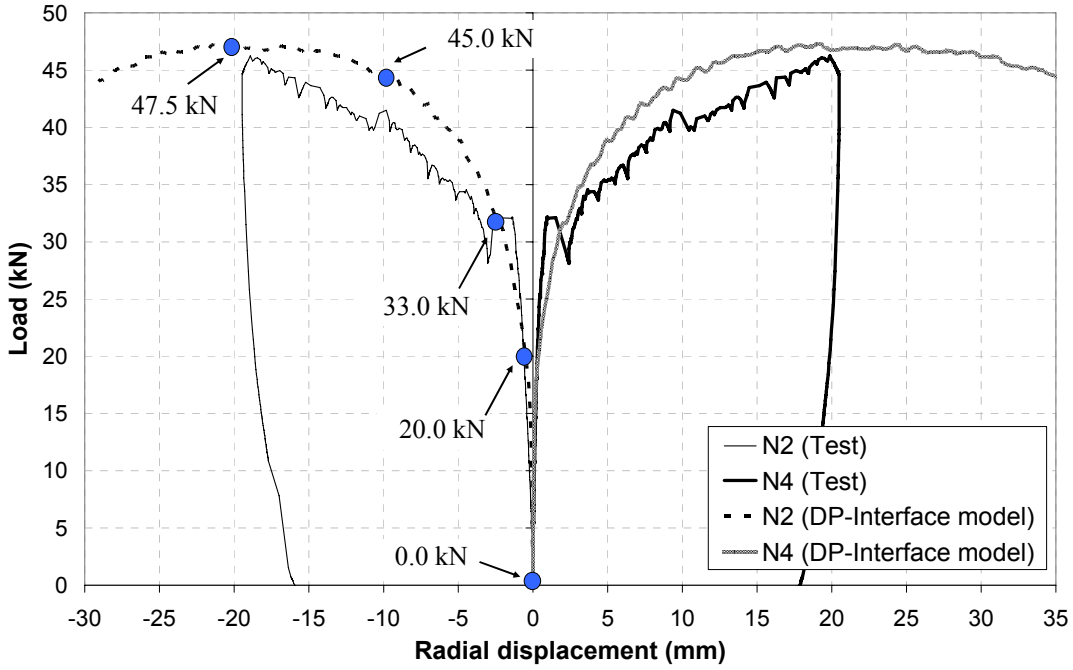

Figure 5.24 Arch deflection from the damaged plasticity interface model with specified points

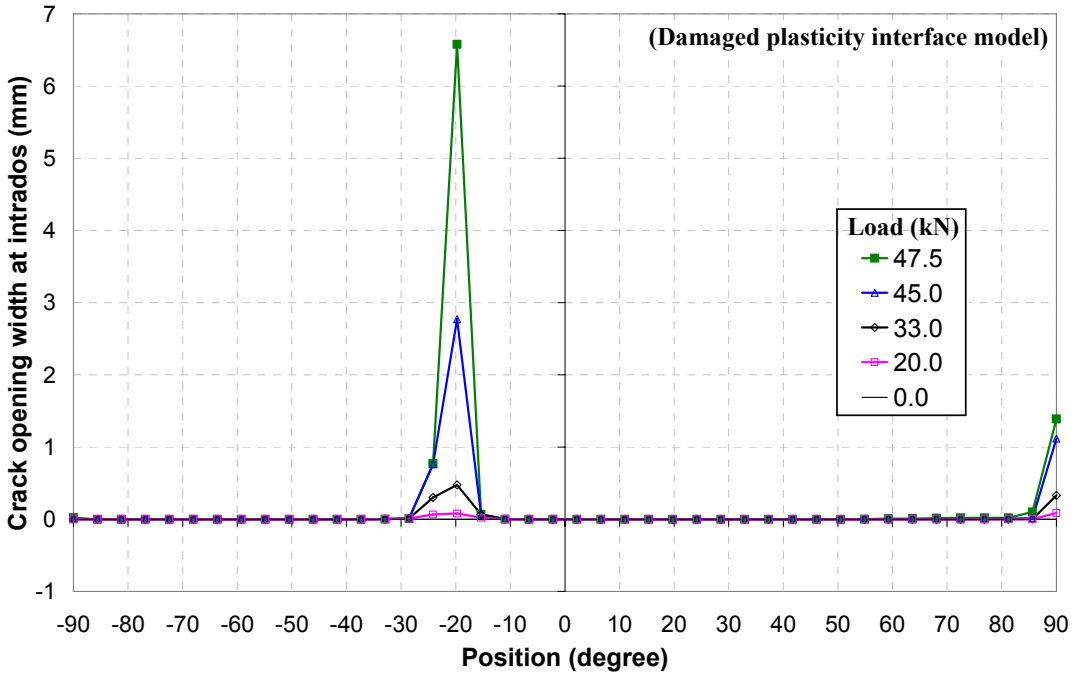

Figure 5.25 Crack opening width at intrados from the damaged plasticity interface model

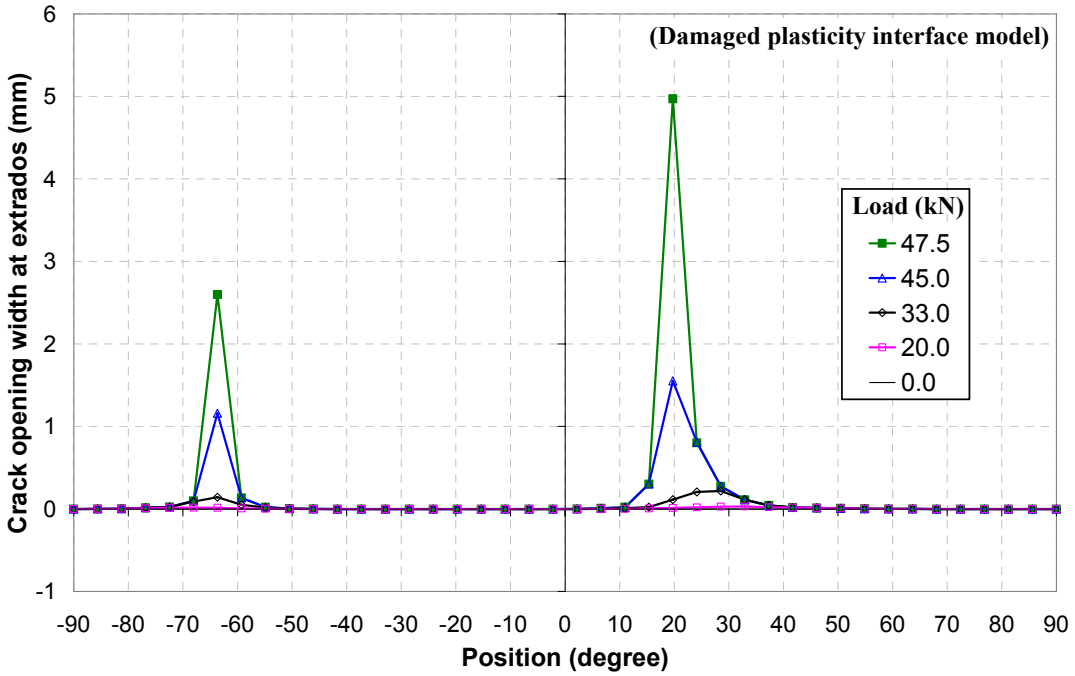

Figure 5.26 Crack opening width at extrados from the damaged plasticity interface model

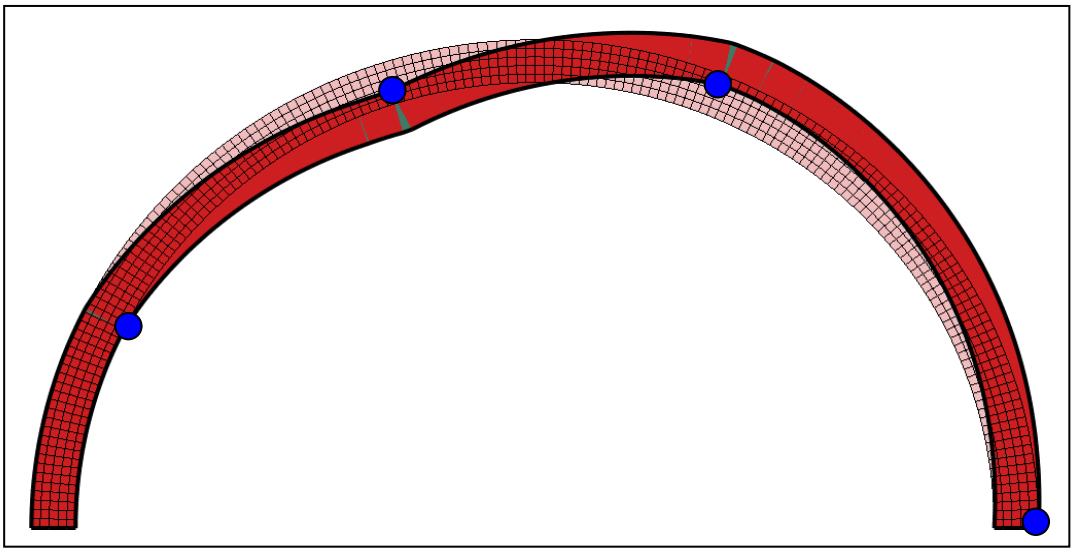

Figure 5.27 Four hinge mechanism obtained from the damaged plasticity interface model (scale factor=4)

The crack opening width at both the intrados and extrados obtained from the detailed solid model are shown in Figure 5.29 and 5.30 corresponding to the five load levels specified in Figure 5.28. It is clear that the four hinge mechanism is formed at the locations of -60°, -20°, 20° and 90°, which is very close to that obtained from the test. The four major cracks opened widely when load reached about 31kN. The negative values implied that the mortar joint tended to close, which can be attributed to the non-zero thickness solid elements used to model the mortar. The total crack opening width at the intrados is the same as that at the extrados due to the compatibility of deformation. The four hinge mechanism at the ultimate load obtained from the detailed solid model is shown in Figure 5.31.

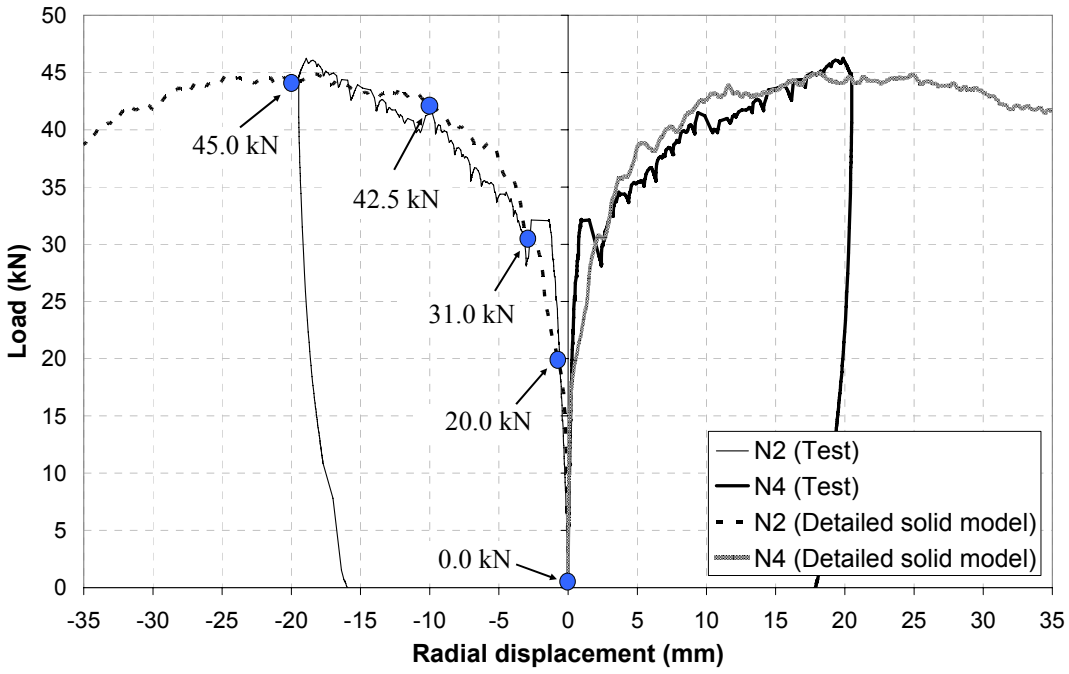

Figure 5.28 Arch deflection from the detailed solid model with specified points

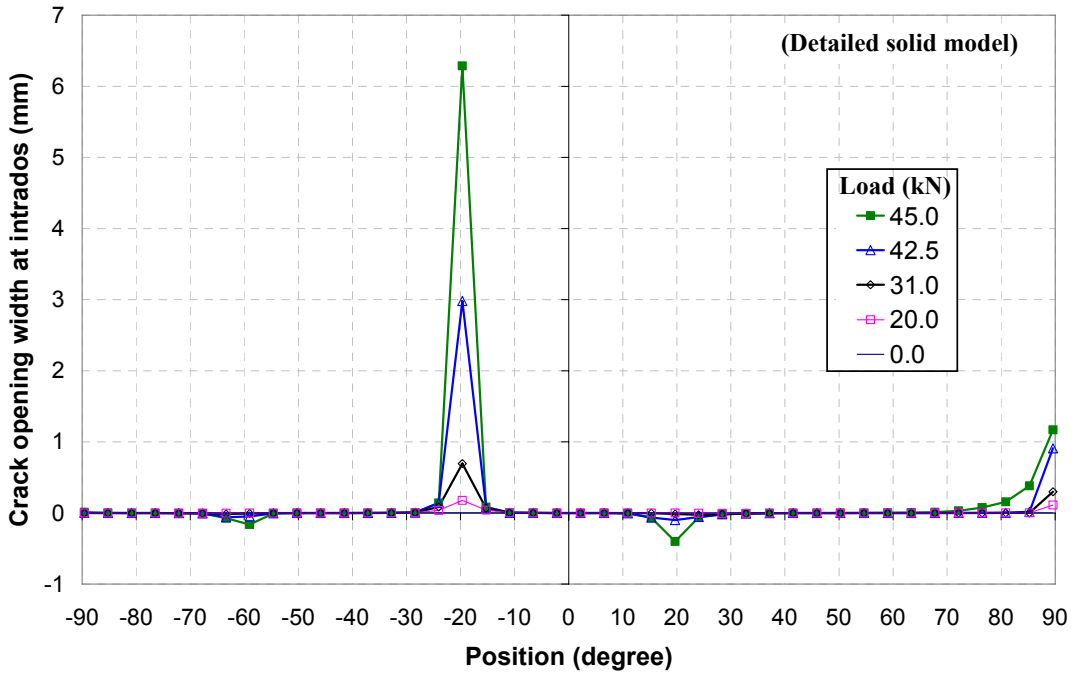

Figure 5.29 Crack opening width at intrados from the detailed solid model

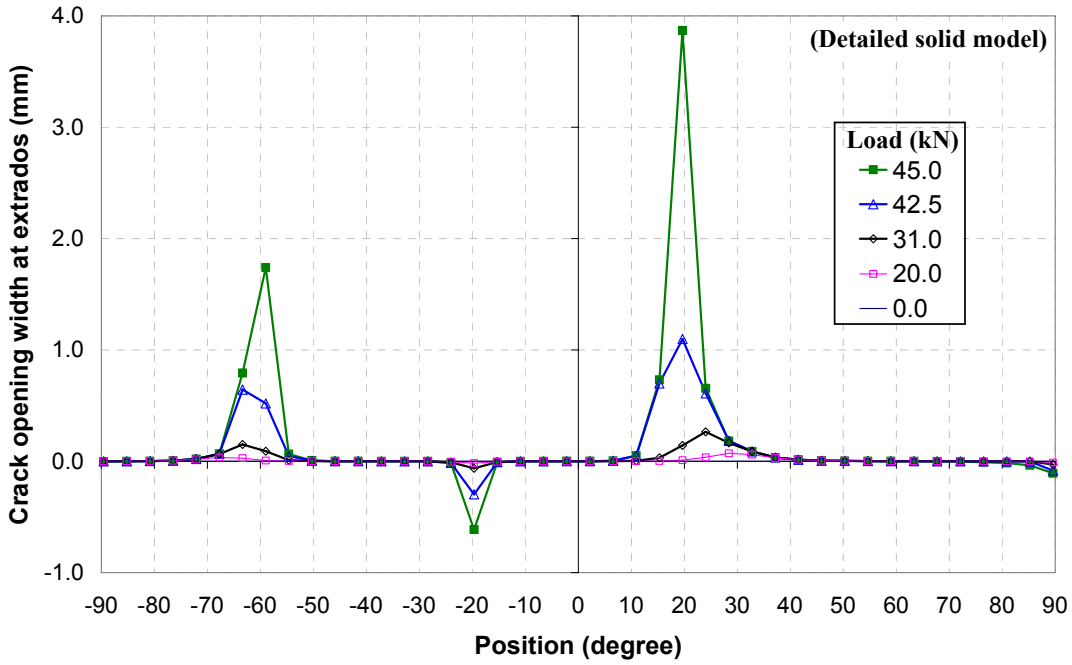

Figure 5.30 Crack opening width at extrados from the detailed solid model

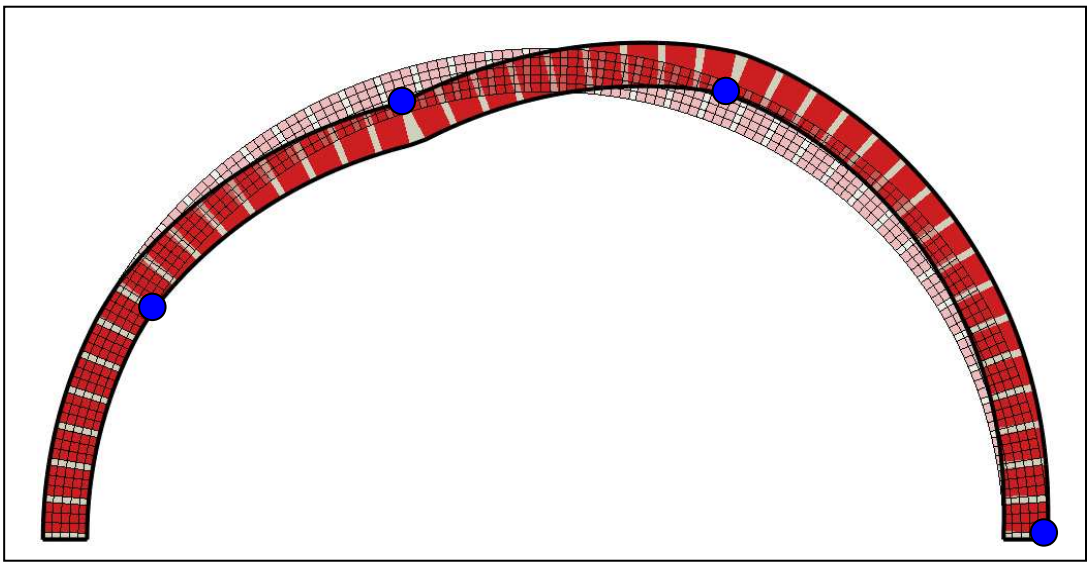

Figure 5.31 Four hinge mechanism obtained from the detailed solid model (scale factor=4)

To summarise, firstly, all the models can successfully simulate the four hinge mechanism failure mode with almost identical hinge positions compared to test

results. The comparison between test and models in regard to the hinge positions is summarized in Table 5-9. The damaged plasticity interface model and the detailed solid model delivered more accurate predictions of the hinge locations. Secondly, all of the models can capture the load at the formation of four cracks at about 33kN. Thirdly, the hinge beneath the loading area (-20°) formed first, and the four hinge mechanism formed once the crack width significantly increased.

Table 5-9 Summary of the hinge mechanism

		Location of the four hinges
Test	Northern arch	-68°, -20°, 20°, 90°
	Southern arch	-68°, -20°, 20°, 90°
Isotropic model		-65°, -20°, 29°, 90°
Interface model	Traction-opening interface model	-65°, -20°, 25°, 90°
	Damaged plasticity interface model	-65°, -20°, 20°, 90°
Detailed model		-60°, -20°, 20°, 90°

5.6.4 Mechanism analysis validation

Although the results from the models are in good agreement with the test data, a classical mechanism analysis was conducted to compare the loading capacity and hinge positions of the masonry arch to verify the parameters and the results. The details of the mechanism method has been reviewed in Chapter 2 and can be found in the literature such as Harvey (1988), Heyman (1982), Hughes et al. (2002). The classical mechanism method has been used to determine the load carrying capacity of masonry arches. It is based on the estimation of the thrust line, which is related to the

hinge positions. The resulting failure load can be determined once the hinge positions are selected. Each hinge position is then relocated until the lowest of the upper bound collapse load (minimum capacity) is determined.

The program developed by Hughes et al. (2002) was used to analyse the masonry arch, because it incorporates masonry yielding, passive backfill pressure effects, and geometric non-linear effects. The parameters used for the mechanism analysis is summarized in Table 5-10. The hinge mechanism determined from the mechanism analysis is shown in Figure 5.32. The comparison of the results from test, FE models, and mechanism analysis is summarized in Table 5-11. The datails of spreadsheet calculation was reported in Appendix 2.

Table 5-10 Parameters for mechanism analysis

Parameters		Values
Masonry	Density (kg/m^3)	2450
	Compressive strength (MPa)	25
Sand backfill	Density (kg/m^3)	1520
	Internal friction angle Φ	33 º
Load	Load dispersion angle θ	30 º

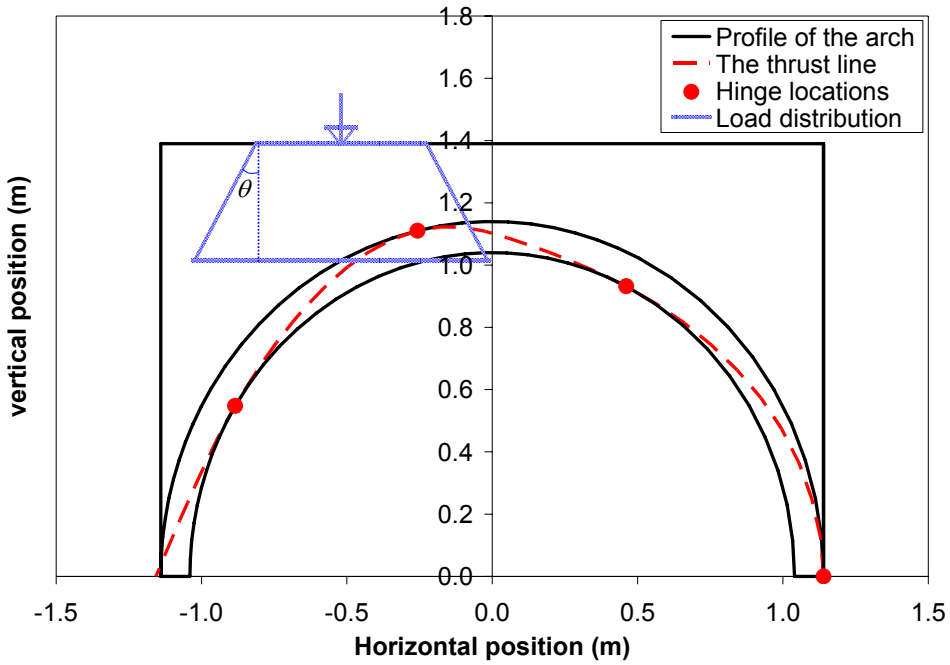

Figure 5.32 The hinge mechanism obtained from the mechanism analysis

Table 5-11 Comparison of the results

		Loading capacity (kN)	Location of four hinges
Test	Northern arch	46.2	-68°, -20°, 20°, 90°
	Southern arch	49.7	-68°, -20°, 20°, 90°
Homogeneous model		42.5	-65°, -20°, 29°, 90°
Meso-interface model	Traction-opening interface model	50.0	-65°,-20°,25°,90°
	Damaged plasticity interface model	47.5	-65°, -20°, 20°, 90°
Detailed solid model		45.0	-60°, -20°, 20°, 90°
Mechanism analysis		41.9	-58°, -13°, 26°, 90°

It is clear that the loading capacity predicted from all the FE models and the mechanism analysis method is comparable with that from the test, although the

mechanism method leads to a conservative prediction. The loading capacity obtained from the homogeneous model was the lowest of all of FE models. The mechanism obtained from both FE models and mechanism analysis is in good agreement with that from the test. The damaged plasticity interface model delivers the most accurate prediction compared with the other models.

The length of loading plate was changed from 570mm for the original arches to 670mm for the strengthened arches during the test as described in Chapter 3. The wider loading plate implies a greater confinement for the backfill, and thus leads to a greater load carrying capacity. This effect was investigated using the mechanism analysis. All parameters in Table 5-10 were kept constant expecting the length of plate. The results are summarized in Table 5-12. It is clear that the wider loading plate delivered a greater loading capacity with a slight modification in the location of hinges.

Table 5-12 Comparison of the results from different length of loading plate

		Loading capacity (kN)	Location of four hinges
Test	Northern arch	46.2	-68°, -20°, 20°, 90°
	Southern arch	49.7	-68°, -20°, 20°, 90°
Mechanism analysis	570mm plate	41.9	-58°, -13°, 26°, 90°
	670mm plate	45.5	-57°, -12°, 27°, 90°

5.6.5 Contact behaviour between sand and arches

The presence and stiffness of the back-fill can significantly affect the arch behaviour by adding additional compression in the arch and dispersing the concentrated forces over a greater area. Apart from these, the height of fill at the crown also has significant effects on the arch behaviour. Meanwhile, the development of mechanism leads to a stress redistribution in the backfill. The contact behaviour between the backfill and extrados of arches are studied in this section in order to investigate the relationship between the hinge mechanism and the interfacial stresses at the contact interface.

The interfacial shear stress distribution at the interface between sand backfill and the extrados of loaded arch obtained from all the FE models are shown in Figure 5.33 (homogeneous model), 5.34 (traction-opening interface model), 5.35 (damaged plasticity interface model), and 5.36 (detailed solid model), respectively. A positive value represents an anticlockwise interfacial shear stress. The stress distributions obtained from all models are very similar (Figure 5.37). The development of the interfacial shear stress can be related to the hinge mechanism as follows. Before the cracks are formed (below 30kN), the differential deformation between the arch and backfill lead to the development of the interfacial stresses. Once the crack is formed at about 30kN, there is a sharp change at the stress at each hinge location (at about -65°, -20°, 20°, 90°). The stress increases continuously while loading is over 30kN. In addition, the timber wall can deform laterally because it was only restrained at the top and bottom as the test, which leads to the decreases of the passive pressure and

consequently the drop of the stress in the portion of 50° - 60°.

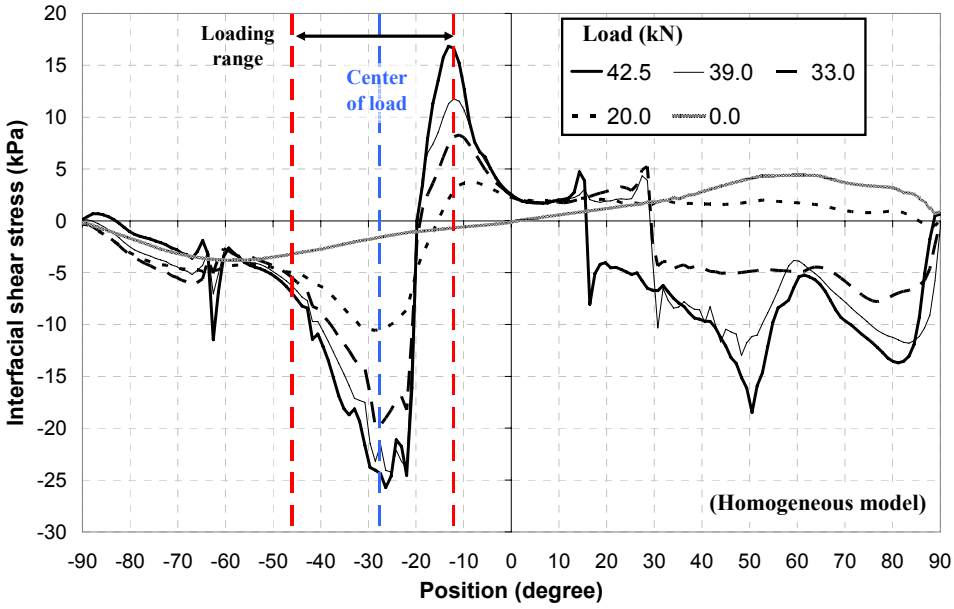

Figure 5.33 Interfacial shear stress at the interface between sand and extrados from the homogeneous model

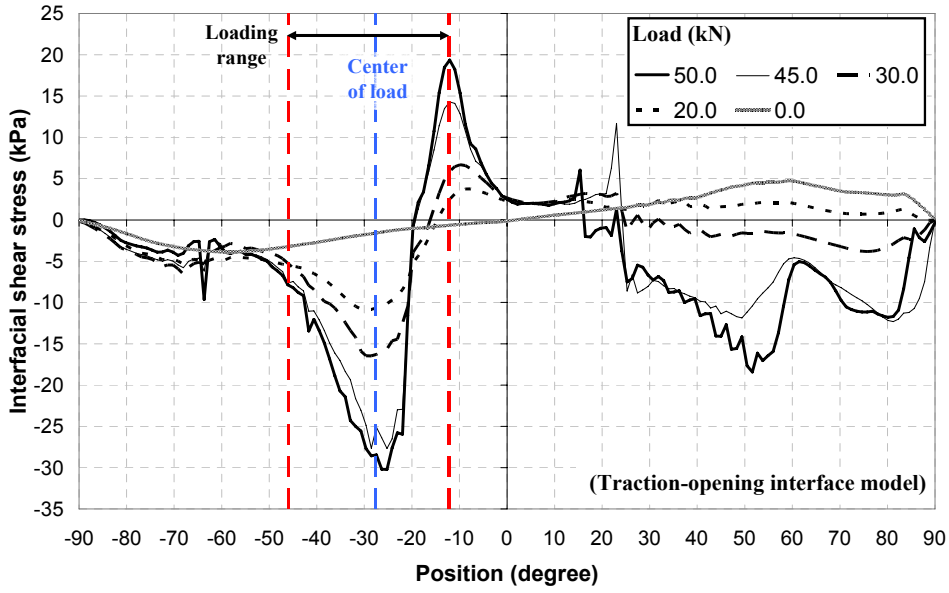

Figure 5.34 Interfacial shear stress at the interface between sand and extrados from the traction-opening interface model

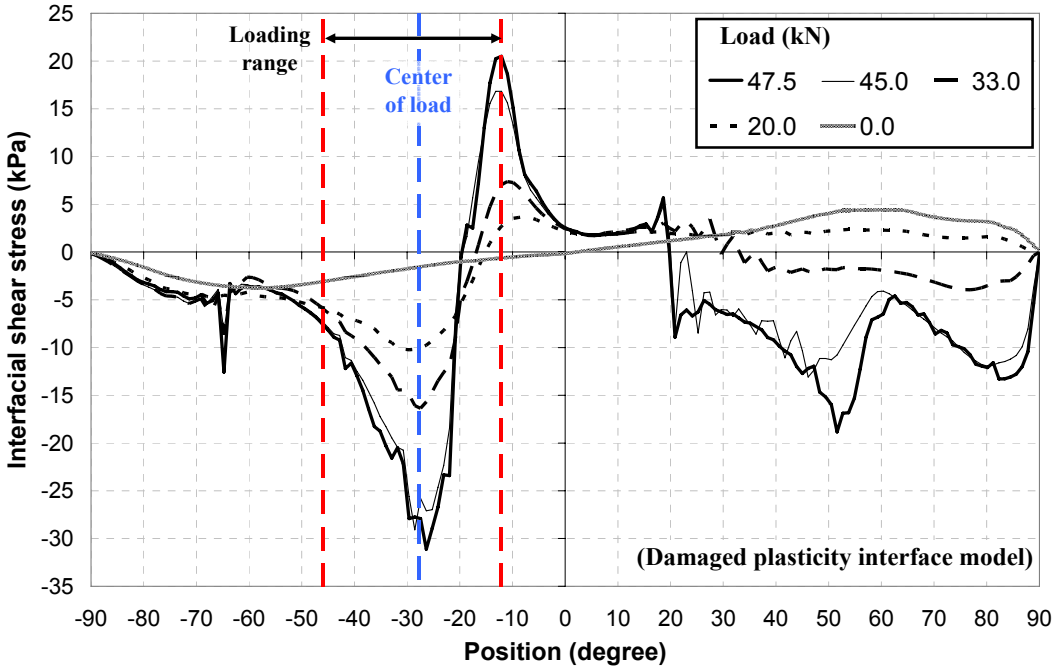

Figure 5.35 Interfacial shear stress between sand and arch extrados from the damaged plasticity interface model

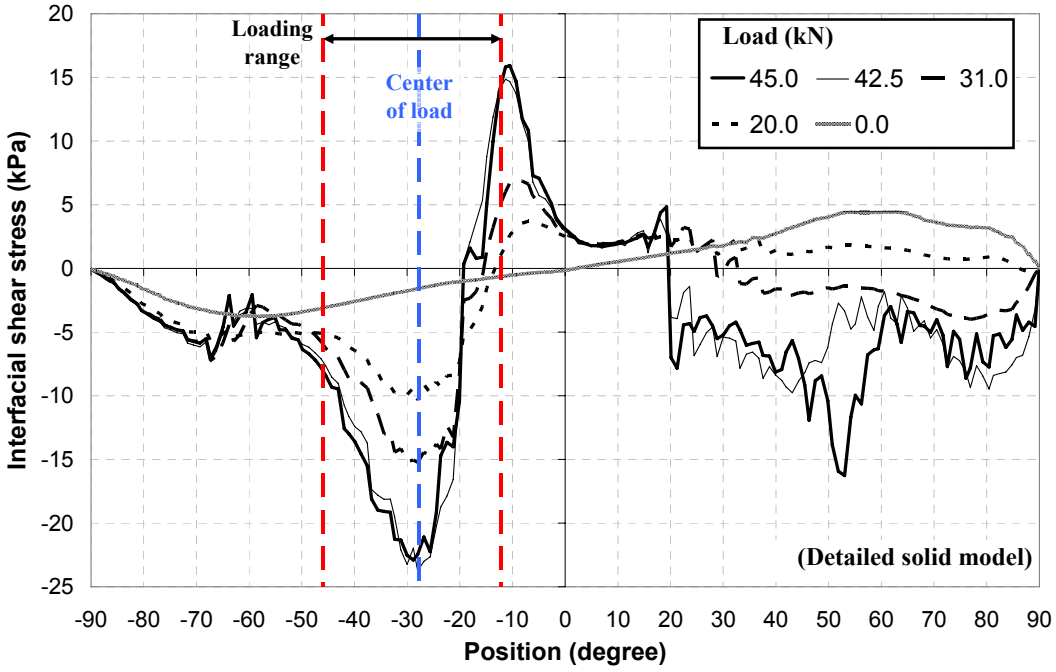

Figure 5.36 Interfacial shear stress between sand and arch extrados from the detailed solid model

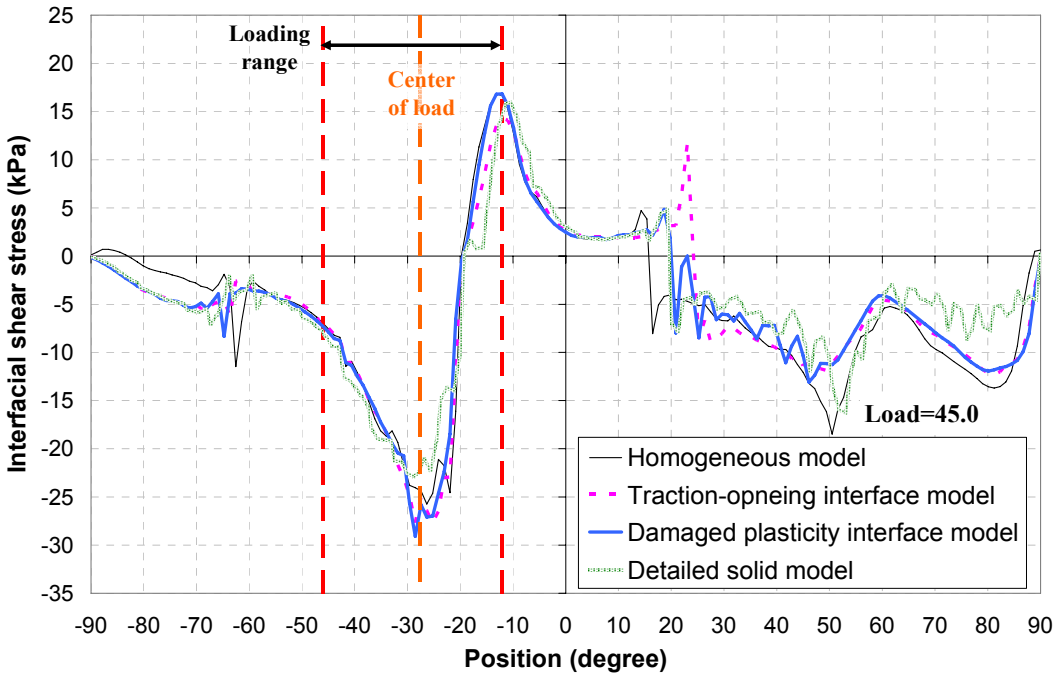

Figure 5.37 Interfacial shear stress between sand and arch extrados from different models

The interfacial normal stress distribution at the interface between sand backfill and the extrados of loaded arch obtained from all FE models are shown in Figure 5.38 (homogeneous model), 5.39 (traction-opening interface model), 5.40 (damaged plasticity interface model), and 5.41 (detailed solid model), respectively. A positive value of the interfacial normal stress indicates the interface is under compression. It can be found that the stress distributions obtained from all of the models are similar (Figure 5.42). Before the cracks are formed (below around 30kN), the normal stress increases with the applied load. Once the cracks are formed at about 30kN, there was a sharp change at the stress at each hinge location. The stress increases continuously when loading is over 30kN. The reduction of stress between 50° and 60° can be attributed to the reduction of the passive pressure.

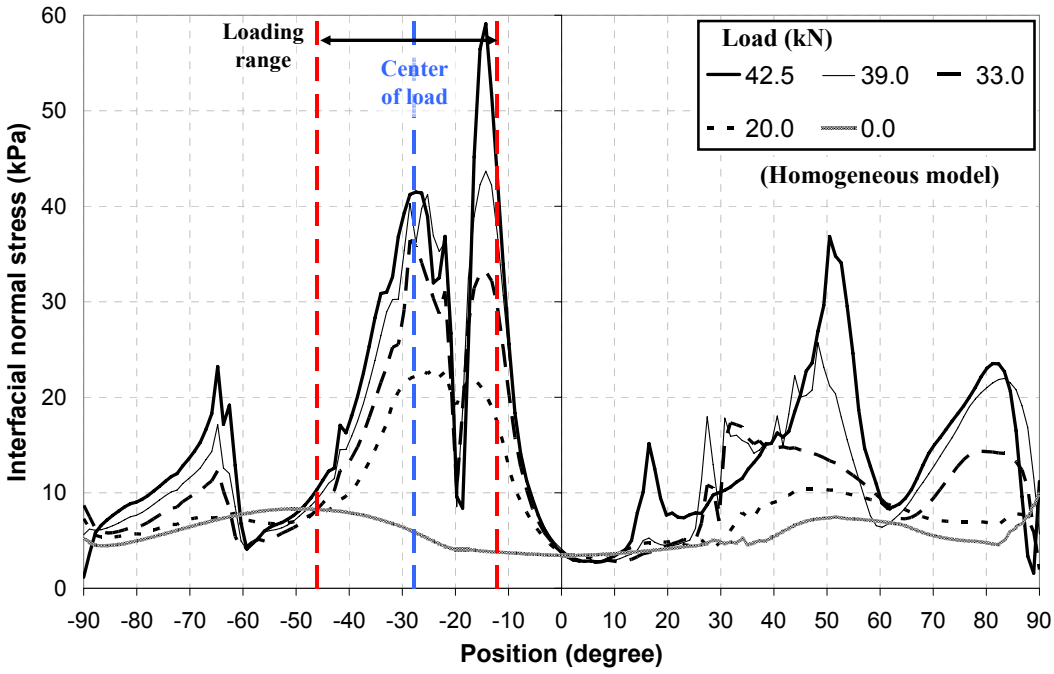

Figure 5.38 Interfacial normal stress at the interface between sand and extrados from the homogeneous model

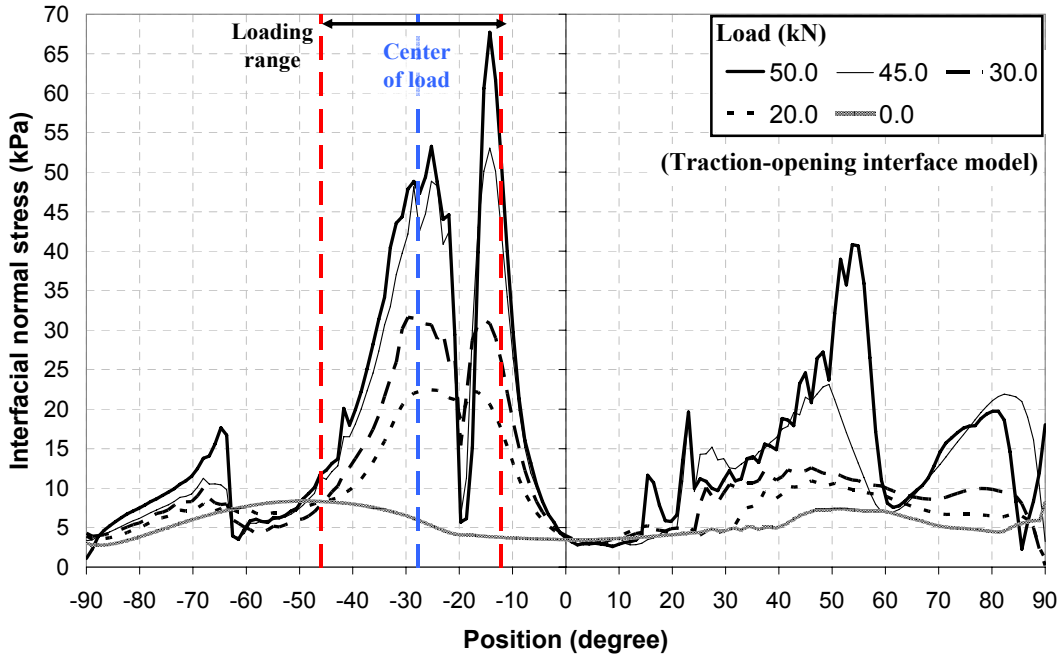

Figure 5.39 Interfacial normal stress at the interface between sand and extrados from the traction-opening interface model

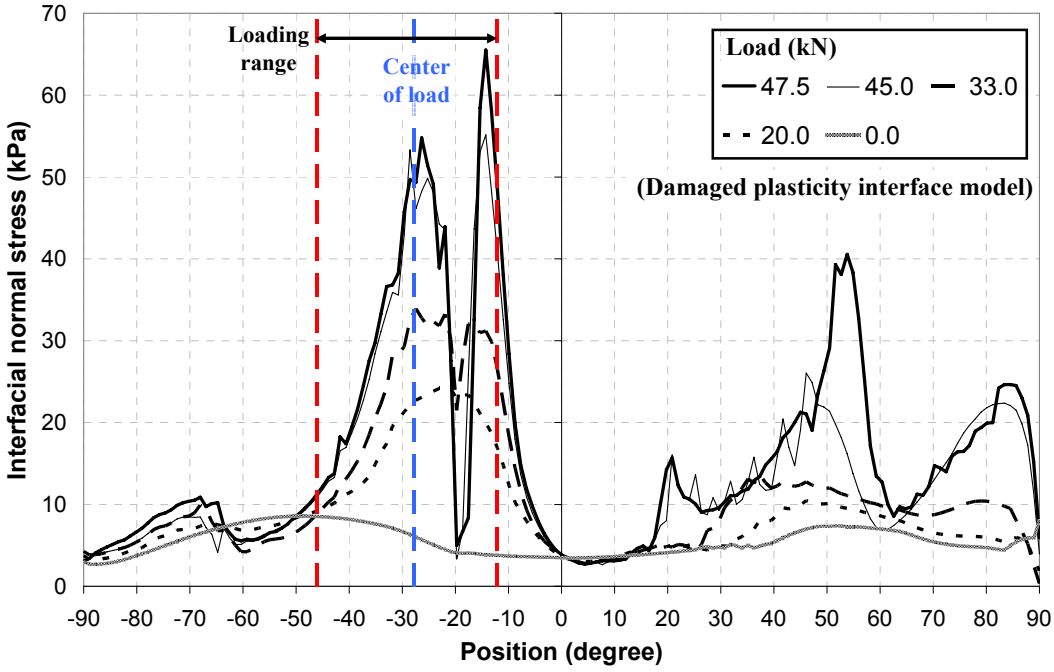

Figure 5.40 Interfacial normal stress between sand and arch extrados from the damaged plasticity interface model

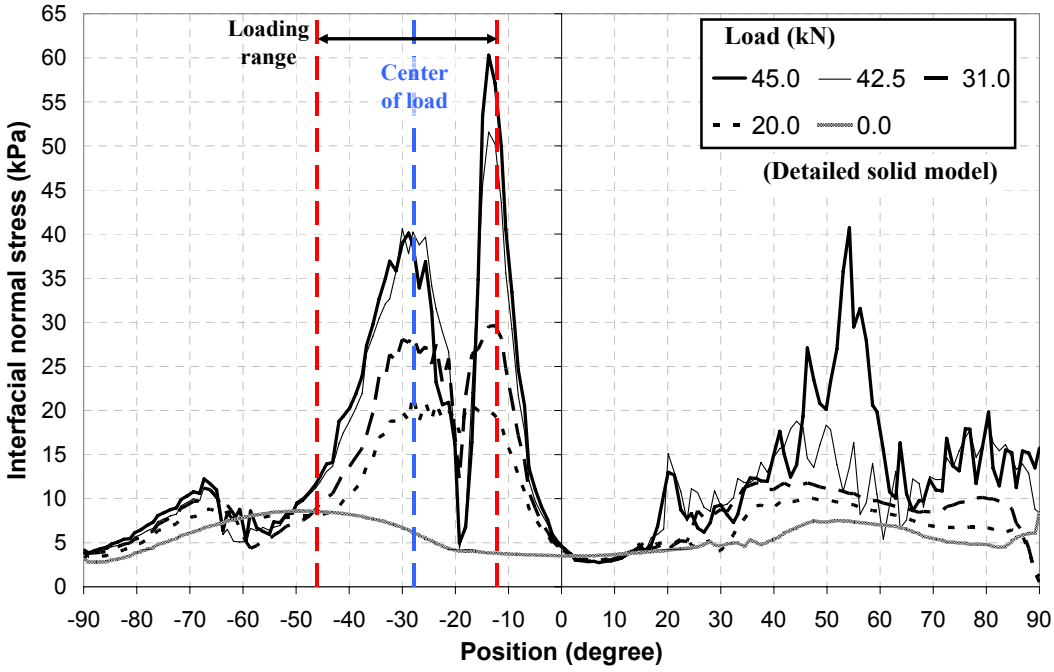

Figure 5.41 Interfacial normal stress between sand and arch extrados from the detailed solid model

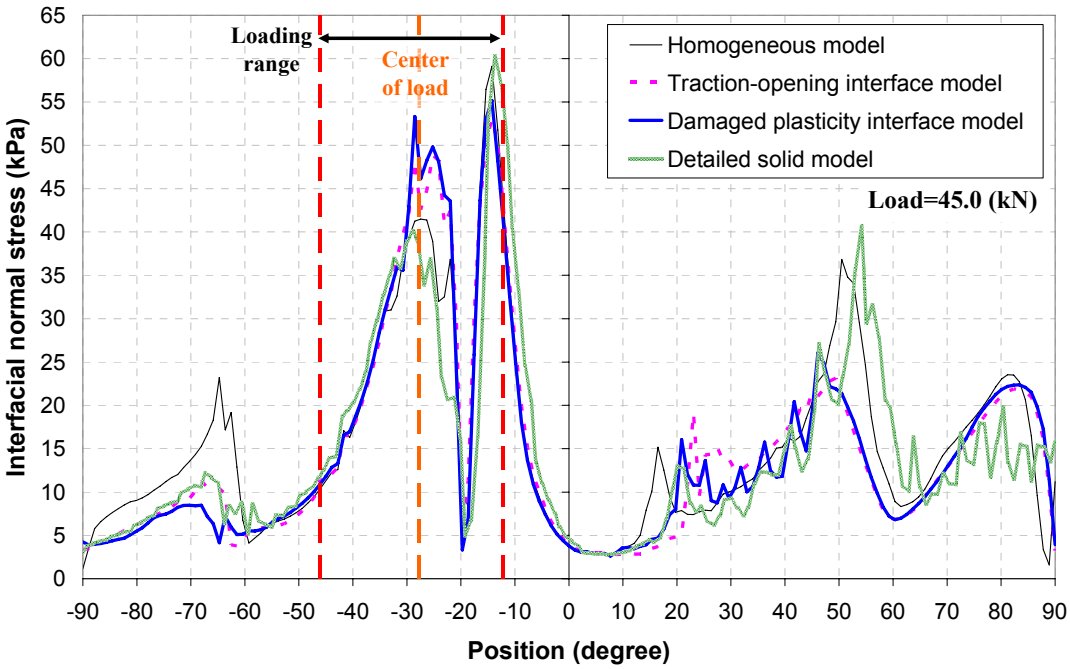

Figure 5.42 Interfacial normal stress between sand and arch extrados from different models

5.6.6 Comparison of the models

After investigating the results from the different FE models as summarized in Table 5-11, it can be concluded that all the models give comparable predictions for the masonry arches. However, each model has their advantages and disadvantages. The homogeneous model is the simplest, but it gives the most conservative prediction because the weaker tensile strength is smeared over the whole arch. A hinge can also form anywhere, such as inside a brick which is not realistic, because of the homogenisation. The traction-opening interface model cannot capture the mortar interface behaviour correctly because it does not consider the enhancement of shear strength when the interface is under compression. Although the damaged plasticity interface model gives good predictions, it is not convenient for modelling more

complex structures such as FRP strengthened masonry arches because it will lead to modelling and numerical difficulties when two zero thickness interfaces intersects. The detailed solid model can deliver good predictions compared with the test. It is also applicable for modelling of FRP strengthened masonry arch structures, which is one of the purposes of this study.

5. 7 Parametric study

In order to understand the effects of parameters involved in the modelling of masonry arch structures, a parametric study was conducted and several material parameters of the masonry and backfill were investigated. In terms of masonry, due to the lack of knowledge about the tensile behaviour of the mortar interface, the effects of the fracture energy and the tensile strength of the mortar interface were investigated. For the backfill, the effects of the cohesion stress and the internal friction angle were investigated. A model without backfill is also produced to study its effects. The detailed solid model was used in this study due to the mentioned advantages compared with other models in Section 5.6.6.

5.7.1 The effect of the fracture energy of the mortar joint

For the mode-I fracture energy of the mortar interface G_{cn}^{0}, there is no widely known equation to determine it and it is difficult to obtain from the test. Lourenço (1996) reported that the mode-I fracture energy varies from 0.005Nmm/mm^2 to 0.02Nmm/mm^2 when the interface tensile strength ranges from 0.3MPa to 0.9MPa from several displacement controlled test. In the current study, the tensile strength is

even smaller: 0.1MPa as obtained from the test.

In the proposed detailed model, the fracture energy was estimated to be 0.066Nmm/mm^2 from Eq. 5-4. However, this equation is original designed for the concrete material and the fracture energy is related to the compressive strength and the maximum aggregate size. In the current FE model, the compressive stress was taken as the compressive strength of mortar (12MPa) and the maximum aggregate size was assumed as 20mm. The smallest value reported by Lourenço (1996) (0.005Nmm/mm^2) is adopted to compare with that used in the proposed detailed model. The results are shown in Figure 5.43. It is clear that the smaller fracture energy results in a lower loading capacity prediction, but the difference of load carrying capacity between these two cases is less than 5%. The loading-deflection responses for the two cases are similar. Clearly, a bridge with a lower interface fracture energy requires less applied load to form a mechanism.

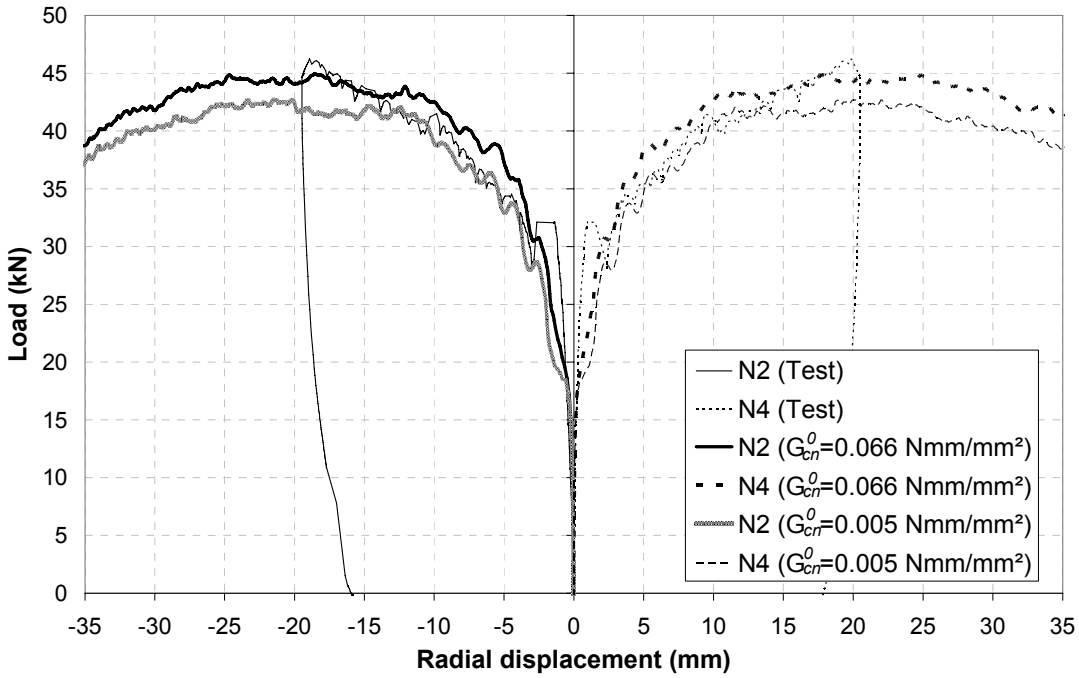

Figure 5.43 Load-deflection curves from the detailed models with different fracture energy of the mortar interface G_{cn}^0

5.7.2 The effect of the tensile strength of the mortar interface

The effect of the tensile strength (f_{ti}^0) is shown in Figure 5.44. It is seen that a smaller tensile strength led to a lower loading capacity. However, when a significantly large tensile strength is applied, for example 1.0MPa, a significant increase on both the loading capacity and stiffness is experienced. This is because lower joint opening width and higher load to the onset of the mechanism.

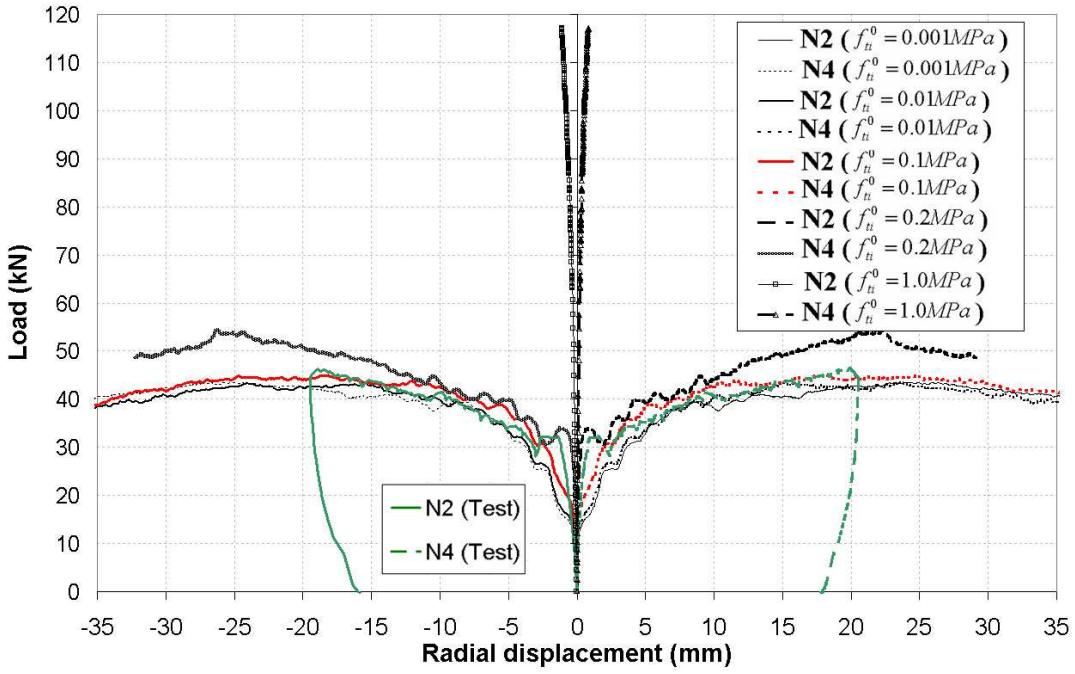

Figure 5.44 Load-deflection curves from the detailed models with different tensile strength of the mortar interface f_{ti}^0

5.7.3 Effect of sand backfill

In order to investigate the effect of the sand backfill on the load capacity of the arch, a model without backfill was simulated. The FE model of a masonry arch without backfill and its loading position are shown in Figure 5.45. The results from both models are shown in Figure 5.46. The model without sand backfill gives a significantly lower loading capacity. The load drops once the four hinge mechanism is formed at about 33kN. The model including backfills produces a greater loading capacity because the dead weight of the backfill effectively pre-stresses the masonry arch, thereby increases its load carrying capacity; also prevents rotational deformation at hinge locations (Gilbert and Melbourne, 1994; Heyman, 1980). Apart from this, the backfill also has two further beneficial effects: it disperses the live load;

and it provides a passive restraint to the movement of the arch when the latter sways into the fill. All of these effects can significantly enhance the load carrying capacity of a masonry arch bridge (Harvey, 1988; Heyman, 1982; Hughes et al., 2002).

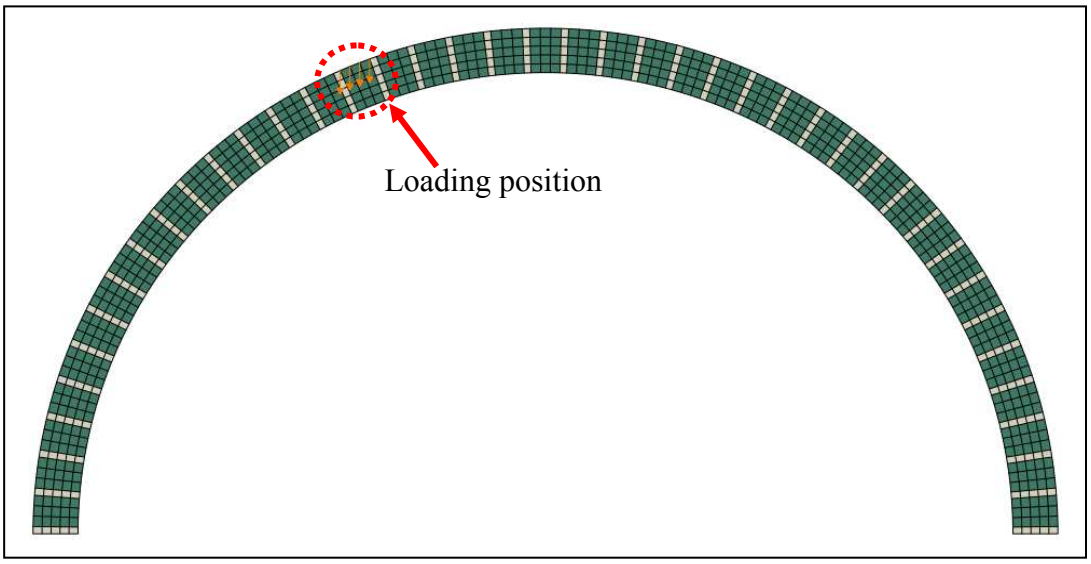

Figure 5.45 FE model of a masonry arch without backfill

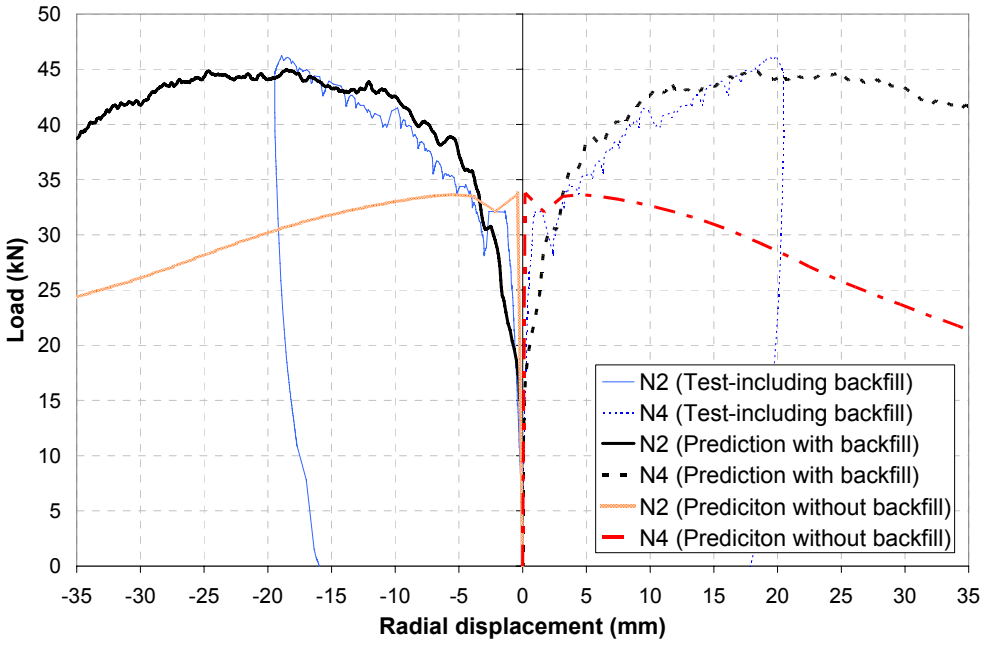

Figure 5.46 FE predictions from models with and without sand backfill

5.7.4 Effect of the sand material models

In the proposed detailed model, the sand backfill is modelled using the Mohr-Coulomb (M-C) plasticity model. The effect of the sand material is investigated in terms of the cohesion strength (c) and the internal friction angle (Φ).

Sand is usually treated as a cohesionless material; however, sand is usually given a small cohesion stress to avoid numerical problems during numerical modelling (Ai, 2010). A small cohesion may also arise from linear fitting of the test results. A cohesion of 100Pa was chosen in the proposed detailed model because it is the smallest value which can successfully avoid numerical difficulties and achieve a converged solution. Two larger cohesion stresses (0.5kPa and 1kPa) are applied to investigate its effect here. It is shown in Figure 5.47 that a larger cohesion stress leads to a higher loading capacity. This is because a higher cohesion strength results in an increased elastic behaviour of sand and a higher dispersal so the loading is more evenly distributed on the arch. Figure 5.48 and Figure 5.49 showed the interfacial shear stress distribution and the interfacial normal stress distribution from the models with different cohesion stress respectively. It is clear that a larger cohesion stress delivers an evener load distribution and greater interfacial stresses.

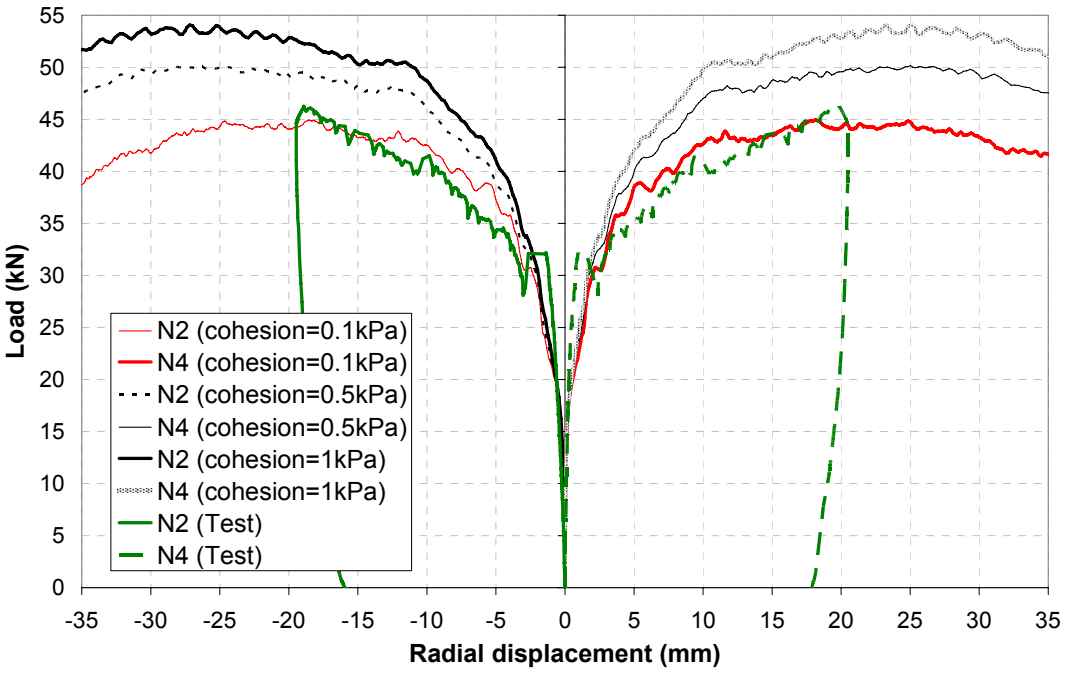

Figure 5.47 Load-deflection curves from the detailed model with varying cohesion stress of the backfill (*c*)

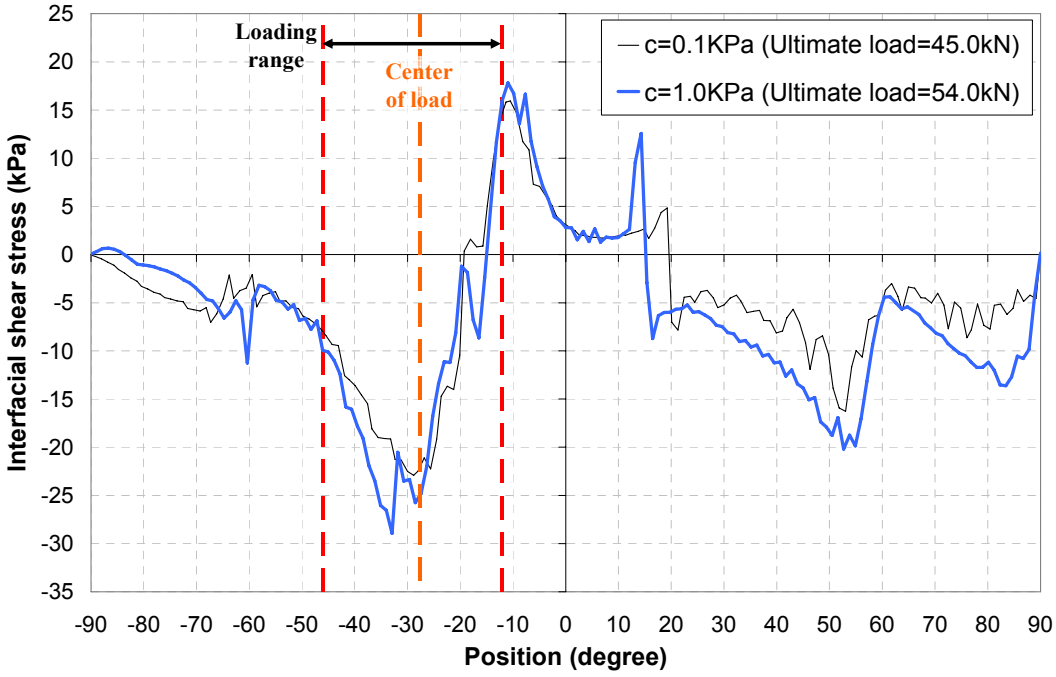

Figure 5.48 Interfacial shear stress at the interface between sand and extrados with different cohesion stress of the backfill

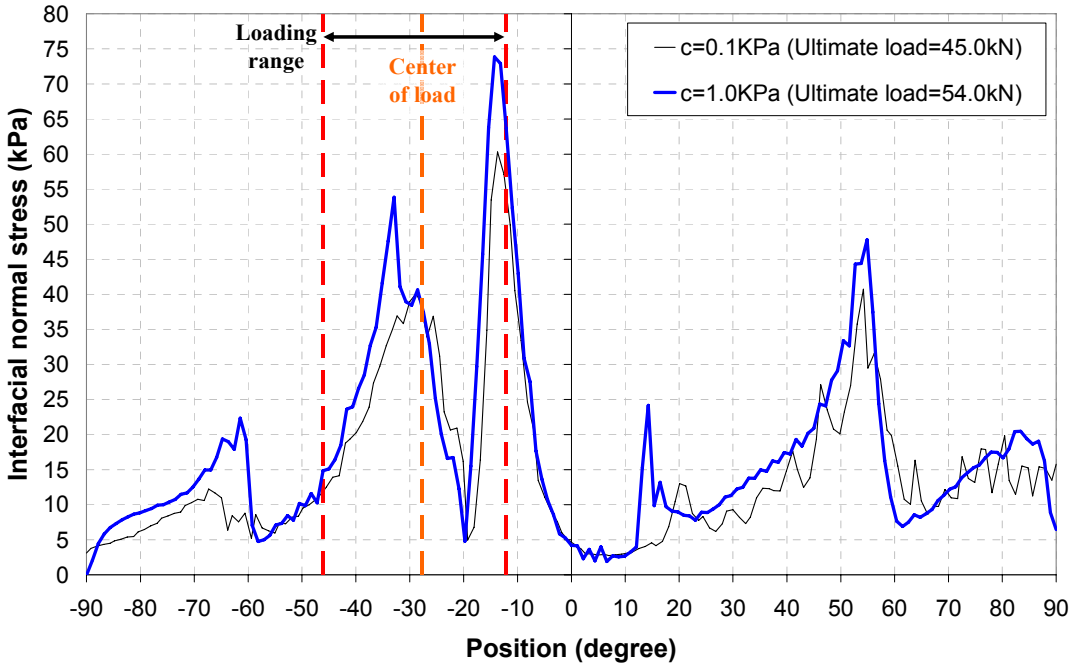

Figure 5.49 Interfacial normal stress at the interface between sand and extrados with different cohesion stress of the backfill

An internal friction angle of 33º obtained from the test was used in the proposed detailed model. The effect of the internal friction angle Φ is shown in Figure 5.50. It is clear that a larger internal friction angle leads to a higher loading capacity and stiffness of the arch. This is because a larger internal shear friction implies a higher shear strength under the same conditions, leading to a similar effect to a larger cohesion. The increases in the thrust forces eventually can increase the bending and shear resistance. Figure 5.51 and Figure 5.52 showed the interfacial shear stress distribution and the interfacial normal stress distribution from the models with different internal friction angle respectively. It is clear that a greater internal friction angle leads to more fluctuations in the stress distribution and greater interfacial stresses.

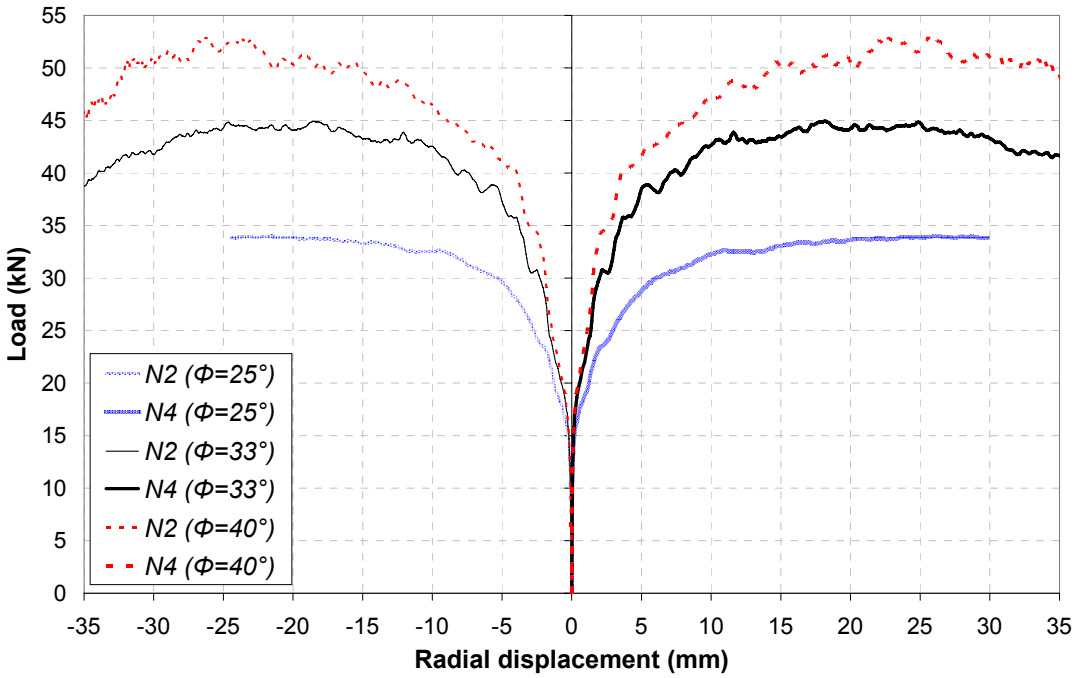

Figure 5.50 Arch deflections from the detailed solid models with varying internal friction angles of backfill Φ

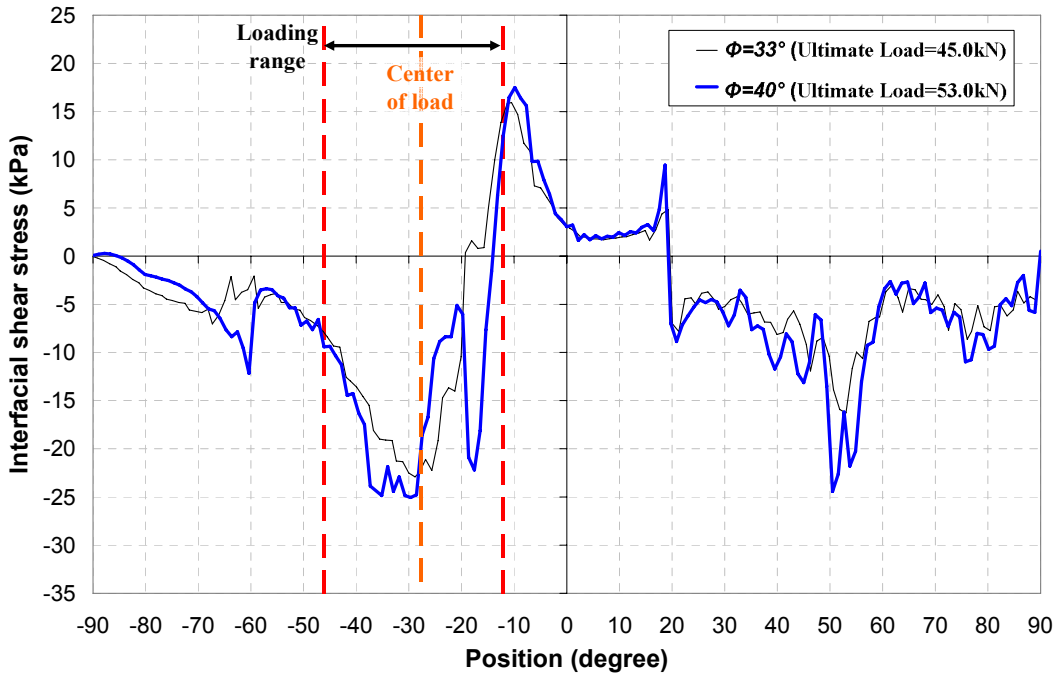

Figure 5.51 Interfacial shear stress at the interface between sand and extrados with different internal friction angles of the backfill

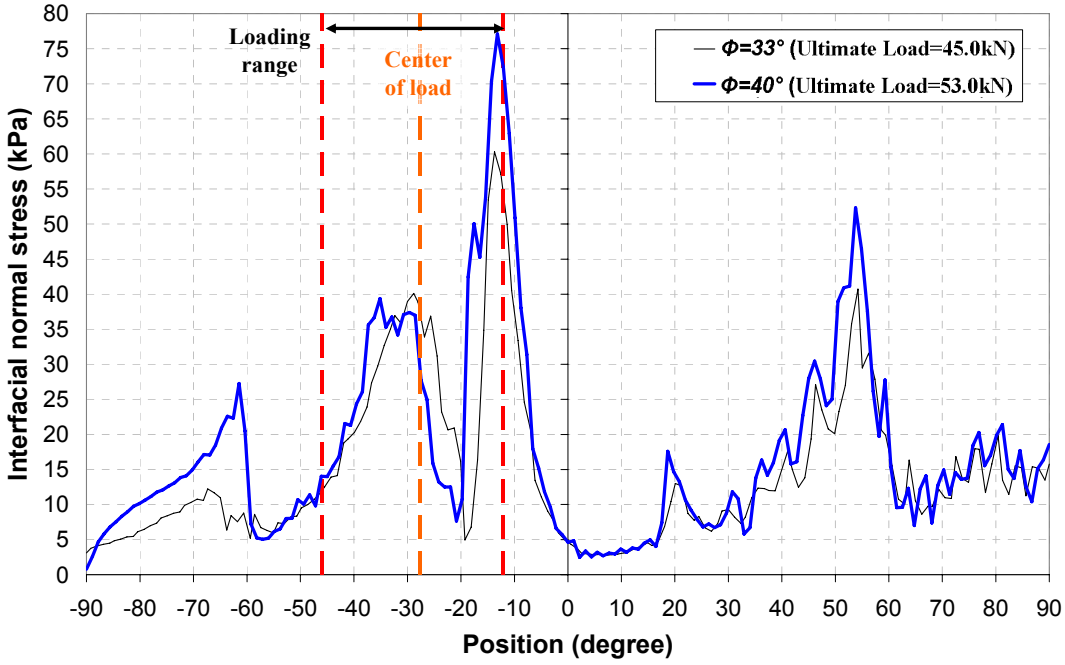

Figure 5.52 Interfacial normal stress at the interface between sand and extrados with different cohesion stress of the backfill

5. 8 Conclusions

This chapter has described a numerical study on masonry arch bridges with sand backfill. The arches were modelled using four different FE models: homogeneous model; traction-opening interface model, damaged plasticity interface model and detailed solid model. All models can successfully predict the behaviour of the masonry arches in regard to the load carrying capacity, hinge mechanism, and the contact behaviour between the backfill and the arches. The failure mode of the masonry arches is the four-hinge mechanism, which is significantly influenced by the modelling of the mortar interface. Therefore, in order to accurately capture the mechanism failure of masonry arch, the model including the interface is recommended. The increases of the tensile strength and the fracture energy of the

mortar interface leads to an increasing of the loading capacity.

The backfill has a significant effect on the load carrying capacity of the masonry arches. The presence of the backfill can increase the loading capacity of the masonry ach because it can disperse the load and provide a passive pressure to arch ring deformations. The sand backfill increase body shear resistance due to increased compression forces. The interaction between the backfill and the masonry is related to the formation of the mechanism and the lateral boundary conditions. An increase of the cohesion strength and the internal friction angle of the backfill lead to an increase of the capacity.

The damaged plasticity interface model and the detailed solid model give the best predictions. However, from the view of FE modelling, the detailed solid model is the most suitable for modelling of FRP strengthened masonry arches.

CHAPTER 6

FINITE ELEMENT MODELLING OF A CONCRETE MASONRY ARCH BRIDGE STRENGTHENED WITH FRP

6. 1 Introduction

Fibre reinforced polymer (FRP) systems are increasingly used for bridge repair and strengthening, with particularly widespread application to concrete bridge (ACI, 2008; CNR, 2006). However, the application of FRP composites to masonry structures is less well established, especially for masonry arch structures, although it has been the subject of research and development in recent years (De Lorenzis, 2008). Apart from the experimental study (Bati et al., 2007; Foraboschi, 2004; Valluzzi et al., 2001) and analytical study (Bati and Rovero, 2008; Chen, 2002), a very small number of studies have been devoted to the numerical modelling of reinforced masonry arches compared with reinforced concrete structures and reinforced masonry walls (Basilio, 2007; Drosopoulos et al., 2007; Kyriakides et al., 2012).

As reviewed in Chapter 2, five failure modes have been identified for FRP strengthened masonry arches: 1) mechanism failure; 2) sliding failure along the mortar joints; 3) compressive failure of the masonry (when there is a large amount of FRP strengthening); 4) tensile rupture of FRP; and 5) debonding failure at the interface between FRP and masonry (Bati and Rovero, 2008; Chen, 2002; De

Lorenzis, 2008; Foraboschi, 2004; Valluzzi et al., 2001). If arches are pre-damaged due to the formation of mechanism, the debonding failure usually starts from the existing hinge positions and develops towards either side of the hinge. For strengthening undamaged arches, the debonding occurs at the portion of masonry under greatest tensile or shear load. Debonding of the strengthening system often occurs slightly inside the masonry next to the FRP-masonry interface. The bond behaviour between FRP and masonry plays a significant role in the first two failure modes and in the debonding failure mode. An understanding of the bonding behaviour is therefore important for understanding the failure of FRP strengthened masonry arches. Less attention has been paid to numerical studies on FRP strengthened masonry arches due to the complex of masonry itself and the bond behaviour between FRP and masonry. As well as the masonry unit, the mortar-interface has significant effects on the performance of FRP strengthened arch structures because they are the weakest parts of the masonry assemblage. The bond interface between FRP and masonry is even more complicated due to material discontinuities in the system and the existence of both normal and shear interfacial stresses arising from the curved bond line. This chapter focuses on the numerical study of FRP strengthening masonry arch structures using the finite element (FE) method.

This chapter starts with a review of existing FE modelling strategies of FRP strengthened masonry arch structures to highlight challenges involved in numerical modelling. A detailed solid model for masonry and an interface model approach for modelling bond joint between masonry and FRP are then developed. A concrete

damaged plasticity model was used to model the masonry unit and the mortar interface. A mixed mode interface constitutive law, including both modes I and II, was used to model the bond behaviour between masonry and FRP. Apart from these aspects, two different modelling strategies were adopted, one without considering the existing damages from the previous tests and other considering these damages. The comparison between numerical and the test results is presented in order to exam the proposed FE models. The key parameters involved in the FE model are investigated to achieve an understanding on the behaviour of such strengthened structures.

6. 2 Existing FE modelling strategies

Chapter 2 has presented a comprehensive review on FRP strengthened masonry arch structures. This section focus on the FE modelling strategy of the strengthened masonry arch structures to highlight the challenges involved in numerical modelling and eventual solutions.

In the present study, the detailed solid model developed in Chapter 5 was used to model the masonry arch bridge. This detailed solid model simulates the masonry units with its actual size and mortar-interface as the geometry of mortar but with a small tensile strength to capture the interface behaviour.

As reviewed in Chapter 2 and 4, in terms of the bond behaviour between FRP and its substrate, three approaches have been adopted in the previous studies: 1) detail model approach which models the debonding in details in substrates material and therefore requires very a fine mesh (such as, Lu et al. (2006; 2005b)); 2) interface

model approach which uses a zero-thickness interface element with a constitutive law considering the bond-slip relationship to directly model the bond behaviour between FRP and its substrate (such as, Diab and Wu (2007); Salomoni et al. (2011)); 3) crack band model which defines a range of substrate underneath the bond interface with modified constitutive laws (such as, Coronado and Lopez (2007; 2010)). The detail model approach is not appropriate for modelling large structures such as masonry arch bridges due to the consideration of computational effort (Chen et al., 2011). The crack band model requires more parameters for the band zone and thus is not suitable for a prediction model (Coronado and Lopez, 2007). Therefore, the interface model is adopted in this study to model the bond behaviour between FRP and masonry arches.

For a 2-D FE model including the interface elements at the FRP-masonry joints, there was a challenge in dealing with locations where multiple interfaces meet, for example, where the mortar-brick interface and the FRP-masonry interface intersect. All nodes of the element have the same coordinates when two zero-thickness interfaces intersect, which is not permitted in the FE modelling. Existing FE models adopted several methods to tackle this challenge. Drosopoulos et al. (2007) included only zero thickness interface elements for the brick-mortar interfaces and modelled the FRP-to-masonry bond interface using a frictional contact method for mode-II behaviour and spring elements for mode-I behaviour. Basilio (2007) and Kyriakides et al. (2012) adopted the same six-node interface elements (available in DIANA) for both the brick-mortar interface and the FRP-to-masonry bond to achieve mesh compatibility. Unfortunately, such 6 node interface element is not available in

ABAQUS (2007).

In this study, a detailed solid model for masonry and an interface model for the FRP-to-masonry bond were adopted. The mesh compatibility can be achieved because the mortar interface is smeared in the mortar. Compared with the aforementioned approach using frictional contact elements, the present model includes zero thickness interface elements for the FRP-to-masonry bond and is able to consider the mixed mode behaviour.

6. 3 Finite element model

The two span masonry arch bridge in the experimental study described in Chapter 3 is modelled using ABAQUS (2007). The details of arches are shown in Figure 6.1. The masonry arch bridge was strengthened by bonding FRP plates into their intrados. A 2-D plan strain assumption is assumed and a displacement control method is adopted. The loading on the bridge includes the gravity and the applied load. The loading plate was not included in the model and the load was directly applied into the sand backfill in the position of loading plate. The entire arches are modelled and the loading plate is not included in the model. That is because loading was only applied on a single span in the tests so the problem was unsymmetrical. The actual width of each material was applied to the out-of-plane thickness in the models.

In terms of the boundary conditions, the abutments were restrained in all directions because they were connected to the strong floor, as shown in Figure 6.1. The timber retaining wall at each end of the bridge was securely connected to the side wall, and

substantial support of the end walls was provided by an arrangement of steel beams which were bolted to the floor (Prentice, 1996). Therefore, the boundary at both ends is not fully restrained but deformable laterally. This deformation was observed during the test and led to a gap between the abutment and the timber walls, and consequently some sand leaked out from this gap. The boundary at both ends thus was modelled using springs (element: Spring A). The stiffness of the springs was determined by treating the timber wall as an elastic plate with three edges simply supported and the top edge free. The spring stiffness is determined as the inverse of the deflection at the relevant location under a unit concentrated load at the same location. Details can be found in Chapter 5. The models of sand backfill, the abutments and the timber retaining walls are same as that in the modelling of unstrengthened masonry arch described in Chapter 5.

The arches were tested until the formation of a hinge mechanism and then strengthened by bonding FRP into their intrados. However, this damage situation (hinge mechanism) was initially not simulated for simplicity. An advanced model including the damage situation was developed in later of this chapter (section 6.5.2). The FE mesh is shown in Figure 6.2.

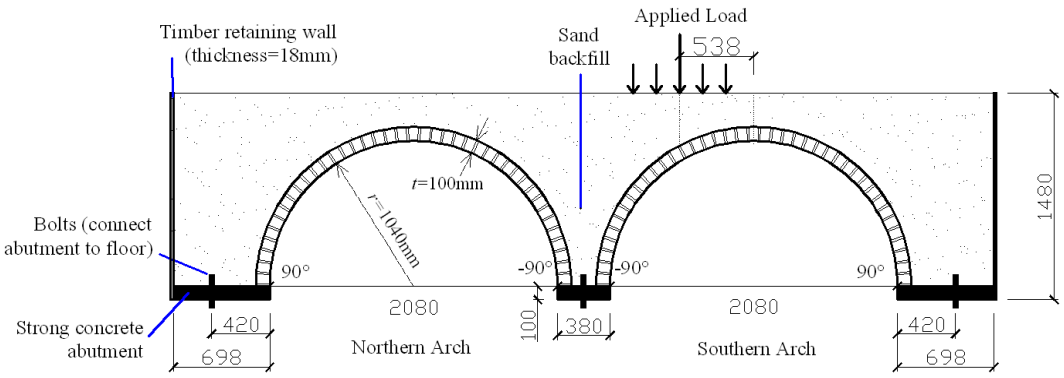

Figure 6.1 The test masonry arch bridge (mm)

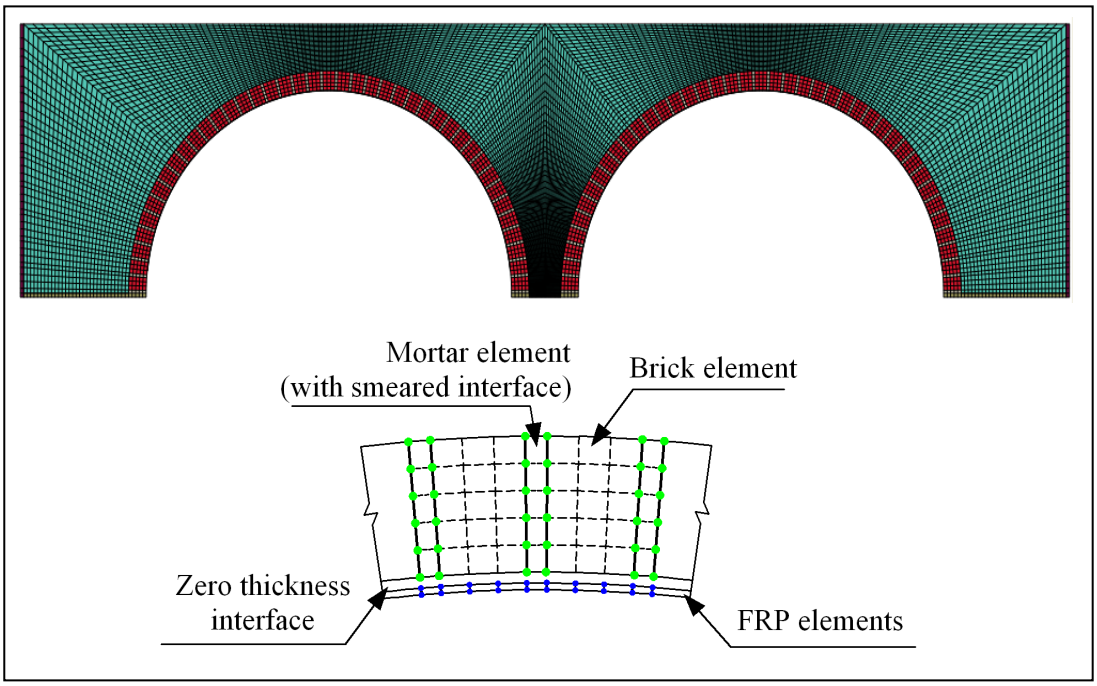

Figure 6.2 FE mesh of FRP strengthened masonry arch bridge

6.3.1 Modelling of masonry arches

The detailed solid model developed in Chapter 5 is used to model the masonry arches. Apart from modelling the masonry units with its actual size, the detailed solid model simulates the mortar-interface as the geometry of mortar but with a low tensile

strength representing the tensile strength of the mortar-brick interface. The masonry unit and mortar layer are modelled using the plane strain element (CPE4) with common nodes. The average thickness of mortar was 15mm and there were total of 41 bricks in the model bridge. The element size for mortar was about 15×20mm^2 and that for masonry unit was about 20×20mm^2.

A concrete damaged plasticity model available in ABAQUS (2007) was used to model both the masonry unit and mortar. The parameters used are summarised in Table 6-1.

Table 6-1 Material parameters of the masonry arch bridge

Materials	Parameters	Values
Bricks	Compressive strength f_{cb}	58.2 (MPa)
	Tensile strength f_{tb}	4.1 (MPa)
	Fracture energy G_{fb}^{I}	0.12 (Nmm/mm^2)
Mortar joint	Compressive strength f_{ci}	12 (MPa)
	Tensile strength f_{ti}^{0}	0.1 (MPa)
	Mode-I fracture energy G_{cn}^{0}	0.066 (Nmm/mm^2)

The uniaxial compression behaviour of both masonry unit and mortar is modelled using the relationship proposed by Saenz (1964) for plain concrete:

$$\sigma_c = \frac{E_0 \varepsilon_c}{1 + \left(\frac{E_0 \varepsilon_p}{\sigma_p} - 2 \right) \left(\frac{\varepsilon_c}{\varepsilon_p} \right) + \left(\frac{\varepsilon_c}{\varepsilon_p} \right)^2} \tag{6-1}$$

where σ_c and ε_c are respectively the compressive stress and strain, σ_p and ε_p are the experimentally determined maximum stress and its corresponding strain which are taken to be the compressive strength and 0.0022 respectively, E_0 is the elastic modulus of material.

The tensile behaviour of both concrete brick and mortar joint is modelled using the model developed by Hordijk (1991) for plain concrete as Eq. 6-2. Pluijm (1997) verified that this formulation can describe the tensile behaviour of both the unit and the mortar.

$$\frac{\sigma_t}{f_t} = \left[1 + \left(c_1 \frac{w_t}{w_{cr}}\right)^3\right] e^{\left(-c_2 \frac{w_t}{w_{cr}}\right)} - \frac{w_t}{w_{cr}}\left(1 + c_1^3\right) e^{(-c_2)}, \; w_{cr} = 5.14 \frac{G_F}{f_t} \quad (6\text{-}2)$$

where w_t is the crack opening displacement, w_{cr} is the crack opening displacement at the complete loss of tensile stress, σ_t is the tensile stress normal to the crack direction, f_t is the uniaxial tensile strength, and c_1 =3.0 and c_2 =6.93 are dimensionless constants determined from tensile tests. It is noticed that c_1 and c_2 may be variable because they depend on water/cement ratio and the strength of the mortar.

A damage model based on the plastic degradation theory developed in Chapter 4 was applied to describe the damage effects of both bricks and mortar interface. The details of this damage model can be found in Chapters 4 and 5.

6.3.2 Modelling of masonry-to-FRP bond interface

The FRP-to-masonry bond interface was modelled using the zero thickness cohesive elements (COH2D4) available in ABAQUS (2007) as shown in Figure 6.2. The cohesive elements connect to the masonry arches through the common nodes. There are two types of interface element at the FRP-to-masonry bond interface, one between FRP and bricks, the other between FRP and mortar.

The bond behaviour between masonry and FRP was modelled using a traction opening constitutive model available in ABAQUS (2007). Both mode-I (normal) and mode-II (shear) bond behaviour were modelled because the interfacial normal stress that coexists with the interfacial shear stress due to the curved bond joint. The individual local bond behaviour was modelled by introducing a bond-slip relationship for mode-II or a traction-opening relationship for mode-I behaviour. The interaction between two modes was modelled by a power law criterion (Eq. 6-9).

In terms of the FRP-to-brick bond behaviour, there is less research on the mode-I debonding behaviour. The failure of a FRP-to-concrete bond joint under tensile action being perpendicular to the bond interface occurs usually in the concrete (Coronado and Lopez, 2008). To investigate the mode-I behaviour of the bond interface of FRP-to-masonry, Oliveira et al. (2011) conducted a pull-off test with action being perpendicular to the bond interface. The results showed that failure was due to the ripping of a thin layer of brick and mortar. It is similar to that in the FRP-to-concrete bonded joint. The masonry tensile strength is adopted to model the mode-

I behaviour of the FRP-to-brick bond because the debonding strain predicted by Lu et al.'s (2005a) model using the masonry tensile strength (1.99MPa) is in good agreement with the test value as discussed in Chapter 3. A traction-opening model as shown in Figure 6.3a is used to describe the mode-I behaviour of the bond joint. A linear softening is assumed for simplicity. The interfacial elastic stiffness for the traction-opening model in mode-I (k_{nn}) is given by $k_{nn}=E/L$, where E is the elastic modulus of masonry determined experimentally as 16000MPa, L is the constitutive thickness of the interface layer and set as unit thickness in the FE model, which ensure that the nominal strain has the same value as the separation when the geometry thickness of interface is equal to zero (ABAQUS, 2007). The mode-I fracture energy of masonry G_f^I is estimated from the CEB-FIB (1991) model for concrete which is related to the cylinder compressive strength f_c (masonry compressive strength 25MPa in this study) and maximum aggregate size d_a (assuming 20mm in this study) as Eq. 6-3:

$$G_F = \left(0.0469 d_a^2 - 0.5 d_a + 26\right)\left(\frac{f_c}{10}\right)^{0.7} \tag{6-3}$$

For the mode-II behaviour of FRP-to-brick bond interface, the bilinear bond-slip model developed by Lu et al. (2005a) as shown in Figure 6.3b is adopted. The parameters involved in the bond-slip model are:

$$\tau_{\max} = 1.5 \cdot \beta_w \cdot f_t \tag{6-4}$$

$$G_f^{II} = 0.308 \cdot \beta_w^2 \cdot \sqrt{f_t} \tag{6-5}$$

$$s_s^0 = 0.0195 \cdot \beta_w \cdot f_t \tag{6-6}$$

$$\beta_w = \sqrt{\frac{2 - b_f / b_c}{1 + b_f / b_c}} \tag{6-7}$$

where $\tau_{\max}$ and S_s^0 are the maximum interfacial shear stress and the corresponding slip, f_t is the tensile strength of the masonry, G_f^{II} is the mode-II fracture energy of the bond interface, β_w is the width ratio factor proposed by Chen and Teng (2001), b_f and b_c are the width of FRP and masonry arches.

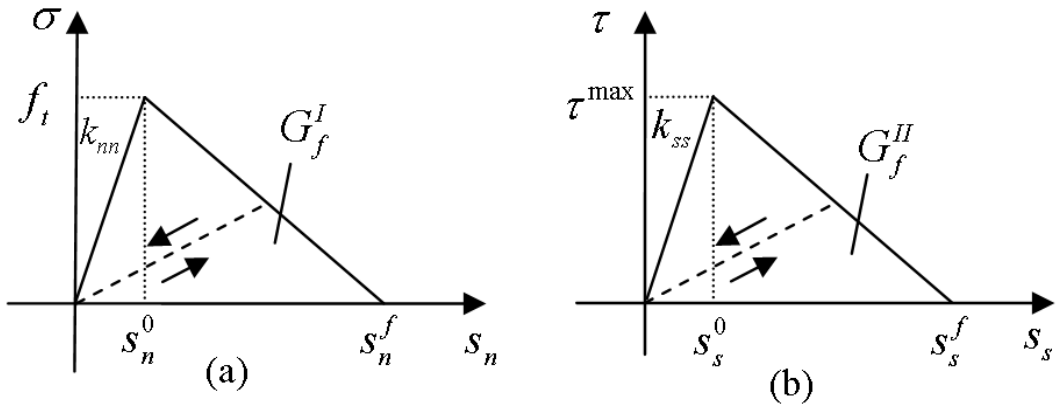

Figure 6.3 Traction-opening relationship of FRP-to-masonry bond behaviour: (a) mode-I, (b) mode-II

In terms of the FRP-to-mortar bond interface, the mode-I behaviour was modelled by the traction-opening relationship shown in Figure 6.3a. The maximum interfacial normal stress f_t was taken as the tensile strength of the mortar-brick interface

(0.1MPa). The mode-I fracture energy G_f^I was assumed as 0.005Nmm/mm^2 and the interfacial elastic stiffness k_{nn} is assumed as 5000MPa/mm.

For the mode-II behaviour of FRP-to-mortar interface, the bilinear bond-slip model shown in Figure 6.3b was adopted. However, the bond-slip model developed by Lu et al. (2005a) may not be suitable for very low tensile strength materials such as the case here. In order to estimate the mode-II fracture energy G_f^{II}, the maximum slip S_s^f for FRP-to-mortar interface is assumed to be equal to that for the FRP-to-brick interface, the maximum interfacial shear stress $\tau_{\max}$ and the corresponding slip S_s^0 are calculated using Eqs. 6-4 and 6-6. The material properties for the bond interfaces are summarized in Table 6-2.

Table 6-2 Material properties of bond interfaces

Parameters		3 FRP plate strengthening (North arch)		6 FRP plate strengthening (South arch)	
		FRP-bricks	FRP-interface	FRP-bricks	FRP-interface
Mode-I	f_t (MPa)	1.99	0.1	1.99	0.1
	G_f^I (Nmm/mm^2)	0.066	0.005	0.066	0.005
	k_{nn} (MPa/mm)	16000	5000	16000	5000
Mode-II	τ_{max} (MPa)	3.71	0.18	3.29	0.16
	G_f^{II} (Nmm/mm^2)	0.67	0.03	0.53	0.02
	k_{ss} (MPa/mm)	76.9	76.9	76.9	76.9

The interaction between the two modes was modelled using a damage initiation (Eq. 6-8) and a damage evolution law (Eq. 6-9). The damage initiation law is used to define the onset of damage, corresponding to the initiation of softening (ABAQUS, 2007). The damage evolution law describes the rate at which the material stiffness is degraded once the corresponding initiation criterion is reached (ABAQUS, 2007).

The maximum stress criterion (Eq. 6-8) is used to model the damage initiation law in this study.

$$\max\left\{\frac{\langle\sigma\rangle}{f_t}, \frac{\tau}{\tau_{\max}}\right\} = 1 \tag{6-8}$$

The Macaulay brackets in Eq. 6-8 signifies that pure compressive stress state does not initiate damage (ABAQUS, 2007). This criterion also implies that the shear stress does not increase when the interface is under compression.

A power law criterion available in ABAQUS (2007), which was originated from the model proposed by Wu and Reuter (1965), is used to define the damage evolution behaviour. The power law criterion is defined in terms of an interaction between the energy release rates as following:

$$\left(\frac{G_I}{G_{IC}}\right)^{\alpha} + \left(\frac{G_{II}}{G_{IIC}}\right)^{\alpha} = 1 \tag{6-9}$$

where G_{IC} and G_{IIC} refer to the critical fracture energies required to cause failure in the pure normal (mode-I) and shear (mode-II) direction, respectively. G_I and G_{II} represent the work done by the traction and its conjugate relative displacement in the normal and shear direction, respectively. α is the power ration to define the interaction behaviour. In this study, $\alpha=2$ was assumed in the current model and the effects of this parameter was investigated in the later of this chapter.

6.3.3 Modelling of FRP

The FRP composite is modelled using a plane stress element (CPS4) available in

ABAQUS (2007). The thickness of FRP was 1.4mm. The elements of FRP are connected to the bond interface elements through sharing common nodes.

The mechanical properties of FRP composites depend on the fibre orientation and distribution and the relative proportions of fibre and matrix. Their macro properties can be estimated from the fibre and adhesive properties using the law of mixtures (Vinson and Sierakowski, 2002). In this study, the matrix was assumed to have the same properties as the adhesive. Thus, the properties of the FRP can be deduced from the fibre and adhesive properties and fibre volume ratio.

The law of mixture which Vinson and Sierakowski (2002) suggested is an approach developed by Hahn (1980) to predict the mechanical properties of FRPs by codified results for unidirectional fibres of circular cross section which are randomly distributed in a plane normal to the fibre direction. This approach assumes that both the fibre and matrix are isotropic materials and that the FRP composite behaves as a transversely isotropic material. Assuming the properties are the same in the 2-3 plane, and different in the 1 plane, which is normal to the 2-3 plane, the elastic properties involve only five engineering constants, namely, E_1, E_2, ν_{12}, ν_{23}, and G_{12}, where 1 is the fibre direction, E_1 and E_2 are the longitudinal modulus and transverse modulus of FRP respectively, ν_{12} and ν_{23} are the major Poisson's ratio in 1-2 plane and the Poisson's ratio in 2-3 plane, respectively, and G_{12} is the shear modulus in 1-2 plane.

Based on the rules of mixtures, and assuming that the fibres and the matrix deform compatibly when an FRP lamina is subjected to uniaxial loading in the fibre direction,

the longitudinal modulus E_1 and the major Poisson's ratio ν_{12} of FRP can be found from the following simple equations:

$$E_1 = E_f V_f + E_{mx} V_{mx} \tag{6-10}$$

$$\nu_{12} = \nu_f V_f + \nu_{mx} V_{mx} \tag{6-11}$$

where E_f is the elastic modulus of the isotropic fibres; ν_f is the major Poisson's ratio of the fibres; E_{mx} and ν_{mx} are the elastic modulus and the Poisson's ratio of the matrix, respectively; and V_f and V_{mx} are the volume fractions of fibres and matrix, respectively. For the rest of the elastic constants Hahn (1980) states the following equations:

$$P = \frac{\left(P_f V_f + \lambda P_{mx} V_{mx}\right)}{\left(V_f + \lambda V_{mx}\right)} \tag{6-12}$$

in which

P = FRP composite properties $1/G_{12}$, $1/G_{23}$, or $1/K_T$

P_f = fibre properties $1/G_f$, or $1/K_f$

P_{mx} = matrix properties $1/G_{mx}$, or $1/K_{mx}$

in the above K_T is the plane strain bulk modulus,

$K_f = E_f/2(1-\nu_f)$ and $K_{mx} = E_{mx}/2(1-\nu_{mx})$. The λ values are given by:

when $P = 1/G_{12}$,

$$\lambda_6 = \frac{1+G_{mx}/G_f}{2} \tag{6-13}$$

when $P = 1/G_{23}$

$$\lambda_4 = \frac{3-4\nu_{mx}+G_{mx}/G_f}{4(1-\nu_{mx})} \tag{6-14}$$

When $P = 1/K_T$

$$\lambda_K = \frac{1+G_{mx}/K_f}{2(1-\nu_{mx})} \tag{6-15}$$

The transverse modulus of FRP, E_2, can be found from the following equation:

$$E_2 = \frac{4K_T G_{23}}{K_T + mG_{23}} \tag{6-16}$$

where

$$m = 1 + \frac{4K_T \nu_{12}^2}{E_1} \tag{6-17}$$

Hahn (1980) suggests that for most structural composites, $G_{mx}/G_f < 0.05$, then $\lambda_6 \approx 0.5$; furthermore, since for most epoxies, $\nu_{mx} = 0.35$, then $\lambda_4 = 0.62$ and $\lambda_K = 0.77$. Finally, the Poisson's ratio, ν_{23}, can be written as:

$$\nu_{23} = \nu_f V_f + \nu_{mx}\left(1 - V_f\right)\left[\frac{1 + \nu_{mx} - \nu_{12}\left(\frac{E_{mx}}{E_1}\right)}{1 - \nu_{mx}^2 + \nu_{mx}\nu_{12}\left(\frac{E_{mx}}{E_1}\right)}\right] \tag{6-18}$$

The parameters from the manufacturer's datasheet for CFRP are summarized in Table 6-3 and the orthotropic properties can be conducted from the above method.

Table 6-3 Properties of CFRP from the manufacturer

E_{11} (GPa)	E_{mx} (GPa)	ν_f	V_f
170	5	0.2	0.63

6. 4 Results and discussions

The results from the FE model are compared with the test results in this section. The deflection, FRP strain, and crack opening width are investigated.

The mesh convergence analysis has been conducted in the Chapter 5 for the unstrengthened arches and shown the mesh convergence is achieved. The average element size for bricks was 21mm×20mm and 18mm×20mm for the mortar interfaces in this study.

6.4.1 Results from the northern arch

The northern arch was repaired by bonding 3 FRP plates onto their intrados. The load-deflection, FRP strain, and crack opening width are investigated in the following sections.

6.4.1.1 Load-deflection response

The comparison of the load-defection responses from the FE model and the test is shown in Figure 6.4. The loading capacity obtained from the FE model (132.2kN) is in good agreement with that from the test (132kN). The initial stiffness (when load is less than 90kN) is also close to that from the test. However, the FE model predicts stiffer results when the load is greater than 90kN. That is probably because the FE model does not consider the existence of the four hinge mechanism and the residual deformation priori to strengthening.

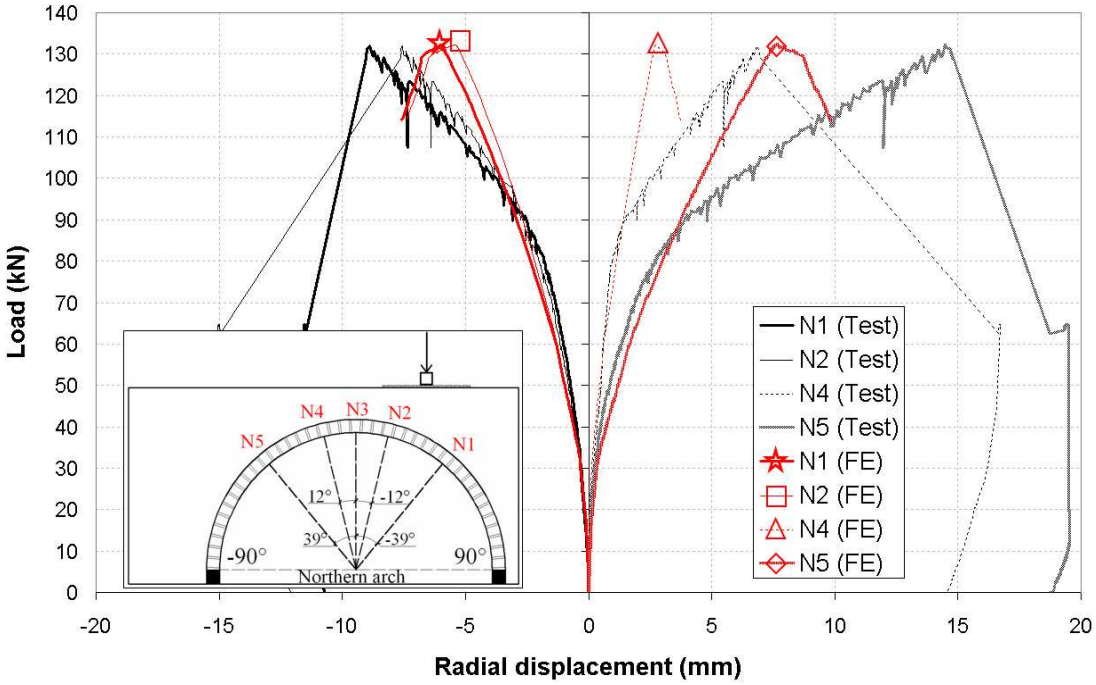

Figure 6.4 Load-deflection curve for the north arch: test vs FE prediction

6.4.1.2 FRP strain responses

The comparison of the FRP strain at the two critical cracks (C_{N1} and C_{NA}) from the test and the FE model is shown in Figure 6.5. It can be seen that the FE prediction for the FRP strain at crack C_{N1} was larger than that from the test. The debonding strain predicted by the FE model is 2491με, which is about 10% larger than the test maximum strain of 2250με. At crack C_{NA}, the FE prediction is smaller than that from the test but shows a similar trend. The FE delivered an unsafe prediction about the debonding strain. It can be attributed to the following reasons: 1) the loading was directly applied onto the sand backfill in the FE model but was on a loading plate in the test; 2) the FE model does not include the existing damages in the masonry arches priori to FRP strengthening; 3) the damage initiation law (Eq. 6-8) does not consider the increase of the shear stress when the interface is under compression; 4)

the method for estimating the lateral boundary conditions representing the timber retaining walls may be not accurate.

The comparison of the distribution of longitudinal FRP strain from the test and the FE model is shown in Figure 6.6. It can be found that the FE model predicts a similar strain distribution as the test. For example, the maximum tensile strain is located at crack C_{N1} which is beneath the loading area; the strain decreases towards either side of the crack. The locations of the two peak compression strain (-40° and 78°) are consistent with the two extrados cracks in the test. The peak compression strain at -40° is larger than that at 78°. The FRP strain at crack C_{NA} at -20° changes from compression to tension when the load increases above 60kN (Figure 6.5), indicating that the intrados at this crack is changed from tension to compression (Figure 6.6).

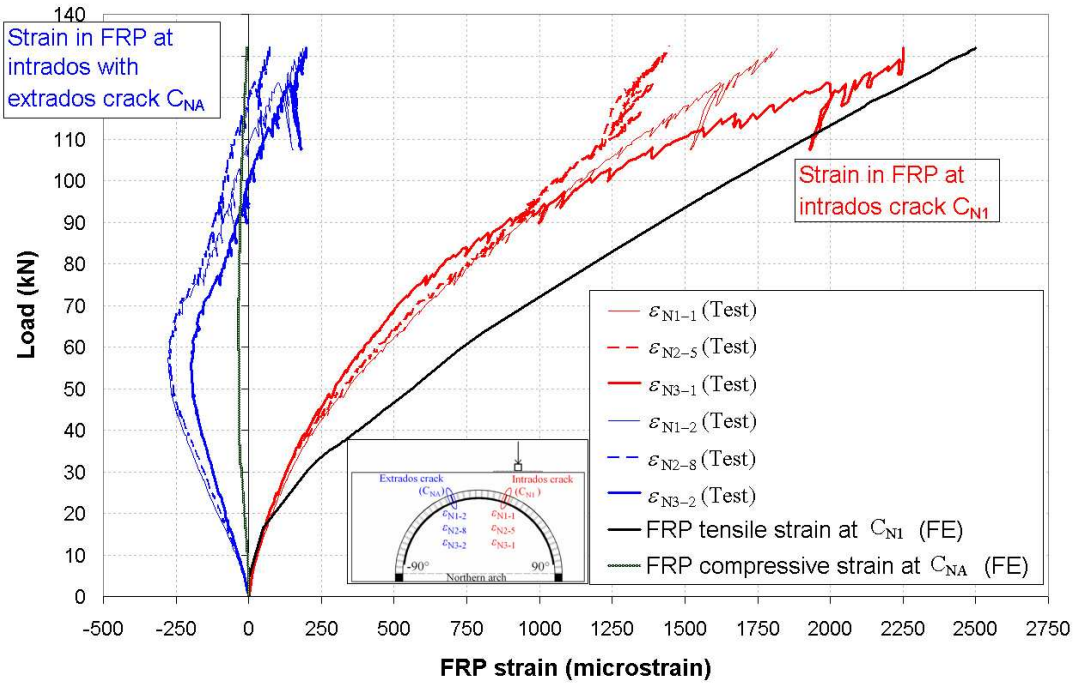

Figure 6.5 FRP strain at two critical cracks in the north arch: test vs FE prediction

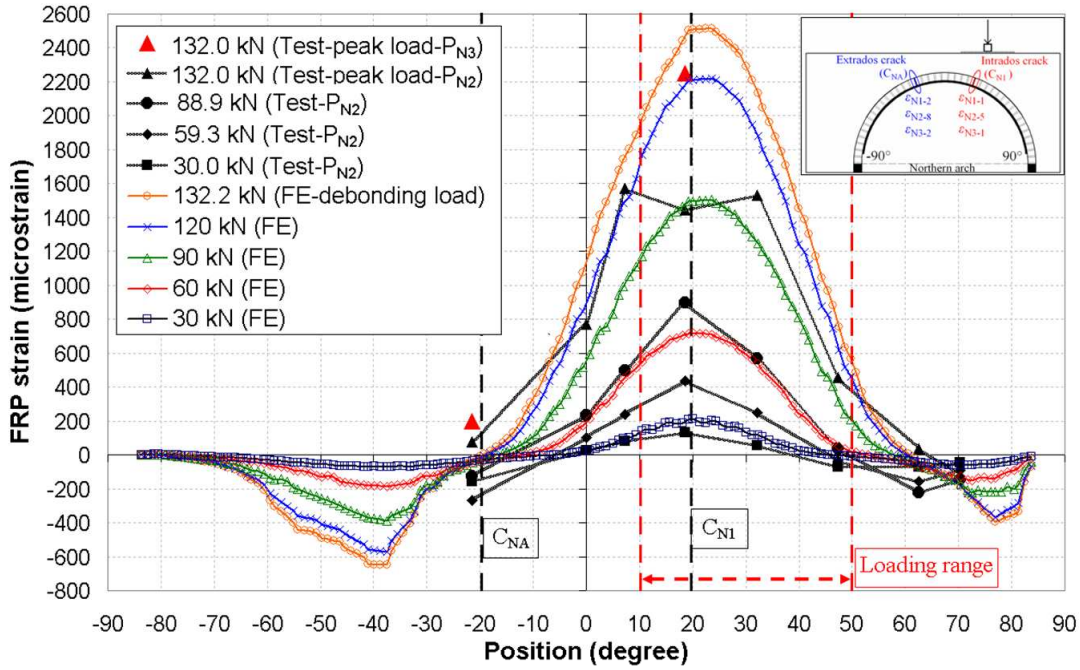

Figure 6.6 Distribution of longitudinal FRP strain (P_{N2} & P_{N3}) in the north arch: FE prediction vs test

6.4.1.3 Masonry joint opening width

The comparison of the joint opening width at two critical cracks (C_{N1} and C_{NA}) from the test and FE prediction is shown in Figure 6.7. It is shown that the joint opening width at crack C_{N1} (w_{N1}) from the FE model was in good agreement with the test results (w_{N1E} & w_{N1W}). The FE prediction for the joint opening width at C_{NA} (w_{NA}) showed the similar trend to the test results (w_{NAE} & w_{NAW}) but the value was smaller. This can be attributed to the aforementioned reasons in section 6.4.1.2. The existing damage from the previous tests was not considered in the FE model, which led to a coarse prediciton on the closing of the joint opening at extrados crack C_{NA}.

The distributions of the crack opening width at the mortar-brick interface in the

intrados and extrados obtained from the FE analysis are shown in Figure 6.8 and Figure 6.9 respectively. It can be found from Figure 6.8 that the FRP strengthening effectively prevents the opening of intrados cracks. Several intrados cracks opened beneath the loading area and consequently resulted in the debonding failure. There is also another major intrados crack at -90° because it was not strengthened by FRP plates, which also led to the significant opening of the crack.

The predicted joint opening width at the extrados (Figure 6.9) was greater than at the intrados (Figure 6.8) due to no the presence of FRP strengthening in the extrados. It can be found from Figure 6.9 that several extrados cracks opened at the range of -65° to -20° and 65° to 85°. The location of the major crack C_{NC} (-38°) matched with that from the test. It is worth noting that the extrados cracks C_{NA} and C_{NB} had formed in the test in the original arch. The extrados crack C_{NB} continuously opened after strengthening but crack C_{NA} closed when the load is greater than 60kN. An additional extrados crack C_{NC} formed during the test on the strengthened arch. In the FE analysis, the opening of the crack C_{NC} is predicted properly. Several extrados cracks at the range of 65° to 85° were predicted by the FE model because this range is closed to the end of FRP strengthening.

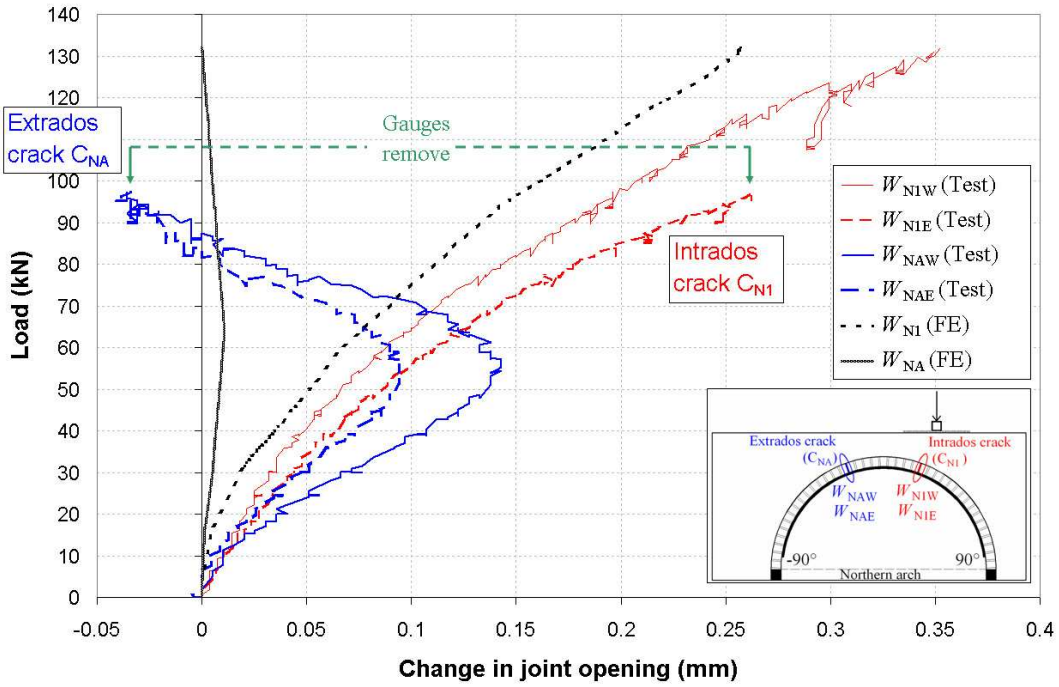

Figure 6.7 Change in joint opening: test vs FE prediction in the north arch

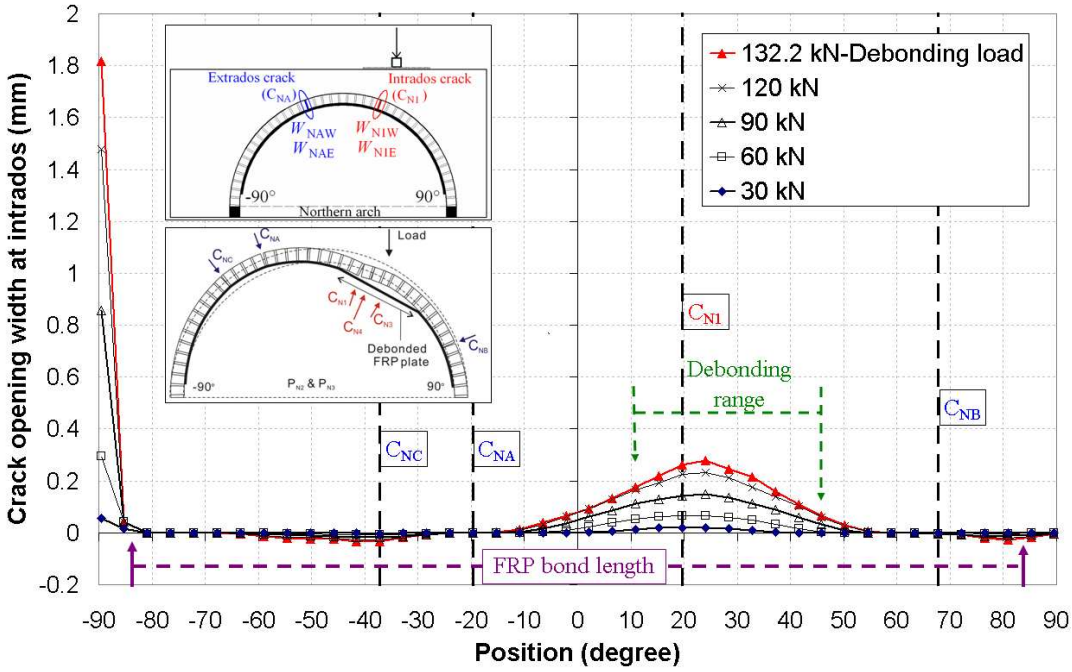

Figure 6.8 FE prediction of joint opening width at the intrados in the north arch

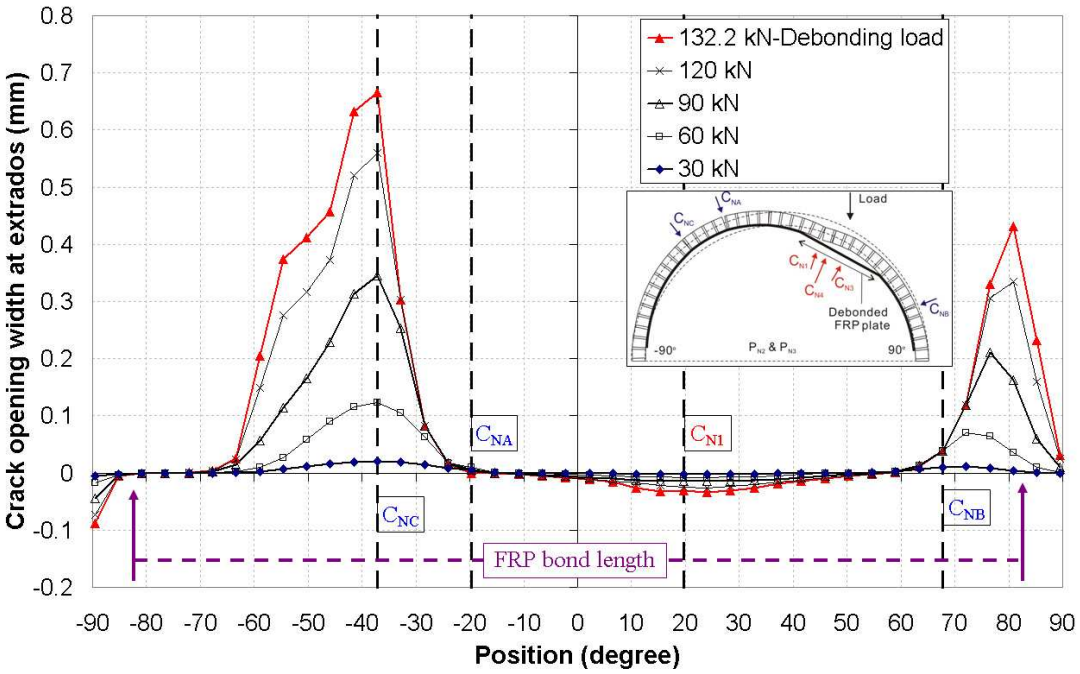

Figure 6.9 FE prediction of joint opening width at extrados in the north arch

6.4.1.4 Discussion of results for the northern arch

The test results show that the FRP strain at intrados below extrados crack C_{NA} changed sign from compression to tension (Figure 6.5) when the load increased above 60kN, leading to the close of this extrados crack (Figure 6.7). It can be attributed to the formation and opening of the neighbouring extrados cracks (C_{NB} and C_{NC} in the test) as shown in Figure 6.9 (two major cracks at -38° and 82° in the FE prediction). The development of those extrados cracks led to the greater deformation when the load is over 90kN as shown in Figure 6.4.

6.4.2 Results from the southern arch

The southern arch was repaired by bonding 6 FRP plates onto the intrados and was

tested after the northern arch was tested to debonding failure. The load-deflection, FRP strain, and crack opening width are analyzed in the following sections.

6.4.2.1 Load-deflection response

The comparison of load-deflection response from the test and FE prediction is shown in Figure 6.10. It can be found that the loading capacity predicted by the FE model (250.1kN) is in good agreement with that from the test (253.8kN). The stiffness was also close to that from the test when the load is less than 180kN. However, the FE model predicts a stiffer response when the load is greater than 180kN. One possible cause of this phenomenon may be that the FE model does not consider the formation of the four hinge mechanism and the residual deformation caused by the loading on the original arches. The differences between the FE prediction and test for the southern arch (Figure 6.10) are smaller than that from the northern arch (Figure 6.4), probably because the residual deformation from the test on the original southern arch is smaller than that from the test on the original northern arch as described in Chapter 3.

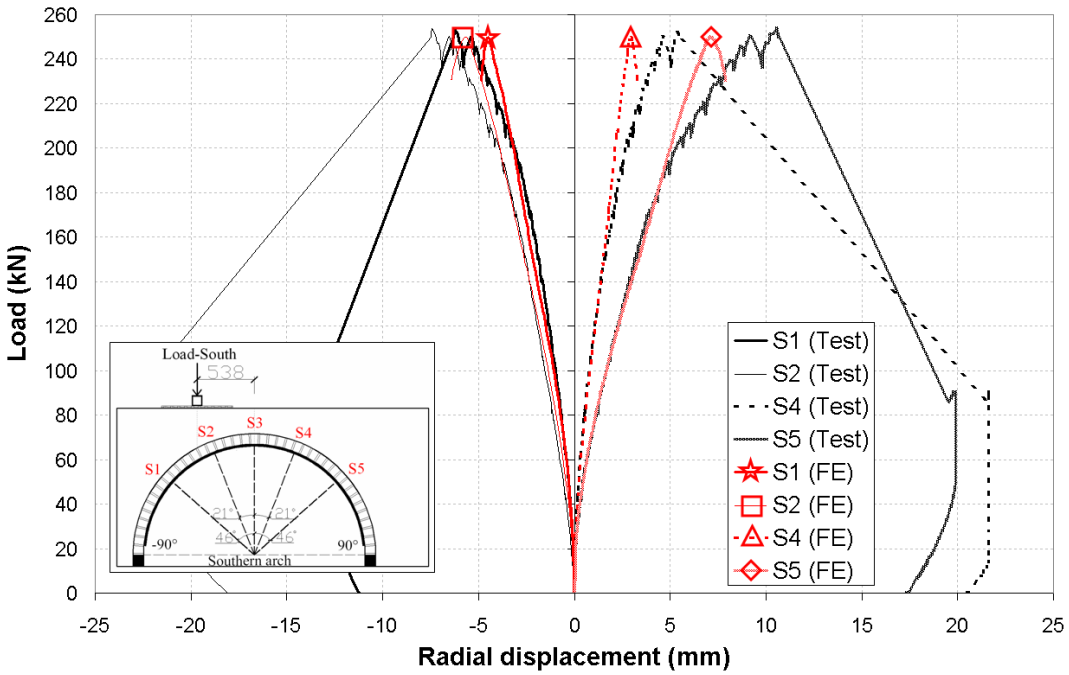

Figure 6.10 Load-deflection for the south arch: test vs FE prediction

6.4.2.2 FRP strain responses

The comparison of FRP strain from test and FE prediction at two critical cracks (C_{S1} and C_{SA}) is shown in Figure 6.11. It can be seen that the FE prediction for the FRP strain at the crack C_{S1} is larger than that from the test results ($\varepsilon_{S1\text{-}1}$, $\varepsilon_{S4\text{-}6}$, $\varepsilon_{S6\text{-}1}$) but has the similar increasing trend. The debonding strain predicted by the FE model is 2302με is very close to the maximum strain obtained from the test (2250 με). For the FRP strain at crack C_{SA}, the FE prediction is in good agreement with test result when the loading is lower than 140kN. The test results at $\varepsilon_{S1\text{-}2}$ and $\varepsilon_{S6\text{-}2}$ indicate that the FRP was under tension when the load is above 200kN. This changing level is at 140kN in the FE prediction. Apart from the reasons summarized in section 6.4.1.2, the differences between FE prediction and test also caused by the effects on the stress distribution from existing debonding failure on the neighbouring (northern) arches,

which is not considered in the FE prediction.

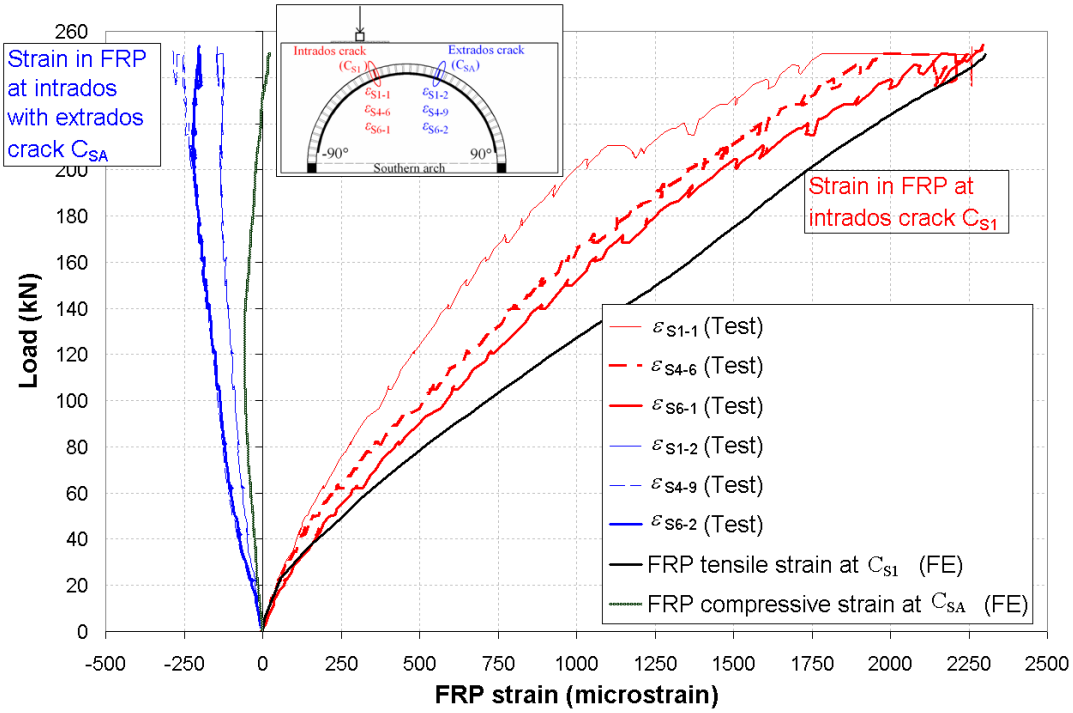

Figure 6.11 FRP strain at two cracks in the south arch: test vs FE prediction

The comparison of the distribution of longitudinal FRP strain from the test and the FE model is shown in Figure 6.12. It can be found that the FE predicts a similar strain distribution as the test, such as, the maximum tensile strain is located at crack C_{S1} beneath the loading area, and the strain reduces towards either sides of the crack. The locations of two large compression strain (-80° and 54°) imply the formation of two extrados cracks. In addition, the maximum compression strain shifting from 40° to 54° indicates the shifting of the position of the extrados cracks. The maximum compression strain (54°) occurred at the portion farther away from the loading area compared with the stain at -80°.

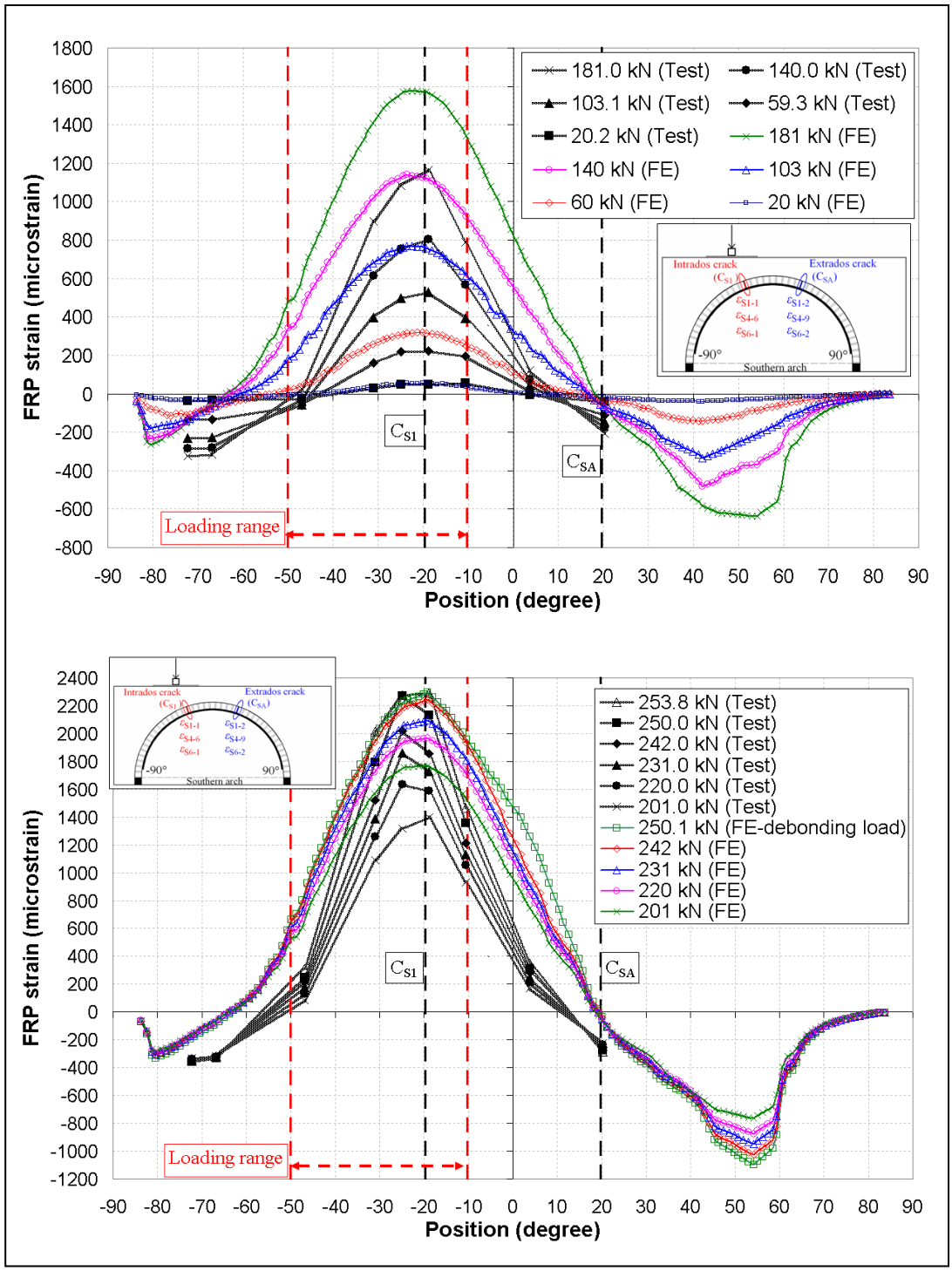

Figure 6.12 Distribution of longitudinal FRP strain in the central plate (P_{S4}) in the south arch: FE prediction vs test

6.4.2.3 Masonry joint opening width

The comparison of the joint opening width at two critical cracks (C_{S1} and C_{SA}) from the test and FE prediction is shown in Figure 6.13. It is shown that the joint opening width at crack C_{S1} from the FE prediction (w_{S1}) is in good agreement with the test results (w_{S1E} & w_{S1W}). The FE prediction for the joint opening width at C_{SA} (w_{SA}) shows the similar trend as the test results (w_{SAE} & w_{SAW}), such as, the crack is closed when the loading is greater than 35kN. The smaller prediction at the crack C_{SA} is because addition extrados cracks are formed. Moreover, the present FE model does not consider the existing damage effects as the test.

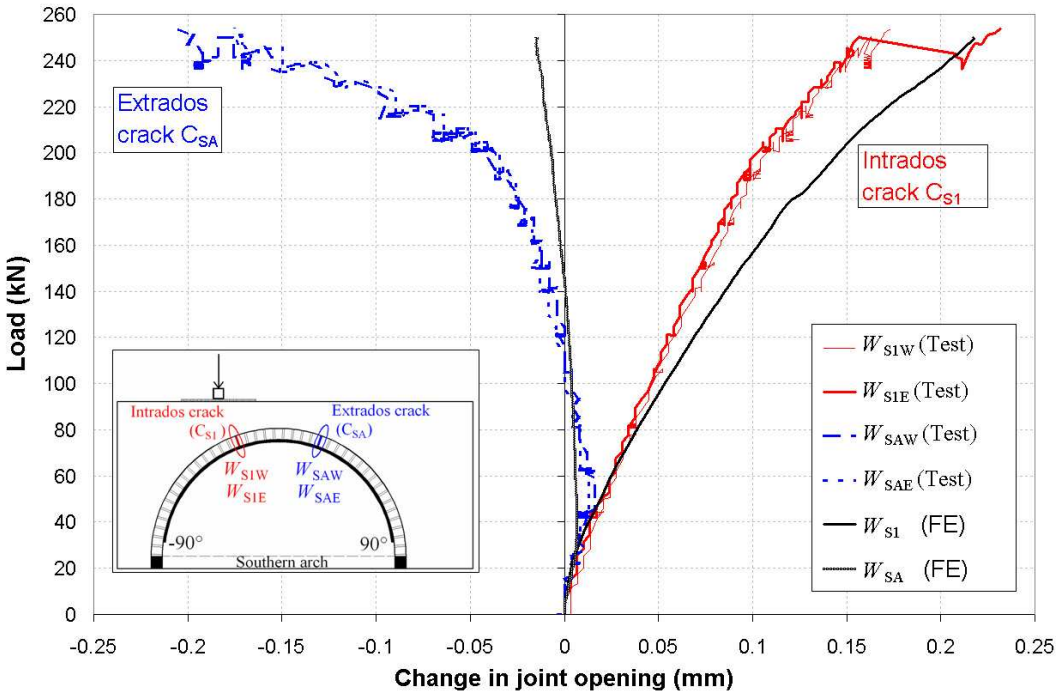

Figure 6.13 Change in joint opening in the south arch: test vs FE prediction

The distributions of the crack opening width in the intrados and extrados obtained from the FE prediction are shown in Figure 6.14 and Figure 6.15, respectively. There

were several intrados cracks opened beneath the loading area and consequently resulted in the debonding failure there. There is another major intrados crack at 90° because it was not strengthened by FRP plates, leading to the dramatic opening of a crack at this location. At the extrados (Figure 6.15), the crack opening width is greater than at the intrados because there is no FRP strengthening exists there. The location of crack C_{SC} (40°) matched with the test results when the load is smaller than 140kN. Above this load, the location of the maximum extrados crack shifted to 54°. This response is corresponding to the FRP strain shifting at the same load (Figure 6.12). Although FE model detected that the crack C_{SD} (-68°) opened, the mortar-interface at -85° showed a greater opening width.

It is worth noting that the extrados crack C_{SA} and C_{SD} had formed in the test on the unstrengthened south arch. The extrados crack C_{SD} opened continuously after strengthening but crack C_{SA} closed when the load is greater than 20kN. The additional extrados crack C_{SC} formed during the test in the strengthened arch. In the FE prediction, the opening of the crack C_{SC} (40°) is detected properly. The opening of additional cracks between 40° to 54° should be caused by the stress redistribution. An additional extrados crack at -85° formed, out of the strengthening region.

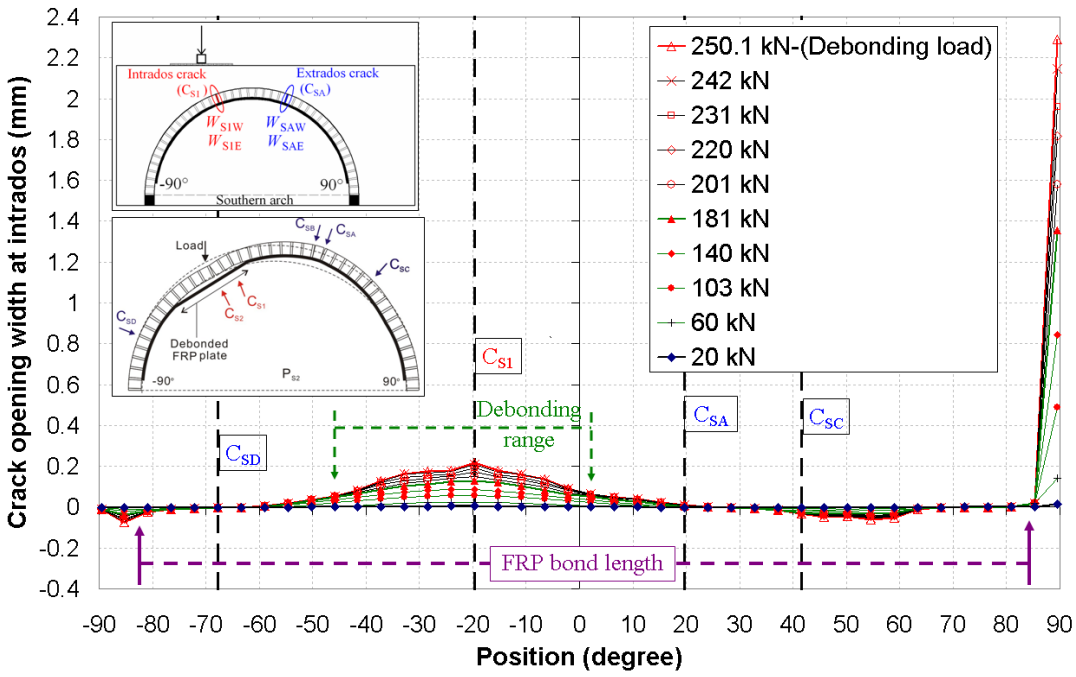

Figure 6.14 FE predicted distribution of crack opening width at the intrados in the south arch

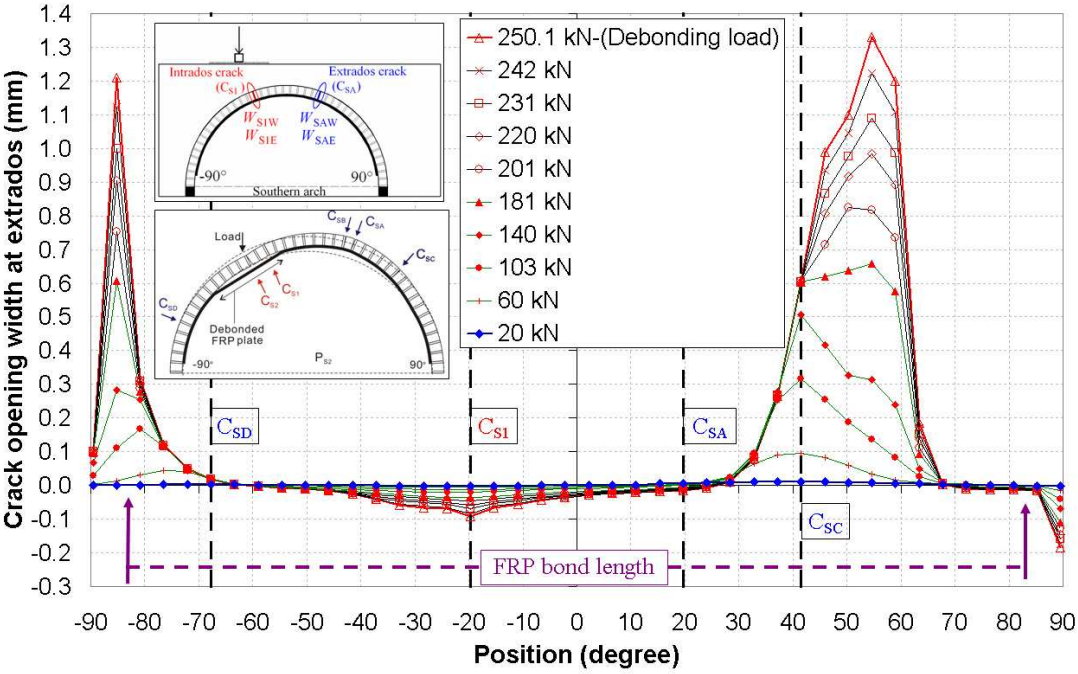

Figure 6.15 FE predicted distribution of crack opening width at extrados in the south arch

6.4.2.4 Discussion of results for the southern arch

The test results show that the FRP strain at intrados below extrados crack C_{SA} changed to tension (Figure 6.11) when the load is above 200kN. It can be attributed to the formation and opening of the neighbouring extrados cracks (C_{SB}, C_{SC} and C_{SD} in the test) as shown in Figure 6.15 (cracks at -85° and 54° in the FE prediction). The development of these extrados cracks led to the greater deformation when the load is over 180kN as shown in Figure 6.10.

6.4.3 Discussion

From the above analysis, the loading capacity predicted by the FE model is in good agreement with the test result for both arches. The FRP strain responses under the loading area from the FE model show a better prediction than that at the extrados cracks for both arches. Similar results are found from the crack opening width results, the cracks beneath the loading area show a better prediction than the extrados cracks from the FE model. The density, stiffness and angle of friction for the backfill could be the reason for the less accurate predictions for the extrados joint opening crack.

The differences about the deflection, FRP strain responses, and crack opening width between FE prediction and test should be caused by the following causes: 1) the loading was directly applied onto the sand backfill in the FE model, which could cause a different stress distribution from that in the test; 2) the FE model does not consider the formation of the four hinge mechanism and the residual deformation from the test of the original arches, which could also cause different stress

distributions; 3) the damage initiation law (Eq. 6-8) does not consider the increase of the shear strength when the interface is under compression; 4) the method to estimate the lateral boundary conditions on the timber retaining walls may be not accurate enough. In addition to the southern arch, the effects from the existing debonding failure at the neighbouring (northern) arch were not considered in the FE model as well.

6. 5 Model upgrade and parametric study

6.5.1 Model includes loading plate

After investigating the results from the proposed FE models, it is found that the FE results are significantly affected by the stress distribution in the backfill. The load was directly applied onto the sand backfill in the proposed FE model, which led to a different stress distribution compared with the actual test situation. Therefore, an advanced FE model including the loading plate was produced as shown in Figure 6.16. The contact properties between the loading plate and the sand backfill is the same as the contact between the timber wall and the sand backfill as described in Chapter 5. The load was applied along a 100mm width as the width of the steel distribution beam.

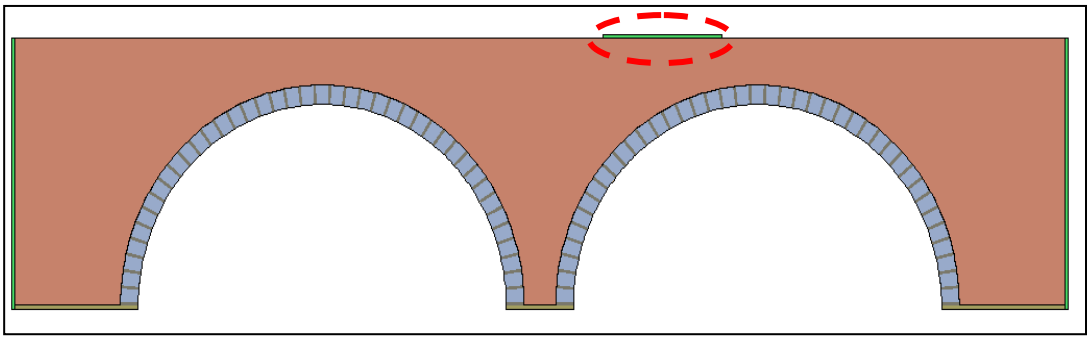

Figure 6.16 FE model including the loading plate

The load deflection responses from the different FE models and test in the northern arch are shown in Figure 6.17. It can be found that the loading capacity obtained from the FE model including the loading plate (131.7kN) is very close to that from the model without loading plate (132.2kN). The FE model including loading plate showed a slightly stiffer response than that from the model excluding the loading plate.

In terms of the FRP strain response, the model without the loading plate predicted a greater debonding strain. The model including the loading plate delivered a better prediction on the debonding stain as shown in Figure 6.18. Although the loading capacities predicted by two FE models are very close (Figure 6.17), the presence of the loading plate has a significant effect on the stress distribution in the sand backfill and results in different stress distributions in the FRP plate (Figure 6.18). Figure 6.18 shows that the FE model including the loading plate gave a better prediction of the FRP strain than that excluding the loading plate. For the distribution of FRP strain, the FE model including the loading plate showed a different strain distribution compared with that without loading plate in the portion beneath the loading (Figure

6.19).

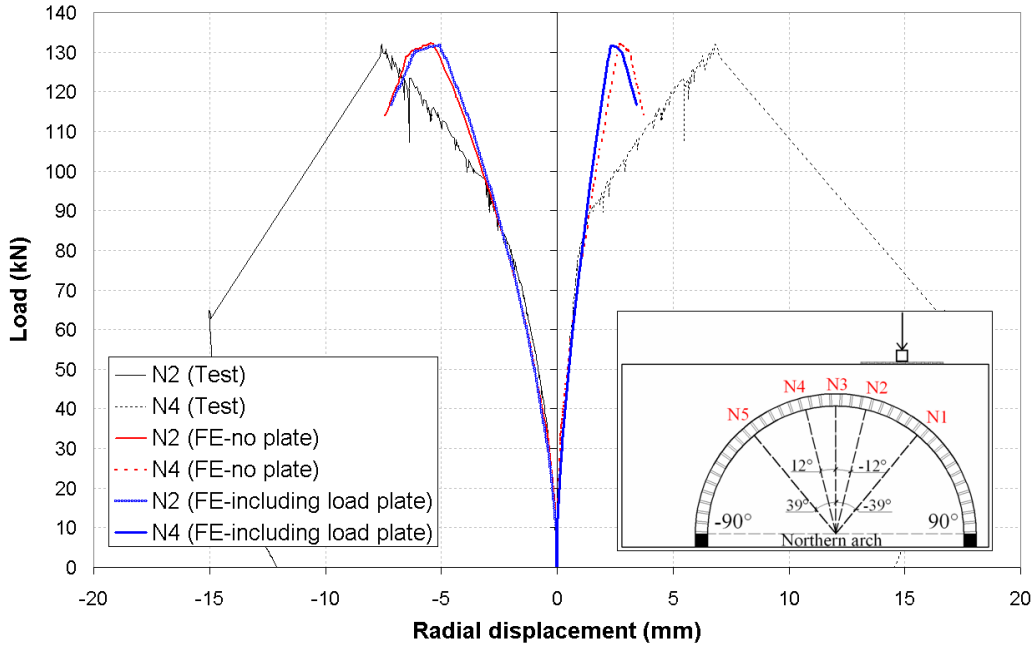

Figure 6.17 Load-deflection from the test and different FE models in the north arch

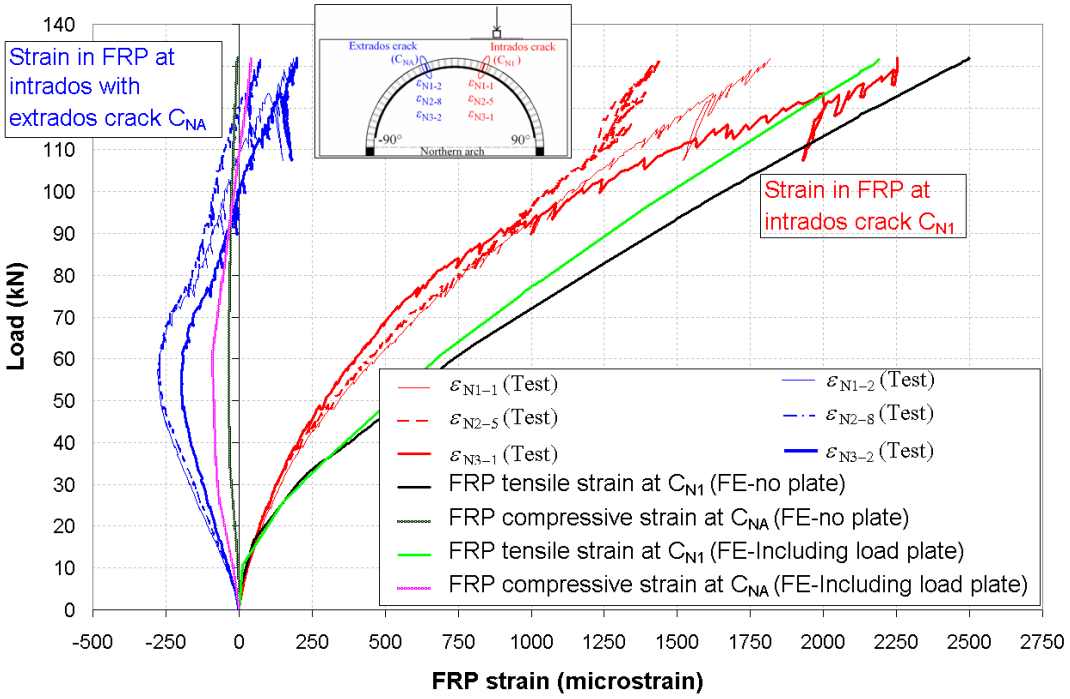

Figure 6.18 FRP strain at two cracks in the north arch: test vs different FE models

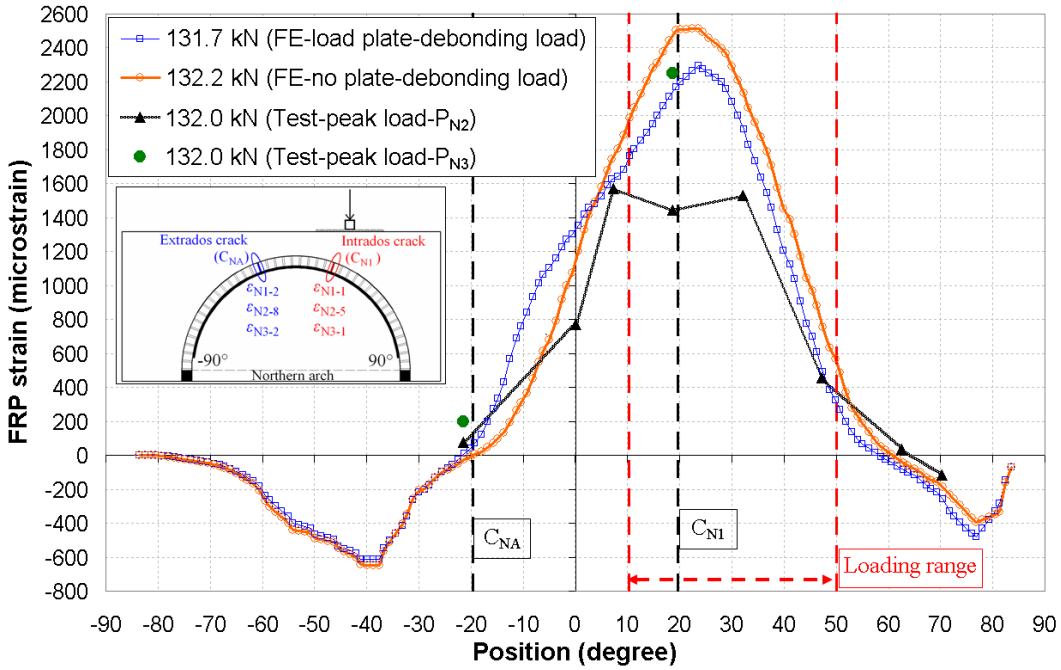

Figure 6.19 Distribution of longitudinal FRP strain in the north arch: different FE models

6.5.2 Model includes pre-damaged condition

The previous FE models did not considered the pre-damaged condition as the test described in Chapter 3. From the previous results, it can be concluded that the differences between FE prediction and the test may be caused by the existing four hinge mechanism and the residual deformation on the arches. Therefore, another advanced model was produced by including the pre-damaged condition.

As explained in Figure 6.20, the original arch was firstly loaded until the same level in the test (46.2kN) with the formation of the four hinge mechanism and then unloaded to zero. The FRP and cohesive elements were then activated before the strengthened arch was loaded until failure. The tracing element technique was

adopted to capture the deformed shape of the FRP and cohesive elements before they were activated. It is worth nothing that the length of loading area changed from 570mm for the original arch to 670mm for the repaired arch in FE model.

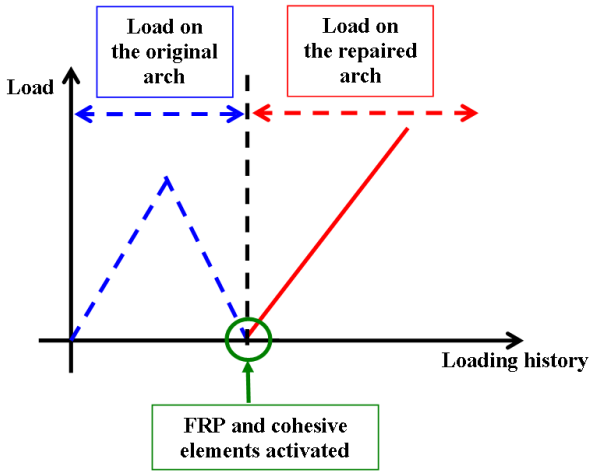

Figure 6.20 Schematic of loading history

The load-deflection response from the model including the pre-damaged condition is shown in Figure 6.21. It is clear that the model including the pre-damage condition delivered better predictions about deformation and the stiffness than the previous model without considering the pre-damaged effects. The load carrying capacities predicted from both models are quite close. There were several loading-unloading cycles in the test to check the instruments and loading frame, which caused more damages. However, there was only one loading-unloading cycle modelled in the FE model. This may lead to the remaining differences between the advanced FE model and the test.

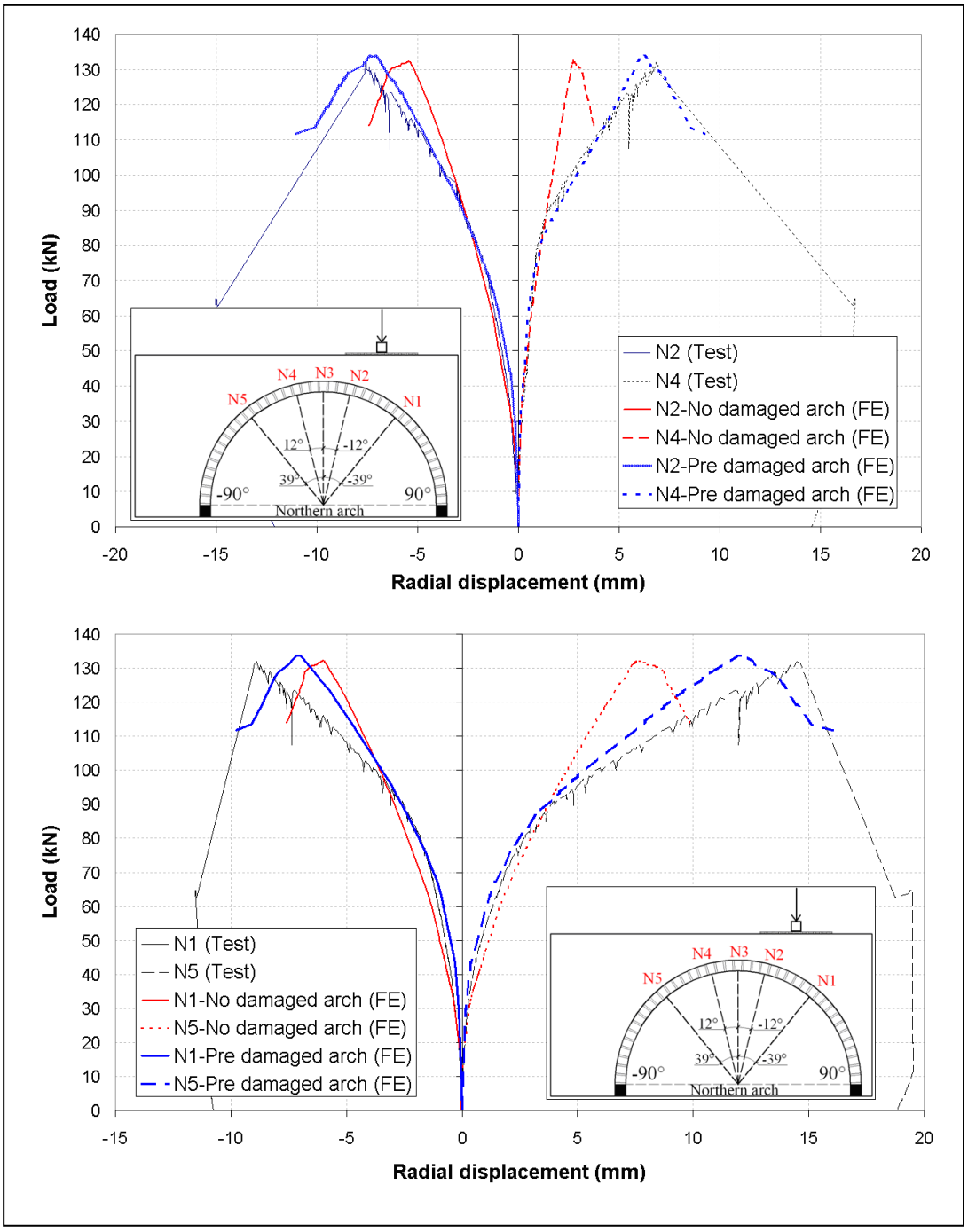

Figure 6.21 Load-deflection from the test and different FE models in the north arch

In terms of FRP strain response, the model including the pre-damaged condition delivered a better and safety prediction compared to that excluding the pre-damaged effects on the debonding strain as shown in Figure 6.22. In addition, the load-FRP

strain responses from the improved model showed more accurate prediction than that from the previous model without considering the pre-damaged effects.

The model including the pre-damaged condition has significant effects on the FRP strain distribution (Figure 6.23). The FE model including the pre-damaged condition showed a lower tensile strain compared with the previous model without considering the damage effects in the portion beneath the loading (Figure 6.23). Moreover, the similar strain distribution from both models indicates that the debonding starts from the highest stress region (beneath the loading) regardless the presence of the pre-damage condition (cracks).

In terms of masonry crack opening width (Figure 6.24), the model including the pre-damaged condition showed better predictions on the opening width and the load-crack opening response compared with the model excluding the damage effects.

It can be concluded that the pre-damaged condition has significant effects on the behaviour of the FRP strengthened masonry arch structures. The pre-damaged condition, hinge mechanism and residual deformation, will lead to a larger deformation and different stress distribution of the repaired structures. In terms of FE modelling, the accuracy of the prediction increases when the pre-damaged condition are properly considered.

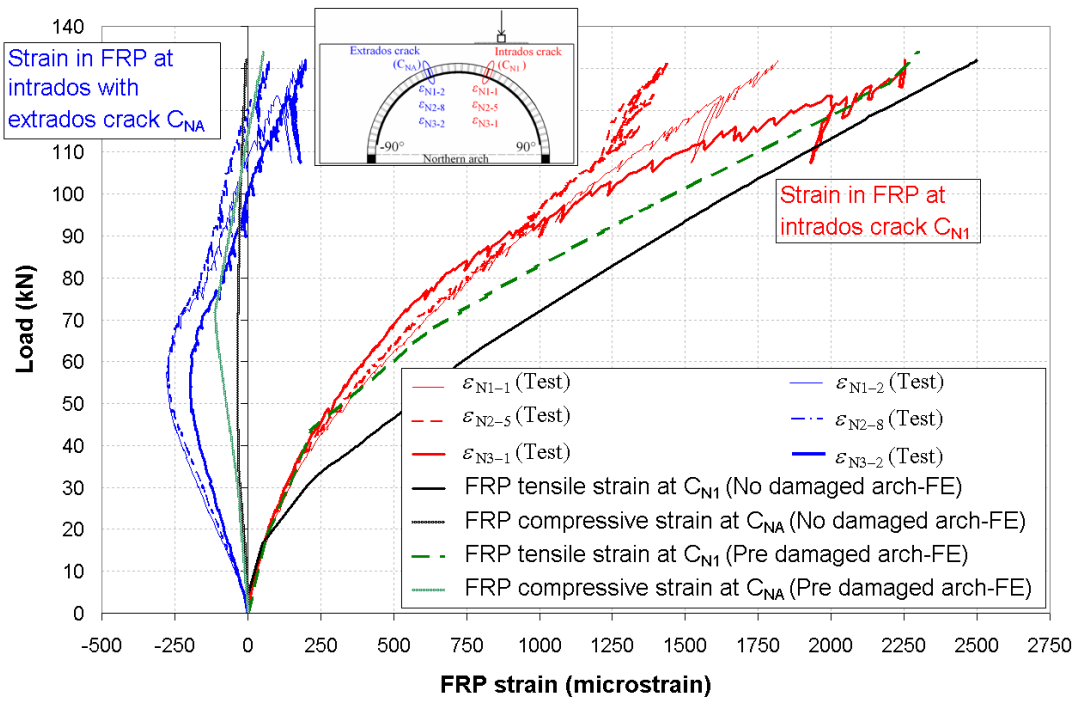

Figure 6.22 FRP strain at two cracks in the north arch: test vs different FE models

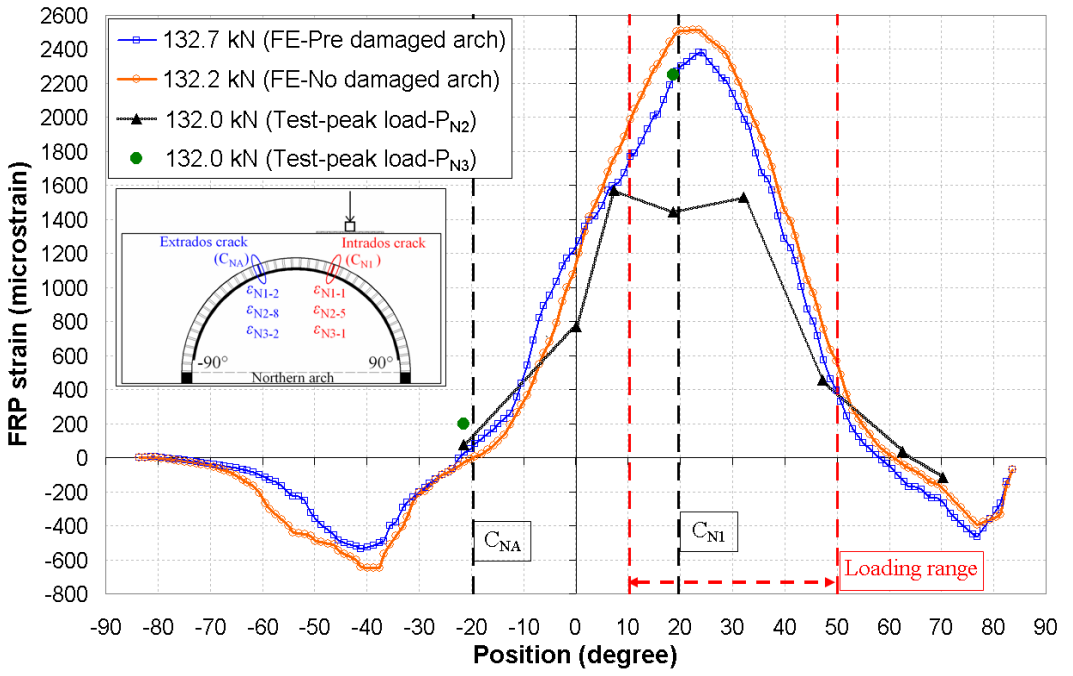

Figure 6.23 Distribution of longitudinal FRP strain in the north arch: different FE models

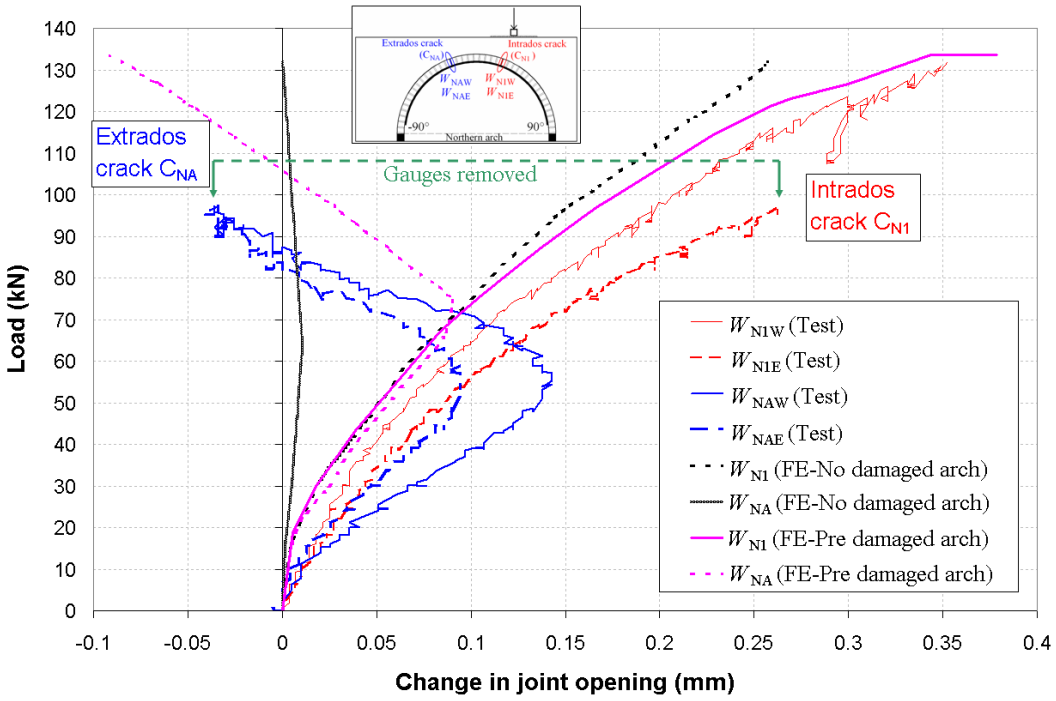

Figure 6.24 Crack opening width in the north arch: different FE models

6.5.3 Parametric study

The bond behaviour of FRP-to-masonry obviously has a significant effect on the FE results. The effects of several parameters involved in the bond joint of FRP-to-masonry, such as, the critical fracture energy, the interaction criterion between two failure modes, the stiffness of the traction-opening law are investigated in this section.

6.5.3.1 Effect of the Mode-I fracture energy at the bond interface

In the current model, the critical mode-I fracture energy at the FRP-to-brick bond interface ($G_f^I(b)$) is taken as the mode-I fracture energy of the masonry as shown in Table 6-2 (0.066N/mm^2). The effect of this parameter is investigated in this section. The results are shown in Figure 6.25. It is seen that the mode-I fracture energy has

negligible effect. That is because the debonding failure is dominated by the properties of mode-II. The mode-I behaviour only takes effects after debonding occurs.

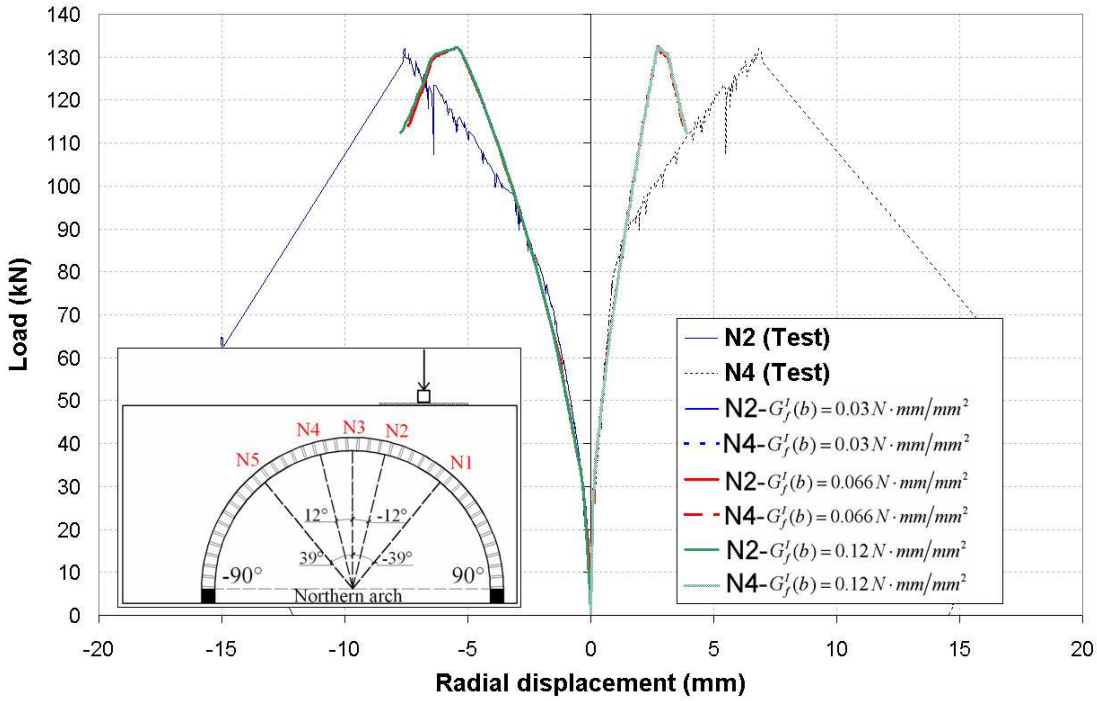

Figure 6.25 Load-deflection results in the northern arch from FE models with different mode-I fracture energy $G_f^I(b)$

6.5.3.2 The effect of the Mode-II fracture energy at the bond interface

The mode-II behaviour of FRP-to-brick should dominate the structural behaviour until debonding occurs. The effect of the mode-II fracture energy at the FRP-to-brick bond interface ($G_f^{II}(b)$) is investigated in this section. The smaller mode-II fracture energy leads to a smaller local slip at bond stress reducing to 0 (S_s^f) as shown in Figure 6.3b.

Figure 6.26 shows the results with different mode-II fracture energies. It is shown that a greater mode-II fracture energy leads to a higher load carrying capacity. However, the global stiffness from different mode-II fracture energies is identical. This is because the elastic part of the bond-slip law was kept constant and only the softening part changes with mode-II fracture energy.

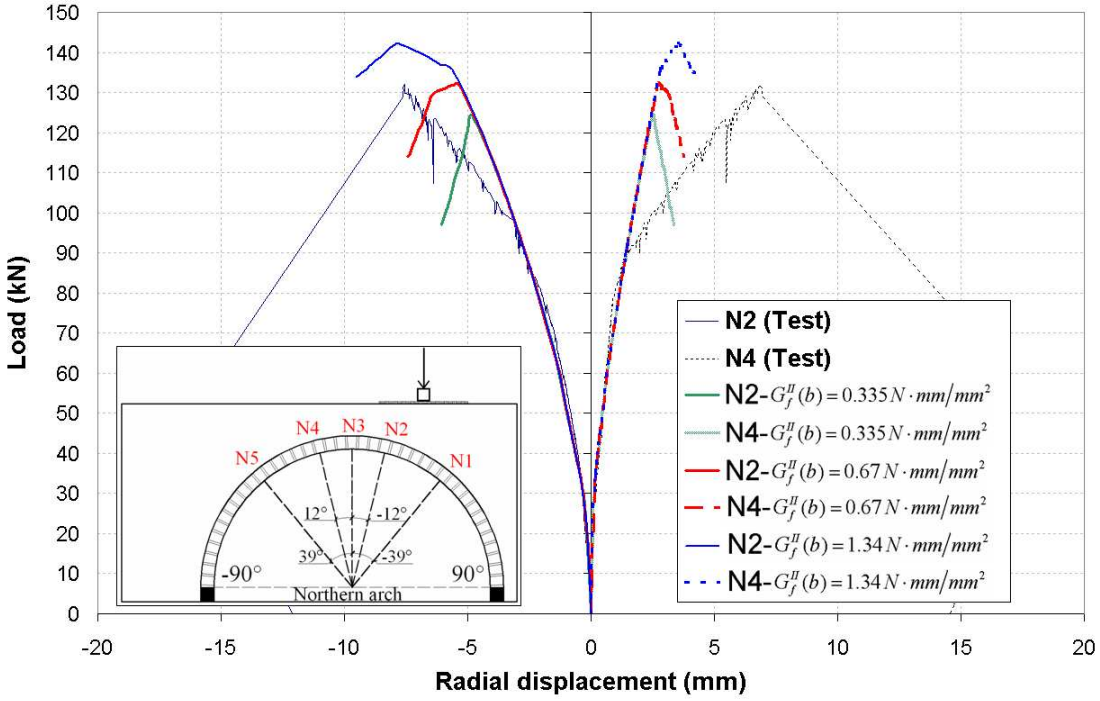

Figure 6.26 Load-deflection results in the northern arch from FE models with different mode-II fracture energy

6.5.3.3 The effect of the interaction criterion between mode I and II

The interaction criterion between the two modes is defined using a power law as in Eq. 6-9. The power is chosen as $\alpha=2$ for the current FE model. The effect of this power ratio was investigated in this section.

Figure 6.27 showed that the results from different power ratios. It is shown that a small power ratio (α=0.5) leads to a small loading capacity. There is negligible effect on the results once the power ratio is greater than 1.

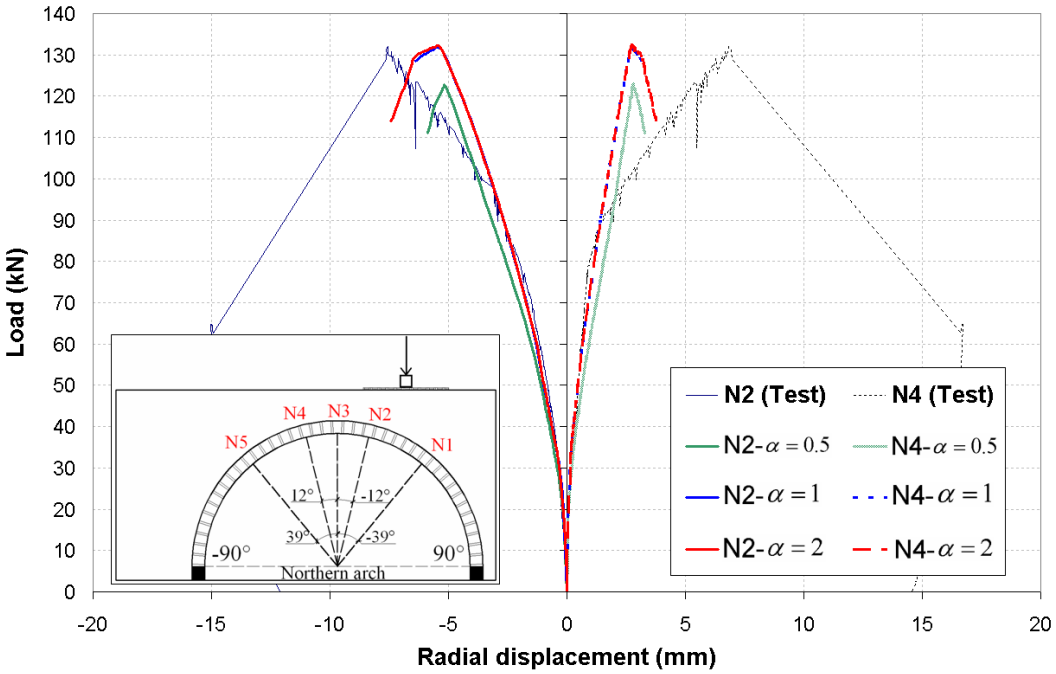

Figure 6.27 Load-deflection results in the northern arch from FE model with different power ratio α

6.5.3.4 The effect of the stiffness of the traction-opening law

The stiffness of the traction-opening law (k_{nn}) in the mode-I behaviour for FRP-to-brick joint is taken as the stiffness of the masonry (16000MPa/mm) in the current model. The stiffness of the traction-opening law for the FRP-to-mortar interface is assumed as 5000MPa/mm because no data is available. A smaller stiffness implies a delay of softening and eventually an increase of the loading capacity.

Figure 6.28 shows the results from different stiffness values. It is clear that a lower stiffness ($k_{nn}/2$) results in a greater loading capacity due to the delay of softening. It indicated that a smaller stiffness of the traction-opening law gives a safe prediction.

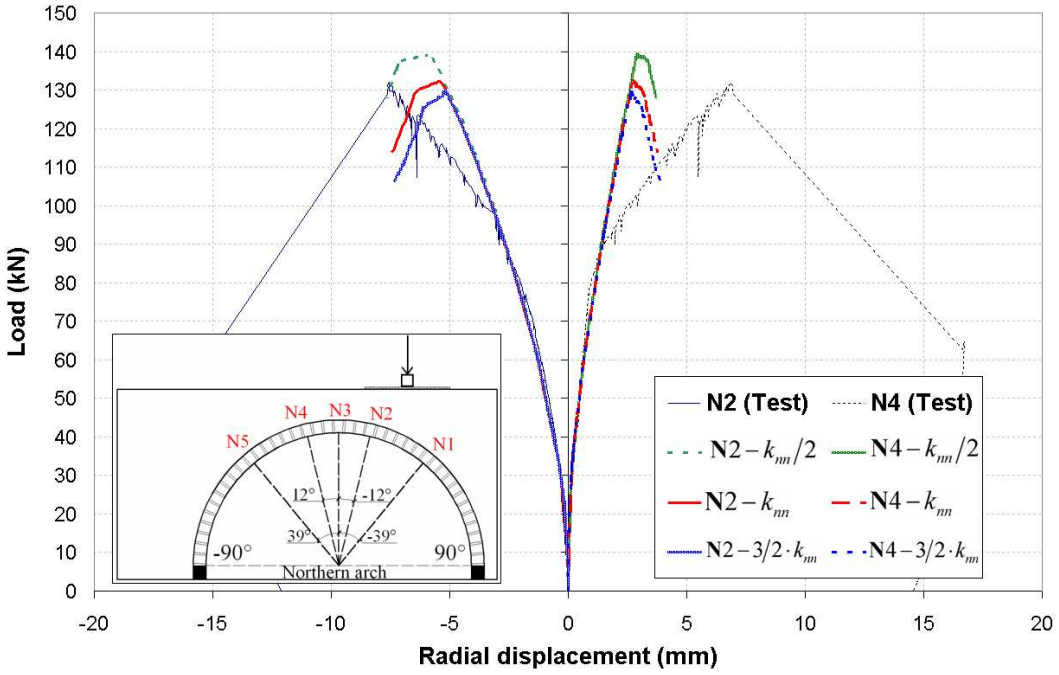

Figure 6.28 Load-deflection results in the northern arch from FE model with different stiffness in the traction-opening law k_{nn}

6. 6 Conclusions

This chapter has presented a numerical study on the FRP strengthened masonry arch bridge. After reviewing the existing FE model strategies, the challenges of FE modelling were addressed. The masonry arch was modelled using the detailed solid model developed in Chapter 5 and the FRP-to-masonry bonded joint was modelled using zero thickness interface elements combined with a mixed bond behaviour model. The FE predictions of the load-deflection, FRP stain, and masonry crack

opening width are investigated and compared with the test results.

The comparison between FE model and test results indicates that the proposed model can deliver a reasonably good prediction on the loading capacity of the strengthened arches, the debonding strain, the distribution pattern of the FRP strain, and the masonry crack opening width. The formation of additional cracks is successfully detected by the FE model. The possible reasons for the differences between the FE predictions and test results are discussed. The existing damage conditions in the test, such as, the formation of the four hinge mechanism and residual deformations; have significant effects on the stress distributions.

In order to investigate the effects of the different models and the material properties of the bond interface, two improved models, one including the loading plate and the other is considering the pre-damaged condition, are conducted, as well as a parametric study. The results showed that the more accurate model with the loading plate lead to a better predictions of the debonding strain. Moreover, a further improved model considering the pre-damaged condition delivers a more accurate prediction compared with the model without considering those effects. With the assistance of the parametric study, it is found that the mode-II behaviour of the bond joint dominates the structural behaviour before debonding failure occurs. The decreasing of the stiffness of the traction-opening behaviour leads to a greater loading capacity.

CHAPTER 7

CONCLUSIONS AND FUTURE WORK

7. 1 Introduction

Masonry arch structures, like arch bridges, are among the oldest structures used worldwide. Through centuries, these structures have accumulated structural damage arisen from causes such as unexpected loading, environmental actions, foundation settlement, lack of maintenance, as well as extreme events such as earthquakes. It is important to safeguard and extend the life of these structures, especially where arch bridges form critical links in the transport network and where major disruption would result in their closure. Fibre reinforced polymer (FRP) composites have been increasingly used for repair and strengthening of structures. Debonding of the bond interface is a common and critical failure mode of these strengthened structures. Due to the complexity of masonry materials and bond behaviour between FRP and masonry arches, FRP strengthened masonry arch structures has drawn significant attention in the past decade, yet a deep understanding in terms of behaviour and modelling strategy remains elusive.

This thesis has presented an extensive study into FRP strengthened structures, focusing on FRP strengthened masonry arch bridges. A review of FRP strengthened masonry and concrete structures in Chapter 2 indicated that the literature mainly focused on the global behaviour of FRP strengthened masonry arches, such as

loading capacity, failure mode and stiffness, with less contribution to the debonding process. In terms of numerical studies, the finite element (FE) modelling of masonry arch structures, especially when backfill is present, and FRP strengthened masonry arch structures has been less investigated due to difficulties on the modelling of masonry and FRP-to-masonry bond interface. In addition, FE modelling of FRP bonding concrete substrate is still a challenge due to the difficulties of modelling of concrete material. For the above reasons the behaviour of the FRP strengthened masonry arches, and the numerical modelling of such strengthening structures need to be deeply studied, which have been the main themes of this thesis.

This chapter presents a summary of and conclusions drawn from the work presented in this thesis. Suggestions for further work in this research area are proposed.

7. 2 Conclusions

7.2.1 Overall conclusions

The load carrying capacity of a concrete masonry arch bridge can be significantly increased by bonding FRP composites into its intrados because the FRP strengthening system allows the line of thrust moving out of the arch profile and restraining the opening of the hinge cracks. The debonding would be the critical failure mode if the amount of FRP is adequate to avoid such failure modes as masonry crushing and FRP rupture. In this case, the ultimate load is reached just after debonding failure occurred. For the test bridge in this study, debonding occurred at an intrados crack beneath the loading position. The FRP did not

completely separate from the masonry arch at the ultimate load, but remained attached at both ends. The post-debonding tie action prevented the catastrophic collapse and maintained the integrity of the arch despite it being excessively deformed.

A meso-scale numerical model of FRP strengthened concrete substrate under single shear (pull-off) test has been developed by modelling the concrete using a concrete damaged plasticity model. A damage model based on the plastic degradation theory for concrete, where the damage effects of concrete after it enters softening range are modelled in terms of the plastic strain degradation rather than the stiffness degradation, has been developed. A close agreement between the simulation and the experimental results demonstrated the ability of the proposed model to produce the global and local behaviour of debonding failure of FRP strengthened concrete structures.

The FE study on the masonry arch structures including backfill was conducted using four different modelling strategies. The accuracy of models was controlled by the model of the unit-mortar interface and backfill materials. The behaviour of the unit-mortar interface which controls the formation of hinge mechanism, together with proper modelling of backfill, dominate the loading capacity and contact between arch and backfill. For modelling the complex system, such as more interfaces existing at the multi-ring arches or FRP strengthened masonry arches, a detailed solid model was developed and successfully overcame the numerical and modelling difficulties using the common zero thickness interface elements.

The FE study on the FRP strengthened masonry arch structures was conducted using a detailed solid model for the masonry arch and a mixed mode model for the FRP-to-masonry bond behaviour. This challenge task was overcome by accurately modelling the mortar interface in the masonry and FRP-to-masonry bond behaviour. The mode-II behaviour of the bond joint controls the structural behaviour before debonding failure occurs. The existing hinge mechanism and residual deformation prior to FRP strengthening can have significant effects on the stress distribution of the structures compared with the undamaged one. The debonding strain of FRP and the failure mode were properly predicted by the proposed FE model.

It can be concluded that the proposed FRP strengthening system can successful improve the performances of the concrete masonry arch structures. Meanwhile, the proposed numerical modelling strategies can give reasonable predictions about the behaviour of both masonry arch structures and FRP strengthened concrete masonry arch structures. In terms of the environmental loading which weathers the surface of voussoirs, the proposed FRP strengthening system may not be applicable due to the much weaker material strength leading to lower bond strength. Alternative strengthening system, for example, mounted steel mesh, may be a better choice.

7.2.2 FRP strengthened masonry arch bridge experiments

Chapter 3 represented a well-designed experimental study of a two span masonry arch bridge strengthened with FRP composites. The behaviour of unstrengthened and strengthened masonry arch bridges has been investigated.

The results showed that the failure of the unstrengthened masonry arch is caused by the formation and development of a hinge mechanism in this study, leading to large deformations and eventual collapse of the masonry arch.

The experiment showed that the loading capacity of the masonry arch bridge can be significantly increased by bonding FRP composites into its intrados. This is because the FRP strengthening allows the line of thrust moving out of the arch profile and restraining the opening of the hinge cracks. These benefits consequently reduced the deformation and increased its stiffness. By restraining the flexural crack opening at the intrados which is necessary for the formation of a hinge mechanism, additional cracks are able to form within the masonry. Furthermore, masonry shear cracks (or mixed mode flexural-shear cracks) are more likely to form when the four hinge mechanism failure load is significantly increased by the FRP strengthening.

Debonding is the critical failure mode of the strengthened masonry arch structures. Therefore, the loading capacity of the strengthened arches is dominated by the behaviour of the bond behaviour between the masonry and FRP composites. In the test conducted in this project, debonding occurred at the intrados beneath the loading position, and two debonding modes were observed. Flexural opening of the masonry crack resulted in shear debonding (mode-II) of the FRP on both sides of the crack, whereas shear deformation in the masonry results in peeling debonding (mode-I) of the FRP to one side of the crack. The debonding at both arches occurred when the strain in one of the FRP plates reached a similar value of about 2250με, although they were strengthened with different amount of FRP composites.

FRP did not completely debond from the masonry arch at the ultimate load, but remained attached at both ends. Thus, a post-debonding tie action prevented catastrophic collapse and maintained the integrity of the arch despite it being greatly deformed. The capacity of the tie mechanism was substantially below the strengthened capacity and hence collapse would have occurred immediately in a load controlled situation.

7.2.3 FE modelling of bond behaviour of FRP-to-concrete

Chapter 4 represented a numerical study on the bond behaviour of FRP-to-concrete substrates. This bond behaviour is commonly investigated experimentally through a single shear (pull-off) test. After reviewing the existing numerical studies, it is shown that the challenge of this task is how to accurately model the concrete in order to properly simulate the entire debonding failure.

A meso-scale model with 1 mm element size was conducted to simulate the debonding failure which usually occurs in a thin layer of concrete (about 2-5mm) under the FRP composites. In terms of the constitutive model of concrete, a concrete damaged plasticity model was adopted and a new damage model was developed. This damage model was developed based on the plastic degradation theory for concrete. The effects of concrete damage after it enters softening were modelled in terms of the plastic strain degradation rather than the common stiffness degradation. This damage model considering both the tension and compression states and can be easily implemented in ABAQUS.

The comparison between FE prediction and experimental data showed that the proposed model can successfully simulate the entire debonding failure and predict the bond strength. The local behaviour of debonding failure, such as, cracking in concrete; can be accurately detected by the FE model as well. The local bond-slip relationship extracted from the FE model is in good agreement with those from the test and analytical model.

The effects of different concrete damage models were investigated, highlighted the ability of the proposed FE model and its accuracy. The effects of the bonding geometry were investigated to verify existing findings, such as, the effective bond length theory, and the effects from support conditions.

7.2.4 FE modelling of masonry arch bridge with sand backfill

Chapter 5 presented a numerical study on the unstrengthened masonry arch bridge which was tested in Chapter 3. The masonry arch bridge failed by the formation of a hinge mechanism. Because the hinges formed at the mortar-brick interface. Therefore, the accuracy of the FE model should be dominated by modelling of the mortar interface.

A total of four FE models were developed in this study. A homogeneous model is the simplest: it treats the masonry as a homogeneous material without modelling the mortar interface. The weaker tensile behaviour is smeared into the entire arch so it eventually predicts the lowest loading capacity. Both the traction-opening interface model and the damaged plasticity interface model used zero thickness interface

elements to model the mortar interface. Although both models delivered reasonably good predictions of the loading behaviour and the associated hinge mechanism, they are not suitable for the complex system once the multi-interfaces intersect, such as the FRP strengthened masonry arches and the multi ring arches. A detailed solid model is finally developed and it smears the unit-mortar interface behaviour, the weak tensile strength, representing the mortar layer, leading to an advantage of being able to accurately model the interface behaviour without the need for modelling the zero thickness interfaces. The modelling of the mortar layer avoids the numerical difficulties involved in the complex systems.

The sand backfill was modelled using a Mohr-Coulomb plasticity model. The backfill has a significant effect on the load capacity of the masonry arch. The presence of the backfill can increase the loading capacity of the masonry arch because it can distribute the load and provide a passive pressure. A contact-friction model is used to describe the interaction between the backfill and the arches. The interaction between the backfill and the masonry arch affects the formation of the mechanism and the lateral boundary conditions.

This chapter forms the foundation for conducting the FE modelling of FRP strengthened masonry arch structures in the next chapter.

7.2.5 FE modelling of FRP strengthened masonry arch

Chapter 6 presented a numerical study on the FRP strengthened masonry arch bridges including the backfill. The strengthened masonry arch structures failed by the

debonding at the FRP-to-masonry interface. Therefore, the accuracy of the modelling of the bond behaviour of FRP-to-masonry together with the modelling of the masonry arches dominates the performance of the FE model.

The masonry arch bridges were modelled using the detailed solid model developed in Chapter 5, which is able to model the structure with the intersection of multi-interfaces. The bond joint of FRP-to-masonry was modelled using zero thickness interface elements and a mixed traction-opening model. The mode-I behaviour of the bond interface is taken as the tensile behaviour of the masonry composites because the test described in Chapter 3 and the existing studies showed the mode-I debonding failure occurs with the brick unit and mortar. The mode-II behaviour of the bond interface was modelled using Lu et al.'s (2005a) bond-slip relationship. Moreover, the mode-II behaviour of the bond joint dominates the structural behaviour before debonding failure occurs. The existing hinge mechanism and the residual deflection due to damage before strengthening have significant effects on the stress distribution in the structure. The debonding strain of FRP and the loading capacity can be accurately predicted by the proposed FE model. The FE model can successfully detect the formation of additional cracks in the strengthened masonry arches. The advanced FE model considering the pre-damaged condition can deliver more accurate predictions compared with the one without considering it.

Through the investigation of the effects of the parameters involved in the FRP-to-masonry bond behaviour, it is found that the mode-II behaviour of bond interface dominates the behaviour of the FRP-to-masonry until debonding occurs. The elastic

behaviour of the bond interface controls the onset of the damage and the softening behaviour of the bond interface dominates the debonding load.

7. 3 Recommendation for the future work

The research work conducted in this study represents an in-depth investigation into the FRP strengthened masonry arch structures, resulting in a good understanding of this type of structures and the fundamental mechanisms. However, the effects of many of the contributory factors have not been investigated due to time limitation. Further research is required to investigate their effects and further improve our understanding so that more rational and economical design methods can be developed. Example areas for further investigation are listed as follows.

a) Only one third scale masonry arch bridge was tested in this study. More tests needs to be conducted with different strengthening parameters, such as different amount of FRP strengthening, and strengthening in different parts of the structure. More detailed FRP strain distribution measurement would be helpful and necessary.

b) The effect of initial damage to the arch structure. The damage situation needs to be accurately simulated in the FE models in order to deliver a good prediction.

c) The bond behaviour of FRP-to-masonry in a curved bond joint needs to be investigated further in experimental study. A hinge mechanism could be used to connect two flat or curved masonry beams which are bonded with FRP. The system can be tested under a bending action as shown in Figure 2.7e. The experimental

results can be validated by using either the proposed the concrete damaged plasticity model or other methods such as more classical fracture mechanics analyses. The interaction between Mode I and Mode II is of particular concern.

d) The interaction between arch and backfill needs to be further investigated in terms of the stress distribution and transfer.

e) In terms of the behaviour of FRP strengthened masonry arch structures, some of the contributory factors have not been investigated in this study and in the literatures. Examples include the shape and thickness of the arch and the thickness of the mortar etc. In particular, the behaviour of multiple-ring arches can behaviour very differently with different failure modes such as ring separation. Further studies are required to understand the effects of these factors.

f) Development of guidelines for the FRP strengthened masonry arch bridges that can be easily used by practice engineers for design and assessment.

REFERENCES

ABAQUS (2007). ABAQUS Analysis user's manual, version 6.7.

Abboud, B. E., Hamid, A. A. and Harris, H. G. (1996). "Flexural Behavior of Reinforced Concrete Masonry Walls under Out-of-Plane Monotonic Loads." *ACI Structural Journal*, 93(3), 327-335.

ACI318 (2002). "Building Code Requirements for Structural Concrete and Commentary ", ACI Committee 318.

ACI (2007). "ACI 440R-07. Report on Fiber-Reinforced Polymer (FRP) Reinforcement for Concrete Structures."Michigan, USA.

ACI (2008). "ACI 440.2R-08. Guide for the Design and Construction of Externally Bonded FRP Systems for Strengthening Concrete Structures." ACI Committee 440, Michigan, USA.

Ai, J. (2010). "Particle Scale and Bulk Scale Investigation of Granular Piles and Silos."PhD Thesis, The University of Edinburgh, Edinburgh

Aiello, M. A. and Sciolti, S. M. (2006). "Bond analysis of masonry structures strengthened with CFRP sheets." *Construction and Building Materials*, 20(1-2), 90-100.

Albert, M. L., Elwi, A. E. and Cheng, J. J. R. (2001). "Strengthening of Unreinforced Masonry Walls Using FRPs." *Journal of Composites for Construction*, 5(2), 76-84.

Alcaino, P. and Santa-Maria, H. (2008). "Experimental Response of Externally Retrofitted Masonry Walls Subjected to Shear Loading." *Journal of Composites for Construction,ASCE*, 12(5), 489-498.

Alfano, G. and Sacco, E. (2006). "Combining interface damage and friction in a cohesive-zone model." *INTERNATIONAL JOURNAL FOR NUMERICAL METHODS IN ENGINEERING*, 68(5), 542-582.

Ali-Ahmad, M., Subramaniam, K. and Ghosn, M. (2006). "Experimental Investigation and Fracture Analysis of Debonding between Concrete and FRP Sheets." *Journal of Engineering Mechanics*, 132(9), 914-923.

Atkinson, R. H., Amadei, B. P., Saeb, S. and Sture, S. (1989). "Response of Masonry Bed Joints in Direct Shear." *Journal of Structural Engineering*, 115(9), 2276-2296.

Audenaert, A., Peremans, H. and Reniers, G. (2007). "An analytical model to determine the ultimate load on masonry arch bridges." *Journal of Engineering Mathematics*, 59(3), 323-336.

Basilio, I. (2007). "Strengthening of arched masonry structures with composites materials." Ph.D Thesis thesis, Universidade do Minho, Guimarães, Portugal.

Bati, S. B. and Rovero, L. (2008). "Towards a methodology for estimating strength and collapse mechanism in masonry arches strengthened with fibre reinforced polymer applied on external surfaces." *Materials and Structures/Materiaux et Constructions*, 41(7), 1291-1306.

Bati, S. B., Rovero, L. and Tonietti, U. (2007). "Strengthening Masonry Arches with Composite Materials." *Journal of Composites for Construction*, 11(1), 33-41.

Bažant, Z. and Jaime, P. (1998). *Fracture and Size Effect in Concrete and Other Quasibrittle Materials* CRC Press, Boca Raton, Florida.

Bažant, Z. and Oh, B. (1983). "Crack band theory for fracture of concrete." *Materials and Structures*, 16(3), 155-177.

Bazant, Z. P. and Becq-Giraudon, E. (2002). "Statistical prediction of fracture parameters of concrete and implications for choice of testing standard." *Cement and Concrete Research*, 32(4), 529-556.

Betti, M., Drosopoulos, G. A. and Stavroulakis, G. E. (2008). "Two non-linear finite element models developed for the assessment of failure of masonry arches." *Comptes Rendus Mécanique*, 336(1-2), 42-53.

Bisby, L. A. (2003). "Fire Behaviour of Fibre-Reinforced Polymer (FRP) Reinforced or Confined Concrete." PhD thesis Thesis, Queen's University, Kingston, Ontario, Canada.

Boothby, Domalik, D. and Dalal (1998). "Service Load Response of Masonry Arch Bridges." *Journal of Structural Engineering*, 124(1), 17-23.

Boothby, T. (1995). "Collapse modes of masonry arch bridges." *J Brit. Masonry Soc*, 9(2), 62-69.

Boothby, T. E. and Roberts, B. J. (2001). "Transverse behaviour of masonry arch bridges." *The Structural Engineer*, 79(9), 21-26.

Brasile, S., Casciaro, R. and Formica, G. (2007). "Multilevel approach for brick masonry walls - Part I: A numerical strategy for the nonlinear analysis." *Computer Methods in Applied Mechanics and Engineering*, 196(49-52), 4934-4951.

Bridle, R. J. and Hughes, T. G. (1989). "The arch revival: The Cardiff arch analysis procedure." *J. Instn Highways & Transportation,*, 36(10), 21-22.

Bridle, R. J. and Hughes, T. G. (1990). "An energy method for arch bridge analysis." *Proc. Instn Civ. Engnrs*, 89, 375-385.

BS 772-6 (2001). "Methods of test for masonry units-Part6: Determination of bending tensile strength of aggregate concrete masonry units."

BS 1052-1 (1999). "Methods of test for masonry-Part 1: Determination of compressive strength."

BS 1052-2 (1999). "Methods of test for masonry-Part 2: Determination of flexural strength."

BS 1052-3 (2002). "Methods of test for masonry-Part 3: Determination of initial shear strength."

BS EN 772-1 (2000). "Methods of test for masonry units-Part1: Determination of compressive strength."

BS EN 998-2 (2010). "Specification for mortar for masonry."

BS ISO 1920-10 (2009). "Testing of concrete-Part 10: Determination of static modulus of elasticity in compression."

Buchan, P. A. and Chen, J. F. (2007). "Blast resistance of FRP composites and polymer strengthened concrete and masonry structures - A state-of-the-art review." *Composites Part B: Engineering*, 38(5-6), 509-522.

Buyukozturk, O., Gunes, O. and Karaca, E. (2004). "Progress on understanding debonding problems in reinforced concrete and steel members strengthened using FRP composites." *Construction and Building Materials*, 18(1), 9-19.

Camata, G., Spacone, E., Al-Mahaidi, R. and Saouma, V. (2004). "Analysis of Test Specimens for Cohesive Near-Bond Failure of Fiber-Reinforced Polymer-Plated Concrete." *Journal of Composites for Construction*, 8(6), 528-538.

Camli, U. S. and Binici, B. (2007). "Strength of carbon fiber reinforced polymers bonded to concrete and masonry." *Construction and Building Materials*, 21(7), 1431-1446.

Cancelliere, I., Imbimbo, M. and Sacco, E. (2010). "Experimental tests and numerical modeling of reinforced masonry arches." *Engineering Structures*, 32(3), 776-792.

Caporale, A., Luciano, R. and Rosati, L. (2006). "Limit analysis of masonry arches with externally bonded FRP reinforcements." *Computer Methods in Applied Mechanics and Engineering*, 196(1-3), 247-260.

Capozucca, R. (2010). "Experimental FRP/SRP-historic masonry delamination." *Composite Structures*, 92(4), 891-903.

Castigliano, A. (1897). *Théorie de l'équilibre des systèmes élastiques et ses applications*, A. F. Negro, Turin.

Cavicchi, A. and Gambarotta, L. (2005). "Collapse analysis of masonry bridges taking into account arch-fill interaction." *Engineering Structures*, 27(4), 605-615.

Cavicchi, A. and Gambarotta, L. (2006). "Two-dimensional finite element upper bound limit analysis of masonry bridges." *Computers & Structures*, 84(31-32), 2316-2328.

Cavicchi, A. and Gambarotta, L. (2007). "Lower bound limit analysis of masonry bridges including arch-fill interaction." *Engineering Structures*, 29(11), 3002-3014.

CEB-FIB (1991). "CEB-FIB MODEL CODE 1990." Thomas Telford.

Cecchi, A., Milani, G. and Tralli, A. (2005). "Out-of-plane loaded CFRP reinforced masonry walls: Mechanical characteristics by homogenization procedures." *Composites Science and Technology*, 65(10), 1480-1500.

Chaimoon, K. and Attard, M. M. (2007). "Modeling of unreinforced masonry walls under shear and compression." *Engineering Structures*, 29(9), 2056-2068.

Chen, G. M., Chen, J. F. and Teng, J. G. (2012). "On the finite element modelling of RC beams shear-strengthened with FRP." *Construction and Building Materials*, 32, 13-26.

Chen, G. M., Teng, J. G. and Chen, J. F. (2010). "RC beams shear-strengthened with FRP: shear resistance contributed by FRP." *Magazine of Concrete Research*, 62(4), 301-311.

Chen, G. M., Teng, J. G. and Chen, J. F. (2011). "Finite-Element Modeling of Intermediate Crack Debonding in FRP-Plated RC Beams." *Journal of Composites for Construction*, 15(3), 339-353.

Chen, J. F. (2002). "Load-Bearing Capacity of Masonry Arch Bridges Strengthened with Fibre Reinforced Polymer Composites." *Advances in Structural Engineering*, 5, 37-44.

Chen, J. F. and Pan, W. K. (2005). "Three dimensional stress distribution in FRP-to-concrete bond test specimens." *Construction and Building Materials*, 20(1-2), 46-58.

Chen, J. F. and Teng, J. G. (2001). "Anchorage Strength Models for FRP and Steel Plates Bonded to Concrete." *Journal of Structural Engineering*, 127(7), 784-791.

Chen, J. F. and Teng, J. G. (2003). "Shear capacity of FRP-strengthened RC beams: FRP debonding." *Construction and Building Materials*, 17(1), 27-41.

Chen, J. F., Yang, Z. J. and Holt, G. D. (2001). "FRP or steel plate-to-concrete bonded joints: effect of test methods on experimental bond strength." *Steel Compos Struct* 1(2), 231-244.

Chen, J. F., Yuan, H. and Teng, J. G. (2007). "Debonding failure along a softening FRP-to-concrete interface between two adjacent cracks in concrete members." *Engineering Structures*, 29(2), 259-270.

Chen, Y., Ashour, A. F. and Garrity, S. W. (2007). "Modified four-hinge mechanism analysis for masonry arches strengthened with near-surface reinforcement." *Engineering Structures*, 29(8), 1864-1871.

Cicekli, U., Voyiadjis, G. Z. and Abu Al-Rub, R. K. (2007). "A plasticity and anisotropic damage model for plain concrete." *International Journal of Plasticity*, 23(10-11), 1874-1900.

CNR (2004). "CNR-DT 200/2004 Guide for the design and construction of externally bonded FRP systems for strengthening existing structures-materials, RC and PC structures, masonry structures." Consiglio Nazionale delle Ricerche (English version), Rome, Italy.

CNR (2006). "CNR-DT 200/2006 Guide for the design and construction of externally bonded FRP systems for strengthening existing structures-materials, RC and PC structures, masonry structures." Consiglio Nazionale delle Ricerche (English version), Rome, Italy.

Concrete Society (2004). "Design guidance for strengthening concrete structures using fibre composites materials." *Technical Report 55*, The Concrete Society, Camberley, UK.

Coronado, C. A. and Lopez, M. M. (2007). "Damage Approach for the Prediction of Debonding Failure on Concrete Elements Strengthened with FRP." *Journal of Composites for Construction*, 11(4), 391-400.

Coronado, C. A. and Lopez, M. M. (2008). "Experimental Characterization of Concrete-Epoxy Interfaces." *Journal of Materials in Civil Engineering*, 20(4), 303-312.

Coronado, C. A. and Lopez, M. M. (2010). "Numerical Modeling of Concrete-FRP Debonding Using a Crack Band Approach." *Journal of Composites for Construction*, 14(1), 11-21.

Crisfield, M. A. (1985). "Finite Element and Mechanism Methods for the Analysis of Masonry and Brickwork Arches." TRL, Crowthorne, England.

De Lorenzis, L. (2008). "Strengthening of masonry structures with fibre-reinforced polymer (FRP) composites." *Strengthening and rehabilitation of civil infrastructures using fibre-reinforced polymer (FRP) composites*, Hollaway, L. C. and Teng, J. G., eds., CRC Press, USA.

De Lorenzis, L., Dimitri, R. and La Tegola, A. (2007). "Reduction of the lateral thrust of masonry arches and vaults with FRP composites." *Construction and Building Materials*, 21(7), 1415-1430.

De Lorenzis, L. and Zavarise, G. (2009). "Interfacial stress analysis and prediction of debonding for a thin plate bonded to a curved substrate." *International Journal of Non-Linear Mechanics*, 44(4), 358-370.

De Lorenzis, L. and Zavarise, G. (2010). "Debonding analysis of thin plates from curved substrates." *Engineering Fracture Mechanics*, 77(16), 3310-3328.

Diab, H. and Wu, Z. (2007). "Nonlinear constitutive model for time-dependent behavior of FRP-concrete interface." *Composites Science and Technology*, 67(11-12), 2323-2333.

Domède, N., Pons, G., Sellier, A. and Fritih, Y. (2009). "Mechanical behaviour of ancient masonry." *Materials and Structures*, 42(1), 123-133.

Drosopoulos, G. A., Stavroulakis, G. E. and Massalas, C. V. (2006). "Limit analysis of a single span masonry bridge with unilateral frictional contact interfaces." *Engineering Structures*, 28(13), 1864-1873.

Drosopoulos, G. A., Stavroulakis, G. E. and Massalas, C. V. (2007). "FRP reinforcement of stone arch bridges: Unilateral contact models and limit analysis." *Composites Part B: Engineering*, 38(2), 144-151.

Drysdale, R. G., Hamid, A. A. and Baker, L. R. (1994). *Masonry Structures, behaviour and design*, Prentice-Hall.

Ehsani, M. R., Saadatmanesh, H. and Velazquez-Dimas, J. I. (1999). "Behavior of Retrofitted URM Walls under Simulated Earthquake Loading." *Journal of Composites for Construction,ASCE*, 3(3), 134-142.

ElGawady, M. A., Lestuzzi, P. and Badoux, M. (2005a). "Aseismic retrofitting of unreinforced masonry walls using FRP." *Composites Part B: Engineering*, 37(2-3), 148-162.

ElGawady, M. A., Lestuzzi, P. and Badoux, M. (2005b). "In-Plane Seismic Response of URM Walls Upgraded with FRP." *Journal of Composites for Construction*, 9(6), 524-535.

ElGawady, M. A., Lestuzzi, P. and Badoux, M. (2007). "Static Cyclic Response of Masonry Walls Retrofitted with Fiber-Reinforced Polymers." *Journal of Composites for Construction,ASCE*, 11(1), 50-61.

Fairfield, C. A. (1994a). "Soil-Structural Interaction in Arch Bridges."PhD Thesis, The University of Edinburgh.

FAIRFIELD, C. A. (1994b). "Soil-structure interaction in arch bridges." PhD Thesis, The University of Edinburgh.

Fairfield, C. A. and Ponniah, D. A. (1994). "MODEL TESTS TO DETERMINE THE EFFECT OF FILL ON BURIED ARCHES." *Proceedings of the ICE - Structures and Buildings*, 104(4), 471-482.

Fanning, P. J. and Boothby, T. E. (2001). "Three-dimensional modelling and full-scale testing of stone arch bridges." *Computers & Structures*, 79(29-30), 2645-2662.

Fanning, P. J., Boothby, T. E. and Roberts, B. J. (2001). "Longitudinal and transverse effects in masonry arch assessment." *Construction and Building Materials*, 15(1), 51-60.

Fedele, R. and Milani, G. (2010). "A numerical insight into the response of masonry reinforced by FRP strips. The case of perfect adhesion." *Composite Structures*, 92(10), 2345-2357.

Fedele, R. and Milani, G. (2011). "Three-dimensional effects induced by FRP-from-masonry delamination." *Composite Structures*, 93(7), 1819-1831.

Fedele, R. and Milani, G. (2012). "Assessment of bonding stresses between FRP sheets and masonry pillars during delamination tests." *Composites Part B: Engineering*, 43(4), 1999-2011.

Foraboschi, P. (2004). "Strengthening of Masonry Arches with Fiber-Reinforced Polymer Strips." *Journal of Composites for Construction*, 8(3), 191-202.

Galati, N., Tumialan, G. and Nanni, A. (2006). "Strengthening with FRP bars of URM walls subject to out-of-plane loads." *Construction and Building Materials*, 20(1-2), 101-110.

Ghobarah, A. and El Mandooh Galal, K. (2004). "Out-of-Plane Strengthening of Unreinforced Masonry Walls with Openings." *Journal of Composites for Construction*, 8(4), 298-305.

Giambanco, G. and Di Gati, L. (1997). "A cohesive interface model for the structural mechanics of block masonry." *Mechanics Research Communications*, 24(5), 503-512.

Giambanco, G., Rizzo, S. and Spallino, R. (2001). "Numerical analysis of masonry structures via interface models." *Computer Methods in Applied Mechanics and Engineering*, 190(49-50), 6493-6511.

Gilbert, M., Casapulla, C. and Ahmed, H. M. (2006). "Limit analysis of masonry block structures with non-associative frictional joints using linear programming." *Computers & Structures*, 84(13–14), 873-887.

Gilbert, M. and Melbourne, C. (1994). "Rigid-Block Analysis of Masonry Structures." *The Structural Engineer*, 72(21), 356-361.

Gilstrap, J. M. and Dolan, C. W. (1998). "Out-of-plane bending of FRP-reinforced masonry walls." *Composites Science and Technology*, 58(8), 1277-1284.

Giordano, A., Mele, E. and De Luca, A. (2002). "Modelling of historical masonry structures: comparison of different approaches through a case study." *Engineering Structures*, 24(8), 1057-1069.

Grande, E., Imbimbo, M. and Sacco, E. (2011a). "Bond behaviour of CFRP laminates glued on clay bricks: Experimental and numerical study." *Composites Part B: Engineering*, 42(2), 330-340.

Grande, E., Imbimbo, M. and Sacco, E. (2011b). "Simple Model for Bond Behavior of Masonry Elements Strengthened with FRP." *Journal of Composites for Construction*, 15(3), 354-363.

Grande, E., Milani, G. and Sacco, E. (2008). "Modelling and analysis of FRP-strengthened masonry panels." *Engineering Structures*, 30(7), 1842-1860.

Grassl, P. and Jirásek, M. (2006). "Damage-plastic model for concrete failure." *International Journal of Solids and Structures*, 43(22-23), 7166-7196.

Hahn, H. T. (1980). "Simplified Formulas for Elastic Moduli of Unidirectional Continuous Fiber Composites." *Composites Technology Review*, 2(3), 5-7.

Hamilton III, H. R. and Dolan, C. W. (2001). "Flexural Capacity of Glass FRP Strengthened Concrete Masonry Walls." *Journal of Composites for Construction,ASCE*, 5(3), 170-178.

Hamoush, S. A., McGinley, M. W., Mlakar, P., Scott, D. and Murray, K. (2001). "Out-of-Plane Strengthening of Masonry Walls with Reinforced Composites." *Journal of Composites for Construction*, 5(3), 139-145.

Haroun, M. A., Mosallam, A. S. and Allam, K. H. (2005). "Cyclic in-plane shear of concrete masonry walls strengthened by FRP laminates." *ACI Special publication SP-230*, 327-340.

Harvey, W. J. (1988). "Application of the mechanism analysis to masonry arches." *The Structural Engineer*, 66(5), 77-84.

Hendry, A. W., Davies, S. R. and Royles, R. (1985). "Test on stone masonry arch at Bridgemill - Girvan." *Contractor Report 7*, TRRL, Crowthorne, Berkshire.

Hendry, A. W., Davies, S. R., Royles, R., Ponniah, D. A., Forde, M. C. and Komeyli Birjandi, F. (1996). "Load Test to Collapse on a Masonry Arch Bridge at Bargower, Strathclyde." *Contractor Report 7*, TRRL, Crowthorne, Berkshire.

Heyman, J. (1966). "The stone skeleton." *Int. J. Solids Struct.*, 2, 249-279.

Heyman, J. (1969). "The safety of masonry arches." *International Journal of Mechanical Sciences*, 11(4), 363-385.

Heyman, J. (1980). "The Estimation Of The Strength of Masonry Arches." *Proc. Instn Civ. Engrs*, 69(4), 921-937.

Heyman, J. (1982). *The masonry arch*, Ellis Horwood limited Publ., Chichster.

Heyman, J. (1996). *Arches, Vaults and Buttresses*, VARIORUM, Hampshire, Great Britain.

Hognestad, E. (1951). "A study of combined bending and axial load in reinforced concrete members (Bull. No. 399)." University of Illinois Engineering Experiment Station.

Hordijk, D. A. (1991). "Local Approach to Fatigue of Concrete." PhD Thesis, Delft University of Technology.

Hughes, T. G. (1995). "Analysis and assessmenot f twin-span masonry arch bridges." *Proc. Instn Civ. Engnrs, Structs & Bldgs*(110), 373-382.

Hughes, T. G. and Blackler, M. J. (1997). "A review of the UK masonry arch assessment methods." *Proc. Instn Civ. Engrs Structs & Bldgs*, 122(3), 305-315.

Hughes, T. G., Hee, S. C. and Soms, E. (2002). "Mechanism analysis of single span masonry arch bridges using a spreadsheet." *Proceedings of the ICE - Structures and Buildings*, 152(4), 341-350.

Juhásová, E., Sofronie, R. and Bairrão, R. (2008). "Stone masonry in historical buildings -- Ways to increase their resistance and durability." *Engineering Structures*, 30(8), 2194-2205.

Kashyap, J., Griffith, M., Mohamed Ali, M. and Oehlers, D. (2011). "Prediction of Load-Slip Behavior of FRP Retrofitted Masonry." *Journal of Composites for Construction*, 15(6), 943-951.

Kuzik, M. D., Elwi, A. E. and Cheng, J. J. R. (2003). "Cyclic Flexure Tests of Masonry Walls Reinforced with Glass Fiber Reinforced Polymer Sheets." *Journal of Composites for Construction,ASCE*, 7(1), 20-30.

Kyriakides, M. A., Hendriks, M. A. N. and Billington, S. L. (2012). "Simulation of Unreinforced Masonry Beams Retrofitted with Engineered Cementitious Composites in Flexure." *Journal of Materials in Civil Engineering*, 24(5), 506-515.

Lee, J. and Fenves, G. L. (1998). "Plastic-Damage Model for Cyclic Loading of Concrete Structures." *Journal of Engineering Mechanics*, 124(8), 892-900.

Lotfi, H. R. and Shing, P. B. (1994). "Interface Model Applied to Fracture of Masonry Structures." *Journal of Structural Engineering, ASCE*, 120(1), 63-80.

Lourenço, P. B. (1996). "COMPUTATIONAL STRATEGIES FOR MASONRY STRUCTURES." Civil Engineering Department, Delft University of Technology, Delft, The Netherlands.

Lourenço, P. B., J.G.Rots and J.Blaauwendraad (1995). "Two Approaches for the Analysis of Masonry Structures: Micro and Macro-Modeling." *HERON*, 40(4), 313-340.

Lourenço, P. B. and Rots, J. G. (1997). "Multisurface Interface Model for Analysis of Masonry Structures." *Journal of Engineering Mechanics*, 123(7), 660-668.

Lourenço, P. B., Rots, J. G. and Blaauwendraad, J. (1998). "Continuum Model for Masonry: Parameter Estimation and Validation." *Journal of Structural Engineering,ASCE*, 124(6), 642-652.

Lu, X. Z., Jiang, J. J., Teng, J. G. and Ye, L. P. (2006). "Finite element simulation of debonding in FRP-to-concrete bonded joints." *Construction and Building Materials*, 20(6), 412-424.

Lu, X. Z., Teng, J. G., Ye, L. P. and Jiang, J. J. (2005a). "Bond-slip models for FRP sheets/plates bonded to concrete." *Engineering Structures*, 27(6), 920-937.

Lu, X. Z., Ye, L. P., Teng, J. G. and Jiang, J. J. (2005b). "Meso-scale finite element model for FRP sheets/plates bonded to concrete." *Engineering Structures*, 27(4), 564-575.

Lubliner, J., Oliver, J., Oller, S. and Oñate, E. (1989). "A plastic-damage model for concrete." *International Journal of Solids and Structures*, 25(3), 299-326.

Lunn, D. S. and Rizkalla, S. H. (2011). "Strengthening of Infill Masonry Walls with FRP Materials." *Journal of Composites for Construction,ASCE*, 15(2), 206-214.

Marfia, S. and Sacco, E. (2005). "Numerical Procedure for Elasto-Plastic No-Tension Model." *International Journal for Computational Methods in Engineering Science and Mechanics*, 6(3), 187-199.

Menetrey, P. and Willam, K. J. (1995). "Triaxial Failure Criterion for Concrete and its Generalization." *ACI Structural Journal*, 92(3), 311-318.

Milani, G. (2010). "3D FE limit analysis model for multi-layer masonry structures reinforced with FRP strips." *International Journal of Mechanical Sciences*, 52(6), 784-803.

Milani, G., Lourenço, P. B. and Tralli, A. (2006a). "Homogenised limit analysis of masonry walls, Part I: Failure surfaces." *Computers & Structures*, 84(3-4), 166-180.

Milani, G., Lourenço, P. B. and Tralli, A. (2006b). "Homogenised limit analysis of masonry walls, Part II: Structural examples." *Computers & Structures*, 84(3-4), 181-195.

Milani, G., Milani, E. and Tralli, A. (2009a). "Upper Bound limit analysis model for FRP-reinforced masonry curved structures. Part I: Unreinforced masonry failure surfaces." *Computers & Structures*, 87(23-24), 1516-1533.

Milani, G., Milani, E. and Tralli, A. (2009b). "Upper bound limit analysis model for FRP-reinforced masonry curved structures. Part II: Structural analyses." *Comput. Struct.*, 87(23-24), 1534-1558.

Milani, G., Rotunno, T., Sacco, E. and Tralli, A. (2006c). "Failure load of FRP strengthened masonry walls: experimental results and numerical models." *Structural Durability and Health Monitoring*, 2(1), 29-50.

Mosallam, A. S. (2007). "Out-of-plane flexural behavior of unreinforced red brick walls strengthened with FRP composites." *Composites Part B: Engineering*, 38(5–6), 559-574.

Nakaba, K., Kanakubo, T., Furuta, T. and Yoshizawa, H. (2001). "Bond Behavior between Fiber-Reinforced Polymer Laminates and Concrete." *ACI Structural Journal*, 98(3), 359-367.

Ng, K. H. (1999). "Analysis of Masonry Arch Bridges."PhD Thesis, Napier University, Edinburgh.

Oliveira, D. V., Basilio, I. and Lourenço, P. B. (2011). "Experimental Bond Behavior of FRP Sheets Glued on Brick Masonry." *Journal of Composites for Construction,ASCE*, 15(1), 32-41.

Page, J. (1993). *Masonry Arch Bridges - TRL State of the Art Review*, HMSO.

Paquette, J., Bruneau, M. and Filiatrault, A. (2001). "Out-of-Plane Seismic Evaluation and Retrofit of Turn-of-the-Century North American Masonry Walls." *Journal of Structural Engineering,ASCE*, 127(5), 561-569.

Pelà, L., Aprile, A. and Benedetti, A. (2009). "Seismic assessment of masonry arch bridges." *Engineering Structures*, 31(8), 1777-1788.

Pham, H. B. and Al-Mahaidi, R. (2007). "Modelling of CFRP-concrete shear-lap tests." *Construction and Building Materials*, 21(4), 727-735.

Pham, H. B., Al-Mahaidi, R. and Saouma, V. (2006). "Modelling of CFRP-concrete bond using smeared and discrete cracks." *Composite Structures*, 75(1-4), 145-150.

Pippard, A. J. S. and Baker, J. F. (1968). *The analysis of engineering structures*, E. Arnold,, London.

Pluijm, R. v. d. (1997). "Non-linear Behaviour of Masonry under tension." *HERON*, 42(1), 25-55.

Prentice, D. J. (1996). "AN APPRAISAL OF THE GEOTECHNICAL ASPECTS OF MULTI-SPAN MASONRY ARCH BRIDGES."Ph.D Thesis, University of Edinburgh.

Quinn, D., Gupta, A., McPolin, D., Taylor, S. E. and Long, A. E. (2011)."Development, validation and application of the innovative FlexiArch system." In: *Proc., 4th Australian Small Bridge Conference 2011*, Albert Park, Melbourne, Australian.

Rankine, W. J. (1857). "On the stability of loose earth." *Philosophical Transactions of the Royal Society of London*, 147, 9-27.

Ricamato, M. (2007). "Numercial and experimental analysis of masonry arches strengthened with FRP materials."PhD thesis, University of Casino, Italy.

Robinson, J. (2000). "Analysis and Assessment of Masonry Arch Bridges."Ph.D Thesis, University of Edinburgh.

Rots, J. G. (1988). "Computational Modeling Of Concrete Fracture." Ph.D Thesis, Delft University of Technology, Delft.

Rots, J. G. (1991). "Smeared and discrete representations of localized fracture " *International Journal of Fracture* 51(1), 45-49.

Royles, R. and Hendry, A. W. (1991). "MODEL TESTS ON MASONRY ARCHES." *ICE Proceedings*, 91(2), 299-321.

Sacco, E. and Toti, J. (2010). "Interface Elements for the Analysis of Masonry Structures." *International Journal for Computational Methods in Engineering Science and Mechanics*, 11(6), 354-373.

Saenz, L. P. (1964). "Discussion of equation for the stress-strain curve of concrete-by Desayi, P. and Krishan, S." *ACI Journal* 61(9), 1229-1235.

Salomoni, V., Mazzucco, G., Pellegrino, C. and Majorana, C. (2011). "Three-dimensional modelling of bond behaviour between concrete and FRP reinforcement." *Engineering Computations*, 28(1), 5-29.

Seim, W. and Pfeiffer, U. (2011). "Local post-strengthening of masonry structures with fiber-reinforced polymers (FRPs)." *Construction and Building Materials*, 25(8), 3393-3403.

Seracino, R., Raizal Saifulnaz, M. and Oehlers, D. (2007). "Generic Debonding Resistance of EB and NSM Plate-to-Concrete Joints." *Journal of Composites for Construction*, 11(1), 62-70.

Stratford, T., Pascale, G., Manfroni, O. and Bonfiglioli, B. (2004). "Shear Strengthening Masonry Panels with Sheet Glass-Fiber Reinforced Polymer." *Journal of Composites for Construction*, 8(5), 434-443.

Su, Y., Wu, C. and Griffth, M. C. (2011). "Modelling of the bond–slip behavior in FRP reinforced masonry." *Construction and Building Materials*, 25(1), 328-334.

Sumon, S. K. (1997). "Repair and strengthening of a damaged arch with built-in ring separation." In: *Proc., 7th international conference on structural faults and repair*, Edinburgh, 69-75.

Täljsten, B. (1996). "Strengthening of concrete prisms using the plate-bonding technique." *International Journal of Fracture*, 82(3), 253-266.

Taylor, S. E., Gupta, A., Kirkpatrick, J. and Long, A. E. (2007). "Testing of a novel flexible concrete arch system." In: *Proc., Advanced Composites in Construction*, University of Bath, Bath, UK.

Teng, J. G., Chen, J. F., Simth, S. T. and Lam, T. (2002). *FRP-strengthened RC structures*, Wiley & Sons, UK.

Teng, J. G., Chen, J. F., Smith, S. T. and Lam, L. (2003a). "Behaviour and strength of FRP-strengthened RC structures: a state-of-the-art review." *Proceedings of the Institution of Civil Engineers*, 156(1), 51-62.

Teng, J. G., Smith, S. T., Yao, J. and Chen, J. F. (2003b). "Intermediate crack-induced debonding in RC beams and slabs." *Construction and Building Materials*, 17(6-7), 447-462.

Teng, J. G., Yuan, H. and Chen, J. F. (2006). "FRP-to-concrete interfaces between two adjacent cracks: Theoretical model for debonding failure." *International Journal of Solids and Structures*, 43(18-19), 5750-5778.

Thavalingam, A., Bicanic, N., Robinson, J. I. and Ponniah, D. A. (2001). "Computational framework for discontinuous modelling of masonry arch bridges." *Computers & Structures*, 79(19), 1821-1830.

Thorenfeldt, E., Tomaszewicz, A. and Jensen, J. J. (1987). "Mechanical properties of high strength concrete and application in design." In: *Proc., Symp. Utilization of High-Strength Concrete*, Stavanger, Norway.

Todeschini, C. E., Bianchini, A. C. and Kesler, C. E. (1964). "Behavior of Concrete Columns Reinforced with High Strength Steels." *ACI Journal Proceedings*, 61(6), 701-716.

Tomazevic, M. (1999). "Earthquake-resistant design of masonry buildings." *Series in innovation in structures and construction*, Imperial College Press, London.

Toutanji, H., Saxena, P., Zhao, L. and Ooi, T. (2007). "Prediction of Interfacial Bond Failure of FRP-Concrete Surface." *Journal of Composites for Construction,ASCE*, 11(4), 427-436.

Triantafillou, T. C. (1998). "Strengthening of Masonry Structures Using Epoxy-Bonded FRP Laminates." *Journal of Composites for Construction,ASCE*, 2(2), 96-104.

Tumialan, J., Galati, N. and Nanni, A. (2003). "Field Assessment of Unreinforced Masonry Walls Strengthened with Fiber Reinforced Polymer Laminates." *Journal of Structural Engineering*, 129(8), 1047-1056.

Tumialan, J. G., Morbin, A., Micelli, F. and Nanni, A. (2002). "FLEXURAL STRENGTHENING OF URM WALLS WITH FRP LAMINATES." In: *Proc., Third International Conference in Infrastructure (ICCI),*, San Francisco, USA.

Turek, M., Ventura, C. E. and Kuan, S. (2007). "In-Plane Shake-Table Testing of GFRP-Strengthened Concrete Masonry Walls." *Earthquake Spectra*, 23(1), 223-237.

Valluzzi, M. R., Tinazzi, D. and Modena, C. (2002). "Shear behavior of masonry panels strengthened by FRP laminates." *Construction and Building Materials*, 16(7), 409-416.

Valluzzi, M. R., Valdemarca, M. and Modena, C. (2001). "Behavior of Brick Masonry Vaults Strengthened by FRP Laminates." *Journal of Composites for Construction*, 5(3), 163-169.

Vermeltfoort, A. T. (2005). *Brick-mortar interaction in masonry under compression*, University Press Facilities, Eindhoven University of Technology,, Eindhoven, The Netherlands

Vinson, J. R. and Sierakowski, R. L. (2002). *The Behavior of Structures Composed of Composite Materials*, KLUWER ACADEMIC PUBLISHERS, Dordrecht, The Netherlans.

White, D. J., Take, W. A. and Bolton, M. D. (2003). "Soil deformation measurement using particle image velocimetry (PIV) and photogrammetry." *Géotechnique*, 53(7), 619-631.

Willis, C. R., Yang, Q., Seracino, R. and Griffith, M. C. (2009). "Bond behaviour of FRP-to-clay brick masonry joints." *Engineering Structures*, 31(11), 2580-2587.

Wu, E. M. and Router, J., R. C. (1965). "Crack Extension in Fiberglass Reinforced Plastics." *T. & AM Report No. 275*, University of Illinois.

Wu, Z. S., Yuan, H., Yoshizawa, H. and Kanakubo, T. (2001). "Experimental/Analytical Study on Interfacial Fracture Energy and Fracture Propagation Along FRP-Concrete Interface." *ACI International SP*, 201(8), 133-152.

Yamasaki, M. and Sasaki, Y. (2010). "Determining Young's modulus of timber on the basis of a strength database and stress wave propagation velocity I: an estimation method for Young's modulus employing Monte Carlo simulation." *Journal of Wood Science*, 56(4), 269-275.

Yang, Y. (1991). "Progressive failure analysis of masonry arch bridges."PhD Thesis, University of Wollongong, Wollongong, New South Wales, Australia.

Yang, Z. J. and Chen, J. (2005). "Finite element modelling of multiple cohesive discrete crack propagation in reinforced concrete beams." *Engineering Fracture Mechanics*, 72(14), 2280-2297.

Yang, Z. J., Chen, J. F. and Proverbs, D. (2003). "Finite element modelling of concrete cover separation failure in FRP plated RC beams." *Construction and Building Materials*, 17(1), 3-13.

Yao, J. and Teng, J. G. (2007). "Plate end debonding in FRP-plated RC beams--I: Experiments." *Engineering Structures*, 29(10), 2457-2471.

Yao, J., Teng, J. G. and Chen, J. F. (2005). "Experimental study on FRP-to-concrete bonded joints." *Composites Part B: Engineering*, 36(2), 99-113.

Yu, T., Teng, J. G., Wong, Y. L. and Dong, S. L. (2010). "Finite element modeling of confined concrete-II: Plastic-damage model." *Engineering Structures*, 32(3), 680-691.

Yuan, H., Teng, J. G., Seracino, R., Wu, Z. S. and Yao, J. (2004). "Full-range behavior of FRP-to-concrete bonded joints." *Engineering Structures*, 26(5), 553-565.

Zhuge, Y. (2010). "FRP-Retrofitted URM Walls under In-Plane Shear: Review and Assessment of Available Models." *Journal of Composites for Construction*, 14(6), 743-753.

Zucchini, A. and Lourenço, P. B. (2004). "A coupled homogenisation-damage model for masonry cracking." *Computers & Structures*, 82(11-12), 917-929.

APPENDIX 1

Calculation for the debond strain by using the model proposed by Chen and Teng (2002)

This section reports the calculation for the debond strain of FRP strengthened concrete masonry arch bridge in the Chapter 3. The paramters were summarized in Table A1-1. The debond strain can be calculated by using Eq A1-1 to A1-5.

Table A1-1 Parameters for calculation of debond strain

Compressive strength of concrete masonry f_{cm} (MPa)	Young's modulus of FRP E_p (GPa)	FRP thickness t_p (mm)	FRP width b_f (mm)		Width of arch b_c (mm)
			North arch	South arch	
25	170	1.4	300	600	1683

$$L_e = \sqrt{\frac{E_p t_p}{\sqrt{f_{cm}}}} = 218\ mm \tag{A1-1}$$

$$P_u = 0.427 \cdot \beta_w \cdot \beta_L \cdot \sqrt{f_{cm}} \cdot b_f \cdot L_e = \begin{cases} 173.8\ kN\ (north\ arch) \\ 307.6\ kN\ (south\ arch) \end{cases} \tag{A1-2}$$

where

$$\beta_w = \sqrt{\frac{2 - b_f / b_c}{1 + b_f / b_c}} = \begin{cases} 1.24\ (north\ arch) \\ 1.10\ (south\ arch) \end{cases} \tag{A1-3}$$

$$\beta_L = 1 \tag{A1-4}$$

The debond strain were:

$$\varepsilon_{debond} = \frac{P_u}{E_P t_P b_f} = \begin{cases} 2430\ \mu strain\ (north\ arch) \\ 2254\ \mu strain\ (south\ arch) \end{cases} \quad \text{(A1-5).}$$

APPENDIX 2

Hughes et al. (2002) spreadsheet calculations for the mechanism analysis of masonry arch bridge

The full details of this program and the software can be found from the following link: http://www.masonry.engineering.cf.ac.uk/. The theory and analysis of this spreadsheet program can be found from Hughes et al. (2002).

The spreadsheet was developed on a Microsoft Excel spreadsheet. The spreadsheet contains six macros that control the initialisation of the analysis, the running of the various modes of analysis and the drawing of the graphs. The main activity within the macros that run the analysis is to set up the appropriate constraints in optimisation routine.

The input data of the geometry of the arch was shown in Table A2-1, the material properties of the masonry arch was shown in Table A2-2, the properties of the backfill was shown in Table A2-3, and the loading condition was shown in Table A2-4.

Table A2-1 Arch geometry data

Span (m)	L	2.08
Rise at crown (m)	rise	1.04
Fill at crown (m)	fill	0.24
Ring thickness (m)	d	0.1

Table A2-2 Masonry material properties

Masonry density (kN/m^3)	dens_m	24.0
Yield stress (N/mm2)	stress	25.0
Mortar Loss (m)	mloss	0.000

Table A2-3 Properties of backfill

Fill density (kN/m3)	dens_f	15.2
Phi (degrees)	phi	33
Factor	e	0.2
Ratio height	f	0.2
Cohesion (kN/m2)	C	0

Table A2-4 Loading condition

Load dimension (m)	wheel	0.57
Dispersion angle (degrees)	disp	30
Position (x/span) (when fixed)		0.25

All remaining cells in the spreadsheet are calculated automatically by running the spreadsheet optimisation macros. The results inclueding the load carrying capacity of the maosnry arch and the corresponding hinge positions will be reported automatically.

APPENDIX 3

List of modelling parameters

This section summaries the modelling parametrs required in the FE analysis in the study. For modelling the bond behaviour of FRP-to-concrete substrates (i.e. concrete bricks in the Chapter 4), the parameters and equations were summarised in Table A3-1.

Table A3-1 Modelling parameters for the bond behaviour of FRP-to-concrete

Model	Equation and parameters	Ref.
Concrete compressive behaviour	$\sigma_c = \frac{E_0 \varepsilon_c}{1 + \left(\frac{E_0 \varepsilon_p}{\sigma_p} - 2\right)\left(\frac{\varepsilon_c}{\varepsilon_p}\right) + \left(\frac{\varepsilon_c}{\varepsilon_p}\right)^2}$	Saenz (1964)
	$E_0 = 4730\sqrt{f_c'}$	ACI 318 (2002)
	$\sigma_p = f_c'$	Cylinder compressive strength or from test
	$\varepsilon_p = 0.002$	CEB-FIP (1991)
Concrete Tensile behaviour	$\frac{\sigma_t}{f_t} = \left[1 + \left(c_1 \frac{w_t}{w_{cr}}\right)^3\right] e^{\left(-c_2 \frac{w_t}{w_{cr}}\right)} - \frac{w_t}{w_{cr}}\left(1 + c_1^3\right) e^{(-c_2)}$ $w_{cr} = 5.14 \frac{G_F}{f_t}$, c_1=3.0, and c_2 =6.93	Hordijk (1991)
	$f_t = 1.4\left(\frac{f_c' - 8}{10}\right)^{\frac{2}{3}}$	CEB-FIP (1991)

	$G_F = \left(0.0469 d_a^2 - 0.5 d_a + 26\right)\left(\frac{f_c'}{10}\right)^{0.7}$ d_a=maximum aggreagte size (20mm usually assumed if no test data available)	
Damage model	$k = \frac{\bar{\varepsilon}^p}{\varepsilon^p} = \frac{\sigma}{f}$ $d = \frac{(1-k)\varepsilon^p}{(1-k)\varepsilon^p + \sigma / E_0}$	Developed in Chapter 4

For modelling of masonry arch bridge with sand backfill in Chapter 5, the parameters were summarized in Table A3-2.

Table A3-2 Modelling parameters for the masonry arch bridge

Model		Parameters	Ref.
Concrete brick	Compressive behaviour	$f_{cb} = 58.2\ MPa$	Test
		$E_b = 4730\sqrt{f_{cb}}$	ACI 318 (2002)
		$\sigma \sim \varepsilon$ (Eq. 5-1)	Saenz (1964)
	Tensile behaviour	f_{tb} (Eq. 5-12)	ACI 318 (2002)
		$\sigma \sim w$ (Eq. 5-2 & 5-3)	Hordijk (1991) Pluijm (1997)
		G_{fb}^I (Eq. 5-4)	CEB-FIP (1991)
Mortar joint	Compressive behaviour	$f_{ci} = 12\ MPa$	BS 998-2 (2010)
		$\sigma \sim \varepsilon$ (Eq. 5-1)	Saenz (1964)
	Tensile behaviour	$f_{ti} = 0.1\ MPa$	Test
		$\sigma \sim w$ (Eq. 5-2 & 5-3)	Hordijk (1991) Pluijm (1997)
		$G_{cn}^0 = 0.066\ Nmm/mm^2$	CEB-FIP (1991)

		(Eq. 5-4) Effects of this parameter was investigated in section 5.7.1.	
Sand backfill	Mohr-Coulomb plastic model	$E_{sand}=10\ MPa$.	Suggested by Fairfield (1994b), Prentice (1996) and Thavalingam et al. (2001) for the same sand.
		$\phi = 33^o$ (internal friction angel)	Test
		$c=100Pa$ (cohesion of material)	Assumprtion for cohesionless material to avoid the numercial problem when c is too small

For modelling of FRP strengthening masonry arch bridge in Chapter 6, apart from the parameters for the masony arch, the parameters for the bond interface were already summarized in Table 6-2.